

6L00619

BOREHOLE-TO-SURFACE DIRECT CURRENT RESISTIVITY EXPERIMENT

by

Erika Gasperikova

A thesis submitted to the faculty of
The University of Utah
in partial fulfillment of the requirements for the degree of

Master of Science

in

Geophysics

Department of Geology and Geophysics

The University of Utah

June 1996

Copyright © Erika Gasperikova 1996

All Rights Reserved

THE UNIVERSITY OF UTAH GRADUATE SCHOOL

SUPERVISORY COMMITTEE APPROVAL

of a thesis submitted by

Erika Gasperikova

This thesis has been read by each member of the following supervisory committee and by majority vote has been found to be satisfactory.

Chair: Alan C. Tripp

Gerard T. Schuster

Ronald L. Bruhn

THE UNIVERSITY OF UTAH GRADUATE SCHOOL

FINAL READING APPROVAL

To the Graduate Council of the University of Utah:

I have read the thesis of _____ Erika Gasperikova _____ in its final form and have found that (1) its format, citations, and bibliographic style are consistent and acceptable; (2) its illustrative materials including figures, tables, and charts are in place; and (3) the final manuscript is satisfactory to the supervisory committee and is ready for submission to The Graduate School.

Date

Alan C. Tripp
Chair: Supervisory Committee

Approved for the Major Department

John M. Bartley
Chair

Approved for the Graduate Council

Ann W. Hart
Dean of The Graduate School

ABSTRACT

Surface-to-borehole and cross-borehole electric resistivity measurements have been promoted for many years as a means of better resolving geothermal or hydrocarbon reservoirs - thereby facilitating better production of the reservoir. Although enthusiasm for these techniques has been high, a great deal of progress in understanding data collection and interpretation needs to be made before the technique is of practical use.

This thesis addresses these needs in several ways. First it examines the application of a direct current (DC) resistivity tensor bipole-dipole regional data collection technique to the problem at hand, using both surface and buried electrodes. It then applies the technique to a field experiment in the Ferron Sandstone, which has a great deal of geologic control and target zones which are fairly shallow. Finally, the data is interpreted using available interpretation software and correlated with known geology.

As advertised in previous works, the tensor bipole-dipole method proves to be a rapid means of areal reconnaissance, even when used with downhole electrodes. Model studies demonstrate that the use of a downhole electrode greatly increases the resolution of the technique with respect to depth. Unfortunately, even so, three-dimensional (3-D) geoelectric features affect the data so strongly that a two-dimensional (2-D) interpretation algorithm proved dimensionally inadequate for data interpretation, while a 3-D fully-rigorous volume integral equations scheme was very expensive to use, in part due to the lack of layered earth Green's functions, which

forced the discretization of the discrete layers at the field site.

The final model used to interpret the data contained major geoelectric units at the field site, and gave a gross match to the field data, but the inadequacy of the interpretation software prevented an adequate utilization of all the information contained in the data. Additional data with the transmitter borehole electrode at varying depths in the borehole would have increased the resolution of the method, as demonstrated by model studies.

In conclusion, the "pilot field study" discussed in the thesis demonstrates that borehole-to-surface electrical studies of a shallow reservoir is possible, but interpretation of any but gross features will require modeling algorithms of great versatility, as well as a great deal of attention to constraining known geoelectric features.

TABLE OF CONTENTS

	Page
ABSTRACT	iv
LIST OF FIGURES	vii
ACKNOWLEDGMENTS	xix
1. INTRODUCTION	1
2. GEOLOGICAL SETTING	5
3. TARGET DEFINITION	14
4. DATA ACQUISITION	23
5. TENSOR CALCULATIONS	28
6. MODELING	34
7. DISCUSSION AND INTERPRETATION OF FIELD DATA	43
8. CONCLUSIONS	99
APPENDICES	
A. THEORETICAL RESPONSE OF 1-D AND 2-D CONDUCTIVE STRUCTURES IN A RESISTIVE BACKGROUND	101
B. THEORETICAL RESPONSE OF 1-D AND 2-D RESISTIVE STRUCTURES IN A LOW RESISTIVITY BACKGROUND	154
C. EFFECT OF INHOMOGENEITIES AT TRANSMITTER OR RECEIVER LOCATIONS	182
REFERENCES	191

LIST OF FIGURES

Figure	Page
1. Location map of the Ferron Sandstone Member of the Mancos Shale.	6
2. Schematic illustration of the river-dominated delta.	8
3. Schematic cross-section showing the stacking pattern of the upper Ferron Sandstone.	11
4. Stratigraphic correlation - Ferron Sandstone, Muddy Creek Area, Utah.	16
5. Field setup for borehole-to-surface DC resistivity experiment. A ₁ , A ₂ , B ₁ , B ₂ , B ₄ , B ₅ are surface current electrodes, while B ₃ and B ₆ are downhole current electrodes, M, N, N' are potential electrodes which move around the grid 1, 2, 3, 4, 5, 6, 7, 8, 9 are line numbers	24
6. Discretization grid for 2-D finite element algorithm.	35
7. Total apparent resistivity range in percentage of background resistivity for different resistivity contrasts.	40
8. Schlumberger sounding curve for the 1-D model based on information from UURI#1 well-log.	45
9. Schlumberger sounding curve for the 1-D model based on information from UURI#2 well-log.	47
10. Schlumberger sounding curves for a 1000 Ohm-m layer in 100 Ohm-m resistive background with and without a 10 Ohm-m layer below it.	49
11. Contour map of the total apparent resistivity for a) 25 m thick 10 Ohm-m layer 125 m deep in a 100 Ohm-m background b) 5 m thick 2 Ohm-m layer 125 m deep in a 100 Ohm-m background.	51

12.	Total apparent resistivity curves vs. distance for UURI#1.	54
13.	Total apparent resistivity curves vs. distance for UURI#2.	58
14.	Contour map of total apparent resistivity for UURI#1 bipole 1.	63
15.	Contour map of total apparent resistivity for UURI#1 bipole 2.	65
16.	Contour map of total apparent resistivity for UURI#1 bipole 3.	67
17.	Contour map of total apparent resistivity for UURI#2 bipole 1.	70
18.	Contour map of total apparent resistivity for UURI#2 bipole 2.	72
19.	Contour map of total apparent resistivity for UURI#2 bipole 3.	74
20.	Contour map of total apparent resistivity for UURI#1 bipole 2 configuration as a response of 12.5 m thick, 10 Ohm-m, 75 m deep layer overlaid by 12.5 m thick, 5000 Ohm-m, 50 m deep layer in a 100 Ohm-m resistive host.	77
21.	Contour map of total apparent resistivity for UURI#1 bipole 3 configuration as a response of 12.5 m thick, 10 Ohm-m, 75 m deep layer overlaid by 12.5 m thick, 5000 Ohm-m, 50 m deep layer in a 100 Ohm-m resistive host.	79
22.	Canyon influence on the apparent resistivity.	81
23.	Contour map of the P_2 tensor invariant for UURI#1 using bipole 1 and bipole 2.	82
24.	Contour map of the P_2 tensor invariant for UURI#1 using bipole 1 and bipole 3.	84
25.	Contour map of the P_2 tensor invariant for UURI#2 using bipole 1 and bipole 2.	86
26.	Contour map of the P_2 tensor invariant for UURI#2 using bipole 1 and bipole 3.	88

27.	Contour map of total apparent resistivity for UURI#1 bipole 1 configuration, as a response of 12.5 m thick, 10 Ohm-m, 75 m deep layer overlaid by 12.5 m thick, 5000 Ohm-m, 50 m deep layer in a 100 Ohm-m resistive host, with an 80 m deep canyon on the southeast side of the study area and a conductive structure close to UURI#1 location.	91
28.	Contour map of total apparent resistivity for UURI#1 bipole 2 configuration, as a response of 12.5 m thick, 10 Ohm-m, 75 m deep layer overlaid by 12.5 m thick, 5000 Ohm-m, 50 m deep layer in a 100 Ohm-m resistive host, with an 80 m deep canyon on the southeast side of the study area and a conductive structure close to UURI#1 location.	93
29.	Contour map of the P_2 tensor invariant for UURI#1 using bipole 1 and bipole 2, as a response of 12.5 m thick, 10 Ohm-m, 75 m deep layer overlaid by 12.5 m thick, 5000 Ohm-m, 50 m deep layer in a 100 Ohm-m resistive host, with an 80 m deep canyon on the southeast side of the study area and a conductive structure close to UURI#1 location.	95
30.	Total field apparent resistivity contour maps for a 25 m thick, 25 m deep layer, of 10 Ohm-m resistivity, with a background resistivity of 300 Ohm-m. a) bipole 1, b) bipole 2, c) bipole 3	103
31.	Total field apparent resistivity contour maps for a 25 m thick, 50 m deep layer, of 10 Ohm-m resistivity, with a background resistivity of 300 Ohm-m. a) bipole 1, b) bipole 2, c) bipole 3	104
32.	Total field apparent resistivity contour maps for a 25 m thick, 75 m deep layer, of 10 Ohm-m resistivity, with a background resistivity of 300 Ohm-m. a) bipole 1, b) bipole 2, c) bipole 3	105
33.	Total field apparent resistivity contour maps for a 25 m thick, 100 m deep layer, of 10 Ohm-m resistivity, with a background resistivity of 300 Ohm-m. a) bipole 1, b) bipole 2, c) bipole 3	106
34.	Total field apparent resistivity contour maps for a 25 m thick, 125 m deep layer, of 10 Ohm-m resistivity, with a background resistivity of 300 Ohm-m. a) bipole 1, b) bipole 2, c) bipole 3	107
35.	Total field apparent resistivity contour maps for a 25 m thick, 150 m deep layer, of 10 Ohm-m resistivity, with a background resistivity of 300 Ohm-m. a) bipole 1, b) bipole 2, c) bipole 3	108

36.	The P_2 -invariant contour maps for a 25 m thick layer, of 10 Ohm-m resistivity, with a background resistivity of 300 Ohm-m, using bipole 1 and bipole 2.	110
	a) 25 m deep layer	
	b) 50 m deep layer	
	c) 75 m deep layer	
	d) 100 m deep layer	
	e) 125 m deep layer	
	f) 150 m deep layer	
37.	The P_2 -invariant contour maps for a 25 m thick layer, of 10 Ohm-m resistivity, with a background resistivity of 300 Ohm-m, using bipole 1 and bipole 3.	113
	a) 25 m deep layer	
	b) 50 m deep layer	
	c) 75 m deep layer	
	d) 100 m deep layer	
	e) 125 m deep layer	
	f) 150 m deep layer	
38.	Total field apparent resistivity contour maps for a 25 m thick, 200 m wide, 25 m deep body, of 10 Ohm-m resistivity, with a background resistivity of 300 Ohm-m. a) bipole 1, b) bipole 2, c) bipole 3	117
39.	Total field apparent resistivity contour maps for a 25 m thick, 200 m wide, 50 m deep body, of 10 Ohm-m resistivity, with a background resistivity of 300 Ohm-m. a) bipole 1, b) bipole 2, c) bipole 3	118
40.	Total field apparent resistivity contour maps for a 25 m thick, 200 m wide, 75 m deep body, of 10 Ohm-m resistivity, with a background resistivity of 300 Ohm-m. a) bipole 1, b) bipole 2, c) bipole 3	119
41.	Total field apparent resistivity contour maps for a 25 m thick, 200 m wide, 100 m deep body, of 10 Ohm-m resistivity, with a background resistivity of 300 Ohm-m. a) bipole 1, b) bipole 2, c) bipole 3	120

42.	Total field apparent resistivity contour maps for a 25 m thick, 200 m wide, 125 m deep body, of 10 Ohm-m resistivity, with a background resistivity of 300 Ohm-m. a) bipole 1, b) bipole 2, c) bipole 3	121
43.	Total field apparent resistivity contour maps for a 25 m thick, 200 m wide, 150 m deep body, of 10 Ohm-m resistivity, with a background resistivity of 300 Ohm-m. a) bipole 1, b) bipole 2, c) bipole 3	122
44.	The P_2 -invariant contour maps for a 25 m thick, 200 m wide body, of 10 Ohm-m resistivity, with a background resistivity of 300 Ohm-m, using bipole 1 and bipole 2. a) 25 m deep body b) 50 m deep body c) 75 m deep body d) 100 m deep body e) 125 m deep body f) 150 m deep body	123
45.	The P_2 -invariant contour maps for a 25 m thick, 200 m wide body, of 10 Ohm-m resistivity, with a background resistivity of 300 Ohm-m, using bipole 1 and bipole 3. a) 25 m deep body b) 50 m deep body c) 75 m deep body d) 100 m deep body e) 125 m deep body f) 150 m deep body	127
46.	25 m thick, 50 m deep layer, of 10 Ohm-m resistivity, with a background resistivity of 100 Ohm-m. a) total field apparent resistivity contour map for bipole 1 b) total field apparent resistivity contour map for bipole 2 c) P_2 -invariant contour map using bipole 1 and bipole 2	130
47.	25 m thick, 50 m deep layer, of 10 Ohm-m resistivity, with a background resistivity of 200 Ohm-m. a) total field apparent resistivity contour map for bipole 1 b) total field apparent resistivity contour map for bipole 2 c) P_2 -invariant contour map using bipole 1 and bipole 2	131

48.	25 m thick, 50 m deep layer, of 10 Ohm-m resistivity, with a background resistivity of 300 Ohm-m.	
	a) total field apparent resistivity contour map for bipole 1	
	b) total field apparent resistivity contour map for bipole 2	
	c) P_2 -invariant contour map using bipole 1 and bipole 2	132
49.	25 m thick, 50 m deep layer, of 10 Ohm-m resistivity, with a background resistivity of 500 Ohm-m.	
	a) total field apparent resistivity contour map for bipole 1	
	b) total field apparent resistivity contour map for bipole 2	
	c) P_2 -invariant contour map using bipole 1 and bipole 2	133
50.	25 m thick, 50 m deep layer, of 10 Ohm-m resistivity, with a background resistivity of 1000 Ohm-m.	
	a) total field apparent resistivity contour map for bipole 1	
	b) total field apparent resistivity contour map for bipole 2	
	c) P_2 -invariant contour map using bipole 1 and bipole 2	134
51.	25 m thick, 50 m deep layer, of 1 Ohm-m resistivity, with a background resistivity of 300 Ohm-m.	
	a) total field apparent resistivity contour map for bipole 1	
	b) total field apparent resistivity contour map for bipole 2	
	c) P_2 -invariant contour map using bipole 1 and bipole 2	136
52.	25 m thick, 50 m deep layer, of 10 Ohm-m resistivity, with a background resistivity of 300 Ohm-m.	
	a) total field apparent resistivity contour map for bipole 1	
	b) total field apparent resistivity contour map for bipole 2	
	c) P_2 -invariant contour map using bipole 1 and bipole 2	137
53.	25 m thick, 50 m deep layer, of 20 Ohm-m resistivity, with a background resistivity of 300 Ohm-m.	
	a) total field apparent resistivity contour map for bipole 1	
	b) total field apparent resistivity contour map for bipole 2	
	c) P_2 -invariant contour map using bipole 1 and bipole 2	138
54.	25 m thick, 50 m deep layer, of 30 Ohm-m resistivity, with a background resistivity of 300 Ohm-m.	
	a) total field apparent resistivity contour map for bipole 1	
	b) total field apparent resistivity contour map for bipole 2	
	c) P_2 -invariant contour map using bipole 1 and bipole 2	139

55.	25 m thick, 50 m deep layer, of 50 Ohm-m resistivity, with a background resistivity of 300 Ohm-m.	
	a) total field apparent resistivity contour map for bipole 1	
	b) total field apparent resistivity contour map for bipole 2	
	c) P_2 -invariant contour map using bipole 1 and bipole 2	140
56.	25 m thick, 50 m deep layer, of 100 Ohm-m resistivity, with a background resistivity of 300 Ohm-m.	
	a) total field apparent resistivity contour map for bipole 1	
	b) total field apparent resistivity contour map for bipole 2	
	c) P_2 -invariant contour map using bipole 1 and bipole 2	141
57.	25 m thick, 50 m deep layer, of 1 Ohm-m resistivity, with a background resistivity of 100 Ohm-m.	
	a) total field apparent resistivity contour map for bipole 1	
	b) total field apparent resistivity contour map for bipole 2	
	c) P_2 -invariant contour map using bipole 1 and bipole 2	142
58.	25 m thick, 50 m deep layer, of 1 Ohm-m resistivity, with a background resistivity of 200 Ohm-m.	
	a) total field apparent resistivity contour map for bipole 1	
	b) total field apparent resistivity contour map for bipole 2	
	c) P_2 -invariant contour map using bipole 1 and bipole 2	143
59.	25 m thick, 50 m deep layer, of 1 Ohm-m resistivity, with a background resistivity of 300 Ohm-m.	
	a) total field apparent resistivity contour map for bipole 1	
	b) total field apparent resistivity contour map for bipole 2	
	c) P_2 -invariant contour map using bipole 1 and bipole 2	144
60.	25 m thick, 50 m deep layer, of 1 Ohm-m resistivity, with a background resistivity of 500 Ohm-m.	
	a) total field apparent resistivity contour map for bipole 1	
	b) total field apparent resistivity contour map for bipole 2	
	c) P_2 -invariant contour map using bipole 1 and bipole 2	145
61.	25 m thick, 50 m deep layer, of 1 Ohm-m resistivity, with a background resistivity of 1000 Ohm-m.	
	a) total field apparent resistivity contour map for bipole 1	
	b) total field apparent resistivity contour map for bipole 2	

	c) P_2 -invariant contour map using bipole 1 and bipole 2	146
62.	10 m thick, 10 m deep layer, of 10 Ohm-m resistivity, with a background resistivity of 500 Ohm-m. a) total field apparent resistivity contour map for bipole 1 b) total field apparent resistivity contour map for bipole 2 c) P_2 -invariant contour map using bipole 1 and bipole 2	147
63.	10 m thick, 10 m deep layer, of 10 Ohm-m resistivity, with a background resistivity of 500 Ohm-m. a) total field apparent resistivity contour map for bipole 1 b) total field apparent resistivity contour map for bipole 3 c) P_2 -invariant contour map using bipole 1 and bipole 3	148
64.	100 m thick, 250 m wide, 75 m deep body, of 10 Ohm-m resistivity, with a background resistivity of 500 Ohm-m. a) total field apparent resistivity contour map for bipole 1 b) total field apparent resistivity contour map for bipole 2 c) P_2 -invariant contour map using bipole 1 and bipole 2	149
65.	100 m thick, 250 m wide, 75 m deep body, of 10 Ohm-m resistivity, with a background resistivity of 500 Ohm-m. a) total field apparent resistivity contour map for bipole 1 b) total field apparent resistivity contour map for bipole 3 c) P_2 -invariant contour map using bipole 1 and bipole 3	150
66.	100 m thick, 250 m wide, 75 m deep body, of 10 Ohm-m resistivity, with a 10 m thick, 10 m deep layer, of 10 Ohm-m resistivity, in a 500 Ohm-m background. a) total field apparent resistivity contour map for bipole 1 b) total field apparent resistivity contour map for bipole 2 c) P_2 -invariant contour map using bipole 1 and bipole 2	151
67.	100 m thick, 250 m wide, 75 m deep body, of 10 Ohm-m resistivity, with a 10 m thick, 10 m deep layer, of 10 Ohm-m resistivity, in a 500 Ohm-m background. a) total field apparent resistivity contour map for bipole 1 b) total field apparent resistivity contour map for bipole 3 c) P_2 -invariant contour map using bipole 1 and bipole 3	152

68.	Total field apparent resistivity contour maps for a 30 m thick, 20 m deep layer, of 1000 Ohm-m resistivity, with a background resistivity of 100 Ohm-m. a) bipole 1, b) bipole 2, c) bipole 3	156
69.	Total field apparent resistivity contour maps for a 25 m thick, 50 m deep layer, of 1000 Ohm-m resistivity, with a background resistivity of 100 Ohm-m. a) bipole 1, b) bipole 2, c) bipole 3	157
70.	Total field apparent resistivity contour maps for a 25 m thick, 75 m deep layer, of 1000 Ohm-m resistivity, with a background resistivity of 100 Ohm-m. a) bipole 1, b) bipole 2, c) bipole 3	158
71.	Total field apparent resistivity contour maps for a 25 m thick, 100 m deep layer, of 1000 Ohm-m resistivity, with a background resistivity of 100 Ohm-m. a) bipole 1, b) bipole 2, c) bipole 3	159
72.	Total field apparent resistivity contour maps for a 25 m thick, 125 m deep layer, of 1000 Ohm-m resistivity, with a background resistivity of 100 Ohm-m. a) bipole 1, b) bipole 2, c) bipole 3	160
73.	Total field apparent resistivity contour maps for a 25 m thick, 150 m deep layer, of 1000 Ohm-m resistivity, with a background resistivity of 100 Ohm-m. a) bipole 1, b) bipole 2, c) bipole 3	161
74.	The P_2 -invariant contour map for a 25 m thick layer, of 1000 Ohm-m resistivity, with a background resistivity of 100 Ohm-m, using bipole 1 and bipole 2. a) 25 m deep layer b) 50 m deep layer c) 75 m deep layer d) 100 m deep layer e) 125 m deep layer f) 150 m deep layer	163

75.	The P_2 -invariant contour map for a 25 m thick layer, of 1000 Ohm-m resistivity, with a background resistivity of 100 Ohm-m, using bipole 1 and bipole 3.	166
	a) 25 m deep layer	
	b) 50 m deep layer	
	c) 75 m deep layer	
	d) 100 m deep layer	
	e) 125 m deep layer	
	f) 150 m deep layer	
76.	Total field apparent resistivity contour maps for a 25 m thick and 200 m wide body, at the depth of 25 m, of 1000 Ohm-m resistivity, with a background resistivity of 100 Ohm-m. a) bipole 1, b) bipole 2, c) bipole 3	169
77.	Total field apparent resistivity contour maps for a 25 m thick and 200 m wide body, at the depth of 50 m, of 1000 Ohm-m resistivity, with a background resistivity of 100 Ohm-m. a) bipole 1, b) bipole 2, c) bipole 3	170
78.	Total field apparent resistivity contour maps for a 25 m thick and 200 m wide body, at the depth of 75 m, of 1000 Ohm-m resistivity, with a background resistivity of 100 Ohm-m. a) bipole 1, b) bipole 2, c) bipole 3	171
79.	Total field apparent resistivity contour maps for a 25 m thick and 200 m wide body, at the depth of 100 m, of 1000 Ohm-m resistivity, with a background resistivity of 100 Ohm-m. a) bipole 1, b) bipole 2, c) bipole 3	172
80.	Total field apparent resistivity contour maps for a 25 m thick and 200 m wide body, at the depth of 125 m, of 1000 Ohm-m resistivity, with a background resistivity of 100 Ohm-m. a) bipole 1, b) bipole 2, c) bipole 3	173
81.	Total field apparent resistivity contour maps for a 25 m thick and 200 m wide body, at the depth of 150 m, of 1000 Ohm-m resistivity, with a background resistivity of 100 Ohm-m. a) bipole 1, b) bipole 2, c) bipole 3	174

82. The P_2 -invariant contour map for a 25 m thick and 200 m wide body, of 1000 Ohm-m resistivity with a background resistivity of 100 Ohm-m, using bipole 1 and bipole 2. 176
- a) 25 m deep body
 - b) 50 m deep body
 - c) 75 m deep body
 - d) 100 m deep body
 - e) 125 m deep body
 - f) 150 m deep body
83. The P_2 -invariant contour map for a 25 m thick and 200 m wide body, of 1000 Ohm-m resistivity with a background resistivity of 100 Ohm-m, using bipole 1 and bipole 3. 179
- a) 25 m deep body
 - b) 50 m deep body
 - c) 75 m deep body
 - d) 100 m deep body
 - e) 125 m deep body
 - f) 150 m deep body
84. 50 Ohm-m block at transmitter site, with a background resistivity of 500 Ohm-m.
- a) total field apparent resistivity contour map for bipole 1
 - b) total field apparent resistivity contour map for bipole 2
 - c) P_2 -invariant contour map using bipole 1 and bipole 2 184
85. 500 Ohm-m block at transmitter site, with a background resistivity of 50 Ohm-m.
- a) total field apparent resistivity contour map for bipole 1
 - b) total field apparent resistivity contour map for bipole 2
 - c) P_2 -invariant contour map using bipole 1 and bipole 2 185
86. 50 Ohm-m block at receiver grid, with a background resistivity of 500 Ohm-m.
- a) total field apparent resistivity contour map for bipole 1
 - b) total field apparent resistivity contour map for bipole 2
 - c) P_2 -invariant contour map using bipole 1 and bipole 2 187
87. 50 Ohm-m block at current electrode B1 and B2 locations, with a background resistivity of 500 Ohm-m.
- a) total field apparent resistivity contour map for bipole 1

	b) total field apparent resistivity contour map for bipole 2	
	c) P_2 -invariant contour map using bipole 1 and bipole 2	188
88.	500 Ohm-m block at current electrode B1 and B2 locations, with a background resistivity of 50 Ohm-m.	
	a) total field apparent resistivity contour map for bipole 1	
	b) total field apparent resistivity contour map for bipole 2	
	c) P_2 -invariant contour map using bipole 1 and bipole 2	189

ACKNOWLEDGMENTS

This work has been supported by the Department of Energy under contract number DE-AC07-90ID12929.

I wish to express my thanks to the Earth Science Laboratory, in particular, its director Dr. P. M. Wright for the support during this project. I would like to thank Dennis L. Nielson and Susan J. Lutz for valuable geological information about the field site. I thank Bob Turner for drafting some of my figures.

I am grateful to William Frangos and William Doerner for their help with the field data collection.

I thank the Institute of Geological and Nuclear Sciences in New Zealand for permission to use their modeling algorithm. Furthermore, I thank Hugh Bibby and Grant Caldwell who helped me understand tensor calculations and elucidated the modeling algorithms. I am indebted to Grant Caldwell, Prof. Frank Morrison, Ted Asch, and Phil Wannamaker for valuable discussions and helpful suggestions during the interpretation of the field data. I thank Dr. Alan Tripp for his advice during my study in Utah. I thank my committee members for reading my thesis.

I would like to thank Grant Caldwell and Ted Asch for their encouragement and moral support that I have received while I was writing this thesis.

1. INTRODUCTION

There has been a great deal of interest in using borehole-to-borehole and borehole-to-surface electrical measurements to enhance resolution of sub-surface features. In particular, direct current (DC) resistivity measurements using a combination of subsurface and surface electrodes can detect subsurface inhomogeneities which cannot be detected using surface measurements alone. Another advantage of these configurations is that they reduce the influence of near surface, uninteresting, inhomogeneities.

This thesis describes a borehole-to-surface DC resistivity experiment which probed the Ferron Sandstone Member of the Mancos Shale in Emery Co., central Utah, during the summer of 1993. The Ferron Sandstone consists of several relatively resistive sandstone units, which are separated by very thin and conductive shale layers created at the time when sedimentary conditions changed. The purpose of the experiment was to determine whether a borehole-to-surface technique could be used to delineate a relatively deep and thin conductive layer in a resistive environment. The area was particularly interesting because it is an excellent example of a fluvial-dominated deltaic system, and as such has been studied extensively (Lutz et al., 1993; Nielson et al., 1992; Ryer, 1981, 1983; Riemersma, 1989; Riemersma and Chan, 1991; Zelt, 1985). Fluvial-deltaic reservoirs contain the largest developed domestic oil reserves, in the United States, and due to the high degree of reservoir heterogeneity, the largest amount of unrecovered oil. The Ferron Sandstone is a world-class area to study reservoir heterogeneity. Hence our experiment is relevant in deciding whether

borehole-to-surface techniques might be useful for delineating reservoir geometry or heterogeneity.

Successful extraction of useful information from a field survey of this type requires care in both data collection and data interpretation. Both aspects are the subjects of an intensive literature, which includes contributions by Alfano (1962), Snyder and Merkel (1973), Daniels (1977, 1978), and Asch and Morrison (1989).

Unfortunately the proliferation of theoretical work is not matched by experimentation insofar as few borehole-to-surface field experiments have been presented in the literature. Among the few studies, Daniels (1983) made hole-to-surface resistivity measurements over a layered volcanic tuff sequence. He made a qualitative interpretation of his data by creating residual anomaly maps, calculated by subtracting a layered-earth model response from the field data. In a later experiment Bevc and Morrison (1991) demonstrated the sensitivity of borehole-to-surface resistivity measurements in groundwater investigations. This experiment showed that a borehole-to-surface electrical resistivity monitoring system is capable of data accurate enough to map subsurface groundwater flow in special cases.

In order to get the maximum amount of readily interpretable information about electrical properties of an area of interest, recent investigators have abandoned scalar measurements in favor of vector measurements. Bibby and Risk (1973) discussed taking resistivity measurements with two orthogonal receiver dipoles, and defining an apparent resistivity using the total electric field \vec{E} at the receiver site. The measurement of two components of the electric field eliminates data bias due to assuming a preferential transmitter - receiver orientation, as is the case for all dipole-dipole arrays measuring only one component. Model analysis by Doicin (1976) showed that

dependence on the transmitter - receiver orientation can be reduced further if a quadripole source and a quadripole receiver are used.

The new emphasis on augmented field measurements inspired a different approach to interpreting resistivity data via an apparent resistivity tensor linking multiple transmitter and multiple receiver measurements. The apparent resistivity tensor was first introduced by Bibby (1977). The properties of the apparent resistivity tensor were demonstrated for selected simple models by Bibby (1986). Bibby and Hohmann (1993) presented a series of three dimensional (3-D) models to show that many aspects of bipole-dipole mapping can be greatly improved by using two distinct current bipoles in the same location but with different orientations, combined with tensor apparent resistivity analysis.

In order to get maximum information about our study area tensor surface-to-surface and borehole-to-surface bipole-dipole data were gathered. To our knowledge, this is the first time a tensor analysis has been used for a borehole-to-surface experiment.

This thesis describes the field experiment, data modeling and analysis, and their interpretation. It concludes by assessing the applicability of the tensor technique to resolution of small conductive targets at depth.

The thesis proceeds in a methodical fashion. The geology of the Ferron Sandstone is described in Chapter 2. Chapter 3 discusses the geology of the study area in general, and the target of the field experiment in particular. The theory and practice of the field measurements is presented in Chapter 4. Tensor invariants are defined and characterized in Chapter 5. Chapter 6 contains a brief description of the algorithm used in this thesis with some modeling results. The field data and an interpretation is given in Chapter 7. Chapter 8 contains the conclusions and suggestions for future work.

Appendix A presents the theoretical apparent resistivity responses of 1-D and 2-D conductive structures in a resistive background. The responses of 1-D and 2-D resistive structures in a conductive background are presented in Appendix B. Appendix C contains models showing the effect of near-surface inhomogeneities on the measured response.

2. GEOLOGICAL SETTING

The borehole-to-surface DC resistivity experiment was performed in the Ferron Sandstone Member, Emery Co., Utah (Figure 1). The Ferron Sandstone is of interest to petroleum geologists since it is an excellent analog of a heterogeneous fluvial-deltaic reservoir. These reservoirs have potential undiscovered natural gas reserves and therefore evaluating the nature of the heterogeneity is of great economic significance. The Ferron Sandstone itself has been the subject of numerous scientific publications which have tried to develop better techniques of characterizing heterogeneities and it is used as a reservoir analog by a number of petroleum companies (Nielson et al., 1992).

The Ferron Sandstone can be divided into upper and lower members based on age, stratigraphic relationship, and facies analysis. The criteria for this discrimination follow.

The Upper Cretaceous Ferron Sandstone Member of the Mancos Shale is a well-exposed example of rocks deposited in a fluvial-dominated deltaic environment. It was created in a river-dominated deltaic system which existed along the western shoreline of the Interior Cretaceous seaway during late Turonian time (Ryer, 1981). A cartoon of the river-dominated delta is shown in Figure 2. As a delta progrades seaward, the more landward facies come to overlie the more seaward facies in a progradation sequence. The prodelta consists of interbedded mudstone and very fine-grained sandstone. The delta front contains very fine to medium-grained sandstone with minor interbeds of mudstone. The delta front sandstones are locally cut by distributary channels (Ryer, 1981). The distributaries are filled with cross-stratified sandstone,

Figure 1: Location map of the Ferron Sandstone Member of the Mancos Shale (modified after Ryer, 1981).

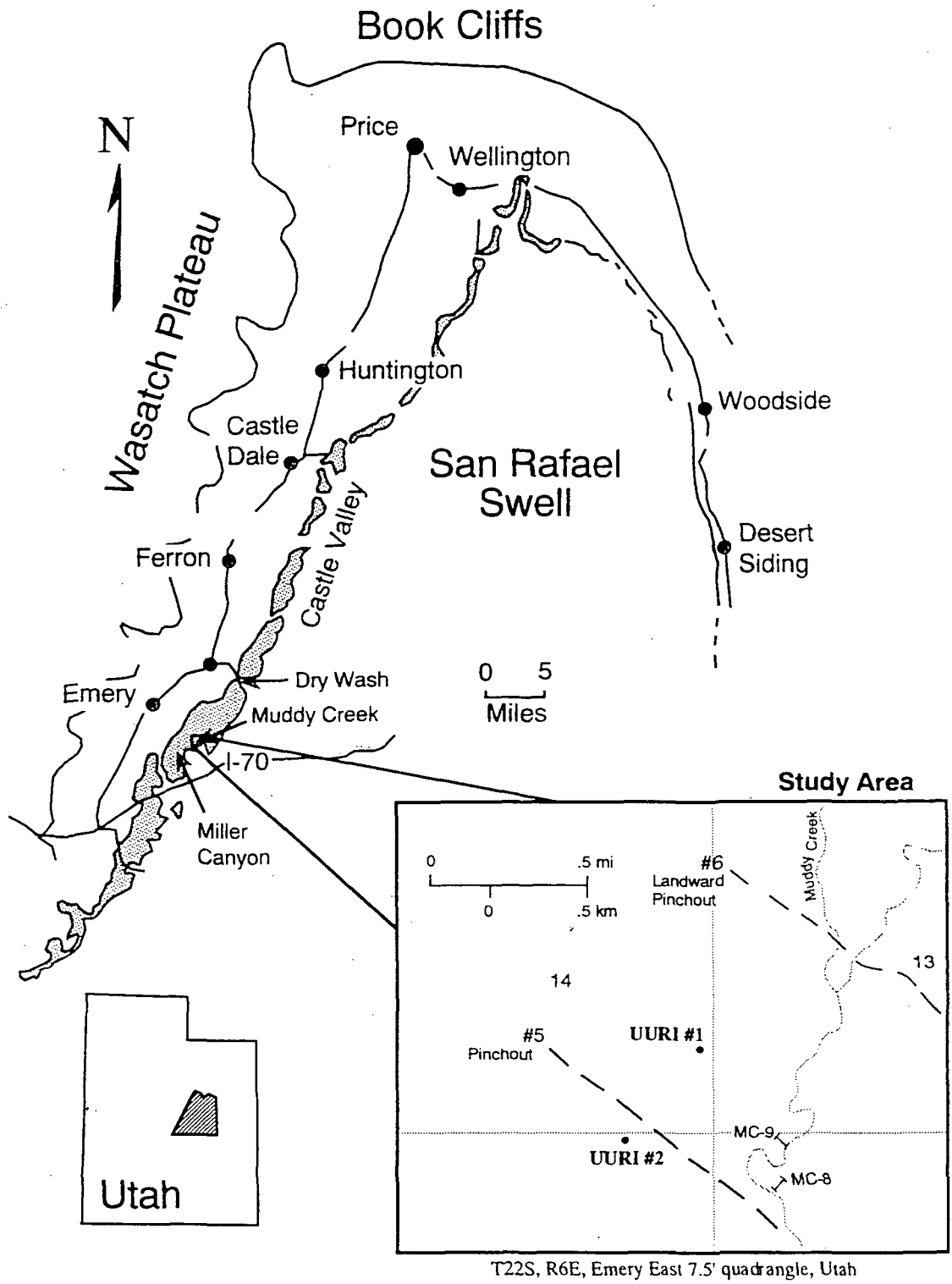
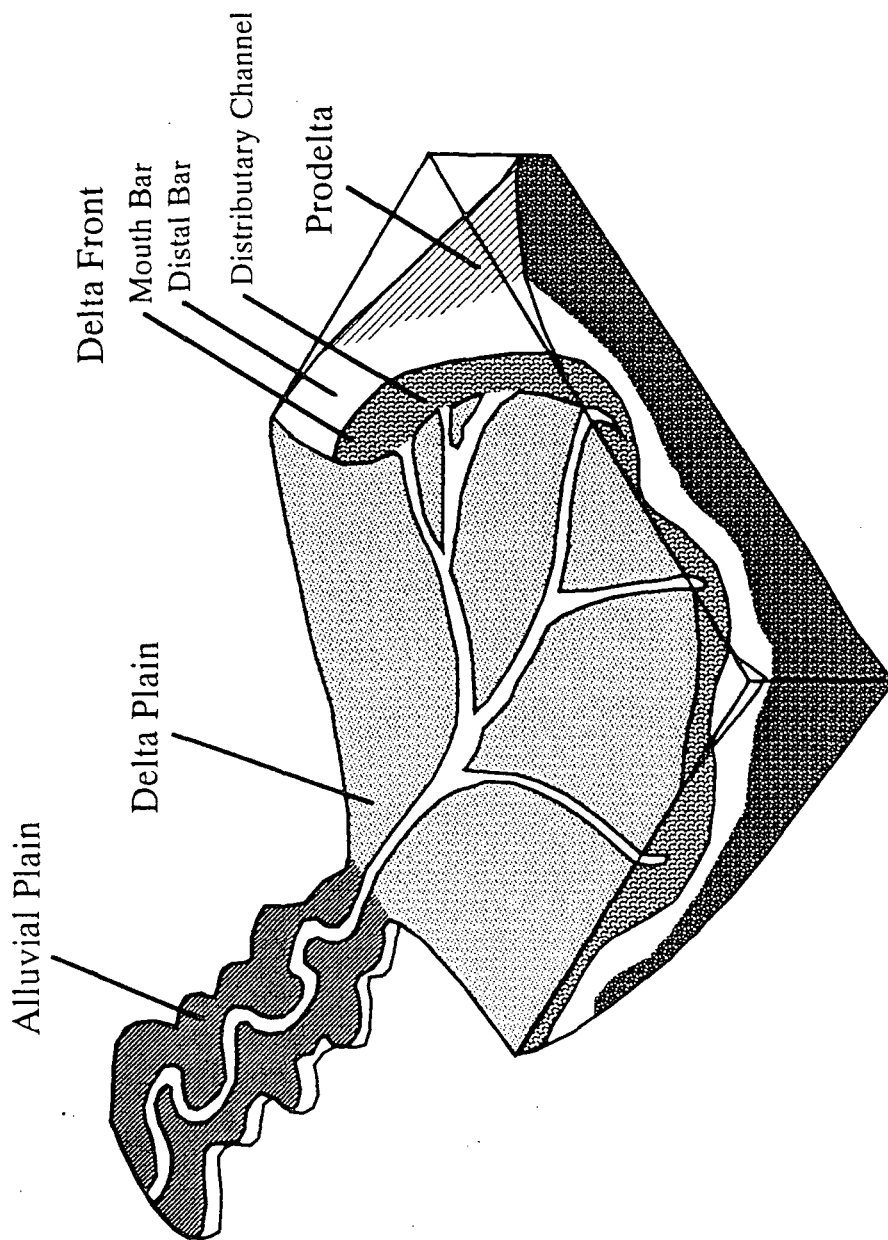


Figure 2: Schematic illustration of the river-dominated delta (modified after Ryer, 1981).



interbedded sandstone and mudstone, or carbonaceous mudstone (Ryer, 1981). The delta plain consists of a variety of subfacies. Bioturbated mudstones and siltstones are overlaid by laminated siltstone and cross-laminated sandstone. Carbonaceous shale or coal are on the top of this sequence. The channel fills may contain sandstone, siltstone, or shale. The alluvial plain consists of coarse to very fine-grained sandstone.

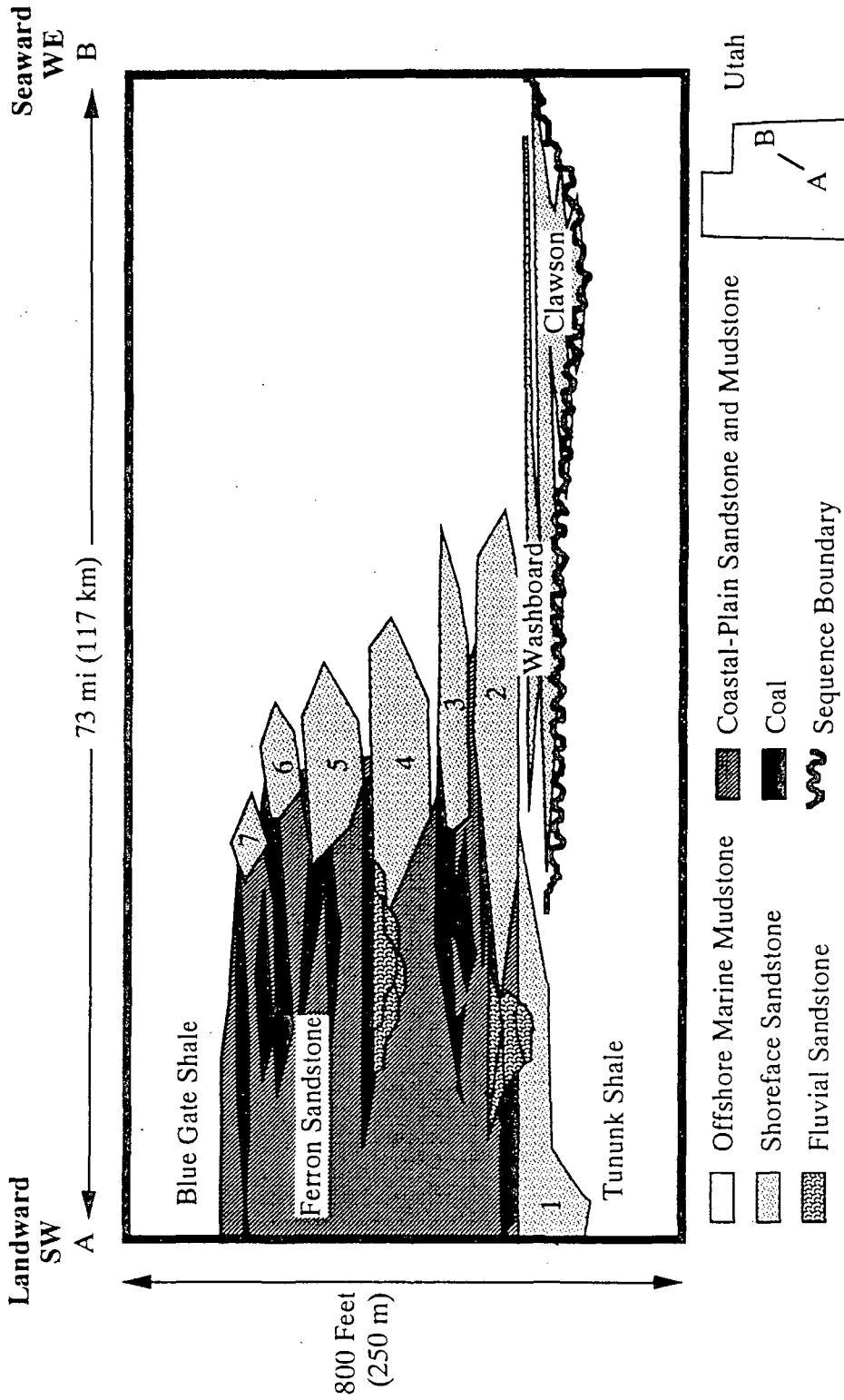
The western shoreline of the Interior Cretaceous seaway underwent a series of major transgressions and regressions during Late Cretaceous time (Kauffman, 1977, in Ryer, 1981). The regressions are represented by eastward-thinning of clastic sediments from the Sevier orogenic belt. The transgressions are represented by westward-thinning tongues of marine mudstone and shale.

According to Ryer (1981) the upper Ferron Sandstone Member is a series of deltaic systems stacked one above another, rather than a single progradation delta. Each deltaic system is underlain and overlain by erosional surfaces associated with preceding and succeeding transgressions. The upper Ferron consists of five major cycles of deltaic sedimentation. The structural dip is generally less than 10° to the northwest with few complications. A schematic cross-section showing the stacking pattern of the Ferron Sandstone is in Figure 3.

The Tununk Member of the Mancos Formation underlies the upper Ferron and is composed of off-shore marine shale that thickens to the southwest, documenting the subsiding foreland basin of the Sevier orogenic belt.

Marine sandstones of the Upper Cretaceous lower Ferron Sandstone Member are overlain by a dark gray marine shale of the Blue Gate Shale Member of the Mancos Shale Formation. These sediments were deposited during a rapid relative sea-level rise and possibly oxygen deficient marine conditions (Riemersma and Chan, 1991).

Figure 3: Schematic cross-section showing the stacking pattern of the upper Ferron Sandstone (modified after Ryer, 1981).



The fissile shale of the Blue Gate Shale Member is easily differentiated from the underlying light gray, silty Tununk Shale Member, where it does not overlie sandstones and siltstones of the lower Ferron, by its dark gray color, fissility and decreased silt content (Riemersma and Chan, 1991). According to Riemersma and Chan (1991) the laminated shale facies is 15 m thick and contains dark gray fissile mudstones interbedded with thin siltstones.

The lower Ferron Sandstone consists of four facies, in ascending order: a bioturbated siltstone facies; an interbedded hummocky cross-stratified sandstone and bioturbated siltstone facies; an amalgamated hummocky cross-stratified sandstone facies; and a bioturbated sandstone facies.

The lower Ferron Sandstone is separated from the upper Ferron at Dry Wash by 30 m of marine shale (Riemersma, 1989). At section 2, east of the town of Ferron, the lower Ferron is separated from the second distal delta front sandstone of the upper Ferron by 16 m of dark gray shale (Ryer, 1983). The second delta front unit is overlain by 5 m of dark gray shale and siltstone, which is in turn overlain by blocky light gray silty shale. Subsurface cross-section and outcrop studies (Ryer, 1983) indicate that basal delta front sandstone of the upper Ferron in southernmost Castle Valley is equivalent to the lower Ferron in northern Castle Valley. In northern Castle Valley, the upper Ferron pinches out into the Blue Gate Shale.

3. TARGET DEFINITION

Increasing the efficiency of hydrocarbon exploitation tends to stabilize the job prospects of explorationists. One way of increasing production efficiency is to develop a means for discovering hidden reserves in known reservoirs. The evaluation of reservoir heterogeneity plays an important role in deducing the presence of unrecognized reserves.

Since the Ferron Sandstone Member of the Mancos Shale in central Utah is considered a classic analog for fluvial-deltaic reservoirs, it is a valuable field site for studying reservoir heterogeneity.

The University of Utah Research Institute (UURI) conducted extensive well-logging in the Ferron area in an attempt to develop techniques for defining reservoir heterogeneity from borehole imaging. Two boreholes, UURI#1 and UURI#2, were used in this project. Natural Gamma Ray Spectrometry, Induction, Resistivity, Neutron/Density Porosity, and Formation Microscanner logs were collected by Schlumberger Well Services in 1991 as a part of the UURI project (Nielson et al., 1992). During this project, complete core profiles were collected for both boreholes as well. The conclusion of this project was that it is not possible to determine the continuity and connectivity of reservoir seals or reservoir bodies on the basis of high resolution Microscanner images, although reservoir heterogeneity in fluvial-dominated deltaic sediments is significant. This raises the question whether a borehole-to-surface DC resistivity survey can be used to delineate reservoir inhomogeneities, since the radius of exploration of the borehole-to-surface technique is much greater than that of well-logging. The stratigraphic correlation map of the Ferron Sandstone given by Lutz

et al. (1993) (Figure 4) contains detailed core profile descriptions together with information from outcrop studies. Seven major sedimentary sequences were identified in this study. Shaly layers are present mostly in a transition zone between two sedimentary sequences. The reservoir seals are mainly shaly layers, while the reservoir bodies are sandstone units. If there is enough resistivity contrast between these units we should be able to map the conductive shale layers in the relatively resistive sandstone environment.

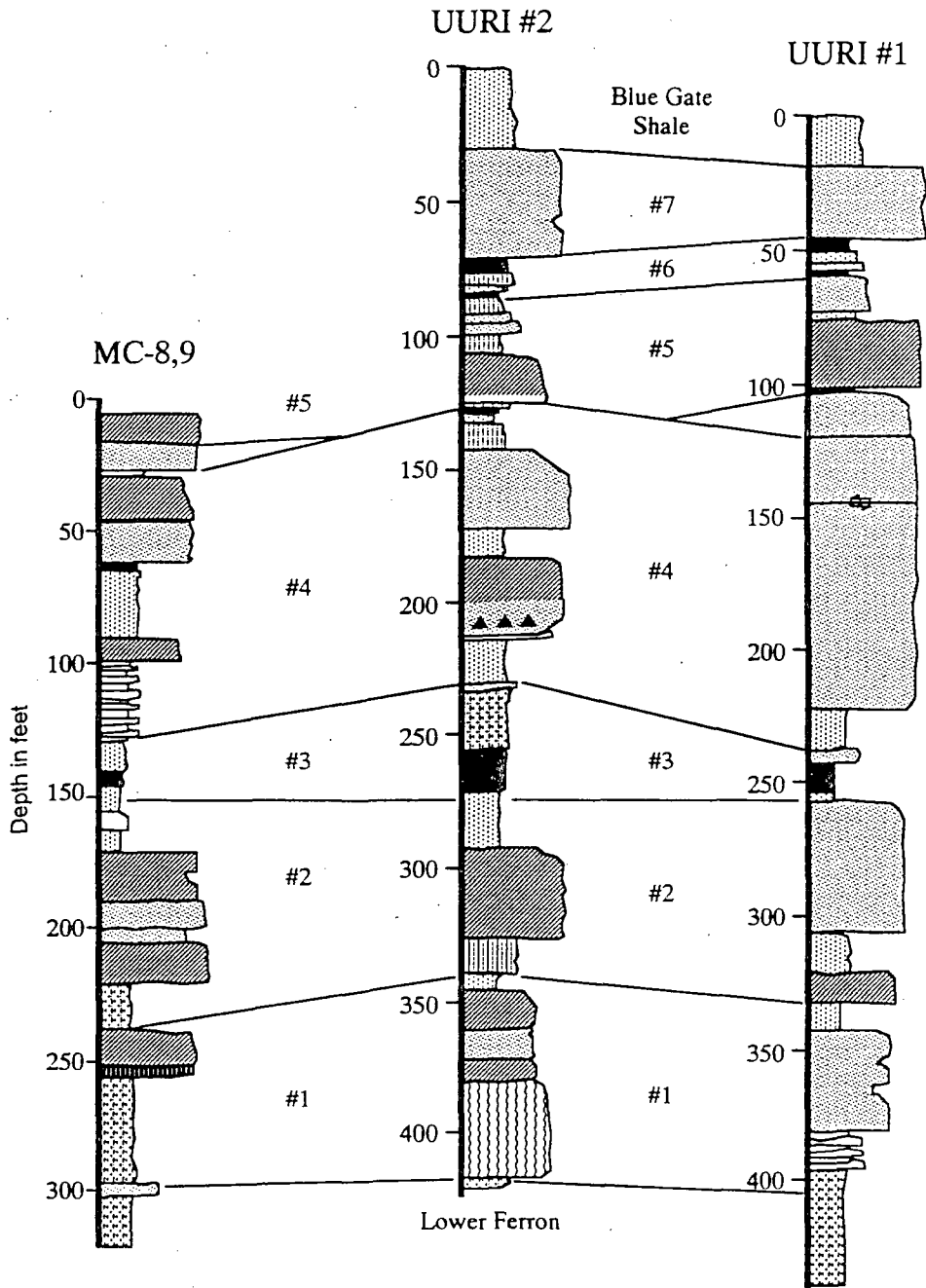
The electrical response of a shale bed depends on the type and quantity of clay or carbonaceous material contained in the shale, the shale's microstructure, and the quantity and character of formation water (Hearst and Nelson, 1985; Ellis, 1987; Schlumberger, 1991). Since the electrical resistivity of shale can vary dramatically as a function of any of these parameters, it is important to try to characterize the shale as well as possible before attempting to map it. A complete suite of logs is useful in assessing whether a mappable contrast between shale and sandstone exists.

Characterizing the shale beds will consist of first identifying their presence and vertical extent in the wells, and then appraising their in-situ resistivity. It might also be possible to develop a model to explain the functional dependence of the shale resistivity on petrophysical parameters.










A gamma ray log is very useful for defining shale beds, because radioactive elements tend to concentrate in clays and shales. Natural Gamma Ray Spectrometry is used to identify clay type and to calculate clay volumes.

Neutron-porosity logs respond primarily to the amount of hydrogen in the formation. They measure porosity by determining the amount of hydrogen, and hence amount of fluid, filling pore spaces. Neutron logs are affected by all protons, including

Figure 4: Stratigraphic correlation - Ferron Sandstone, Muddy Creek Area, Utah
(modified after Lutz et al., 1993).



Legend

- | | | | |
|---|---------------------------------|---|---|
|  | Coal and Carbonaceous Shale |  | Clayey Siltstone |
|  | Crossbedded Sandstone |  | Shale |
|  | Interbedded Sandstone and Shale |  | Bioturbated Mudstone |
|  | Rippled Sandstone |  | Intraclasts |
|  | Sandstone | | #1, 2, ..., 7 Sedimentary Sequence Number |

those in bound water associated with shales. Therefore the apparent porosity in a shaly formation will be greater than the actual effective porosity of the reservoir rock. (Telford et al., 1976).

Density logs record the bulk density of rock, which is a function of porosity and mineralogy. Noncalcareous mudrocks have low densities, whereas sandstone and calcareous mudrocks have higher densities (Zelt, 1985).

In sandstone especially, electrical resistivity is related primarily to rock porosity and pore water conductivity. In a shaly formation, however, the exchangeable cations in clay minerals can greatly influence the conductance. Rocks bearing clay minerals with high cation exchange capacity, such as smectite, can have relatively high conductivities compared to sandstones with the same porosity and pore water conductivity.

In general, the presence of shale is defined by high gamma ray values, high neutron porosity readings, low density porosity readings, and low resistivity in the well logs. Of course, if a particular shale unit is not encountered in a well, then it is impossible to characterize it prior to the borehole-to-surface survey, and its influence on the subsequent data will have to be determined by other means.

There are two drillholes, UURI#1 and UURI#2, in the study area. Complete logs for both boreholes can be found in Nielson et al. (1992). Borehole logs from UURI#1 indicate ten shaly units. Only five of them are more than 3 m thick. The identified layers have low density porosities (less than 10 PU) and relatively high neutron porosities (more than 15 PU), while resistivity changes with each layer. One of these layers is 218 feet (66 m) deep and is about 5 m thick. According to the stratigraphic correlation map of the Ferron Sandstone given by Lutz et al. (1993) it is a mudstone with thin sandstone lenses created in a marginal marine environment and

prodelta. It belongs to the sedimentary sequence 4. The resistivity of this layer is 20-30 Ω -m. The low resistivity (10-20 Ω -m) at the depth of 248 feet (76 m) corresponds to a 3 m thick layer of carbonaceous shale with pyrite. This unit was created in a swamp environment at the lower delta plain and it is a part of the sedimentary sequence 3. The next layer is a 6 m thick layer of mudstone at the depth of 302 feet (92 m) with a resistivity of 40-70 Ω -m. This unit was created in the delta front environment and represents part of the sedimentary sequence 2. A 4 m thick layer 330 feet (101 m) deep has a similar response in borehole logs. Its resistivity is in a range from 30 to 60 Ω -m. This layer consists of interbedded ripple laminated and burrowed fine grained sandstone and shale (Lutz et al., 1993). It was created in the interdistributary bay environment and it belongs to the sedimentary sequence 1. The last layer identified in the borehole logs is an approximately 12 m thick layer of bioturbated sandy mudstone at a depth of 396 feet (121 m). The resistivity of this layer is 40-50 Ω -m. We cannot determine an exact thickness of this layer from the borehole log, because the log ends at 434 feet (132 m), while still inside the layer. This layer belongs to the lower Ferron Sandstone unit and was created in the shallow shelf environment. According to Ryer (1983) and Riemersma (1989) this layer may have a thickness of 15 to 30 m.

There are four high resistivity layers in an electrical resistivity log of UURI#1. The high resistivity response is associated with coal. One of them is 70 feet (21 m) deep and 3 m thick. The second one is at the depth of 88 feet (27 m) and is 5 m thick. Another high resistivity layer is 242 feet (74 m) deep and 2 m thick. The last one is 368 feet (112 m) deep and it is only 1 m thick. The resistivity of these layers is more than 1000 Ω -m.

The resistivity log is very complex in the 154-184 feet (47-56 m) depth interval, where spikes of low resistivities (5-40 Ω -m) alternate with spikes of high resistivities

(more than 2000 Ω -m). According to Lutz et al. (1993) this is a channel of the lower delta plain where it is possible to find finely interlaminated sandstone and shale, coal, cross-bedded sandstone and bioturbated mudstone with a lot of fractures.

In the UURI#2 borehole logs, we identified eight low resistivity zones. Only five of them are thicker than 3 m. The first one is at a depth of 60 feet (18 m). It is described as a bioturbated mudstone created in the delta front environment in the stratigraphic correlation (Lutz et al., 1993). It lays on the boundary between sedimentary sequences 5 and 6. The next layer is 124 feet (38 m) deep and is about 5 m thick. It is a rooted silty shale created in a swamp environment at the lower delta plain. According to the stratigraphic correlation (Lutz et al., 1993) it is a part of the sedimentary sequence 4. A 4 m thick conductive layer 170 feet (52 m) deep consists of carbonaceous shale and interbedded rooted siltstone and carbonaceous mudstone. It was created in the swamp environment of the lower delta plain. The next one is a 212 feet (65 m) deep, 12 m thick conductive layer. It consists of several geological units. An interbedded shale and calcareous laminated sandstone were created in a marginal marine environment. An interbedded planar laminated siltstone and a brownish shale were created in prodelta. A shale and bioturbated mudstone with some finely laminated sandstone beds were created in the interdistributary bay environment. The last two layers belong to the sedimentary sequence 4 as well. Another 10 m thick conductive layer is 270 feet (82 m) deep. It consists of rooted mudstone created in the swamp environment of the lower delta plain and a predominately shale layer created in the interdistributary bay environment. It is a part of the sedimentary sequence 2.

The resistivity of these layers ranges from 10 to 50 Ω -m. Density porosity is in the range 0-15 PU, and neutron porosity is at least 30 PU.

There are only two high resistivity layers in the UURI#2 log. One of them is 70 feet (21 m) deep and 2 m thick. The other one is 256 feet (78 m) deep and 4 m thick. According to Lutz et al. (1993) both are coal layers created in the swamp environment of the lower delta plain. Their resistivities are more than 2000 Ω -m.

All sandstone units have resistivity about 100 Ω -m in both borehole logs.

Borehole logs give us detailed information about the region close to the borehole, while electrical measurements with the electrode configuration used in this field experiment give us information about a very broad area. In our work we wish to extrapolate the resistivity structure away from the borehole, or to sense units not present in the borehole.

Correlating our borehole-to-surface field data to well-log information requires several considerations. First, we can recognize very small features in the borehole logs, which are not possible to detect or recognize with a borehole-to-surface configuration. On the other hand, an electrical survey of this kind is advantageous in that it can help to delineate structures away from the borehole, which are not detected by well-logging. Thus the borehole-to-surface configuration can in principle detect reservoir heterogeneity although its resolution will not be as good as that achieved in borehole logging. This detection was the goal of our experiment at Ferron.

A detailed geological description of Ferron Sandstone given in Chapter 2 and at the beginning of this chapter should make reader aware that our study area has a very complex structure. Our field experiment was designed to investigate an extension of the conductive shale layers at the depth more than 70 m, which were identified in borehole logs, inside the sandstone formation. These layers had the highest resistivity contrast with respect to surrounding units. According to the UURI#1 borehole log and the stratigraphic correlation map (Lutz, et al., 1993) there is a 10-20 Ω -m, 3 m thick layer

of carbonaceous shale with pyrite in the depth of 76 m. The same resistivity response (10-20 Ω -m) in the UURI#2 borehole log has a 10 m thick, 82 m deep conductive layer, which consists of rooted mudstone and shale. These two layers have different compositions and therefore there is a high probability that they are not continuous and pinch out between the two boreholes. Determining the region of the pinchout would be geologically interesting. At the same time, we tried to find out if there is any other conductive body present in that depth interval, which was not detected by well-logging.

4. DATA ACQUISITION

Two drillholes were drilled in this area, UURI#1 and UURI#2. The distance between these boreholes is about 500 m, while their depth is about 150 m. They are cased only for the top several meters. The field setup for the borehole-to-surface DC resistivity experiment is illustrated in Figure 5.

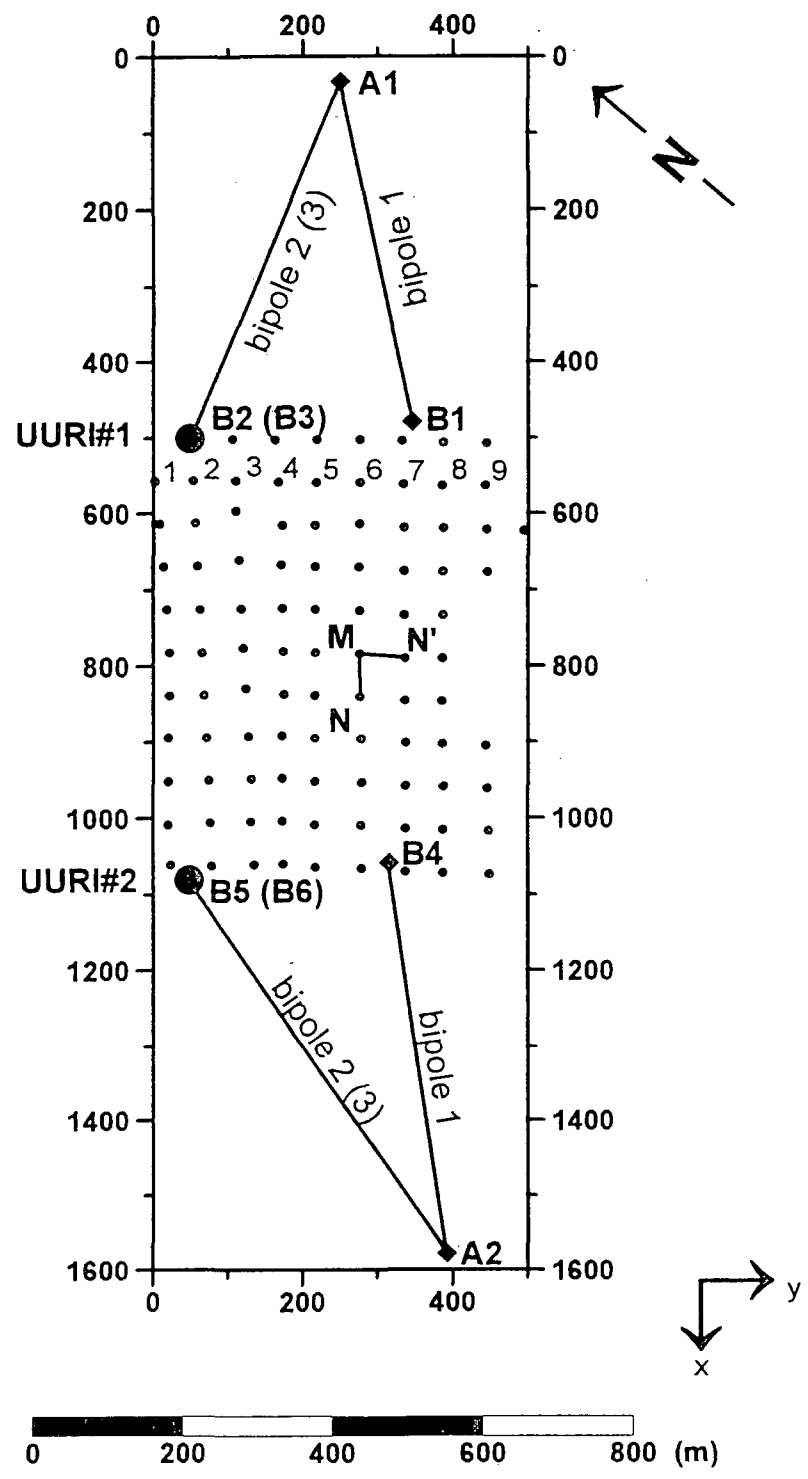
In order to realize the borehole-to-surface field measurements it was necessary to develop a special downhole current electrode. Design was done by William Frangos and its brief description is given below.

Downhole transmitter systems pose several design challenges. It was essential that current be introduced into the earth solely at the point of the downhole electrode in order to meet the assumptions of the data analysis. Accordingly, the cable had to maintain its insulation in the rough environment of the drillhole walls and the downhole electrode had to resist electrolytic corrosion during use, and do so without compromising the point source nature of the current source.

The UURI borehole-to-surface system uses a four-conductor armored logging cable and a specially designed downhole electrode adapter (DTA). The armor effectively protects the enclosed conductors as the cable slides along the rough drillhole walls. The interior insulation is rated to a temperature of 260 °C (500 °F), insuring integrity of the cable assembly from within. However, the metallic armor is conductive, and can redistribute the current from the electrode if care is not taken to prevent it.

The metallic ends of the DTA are machined of a highly corrosion resistant 300-series stainless steel. A 15-inch long insulating mid-section of high temperature nylon

Figure 5: Field setup for the borehole-to-surface DC resistivity experiment.
 $A_1, A_2, B_1, B_2, B_4, B_5$ are surface current electrodes, while
 B_3 and B_6 are downhole current electrodes.
 M, N, N' are potential electrodes which move around the grid.
1, 2, 3, 4, 5, 6, 7, 8, 9 are line numbers.



provides separation between the electrode and the cable armor. The interior cavity is sealed with O-rings, chosen to be the same size as those used in household plumbing. A standard four-conductor logging connector is positioned at the top and a fitting for a sacrificial electrode at the bottom. The four cable conductors are connected together inside the nylon section, allowing parallel conduction through the cable. The actual electrode may be either a piece of standard 3/4-inch threaded water pipe or a metallic rod secured by three set screws. Provision for replaceable electrodes allows using a size appropriate to a particular survey; for the Ferron field experiment, we used a 5-foot section of iron pipe.

Two additional electrical properties of the cable system are important in safe operation: its resistance and inductance. Joule heating due to current flow through the wire resistance has the possibility of raising temperatures beyond safe levels for the insulation, particularly in the portion of cable on the reel, where heat dissipation is less than on the extended part. Inductance in the reel represents a threat to the transmitter through large voltage spikes at the moments of current switching.

Direct measurement of the resistance and inductance yielded values of 30 Ohms and about 10 millihenries, respectively. Empirical evaluation of the cable characteristics during the field survey indicated that the goals declared above were well met. Operating at currents of 1 and 2 amperes for long periods, the coil showed no signs of warming, as observed by feeling the exterior and the steel axle. Isolation between the electrode and the cable armor was verified by measuring voltage between the armor and a surface electrode with the transmitter on and off. The difference was about 6 volts, while the transmitter output voltage was approximately 400 volts.

The downhole electrode system worked well and is recommended for future use.

The area between the two boreholes (roughly 500 m x 500 m) was covered by measurements with different electrode configurations. Asch and Morrison (1989) showed that in order to maximize the effectiveness of borehole-to-surface resistivity measurements, the downhole transmitter electrodes must extend below the target. The optimal depth of the electrode depends on the distance between the target and the boreholes, and on the target size, shape, and conductivity contrast with the surrounding geology. In our case, the target was more than 70 m deep, of an unknown lateral extension, therefore we put our current electrode at the depth of 100 m. There were three different setups of current electrodes A and B for each borehole (Figure 5). The (x, y) coordinates of current electrodes in the vicinity of UURI#1 were

$$A_1 = [32.5, 250.0] \quad B_1 = [478.5, 344.1],$$

$$A_1 = [32.5, 250.0] \quad B_2 = [500.0, 50.0], \text{ and}$$

$$A_1 = [32.5, 250.0] \quad B_3 = [500.0, 50.0] \text{ at the depth of 100 m,}$$

while for UURI#2 they were

$$A_2 = [1577.5, 391.0] \quad B_4 = [1060.0, 315.0],$$

$$A_2 = [1577.5, 391.0] \quad B_5 = [1082.31, 49.98], \text{ and}$$

$$A_2 = [1577.5, 391.0] \quad B_6 = [1082.31, 49.98] \text{ at the depth of 100 m.}$$

All dimensions are in meters.

We took measurements with 50 m dipoles in two orthogonal directions, on a 50 m grid. The grid of measurements is incomplete on the east side of our study area because of the presence of the 80 m deep Muddy Creek Canyon. The presence of this canyon should be considered in the interpretation because of its possible influence on our measurements. A GGT-30 transmitter and a GDP-16 receiver from Zonge Engineering were used for this project. The field site was surveyed with a Pentax electronic distance meter to get the precise position of current and potential electrodes.

5. TENSOR CALCULATIONS

In general the electric field and electric current density vectors for an anisotropic material are related via Ohms law by a resistivity tensor, so that $\bar{E} = \bar{\rho} \bar{J}$. The character of such tensors has been discussed extensively by Landau and Lifshitz (1960), among others. Geophysically, our tack is to estimate $\bar{\rho}$ as a function of position in the earth.

Bibby (1977) defined an apparent resistivity tensor $\bar{\rho}_a$, as a mathematical means of normalizing the observed electric field for the effect of the source-receiver geometry and amount of injected current. Thus, there is a fundamental difference between the apparent resistivity tensor and the resistivity tensor. Therefore the reader should remember that we are using the apparent resistivity tensor in this work.

Calculating the apparent resistivity tensor is an intermediary step in the determination of the subsurface resistivity structure. The tensor is computed from the measured electric fields for each transmitter-receiver setup assuming the current density at the receiver site is the same as for a uniform earth. We will discuss this procedure, largely following Bibby (1977, 1986). Although Bibby assumes surface electrodes, the tensor method can be extended to the case where the transmitting electrodes are either surface or borehole electrodes.

For two different orientations of source bipoles we get the equations:

$$\begin{bmatrix} E_{11} \\ E_{12} \end{bmatrix} = \begin{bmatrix} \rho_{11} & \rho_{12} \\ \rho_{21} & \rho_{22} \end{bmatrix} \begin{bmatrix} J_{11} \\ J_{12} \end{bmatrix} \quad (1)$$

$$\begin{bmatrix} E_{21} \\ E_{22} \end{bmatrix} = \begin{bmatrix} \rho_{11} & \rho_{12} \\ \rho_{21} & \rho_{22} \end{bmatrix} \begin{bmatrix} J_{21} \\ J_{22} \end{bmatrix} \quad (2)$$

where E_{ij} is the measured electric field along the i -th axis due to the j -th transmitter and J_{lk} is the k -th component of electric current in a uniform earth due to the l -th transmitter. Since we assume a uniform earth, J_{lk} is dependent solely on the relative geometry of the transmitter and receiver electrodes.

Now combining the two matrix equations, rewriting them in terms of the components of $\overline{\rho_a}$, and re-arranging terms gives the decoupled equations:

$$\begin{bmatrix} E_{11} \\ E_{21} \\ E_{12} \\ E_{22} \end{bmatrix} = \begin{bmatrix} J_{11} & J_{12} & 0 & 0 \\ J_{21} & J_{22} & 0 & 0 \\ 0 & 0 & J_{11} & J_{12} \\ 0 & 0 & J_{21} & J_{22} \end{bmatrix} \begin{bmatrix} \rho_{11} \\ \rho_{12} \\ \rho_{21} \\ \rho_{22} \end{bmatrix} \quad (3)$$

These equations can be solved via Cramer's rule to give the tensor components $\rho_a(ij)$. The values of the elements $\rho_a(ij)$ will, in general, depend upon the orientation of the electrode arrays used and the measurement coordinate system. Once we know the tensor in one coordinate system, we can transform it into another coordinate system. The tensor relationship ensures that the form of the equations between vectors does not change when the coordinate system changes and defines the way the tensor components in the new coordinate system can be derived from the original components given the coordinate transformation. Once the components $\rho_a(ij)$ have been calculated for a particular coordinate system (Bibby, 1977, 1986; Bibby and Hohmann, 1993) three coordinate invariant apparent resistivities can be extracted.

Bibby (1977, 1986) and Bibby and Hohmann (1993) present and discuss the tensor invariants:

$$P_1 = \frac{1}{2}(\rho_{11} + \rho_{22}) \quad (4)$$

$$P_2 = \sqrt{\det(\rho)} = \sqrt{\rho_{11}\rho_{22} - \rho_{12}\rho_{21}} \quad (5)$$

$$\text{and } P_3 = \frac{1}{2}(\rho_{21} - \rho_{12}). \quad (6)$$

Properties of the apparent resistivity tensor can be deduced theoretically in a number of special cases, as discussed in the papers referenced above. A brief synopsis of these results follows.

For a uniform isotropic half-space the off-diagonal tensor elements equal zero, and the diagonal tensor elements both equal the half-space resistivity. If the resistivity distribution is 2-D then whenever the center of the current electrodes and the receiver position lie along a vertical plane of symmetry of the resistivity structure, the off-diagonal terms also will be zero. For a geometrically complex medium (i.e., a 3-D resistivity structure) all terms will be, in general, different and nonzero. Also, in contrast to the resistivity tensor of a real material, the apparent resistivity tensor will in general be asymmetric.

For a horizontally layered medium the apparent resistivity tensor is symmetric (i.e. $P_3 = 0$), although the components of the resistivity tensor have maximum or minimum values depending on the alignment of the electric field with the pertinent

receiver line. Outside the immediate vicinity of the current source the tensor invariants depend only on the distance from the source and give circular contours.

Large apparent anisotropy is a characteristic of the apparent resistivity tensor for receivers near a vertical resistivity discontinuity. The maximum value for the tensor invariants is in a perpendicular direction to the discontinuity. The minimum value for the tensor invariants is zero. The ratio of maximum to minimum values is equal to the resistivity contrast. Therefore these extreme values can indicate the discontinuity giving both the resistivity contrast and the orientation of the boundary.

P_1 and P_2 tensor invariants are two different forms of the average value of the apparent resistivity tensor. Both can clearly reflect both shape and position of an inhomogeneity, as demonstrated by Bibby and Hohmann (1993). P_1 and P_2 best reflect the variation of resistivity below the measurement site. Since P_2 better characterizes the background resistivity, it was used in the interpretation given by Bibby and Hohmann (1993). If the current bipoles can be treated as dipoles, that is the receiver array is far from the current source, the particular choice of current bipole orientations does not influence the tensor invariants.

Although the P_3 tensor invariant is dimensionally a resistivity, the values of P_3 are not necessarily positive. For example in the 2-D case, the P_3 values will change sign across the axis of symmetry. While P_3 is zero for any 1-D model and along the axis of symmetry in a 2-D model, in a 3-D situation it is, in general, nonzero. The greatest values of P_3 occur immediately outside a 3-D perturbing body, and are not directly indicative of the position of the body.

Determining the components of the apparent resistivity tensor and the associated tensor invariants removes the dependence of the apparent resistivity value

on the coordinate system used for the measurements. Also if the transmitter bipoles can be approximated as dipoles the invariants will be independent of the source orientation.

Since there are four unknown tensor components, four equations linking the components of E and J are needed for their solution. This requires the use of two differently oriented transmitter bipoles. Bibby and Hohmann (1993) numerically experimented with different transmitter orientations and placements and found that determination of the tensor was stable with regard to transmitter orientation for their simple models.

One can give a more precise meaning to what constitutes a good pair of transmitters. Since the orientation of the transmitters will affect the matrix equations (3) which we need to solve, we can analyze the effect of placement and orientation of the transmitters through the effect which the subsequent current terms have on the solution of the matrix equation.

The first stipulation we have is that

$$\begin{vmatrix} J_{11} & J_{12} \\ J_{21} & J_{22} \end{vmatrix} \neq 0 \quad (7)$$

over the receiver grid. This condition ensures that sources have different orientations and guarantees a solution in the case of perfect data. Since the current values are geometrically obtained, it is a simple matter to determine the receiver points at which the determinant is zero.

The amount of noise propagation from data to model parameters is dependent on the condition number (Lanczos, 1961). The condition number as a function of geometry can be assessed by solving the Cayley-Hamilton equation,

$$\begin{vmatrix} J_{11} - \lambda & J_{12} \\ J_{21} & J_{22} - \lambda \end{vmatrix} = 0, \quad (8)$$

for λ_{\max} and λ_{\min} , the maximum and minimum eigenvalues of the system matrix. Then the condition number is the ratio of the λ_{\max} to λ_{\min} .

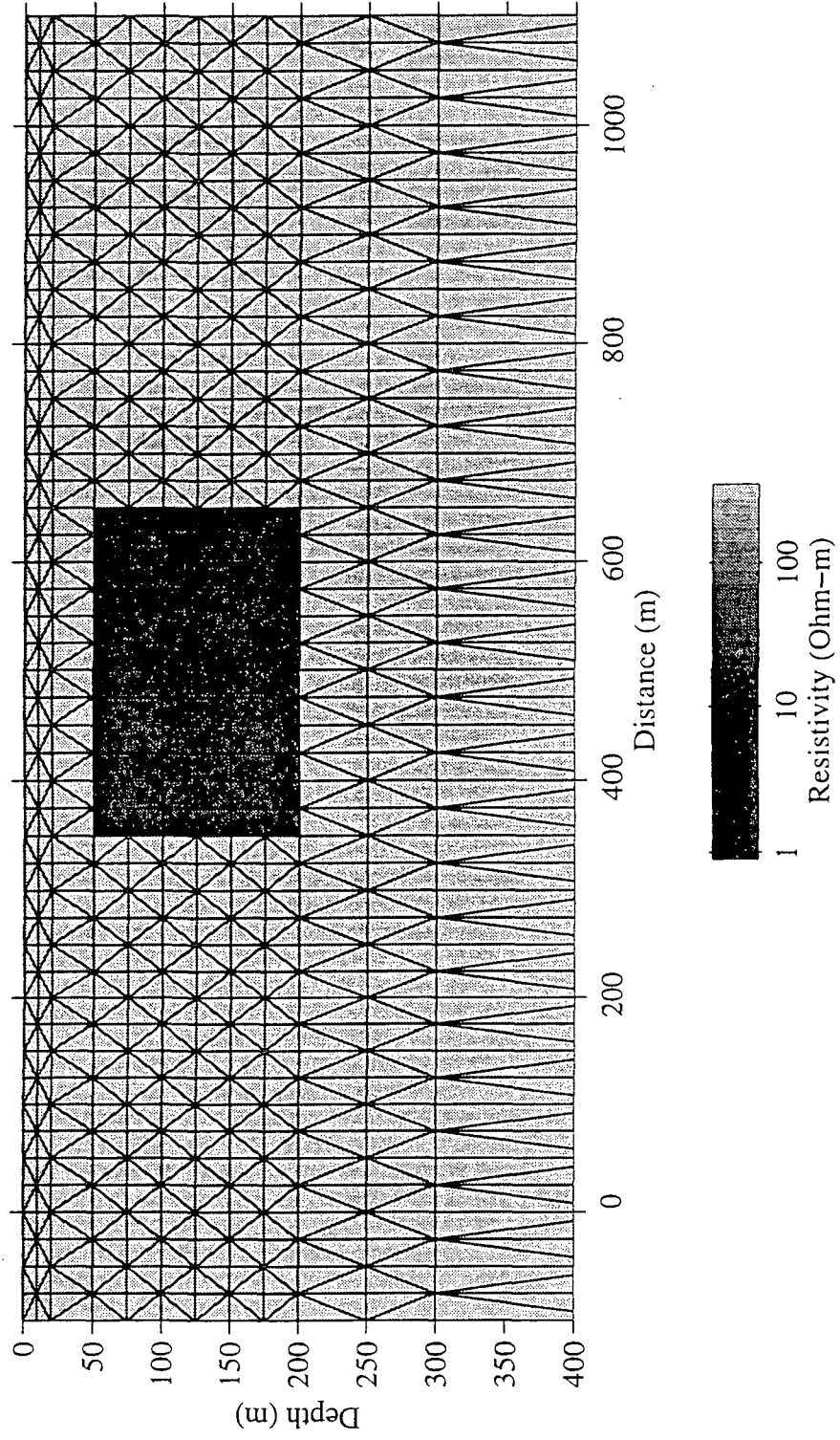
Bibby (1986) and Bibby and Hohmann (1993) only discussed tensor measurements when both transmitter and receiver electrodes are on the earth's surface. In our experiment, in order to increase the resolution of geological units at depth, we placed transmitter electrodes in boreholes. In this case the same theory holds, except that the geometric equations for the current components must be changed to reflect the depth of burial of the transmitter electrode. An adapted formula can be derived using image theory.

6. MODELING

Since we expected to have one-dimensional (1-D) and two-dimensional (2-D) structures in the study area, a 2-D finite element algorithm developed by Bibby (1978) was used for computing the response of 1-D and 2-D structures in this thesis. Since this algorithm was written solely for a surface electrode configuration, it was necessary to modify it for the borehole electrode case.

This 2-D finite element program solves for the potential distribution in or on the surface of a half-space with an arbitrary 2-D conductivity distribution, due to point sources of excitation. Since we assume that the 2-D conductivity distribution has the x - z plane as the symmetry plane, we can Fourier transform out the y -strike direction and reduce our three-dimensional (3-D) discretization problem to a series of 2-D discretizations in the x - z plane. The geometry of the grid remains constant over the 2-D discretization while the physical properties of the grid change. Each of these 2-D problems is solved and then the solutions are back transformed to give the potentials in (x, y, z) space. The discretization grid used in this algorithm is shown in Figure 6. An arbitrarily scaled unit distance can be used in the x and z directions. The scale depends on the scale of the survey. In our case, grid points were separated in the x -direction by 25 m, while the z -separation ranged from 5 to 100 m. Each triangular element is described by the nodes defining the corners of the element. Different resistivity values can be assigned to each mesh element. An example of a 250 m x 150 m single block of 10 Ω -m in 100 Ω -m background is shown by the shaded region in Figure 6. A current electrode can be arbitrarily placed at any x , y , or z position, while the receiver dipoles

Figure 6: Discretization grid for 2-D finite element algorithm.



are limited to the symmetry plane defined by the 2-D mesh. In our case, the receiver dipole separation was 50 m. The output is both single bipole resistivities and tensor parameters. The singularity at the current electrode is removed by calculating secondary potentials only. This is done to increase the accuracy of computation for a given grid size. However, we need to be aware that the calculations along the strike are very dependent on how well the electrode singularity is handled. For example, if receivers occur between a transmitter current electrode and a target, the error in handling the primary field can severely affect the calculated potentials. In the past, this program was tested and certified against other 2-D programs for in-line configurations (i.e. Bibby and Hohmann, 1993). Our experience using half-space models, is that numerical noise in this program is less than 0.2 %, using the suggested discretization criteria.

As we have already discussed, the objective of our work is to map conductive unit inhomogeneities in the survey vicinity. We conducted a series of preliminary modeling exercises to determine the sensitivity of our technique to conductive units at depth. These responses are discussed at length in Appendix A. To better delineate and appreciate these responses, we also calculated a suite of responses for resistive bodies in a conductive earth. These responses are discussed extensively in Appendix B. Since electrical measurements are affected highly by near surface inhomogeneities, we also calculated the effect of near-surface inhomogeneities in the vicinity of transmitter or receiver electrodes on the observed resistivity response. These calculations are presented in Appendix C.

A continuous conductive layer causes a decrease of the background resistivity in the whole measured area, as shown in Appendix A. The same figures show that source effects can be minimized by using a borehole electrode configuration since the

surface receivers are separated from the transmitter by at least the depth of the transmitter. For a 2-D structure a decrease of the apparent resistivity only occurs near the structure, as shown in Appendix A. The gradient in apparent resistivity decreases with increasing depth of an anomalous body, so it is more difficult to locate a deeper structure using these contour maps. The electrode configurations used in this case do not give us much information about structures deeper than 100 m, which is the depth of the downhole electrode.

It was shown by Bibby and Hohmann (1993) that in the case of a 3-D body the P_2 resistivity tensor invariant is the best parameter for delineating the position of the body. As discussed previously, the apparent resistivity tensor contains information from multiple sources, thus avoiding possible biasing due to current disorientation while the invariant avoids possible peculiarities of receiver orientation. The choice of P_2 vs. P_1 was based on numerical tests by Bibby and Hohmann (1993). Tensor calculations proved to be useful in our studies for delineating a 2-D conductive body in a resistive background. The position of the body is characterized by a high gradient in P_2 (Appendix A), which is a good indicator of a vertical discontinuity in the study area. Modeling results show that this particular electrode configuration used in our study is capable of delineating structure in the depth interval 25 m to 75 m. Again, it is difficult to characterize conductors deeper than 100 m, given the limited survey area. In the case of a horizontal layer, the P_2 invariant gives circular contours. The minimum resistivity area changes with layer depth. The maximum response of the shallow structure is close to the source, while the maximum response of the deeper structure is farther away from the source, as we might expect from considering the response of in-line arrays to layered media (Appendix A). When a highly resistive body is present in a low resistivity background both tensor invariants and single source apparent resistivities

greatly underestimate the true body resistivity, which is indicative of response saturation. This is consistent with Bibby and Hohmann's (1993) statement that bipole techniques are insensitive to the precise resistivity of high resistivity bodies.

The total apparent resistivity response for our individual bipoles for conductive layers in resistive backgrounds of varying resistivities are given in Appendix A. The characters of the total apparent resistivity responses for different layer resistivities are illustrated in the same appendix. If the resistivity contrast between the anomalous layer and the background is more than one hundred, the total apparent resistivity response is not very sensitive to the change of the background resistivity (Appendix A); once again a saturation effect. Figure 7 illustrates the total apparent resistivity response with respect to the background resistivity for different resistivity contrasts. For a resistivity contrast of less than 100, the total apparent resistivity response changes significantly for a small change in the resistivity contrast. However, for a resistivity contrast higher than 300, the total apparent resistivity maps are very similar.

Model results in Appendix A demonstrate that a near-surface conductive layer tends to screen any deeper structure. These figures suggest that it is very difficult, if not impossible, to detect a conductive body screened by a conductive layer between the body and the surface transmitting electrode.

A highly resistive layer causes an increase of the measured resistivity response with respect to background resistivity for the surface electrode configuration. However, if the borehole electrode is below this highly resistive layer the resistivity response is less than the background resistivity (Appendix B), because the current requires a greater lateral distance to diffuse through the resistive layer, leading to a decrease in voltage on the earth's surface.

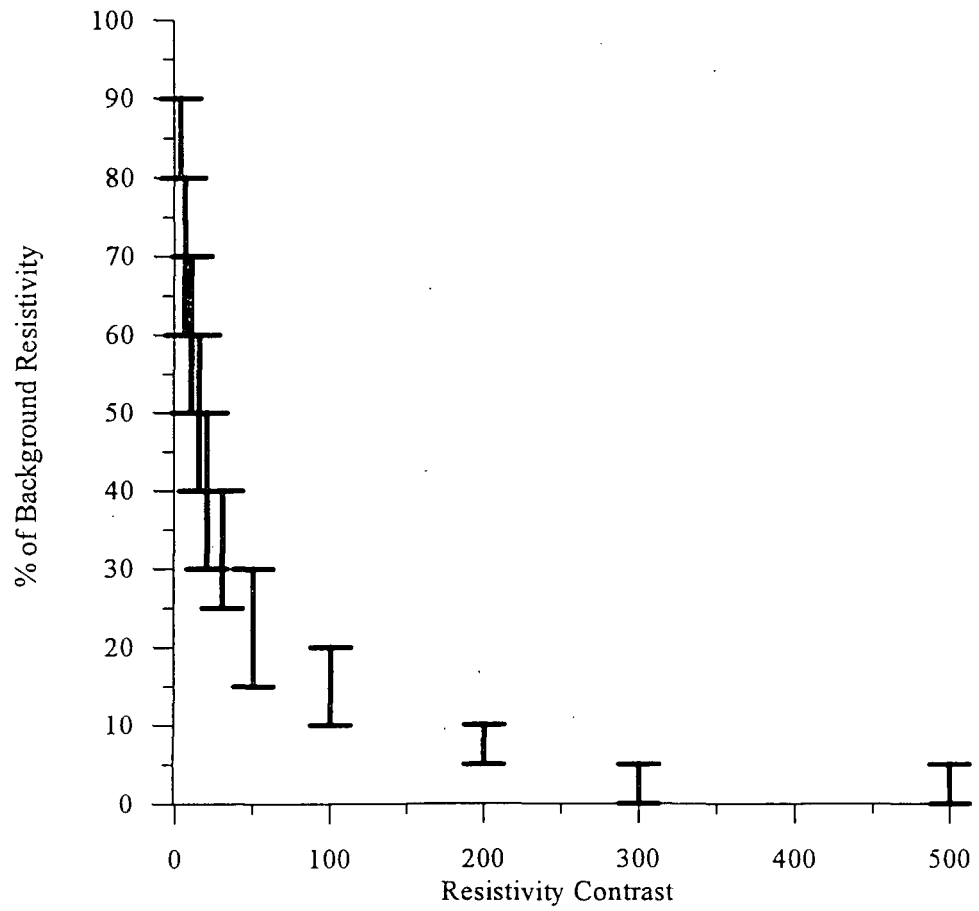


Figure 7: Total apparent resistivity range in percentage of background resistivity for different resistivity contrasts.

To make an interpretation in an area where a resistive body is in a relatively conductive background is very difficult, since the surface and borehole measurements are relatively insensitive to the body resistivity and depth. This is illustrated in Appendix B as well.

The effect of near-surface inhomogeneities near a transmitter or a receiver site on the measured response is illustrated in Appendix C. Modeling results show that conductive near-surface inhomogeneities have a significant influence on the measured apparent resistivity and they increase the ambiguity of our interpretation. If a near-surface inhomogeneity has a high resistivity, its influence on the measured response is negligible.

So in recapitulation, our modeling studies demonstrated the following points.

1) It is possible to detect conductive layers and layer perturbations of a size expected in our survey region underneath the receiver grid as long as such conductive features are not deeper than 100 m. The P_2 invariant is best for detecting these features. Whether surface transmitter responses or a surface electrode and a borehole electrode are used for the tensor calculations seems to make little difference to the resolution of the conductive feature. A shallow conductive layer screens deeper geoelectric units. Thus, in mapping conductive features, we essentially map the depth of the upper-most feature.

2) Resolution of the resistivity of a layer or body which is relatively resistive vis-à-vis the background is very difficult, even if a downhole electrode penetrates the body. Indeed, when a transmitter electrode occurs below a resistive layer, the measured anomaly is conductive.

3) Near-surface resistors in the vicinity of the transmitter have a negligible effect on the receiver reading, while conductive units can have major effects. For this

reason it is very important to try to assess the geoelectric status of the near-surface adjacent to the transmitters in our survey area.

7. DISCUSSION AND INTERPRETATION OF FIELD DATA

The starting 1-D geoelectric resistivity models for the interpretation were constructed by smoothing layer thicknesses and resistivities taken from the downhole resistivity logs of UURI#1 and UURI#2. These logs are discussed in Chapter 3, and provide the "ground truth" in the area. We identified five conductive layers, each thicker than 3 m, and four high resistivity layers in an electrical resistivity log of UURI#1, and five conductive layers and two high resistivity layers in the UURI#2 log. Since well logs have a much finer layer resolution than can be expected from surface resistivity measurements, it is necessary to generalize the features of the well log into a form that could conceivably be resolved for surface data.

Our strategy was to begin with our starting 1-D models and iterate the solution towards a 1-D model that roughly matches the data. This 1-D model provides a first approximation of the geological structure. After we had a model that matched the broad trends or low spatial frequency characteristics present in the data, small features can be introduced in order to match higher spatial frequency components in the data.

As is discussed for example in Bibby (1986), bipole-dipole apparent resistivities in a horizontally layered medium can be derived from the Schlumberger apparent resistivity. Thus, a Schlumberger sounding modeling algorithm can be used to estimate the response of a layered structure for the surface electrode configuration used for the field measurements.

Figures 8 and 9 show the Schlumberger sounding curves for the 1-D models based on our summary of the UURI#1 and UURI#2 well-logs. The model parameters

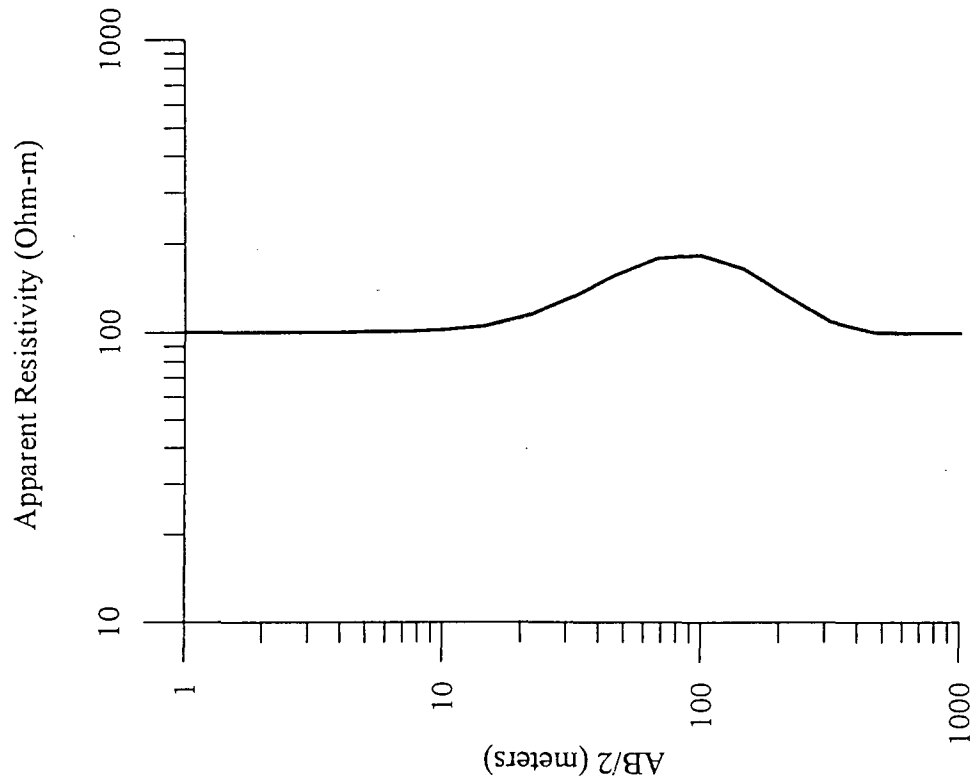
and the layer resistivities and thicknesses are listed on the side of each sounding curve. The apparent resistivity curve for UURI#1 differs from the one for UURI#2. This suggests that if the structure registered by the well-logs is representative of a significant area around each drill hole such a difference should also be detectable in the surface apparent resistivities.

Our modeling studies show that for a situation where a high resistivity layer overlays a low resistivity layer, the surface electrode configuration is sensitive only to the high resistivity layer. The response from a deep conductive layer, below the highly resistive layer is masked, using this kind of electrode configuration. This is illustrated in Figure 10 where the Schlumberger sounding curves for 1-D models with and without conductive layers beneath highly resistive ($1000 \Omega\text{-m}$) layers are shown. The apparent resistivity curves for the model without and with conductive layers are very similar although the conductive layer 115 m deep does influence the data. This result, coupled with the analogous screening result for a highly conductive layer, suggests that a practical primary goal for our interpretation might be to map the first "anomalous" layer in the geoelectric section, be it conductive or resistive, with the secondary goal of mapping any conductors under resistive cover.

Working with the resistivity data, we are in a situation where we can find families of models, all of which cause the same electric field effect at our measuring area within a given measurement accuracy. Thus, in practice the resistivity method will not have an unique interpretation. In the 1-D case this phenomenon is called equivalence. An example of an equivalent response to different resistivity models for bipole-dipole total field apparent resistivity is shown in Figure 11. Figure 11a shows the total apparent resistivity map for a 25 m thick $10 \Omega\text{-m}$ layer 125 m deep in a $100 \Omega\text{-m}$ background due to a bipole with electrodes at $[32.5, 250.0, 0.0]$ m and $[478.1, 344.1,$

Figure 8: Schlumberger sounding curve for the 1-D model based on information from UURI#1 well-log.

UURI#1

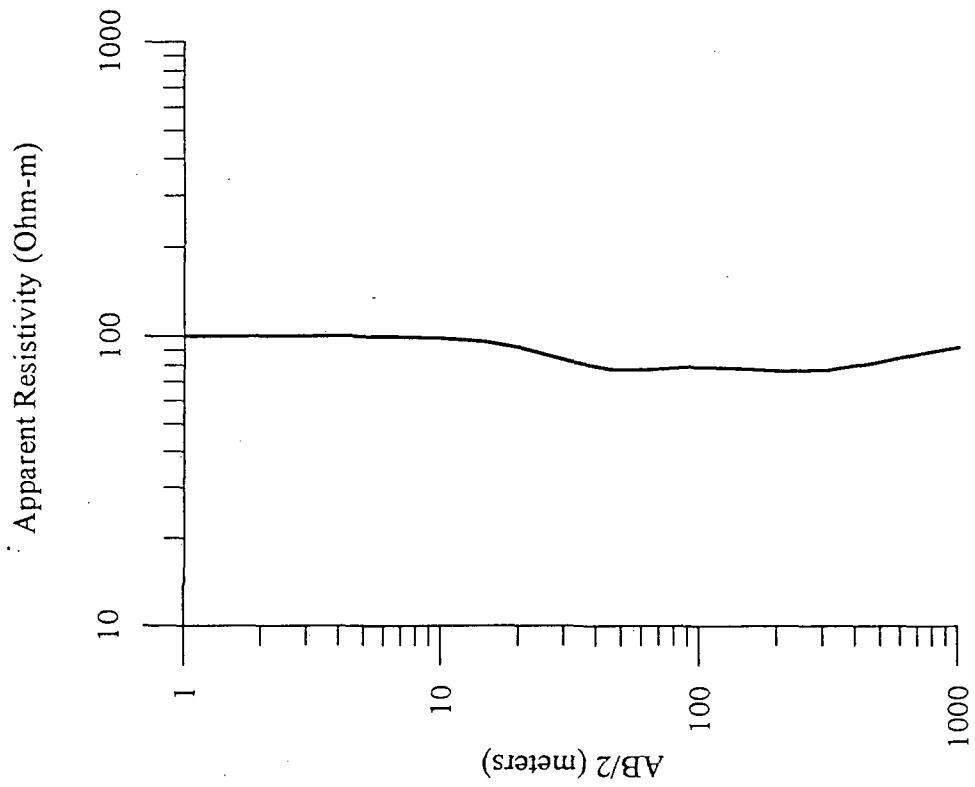


Model:

Layer	Resistivity (Ohm-m)	Thickness (m)
1	100	21
2	1000	3
3	100	3
4	1000	5
5	100	34
6	25	5
7	100	3
8	1000	2
9	15	3
10	100	13
11	55	6
12	100	3
13	45	4
14	100	16
15	45	12
16	100	infinite

Figure 9: Schlumberger sounding curve for the 1-D model based on information from UURI#2 well-log.

UURI#2



Model:

Layer	Resistivity (Ohm-m)	Thickness (m)
1	100	18
2	15	3
3	1000	2
4	100	15
5	35	5
6	100	9
7	25	4
8	100	9
9	40	12
10	100	1
11	1000	4
12	20	10
13	100	infinite

Figure 10: Schlumberger sounding curves for a 1000 Ohm-m layer in 100 Ohm-m resistive background with and without a 10 Ohm-m layer below it.

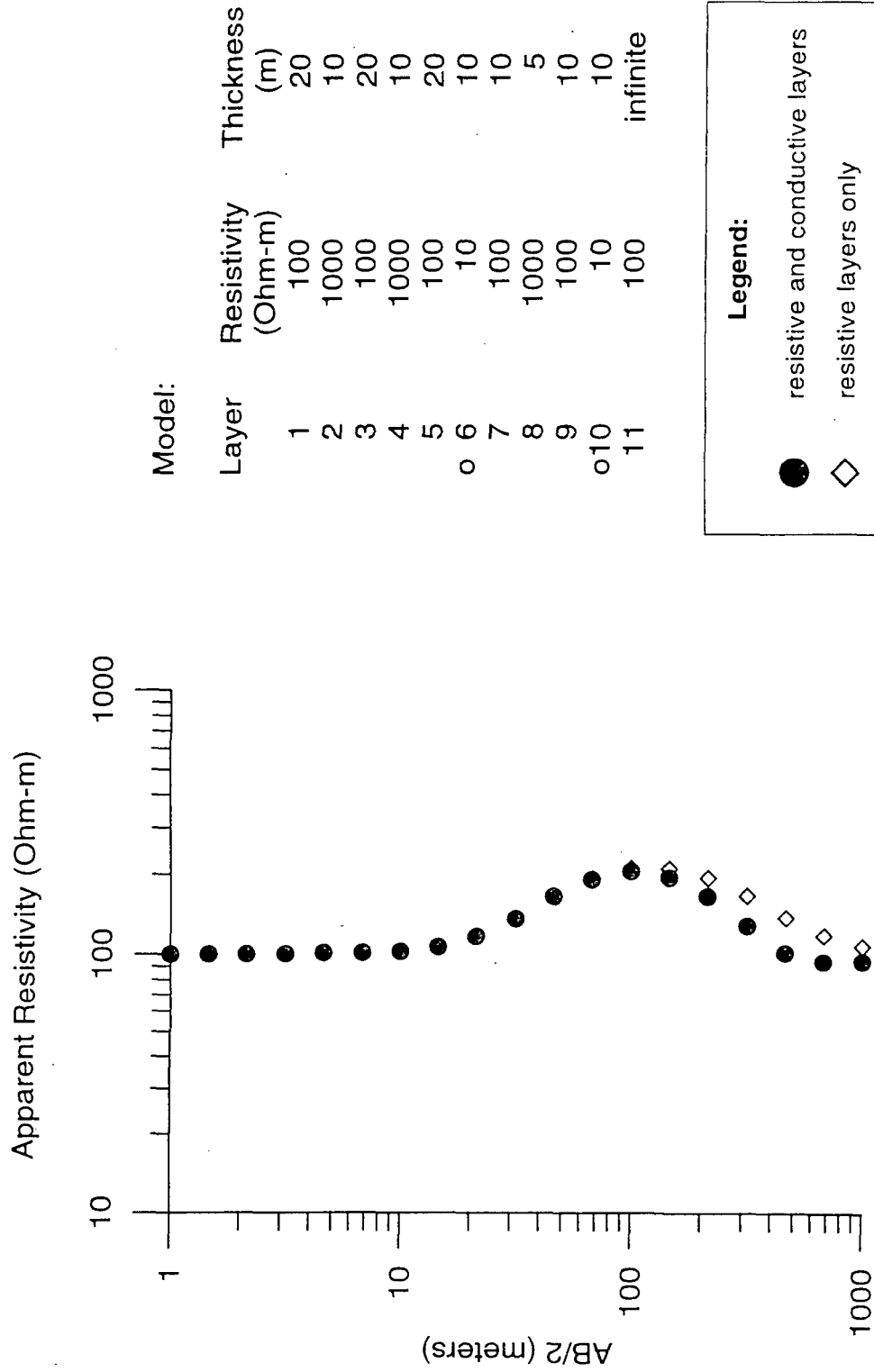
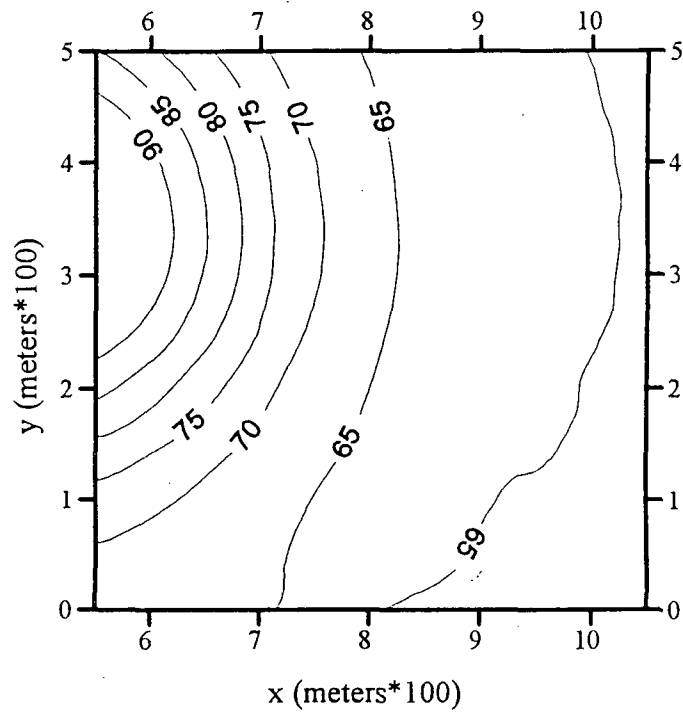
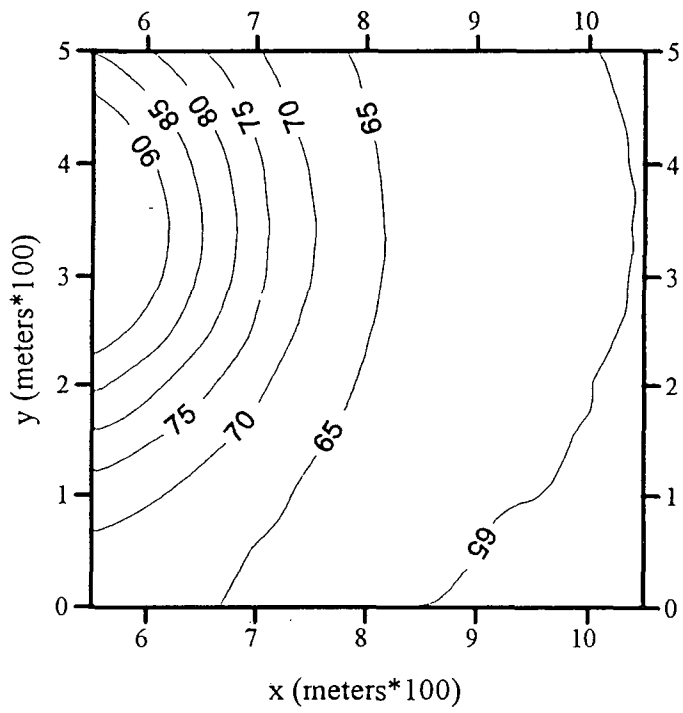


Figure 11: Contour map of the total apparent resistivity for
a) 25 m thick 10 Ω -m layer 125 m deep in a 100 Ω -m background
b) 5 m thick 2 Ω -m layer 125 m deep in a 100 Ω -m background.

a)



b)

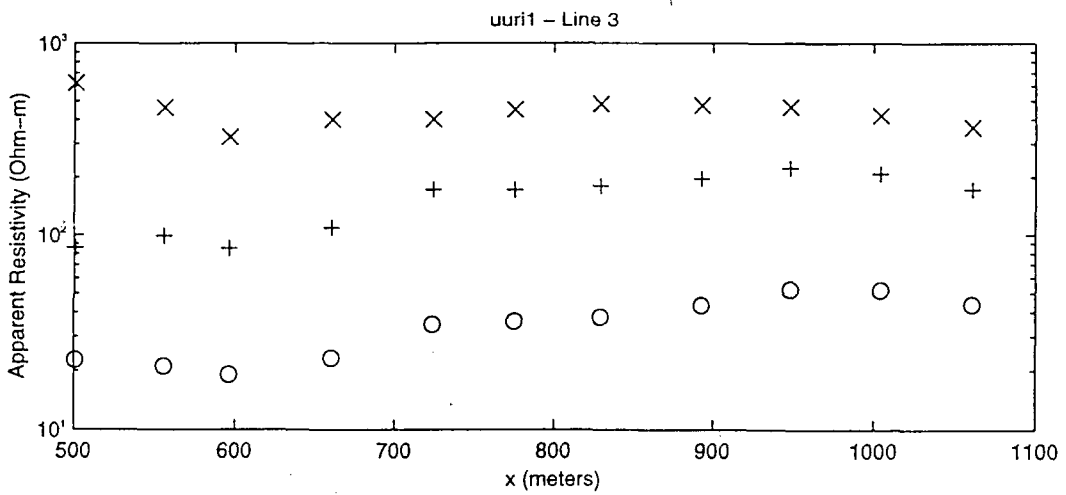
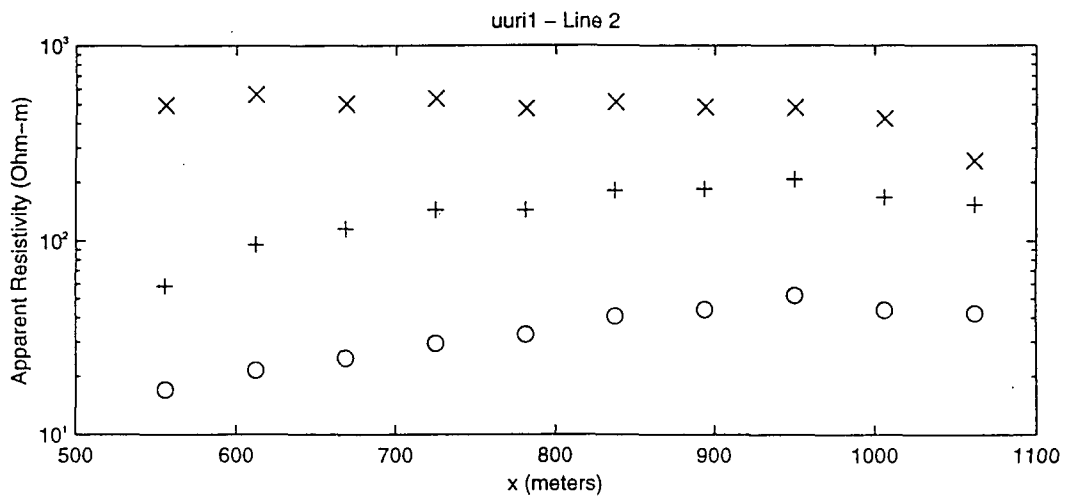
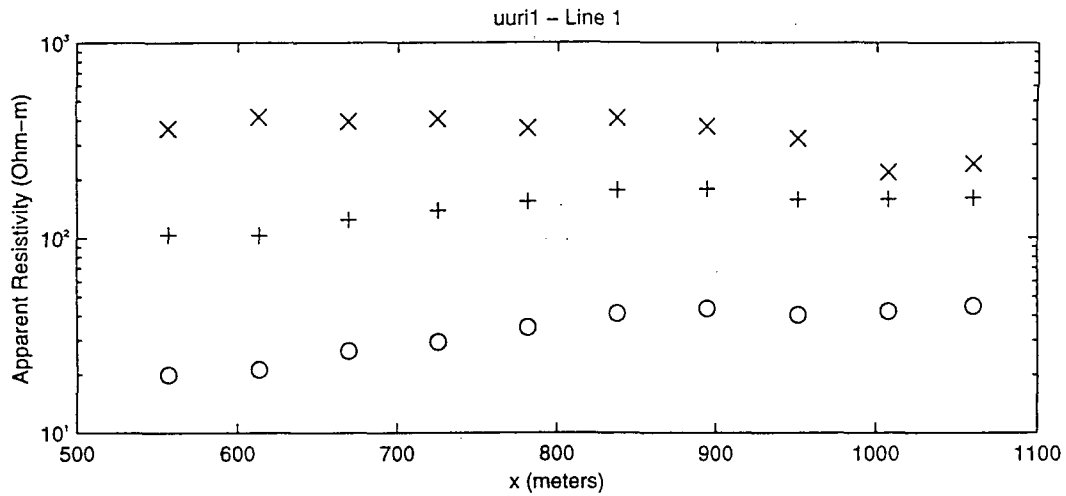


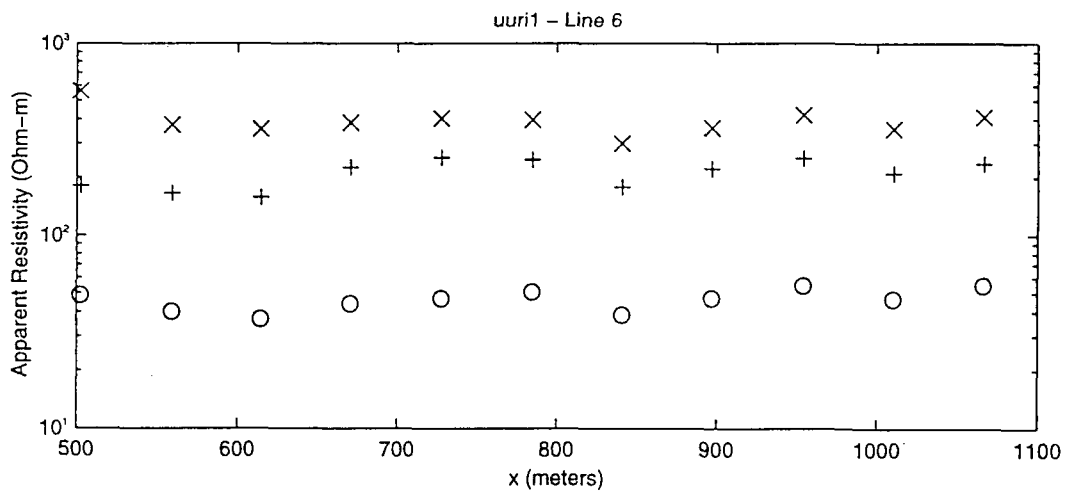
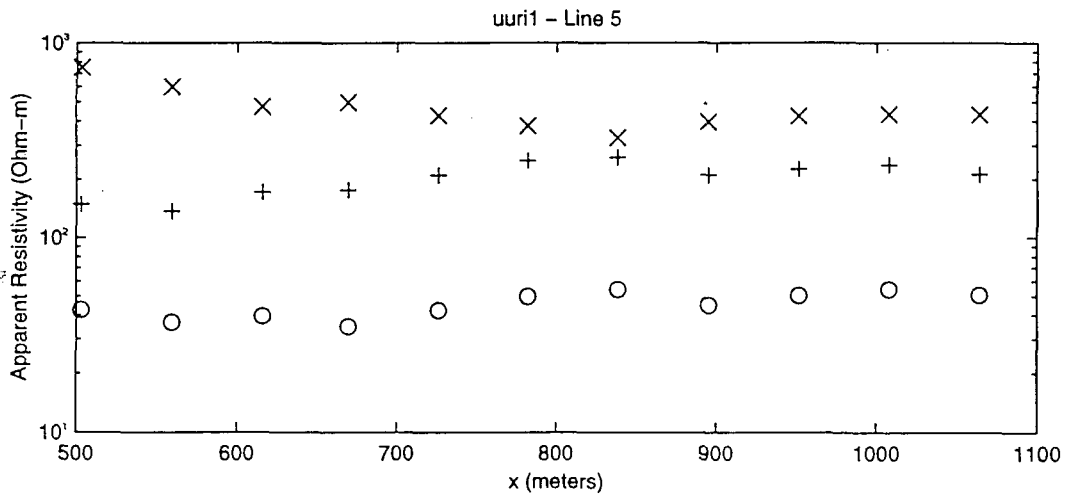
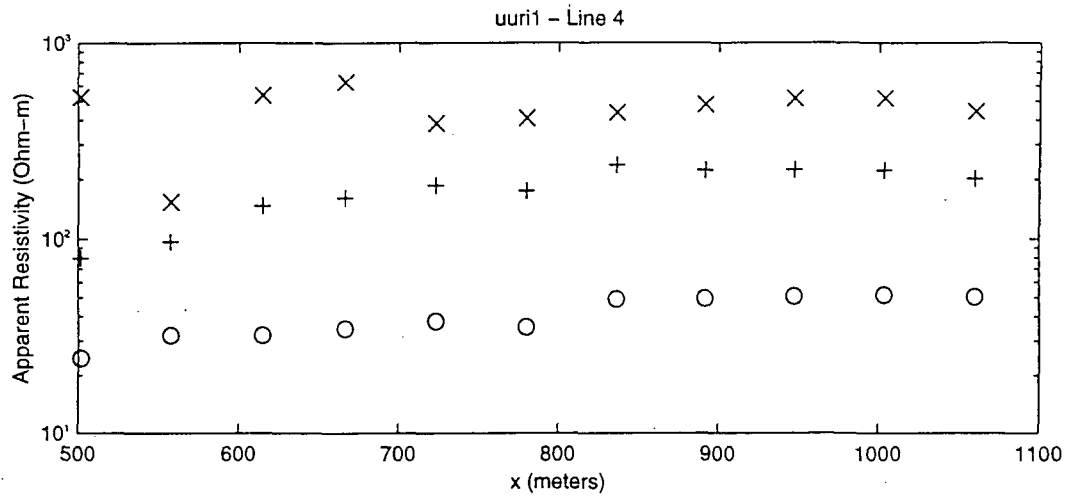
0.0] m. Figure 11b is the total field apparent resistivity map due to a 5 m thick $2 \Omega\text{-m}$ layer 125 m deep in a $100 \Omega\text{-m}$ background. The method is obviously sensitive only to the quotient t/ρ for the anomalous layer. In practice, that means that until we have additional information about the resistivity or thickness of the layer our interpretation will be nonunique. This example demonstrates the great importance of our well-logs in *constraining our interpretation.*

Before we start with an interpretation of our field data it is important to try to specify the immediate environment surrounding the current electrodes. If the conductivity structure is 1-D, the position of the current electrodes does not have a significant influence on the data, and we should get a similar resistivity distribution using the current electrodes in the vicinity of borehole UURI#1 or using the current electrodes in the vicinity of borehole UURI#2. If the structure is 2-D or 3-D these pictures will be different, and the response will depend on the particular position of the electrodes with respect to the anomalous body.

Figure 12 and Figure 13 are plots of the total resistivity curves with increasing distance from the transmitter site along each of nine profiles (Line 1 - Line 9) shown in Figure 5. Line 1 is a profile with y-coordinate close to 0 m in Figure 5. The distance between profiles is 50 m. Each plot shows the total field apparent resistivity for three different electrode configurations used in the field. Figure 12 shows the results for the bipoles in the vicinity of borehole UURI#1 and Figure 13 the results for UURI#2. The resistivity curves in both figures are smooth and without significant lateral variations. For surface electrode configurations (bipole 1 and bipole 2), resistivity increases slightly with depth. Apart of the fact that the curves on each line are displaced from each other, they are approximately the same. This suggests that the DC shift for each transmitter configuration reflects the geoelectric environment of the transmitter

Figure 12: Total apparent resistivity curves vs. distance for UURI#1.
× bipole 1
+ bipole 2
o bipole 3





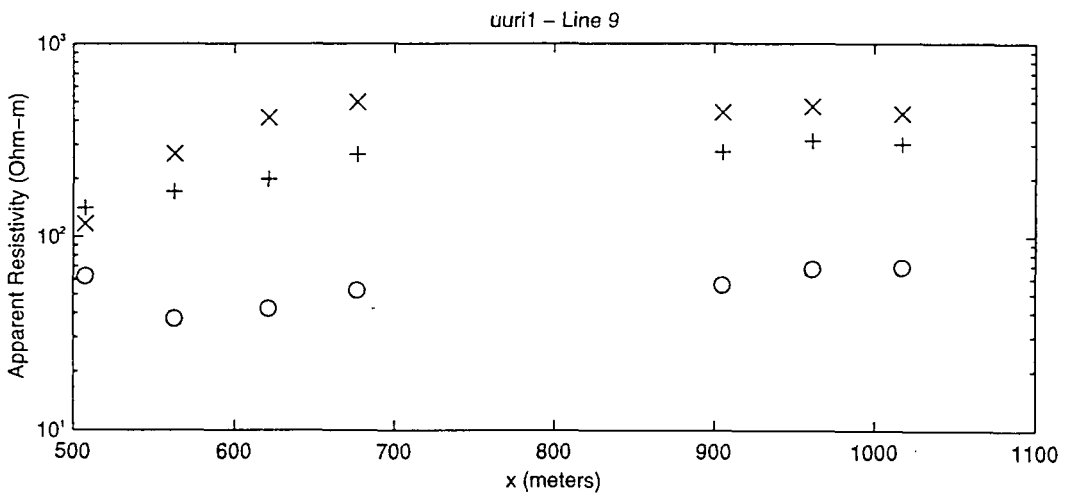
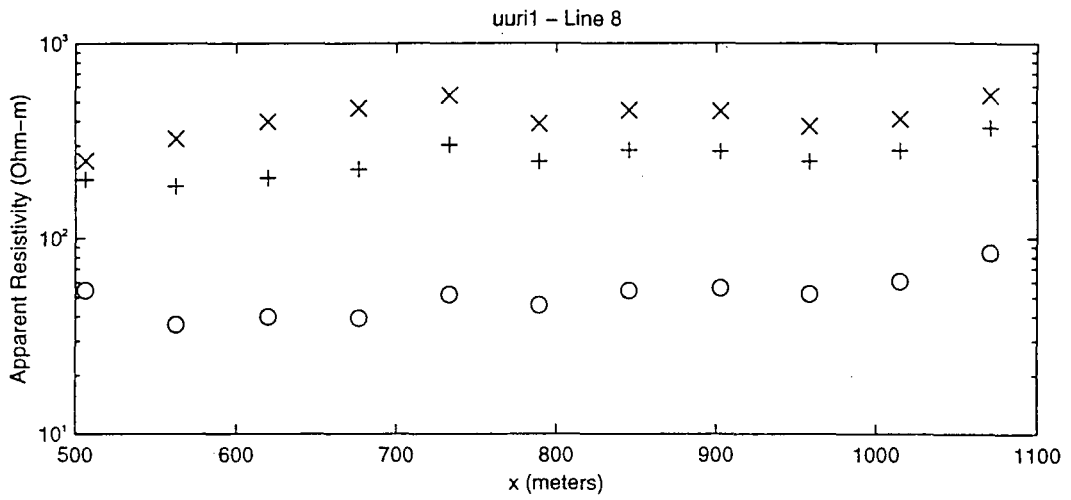
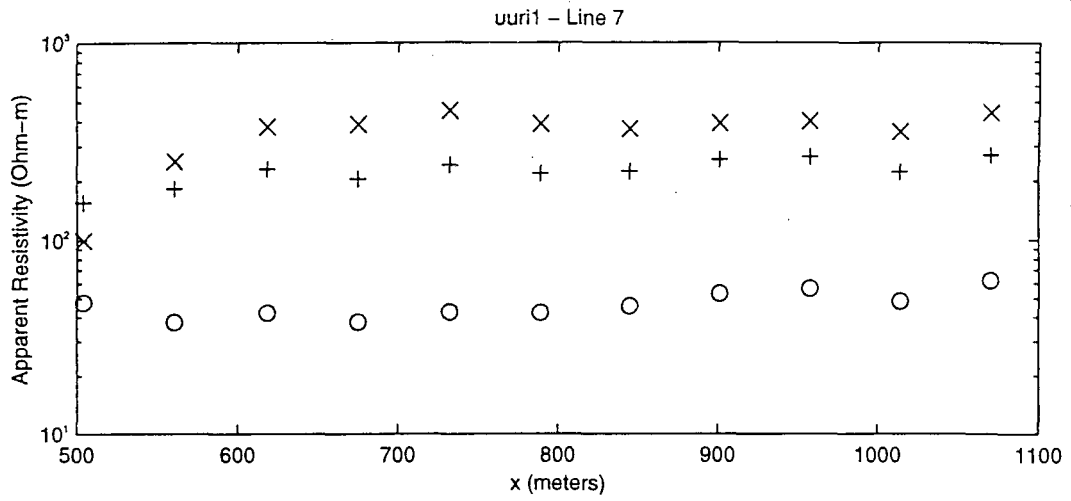
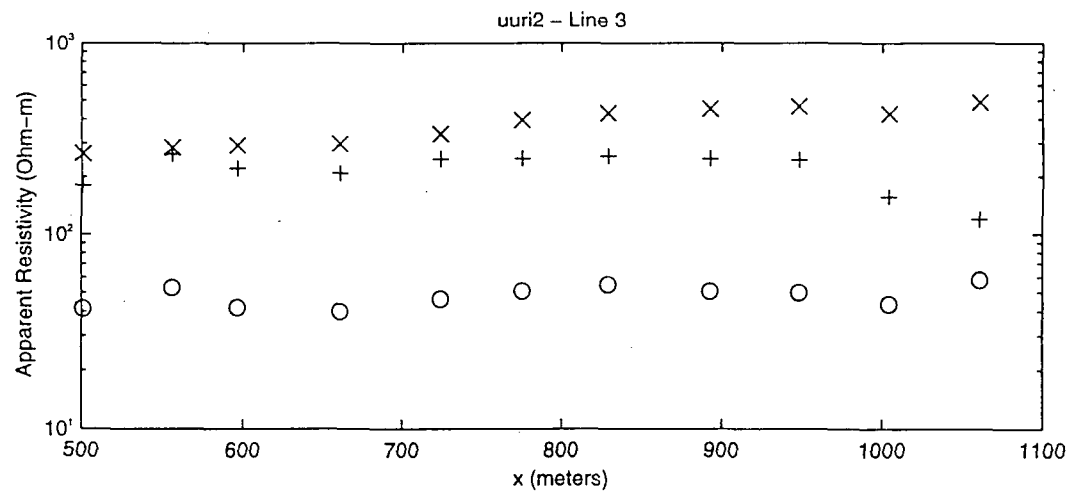
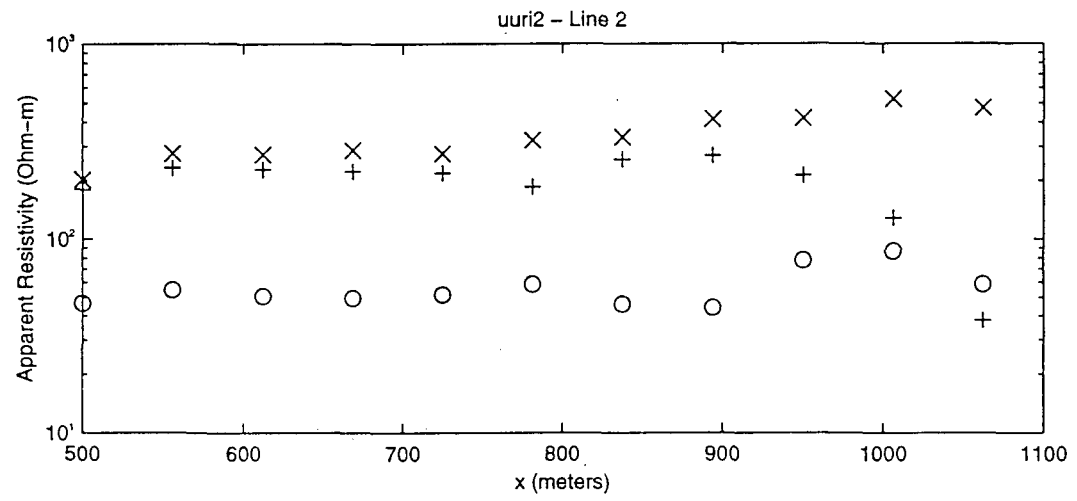
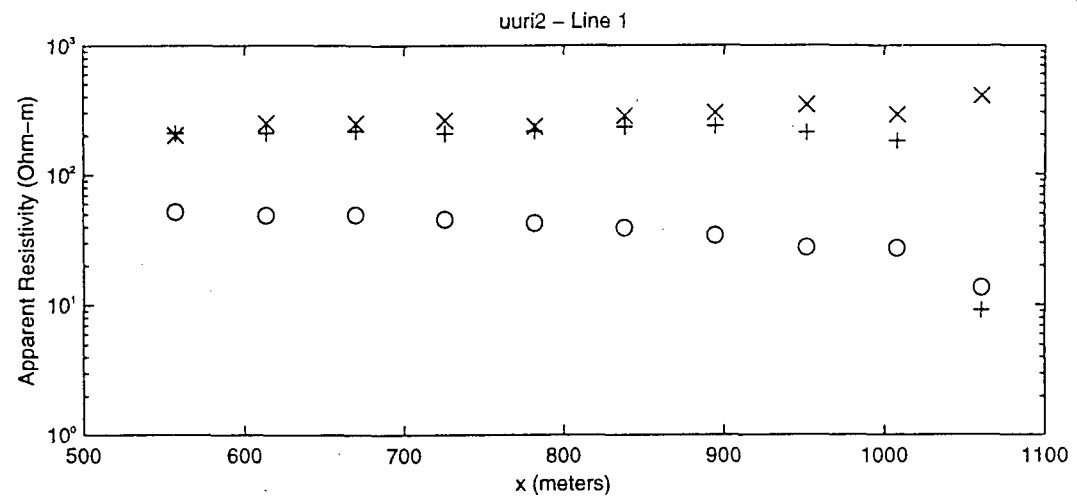
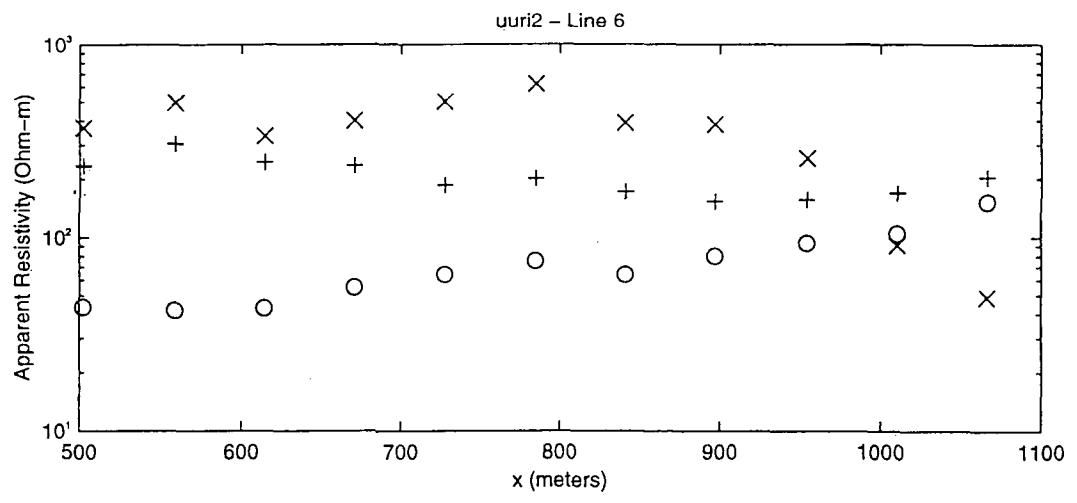
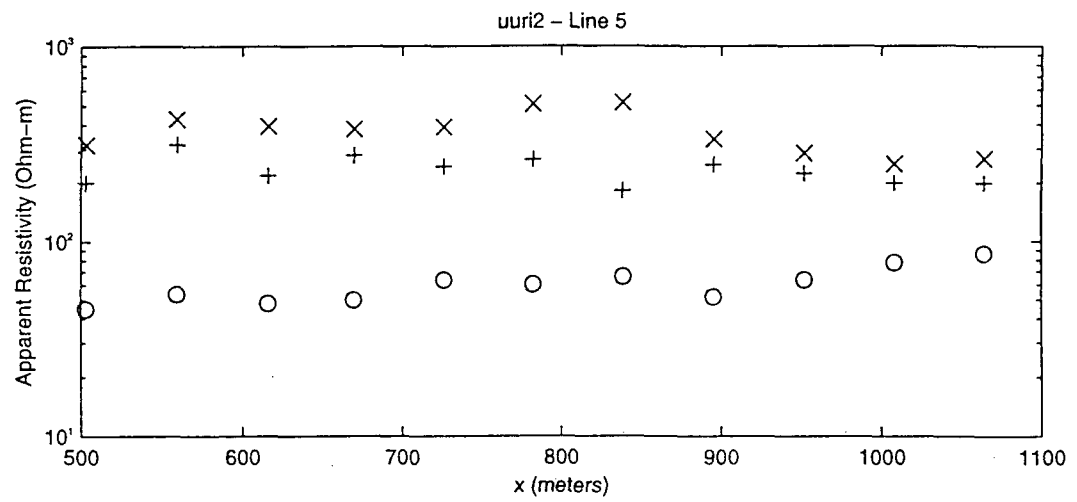
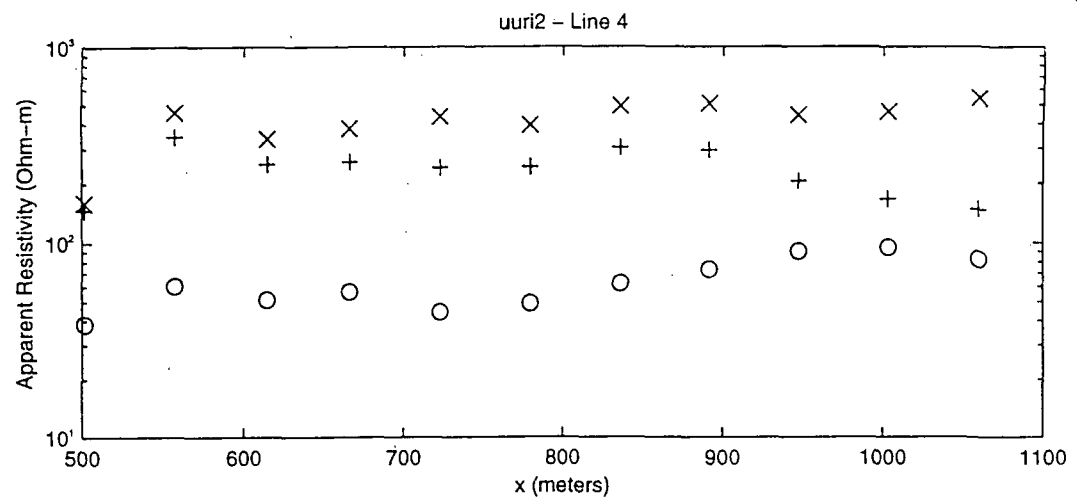
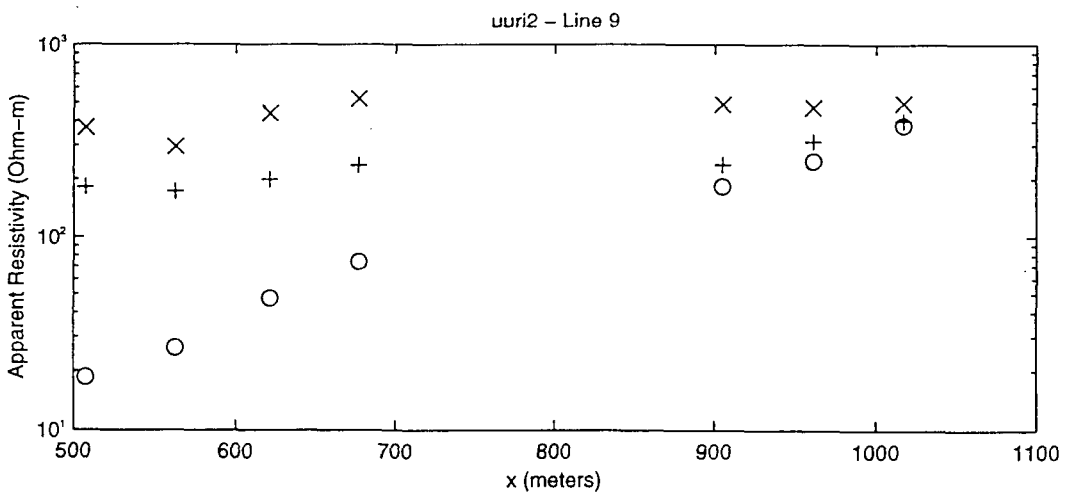
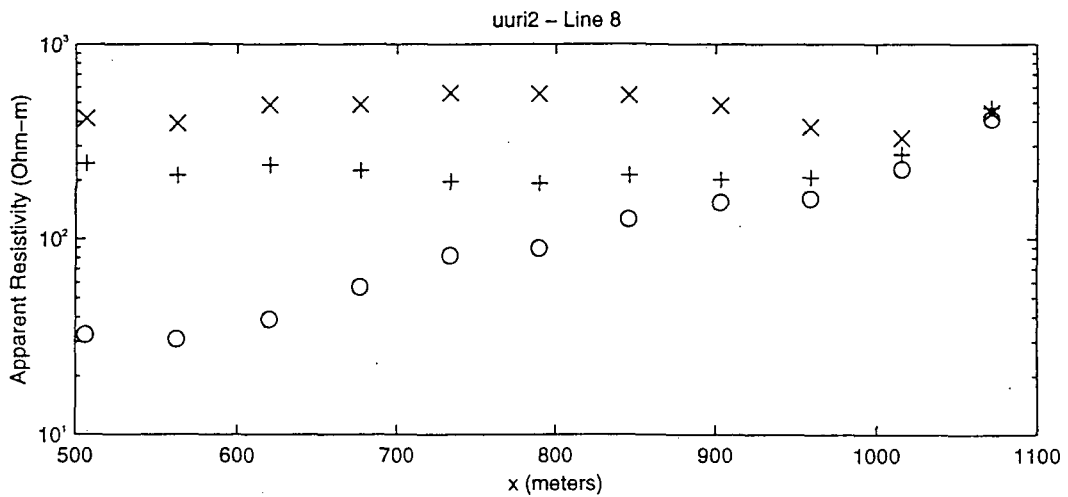
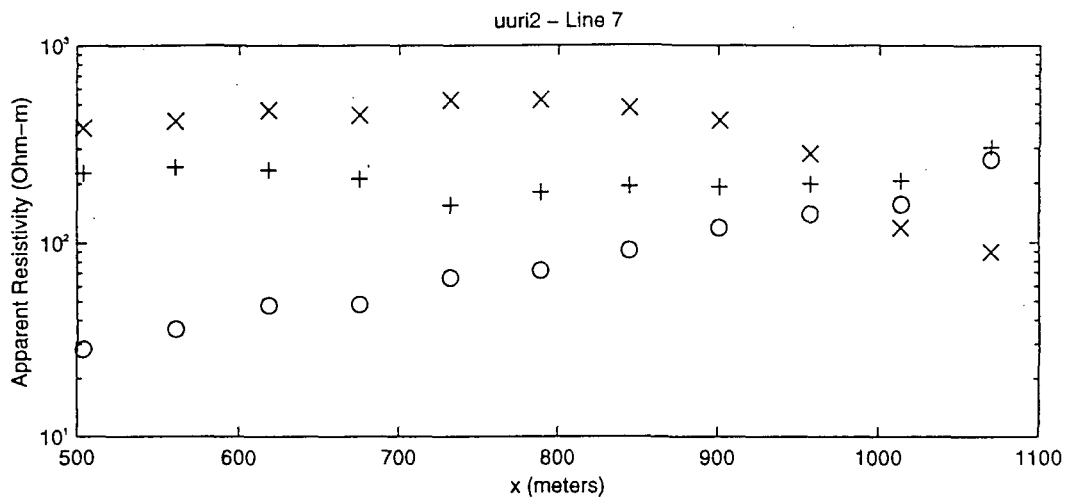


Figure 13: Total apparent resistivity curves vs. distance for UURI#2.
× bipole 1
+ bipole 2
o bipole 3







electrodes, while the major trend of the curves, being similar, reflect the gross geoelectric section in the survey area.

Contour maps of total apparent resistivity for each bipole source in the vicinity of borehole UURI#1 are shown in Figures 14, 15, and 16. The total apparent resistivity for bipole 1, with A_1 and B_1 current electrodes (Figure 14), ranges from 300 Ω -m to 600 Ω -m. The pattern of the apparent resistivity is complex and it is very difficult to distinguish visually the response of the deeper structure from near-surface distortions. In Figure 15, the total apparent resistivity for the measurements made using the current electrodes A_1 and B_2 (bipole 2) varies from 100 Ω -m to 300 Ω -m. The surprising discrepancy between Figures 14 and 15 suggests that the transmitter position is having a major influence on the total field apparent resistivity response. The large difference in the apparent resistivity values suggest that bipole 1 is located in a highly resistive environment, while bipole 2 is located in a more conductive environment. Because A_1 is a common electrode for both bipoles only the environment for current electrodes B_1 and B_2 is involved in this discrepancy.

The total apparent resistivity map for current electrodes A_1 and B_3 (bipole 3) is shown in Figure 16. Although the values of the apparent resistivity are tens of Ω -m, if we compare Figure 16 and Figure 15 a similar contour pattern can be recognized in both figures. The lowest apparent resistivities occur close to the current electrode. The apparent resistivity increases with radial distance from both current electrodes, B_2 and B_3 respectively. The circular contours suggest that the overall resistivity structure is approximately 1-D or layered. Superimposed onto the broad apparent resistivity pattern is a small anomaly that can be seen in the middle of the contour map suggesting the presence of a small 3-D structure.

Figure 14: Contour map of the total apparent resistivity for UURI#1 bipole 1.
 $A_1 = [32.5, 250.0, 0.0]$ m
 $B_1 = [478.5, 344.1, 0.0]$ m

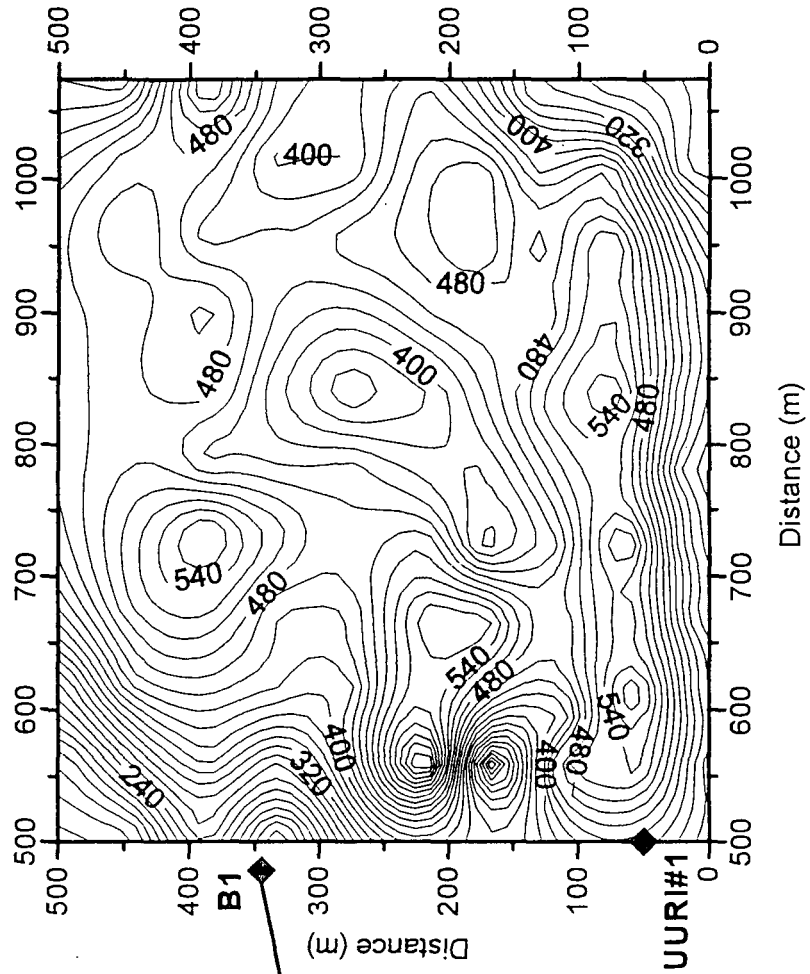


Figure 15: Contour map of the total apparent resistivity for UURI#1 bipole 2.
 $A_1 = [32.5, 250.0, 0.0]$ m
 $B_2 = [500.0, 50.0, 0.0]$ m

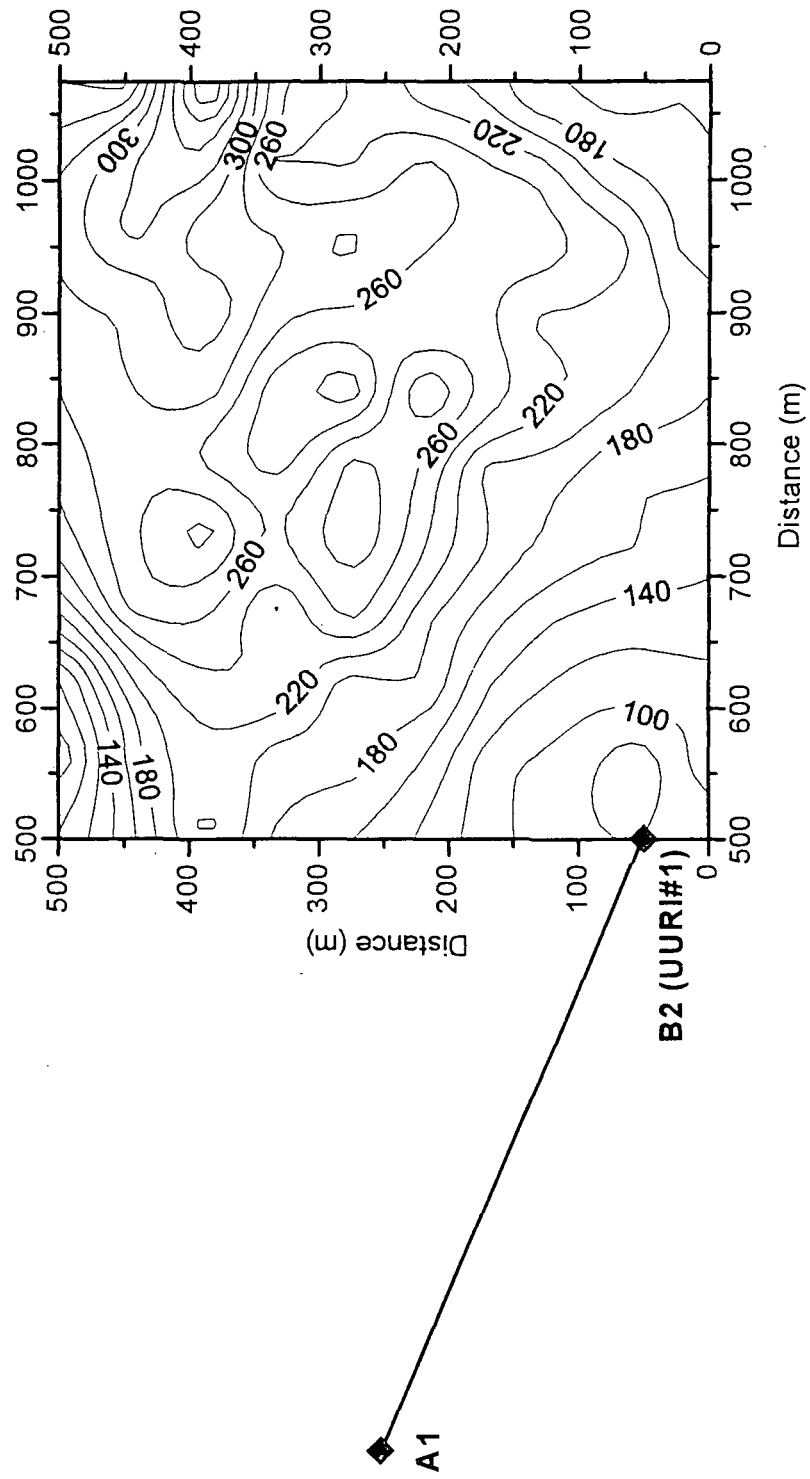
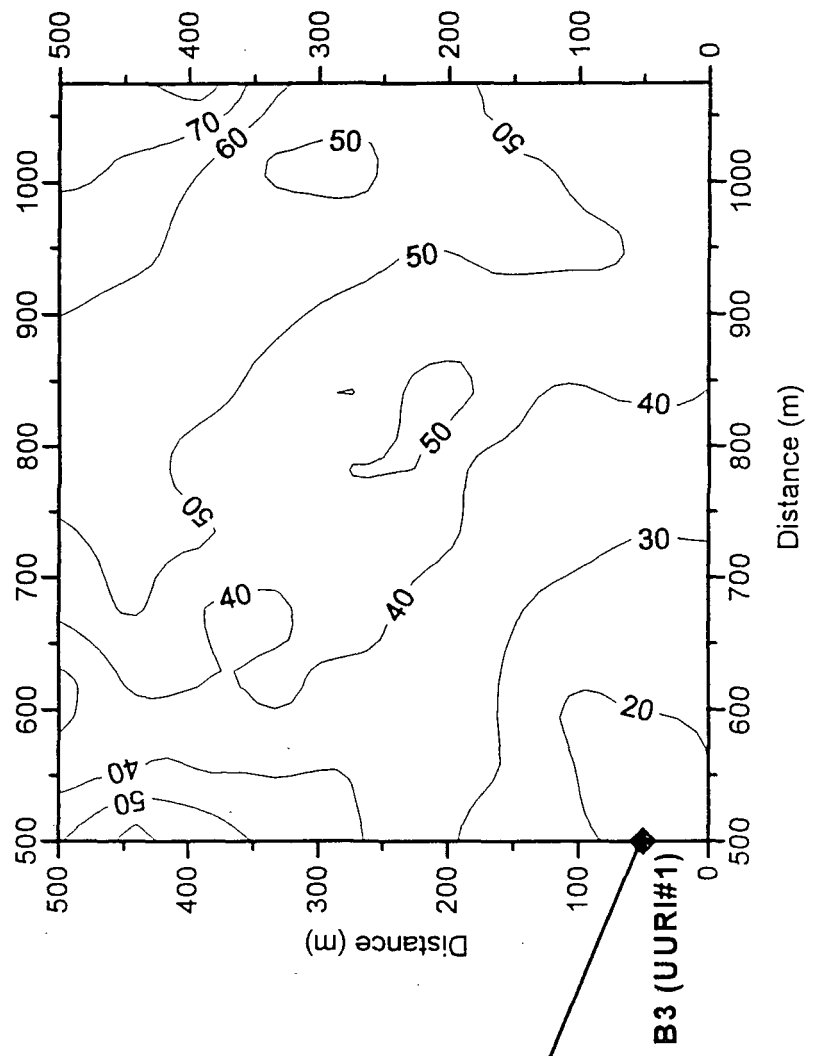


Figure 16: Contour map of the total apparent resistivity for UURI#1 bipole 3.
 $A_1 = [32.5, 250.0, 0.0] \text{ m}$
 $B_3 = [500.0, 50.0, 100.0] \text{ m}$



Figures 17, 18, and 19 show the total apparent resistivity maps for the current electrodes A_2 and B_4 (bipole 1), A_2 and B_5 (bipole 2) and A_2 and B_6 (bipole 3) respectively. The resistivity ranges and contour patterns for the UURI#2 bipoles are similar to those observed for corresponding bipoles of UURI#1.

This again suggests that the major structure in our study area is a layered earth with several smaller structures superimposed. Our previous model studies have shown that the presence of a highly resistive layer could have an important influence on the data interpretation. In our study area, a highly resistive coal layer is interpreted at several depths in both borehole logs. This interpretation is substantiated by the borehole cores, where coal was present at approximately the same depth in both boreholes. Thus we make the assumption that the highly resistive layer at 74 m depth is continuous through the measured area. The presence of the highly resistive layer in our model is important geophysically in that it enables us to model the different responses for surface and borehole electrode configurations as are shown in Figure 15 and Figure 16. On the other hand, this highly resistive layer has a screening effect on deeper conductive layers, which results in poor resolution of variations in underlying conductive layers in our area. The contour maps for bipole 2 and bipole 3 for UURI#1 can be interpreted as the response of a layered earth model with a highly resistive layer above a conductive layer, both in the depth interval 50 m to 100 m. The highly resistive layer alone cannot produce the low resistivities of the borehole electrode configuration. Therefore the presence of the conductive layer below a highly resistive layer in the model is necessary, both of whose depths are less than the borehole electrode position. The total apparent resistivity contour maps for bipole 2 and bipole 3 respectively for UURI#1, as a response of a model consisting of a 12.5 m thick, 10 Ω -m layer at a depth of 75 m overlaid by a 12.5 m thick, 5000 Ω -m, 50 m deep layer, are shown in

Figure 17: Contour map of the total apparent resistivity for UURI#2 bipole 1.
 $A_2 = [1577.5, 391.0, 0.0]$ m
 $B_4 = [1060.0, 315.0, 0.0]$ m

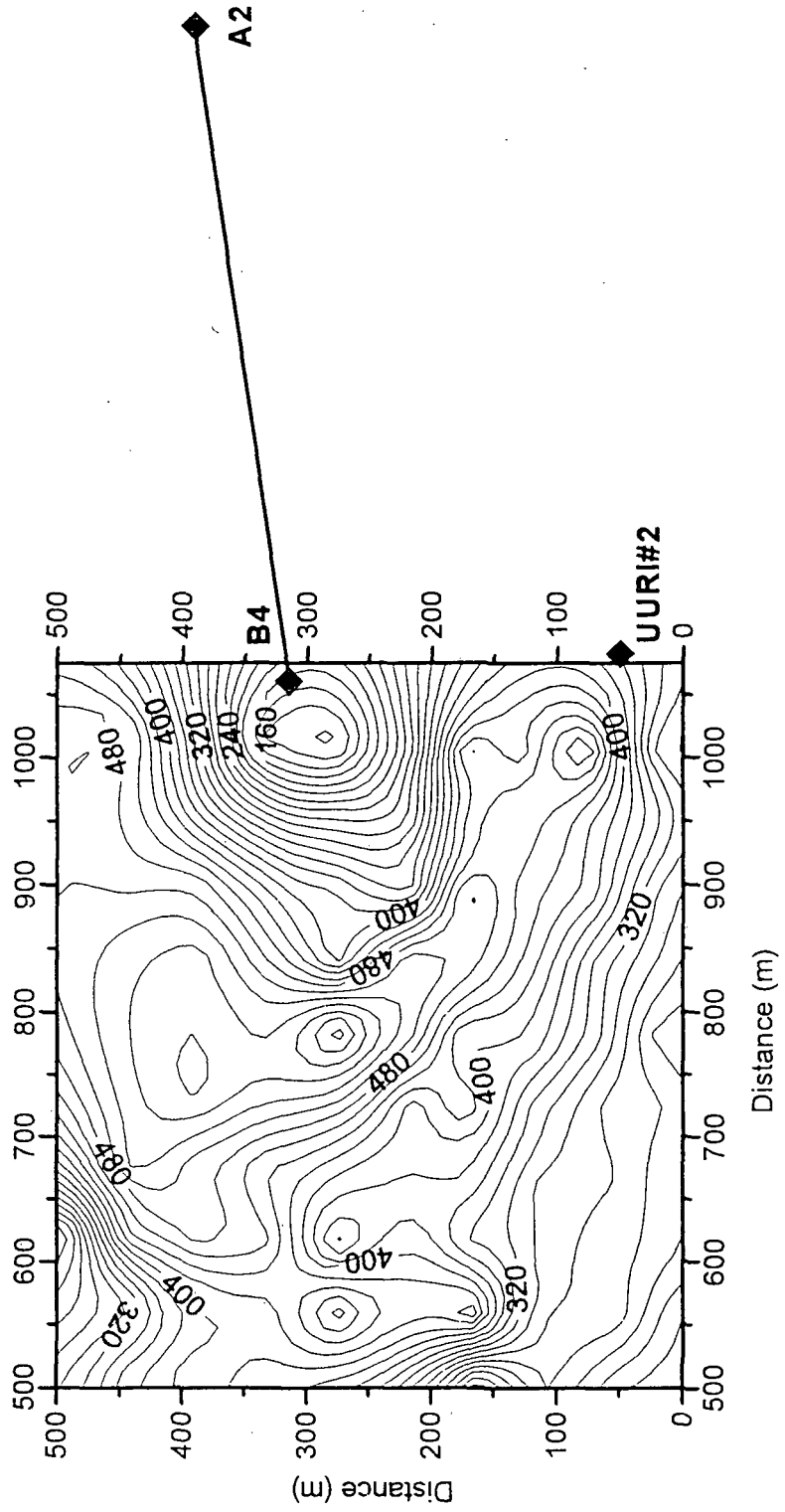


Figure 18: Contour map of the total apparent resistivity for UURI#2 bipole 2.
 $A_2 = [1577.5, 391.0, 0.0]$ m
 $B_5 = [1082.31, 49.98, 0.0]$ m

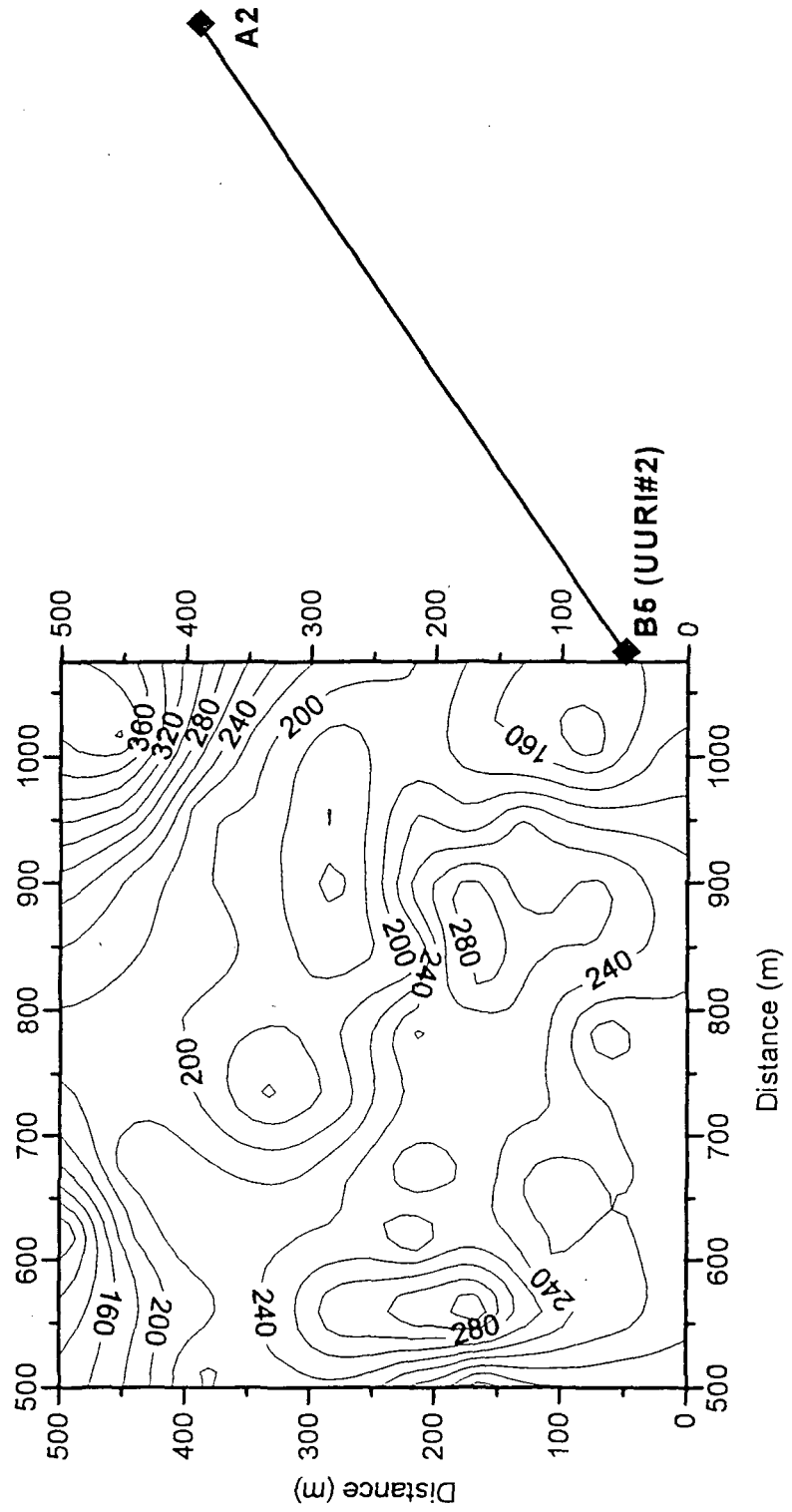
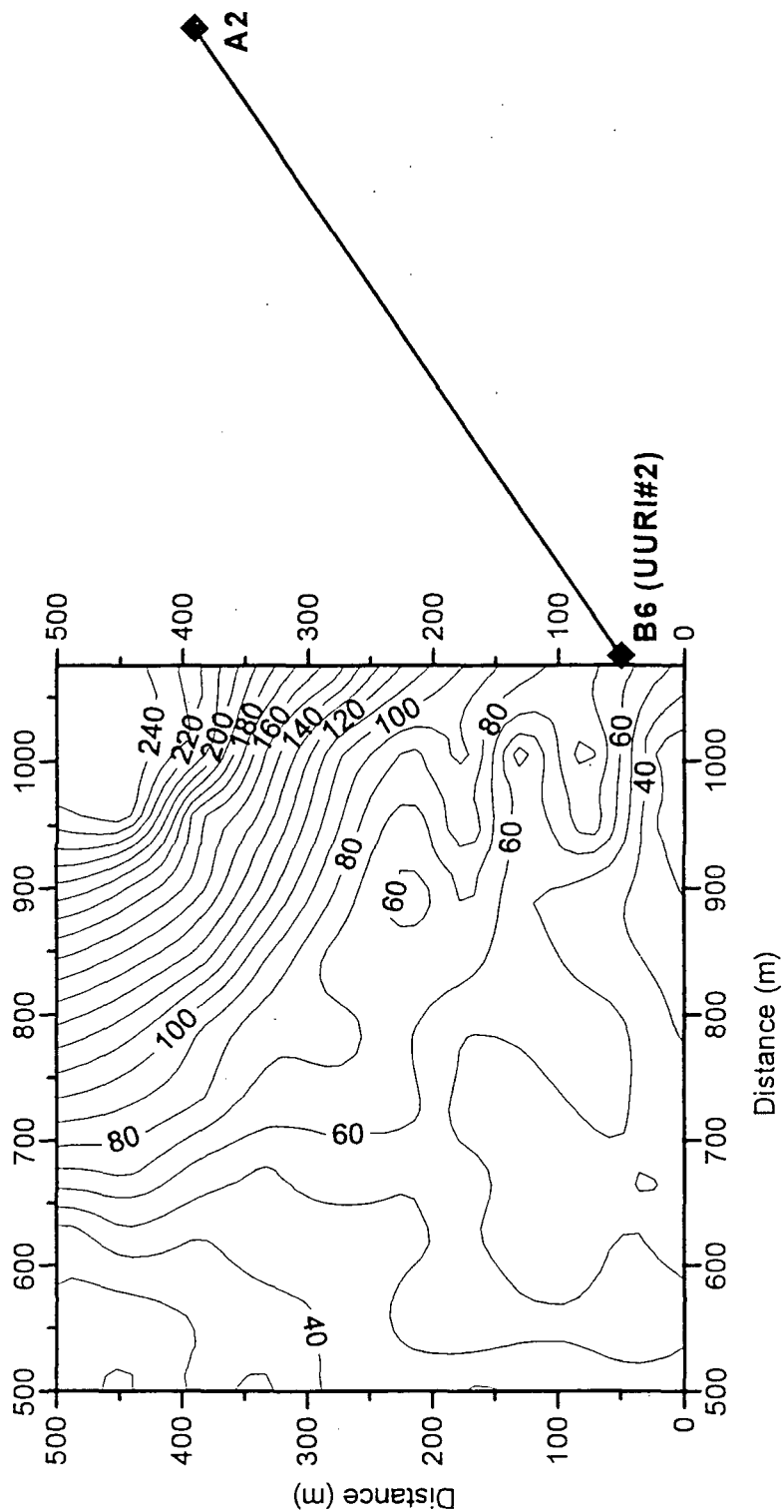


Figure 19: Contour map of the total apparent resistivity for UURI#2 bipole 3.
 $A_2 = [1577.5, 391.0, 0.0]$ m
 $B_6 = [1082.31, 49.98, 100.0]$ m



Figures 20 and 21 respectively. If one compares Figures 20 and 15 and Figures 21 and 16 respectively, it is possible to see that the contour pattern and resistivity range are very similar. The same model, however, does not fit the data for bipole 1. This suggests the presence of a complex geological structure in our study area. Bipole 1 data are characterized by their very high resistivity with respect to bipole 2 data. The presence of the Muddy Creek Canyon close to current electrodes B_1 and B_4 influences the data, but it is not the only cause of the high resistivities in that area. Figure 22 shows the influence of the canyon with a 100 Ω -m half-space background. Our modeling shows that the canyon influence on the bipole 1 data can be as much as 20 % in some parts of the measured area.

Ambiguities in the data interpretation due to transmitter - receiver orientation should be minimized by using tensor calculations. Figures 23 and 24 show the P_2 invariant contour maps calculated using bipole 1 and bipole 2, and bipole 1 and bipole 3 respectively in the vicinity of the borehole UURI#1. Figure 25 and Figure 26 show the P_2 invariant contour maps for a combination of bipole 1 and bipole 2, and bipoles 1 and bipole 3 respectively in the vicinity of the borehole UURI#2. The P_2 invariants calculated for the surface electrode configuration (combination of bipole 1 and bipole 2) are in the range of 200 Ω -m to 400 Ω -m, while the values for the surface-to-borehole configurations are about 50% lower. The contour pattern is consistent for both configurations. We do not see steep gradients or abrupt changes in the calculated values. The model studies of Appendix B show that closed contours of high P_2 resistivities can indicate a high resistivity structure in a more conductive environment. Therefore, in our case, it is feasible that the P_2 invariants are sensing mostly the top highly resistive layer or layers and they are not sensitive to conductive structures below. The other possibility is that the extent of conductive units is much smaller than

Figure 20: Contour map of total apparent resistivity for UURI#1 bipole 2 configuration as a response of 12.5 thick, 10 Ohm-m, 75 m deep layer overlaid by 12.5 m thick, 5000 Ohm-m, 50 m deep layer in 100 Ohm-m resistive host.

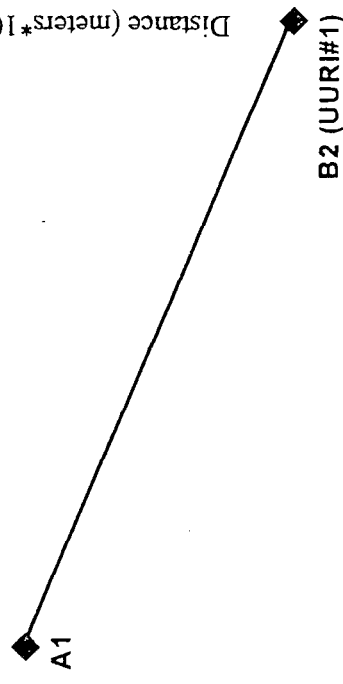
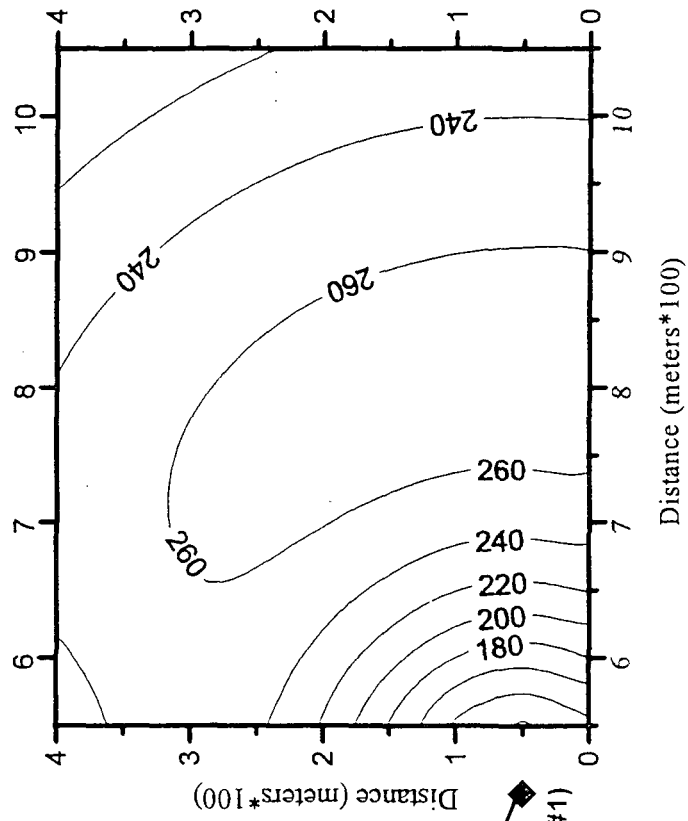
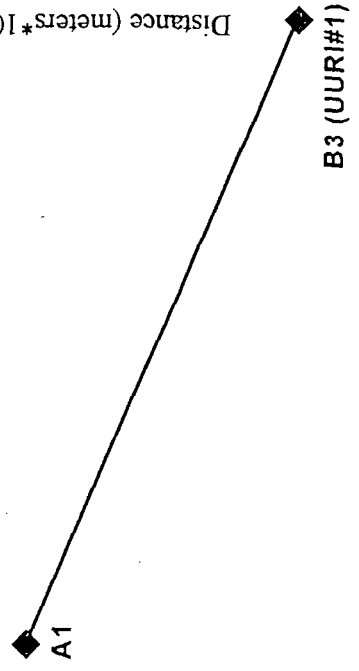
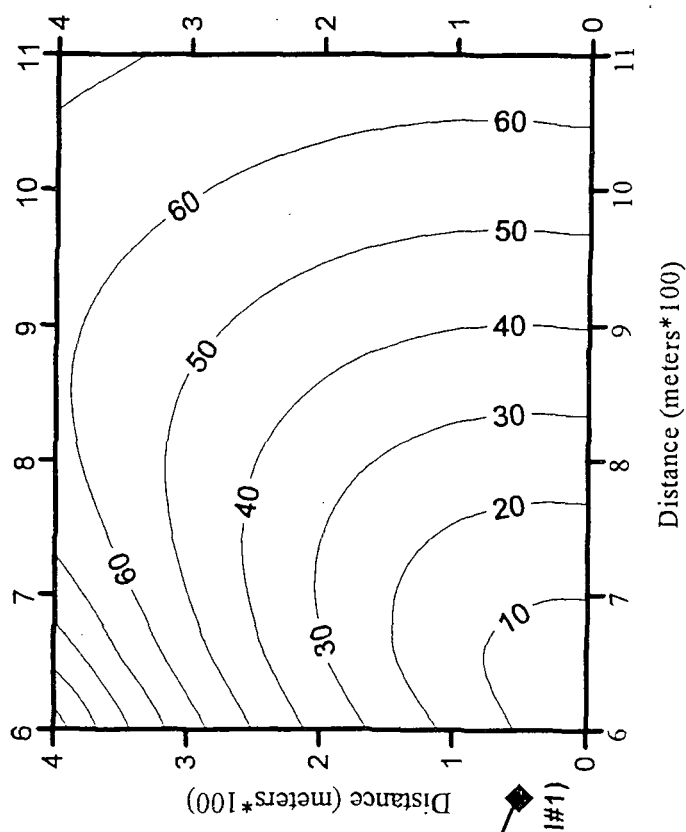


Figure 21: Contour map of total apparent resistivity for UURI#1 bipole 3 configuration as a response of 12.5 thick, 10 Ohm-m, 75 m deep layer overlaid by 12.5 m thick, 5000 Ohm-m, 50 m deep layer in 100 Ohm-m resistive host.



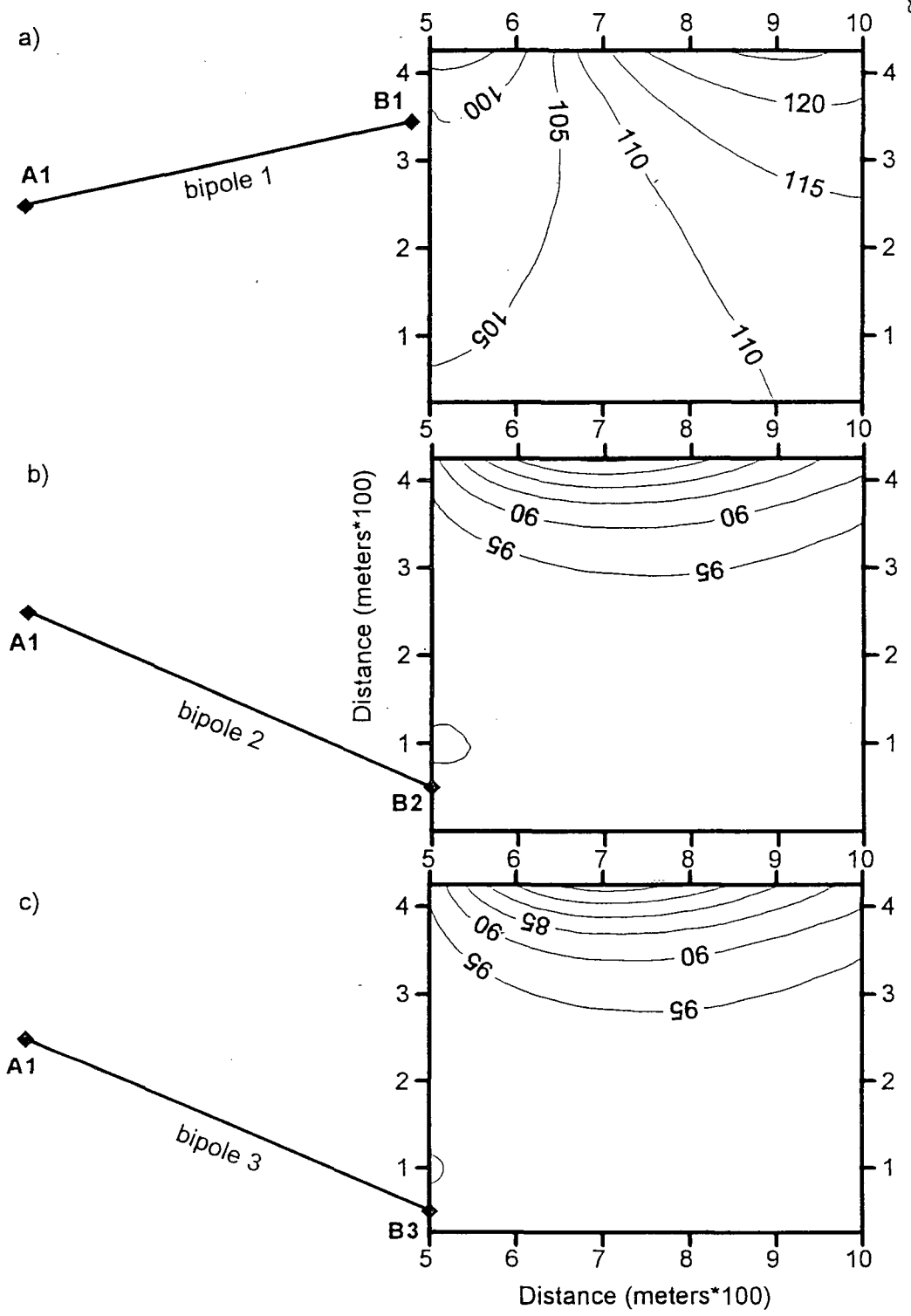


Figure 22: Canyon influence on the apparent resistivity
half-space resistivity: 100 Ohm-m
a) bipole 1
b) bipole 2
c) bipole 3

Figure 23: Contour map of the P_2 tensor invariant for UURI#1 using bipole 1 and bipole 2.

bipole 1: $A_1 = [32.5, 250.0, 0.0]$ m
 $B_1 = [478.5, 344.1, 0.0]$ m

bipole 2: $A_1 = [32.5, 250.0, 0.0]$ m
 $B_2 = [500.0, 50.0, 0.0]$ m

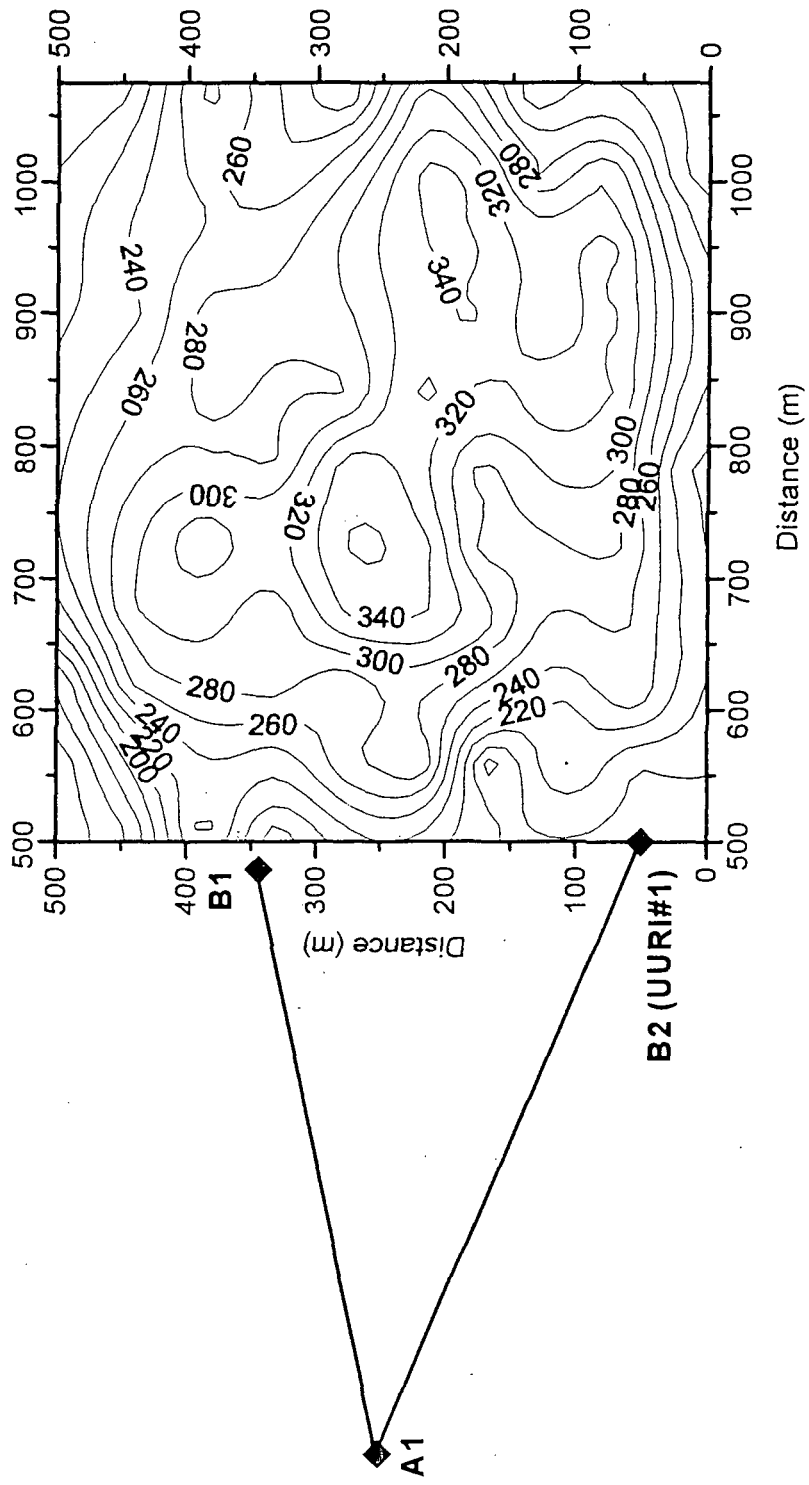


Figure 24: Contour map of the P_2 tensor invariant for UURI#1 using bipole 1 and bipole 3.

bipole 1: $A_1 = [32.5, 250.0, 0.0]$ m
 $B_1 = [478.5, 344.1, 0.0]$ m

bipole 3: $A_1 = [32.5, 250.0, 0.0]$ m
 $B_3 = [500.0, 50.0, 100.0]$ m

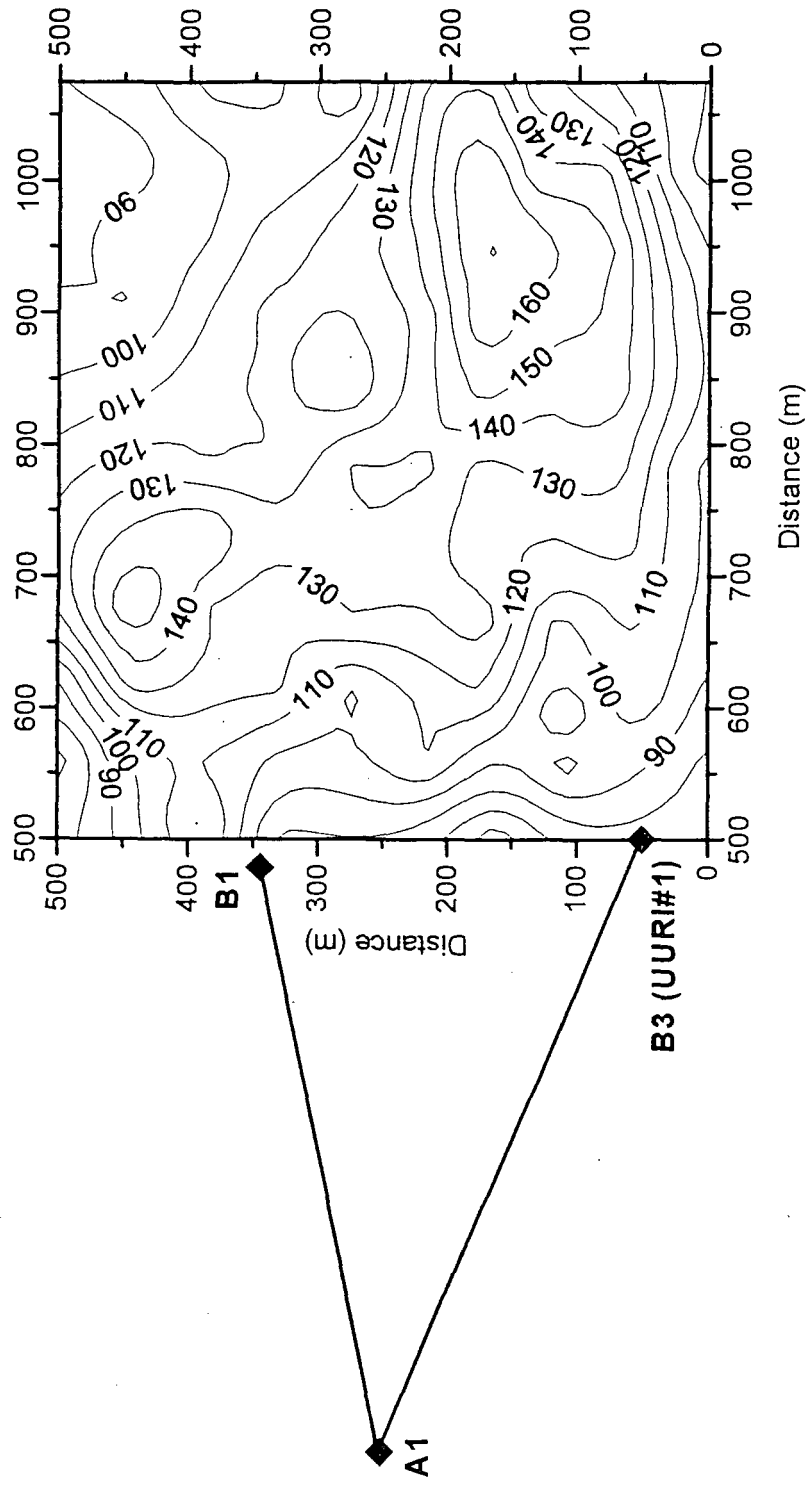


Figure 25: Contour map of the P_2 tensor invariant for UURI#2 using bipole 1 and bipole 2.

bipole 1: $A_2 = [1577.5, 391.0, 0.0]$ m
 $B_4 = [1060.0, 315.0, 0.0]$ m

bipole 2: $A_2 = [1577.5, 391.0, 0.0]$ m
 $B_5 = [1082.31, 49.98, 0.0]$ m

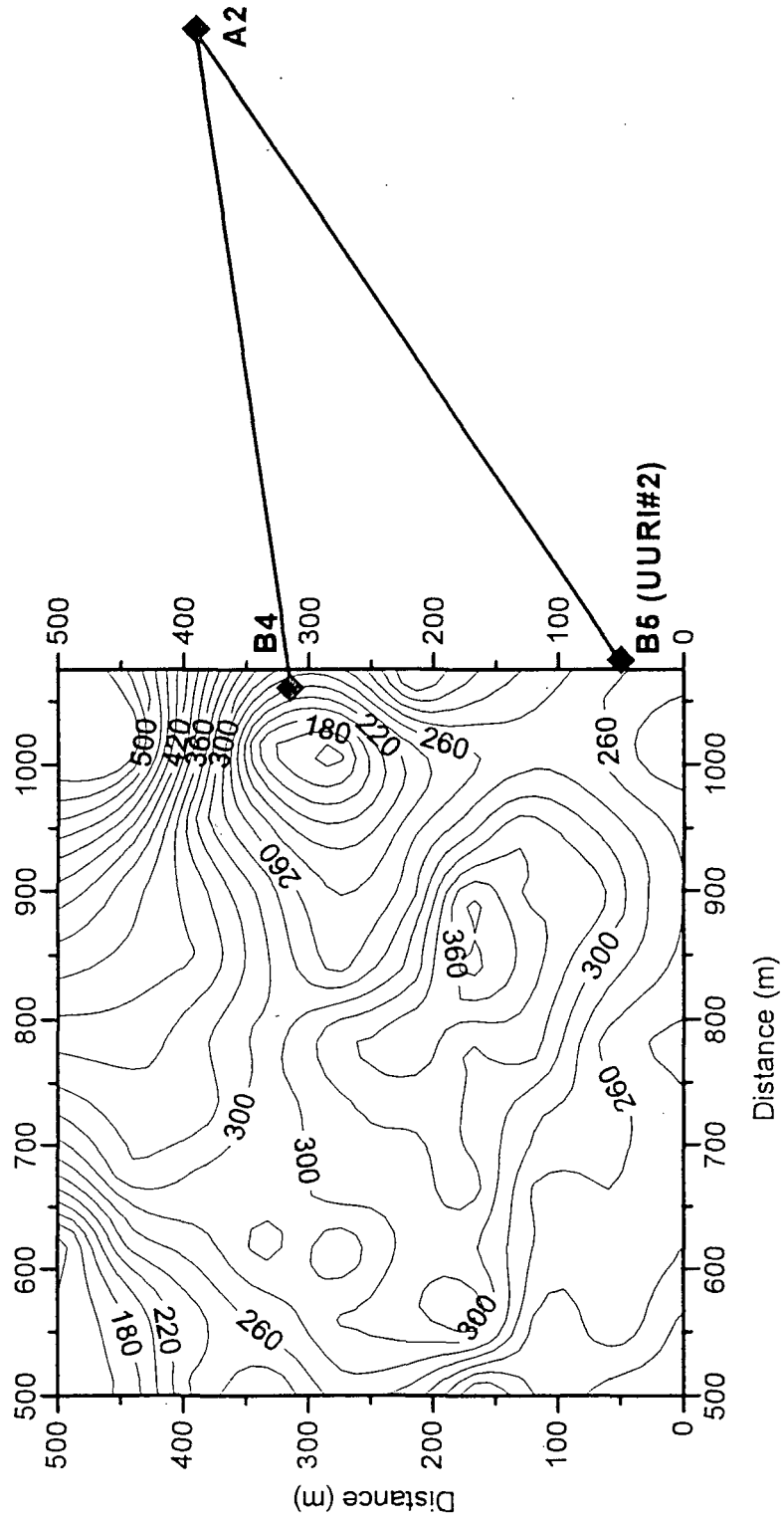
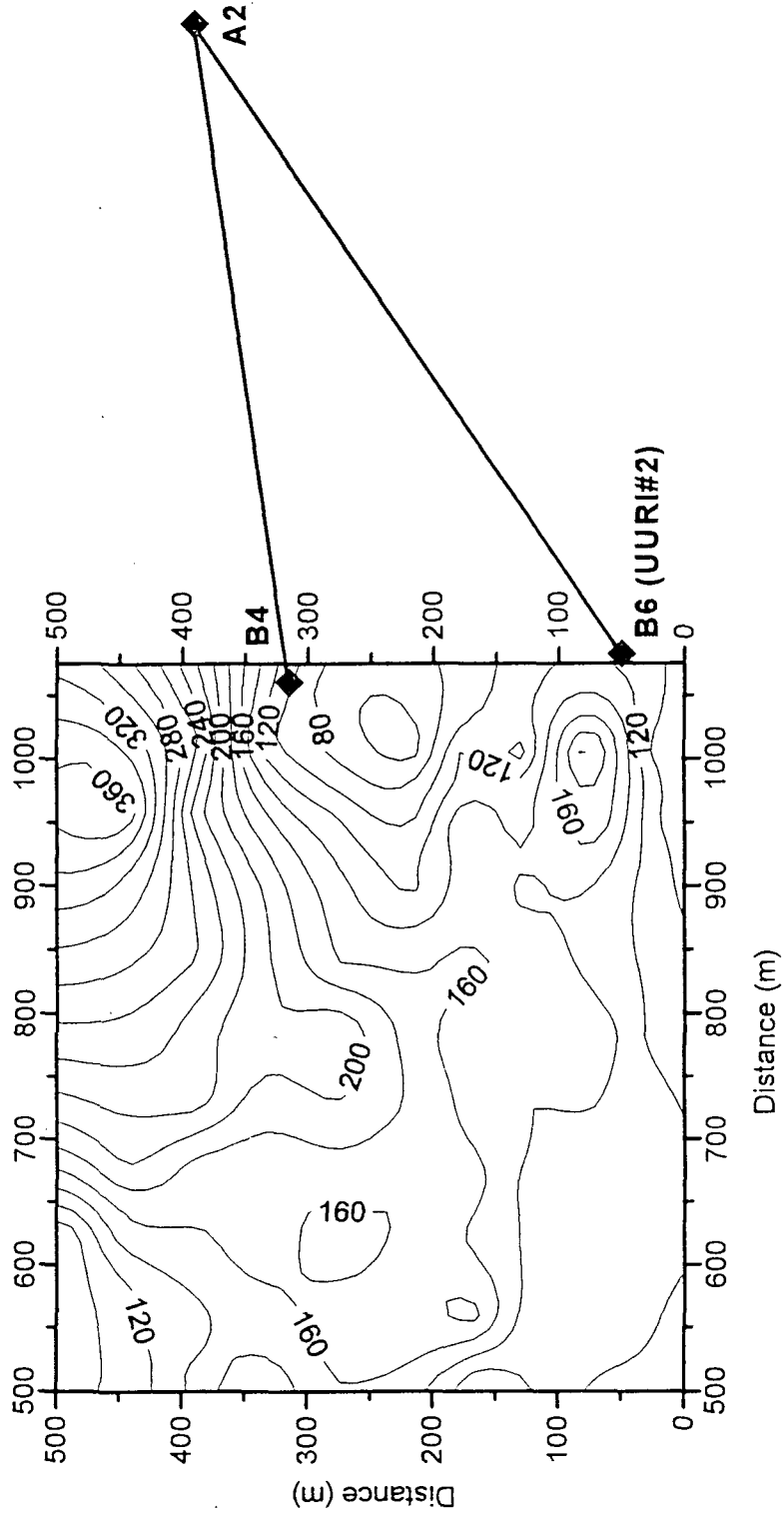


Figure 26: Contour map of the P_2 tensor invariant for UURI#2 using bipole 1 and bipole 3.

bipole 1: $A_2 = [1577.5, 391.0, 0.0]$ m
 $B_4 = [1060.0, 315.0, 0.0]$ m

bipole 3: $A_2 = [1577.5, 391.0, 0.0]$ m
 $B_6 = [1082.31, 49.98, 100.0]$ m



the size of the high resistive structure and therefore the response of the high resistivity structures dominates the response of the conductive body. The 50% difference between the P_2 values for surface-to-surface and borehole-to-surface configurations results from the large difference between the resistivity response of bipole 2 and that of bipole 3.

Model studies have shown that conductive inhomogeneities close to the transmitter site can have a significant influence on the resistivity response. According to drill logs the sandstone unit # 7 was at a depth of 6 m (18 feet) in the borehole UURI#1 and at a 10 m (30 feet) depth in the borehole UURI#2. The upper most layer in the Ferron area is a conductive Blue Gate Shale, which is thickening to the northwest. Thus there is a high probability that borehole UURI#1 is in a much more conductive environment than borehole UURI#2. Taking into account a near-surface conductive feature close to the borehole UURI#1 and a canyon on the southeast side of the study area, for the same model presented in Figure 20 and 21, the total apparent resistivity responses and P_2 invariant contour map for the surface electrode configuration are illustrated in Figures 27, 28, and 29 respectively. The contour patterns in these figures are very similar to those observed in corresponding contour maps of field data. The P_2 invariant contour map for the borehole-to-surface configuration is still different from that calculated from the field data, however.

Although the layered earth model matches the major features of the data, it does not agree well with either well-log. Since there is a discrepancy between the well-logs themselves, part of the disparity between the data interpretation and the well-logs is due to lateral heterogeneity in the geology. However, in large part, we have undoubtedly found a model which is equivalent to the response of the more finely layered model.

Figure 27: Contour map of total apparent resistivity for UURI#1 bipole 1 configuration, as a response of 12.5 thick, 10 Ohm-m, 75 m deep layer overlaid by 12.5 m thick, 5000 Ohm-m, 50 m deep layer in 100 Ohm-m resistive host, with 80 m deep canyon on the southeast side of the study area and conductive structure close to UURI#1 location.

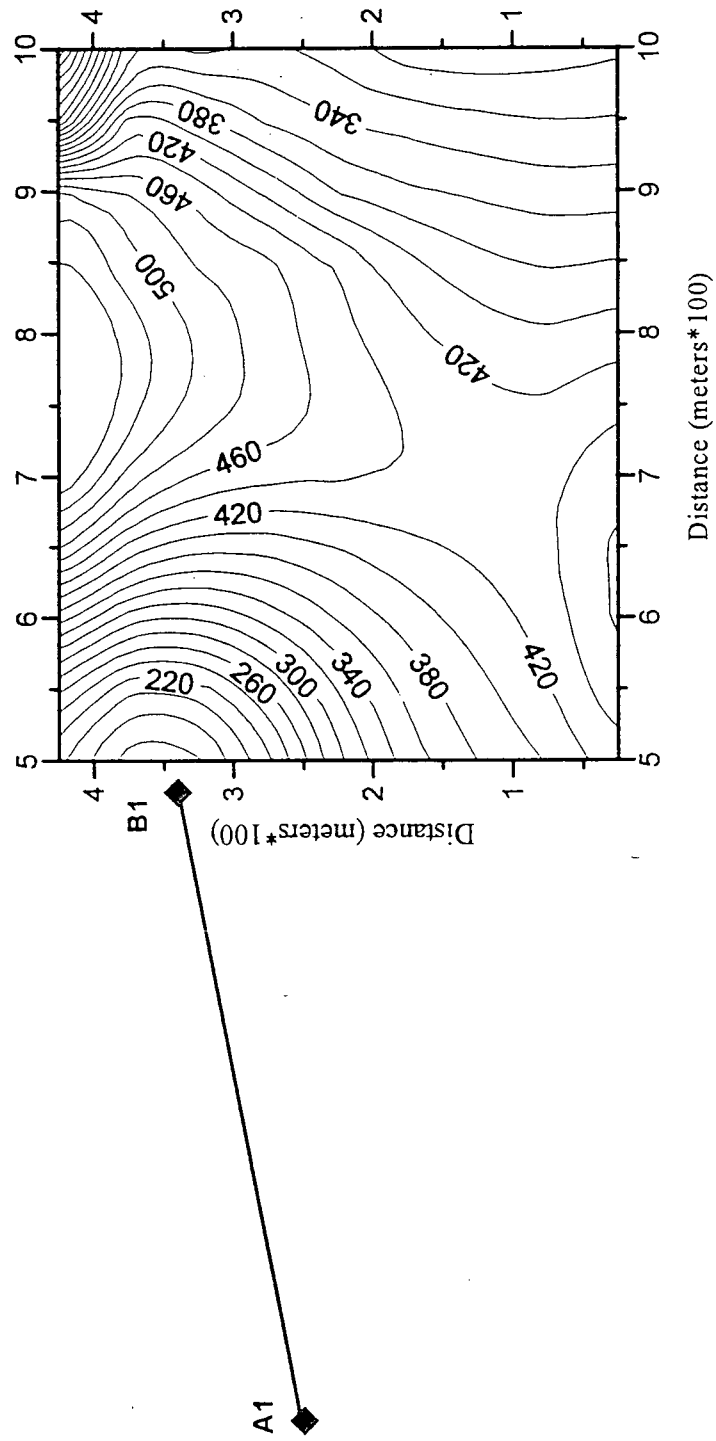


Figure 28: Contour map of total apparent resistivity for UURI#1 bipole 2 configuration, as a response of 12.5 thick, 10 Ohm-m, 75 m deep layer overlaid by 12.5 m thick, 5000 Ohm-m, 50 m deep layer in 100 Ohm-m resistive host, with 80 m deep canyon on the southeast side of the study area and conductive structure close to UURI#1 location.

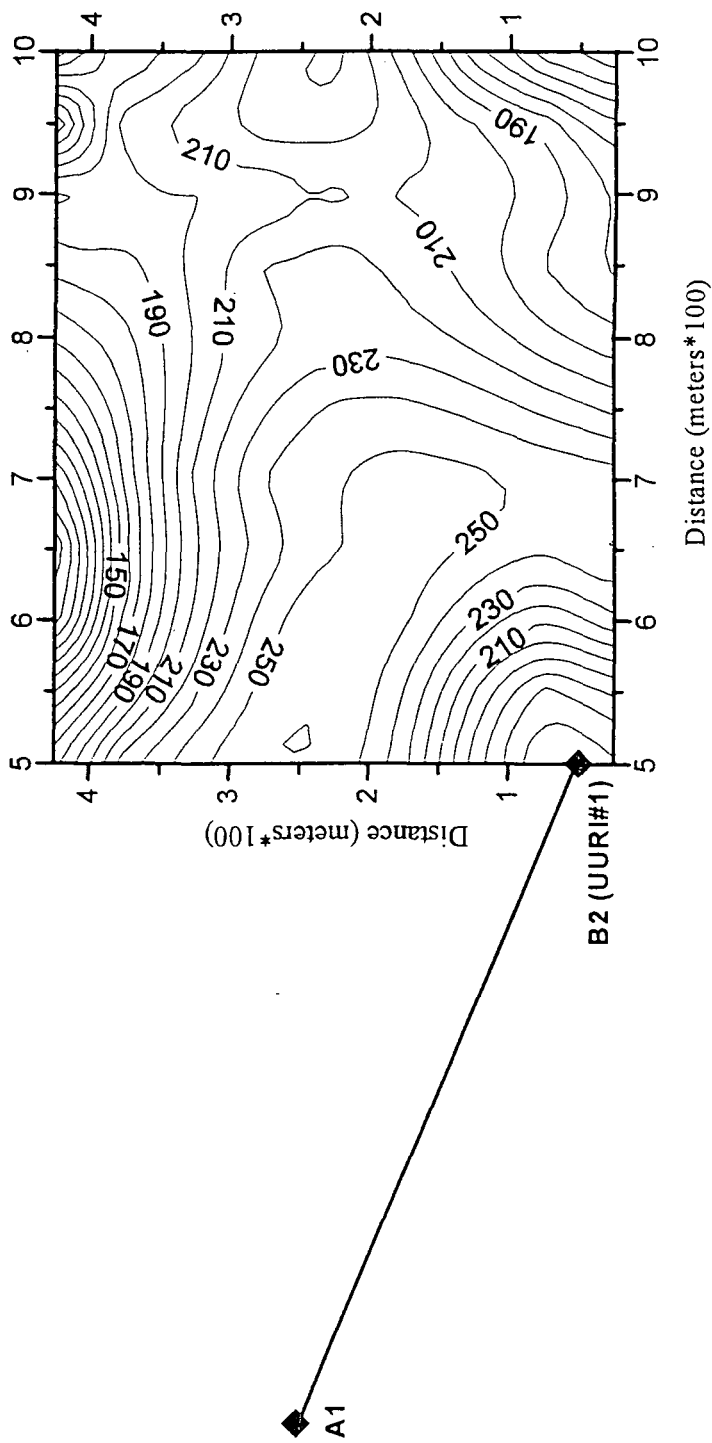
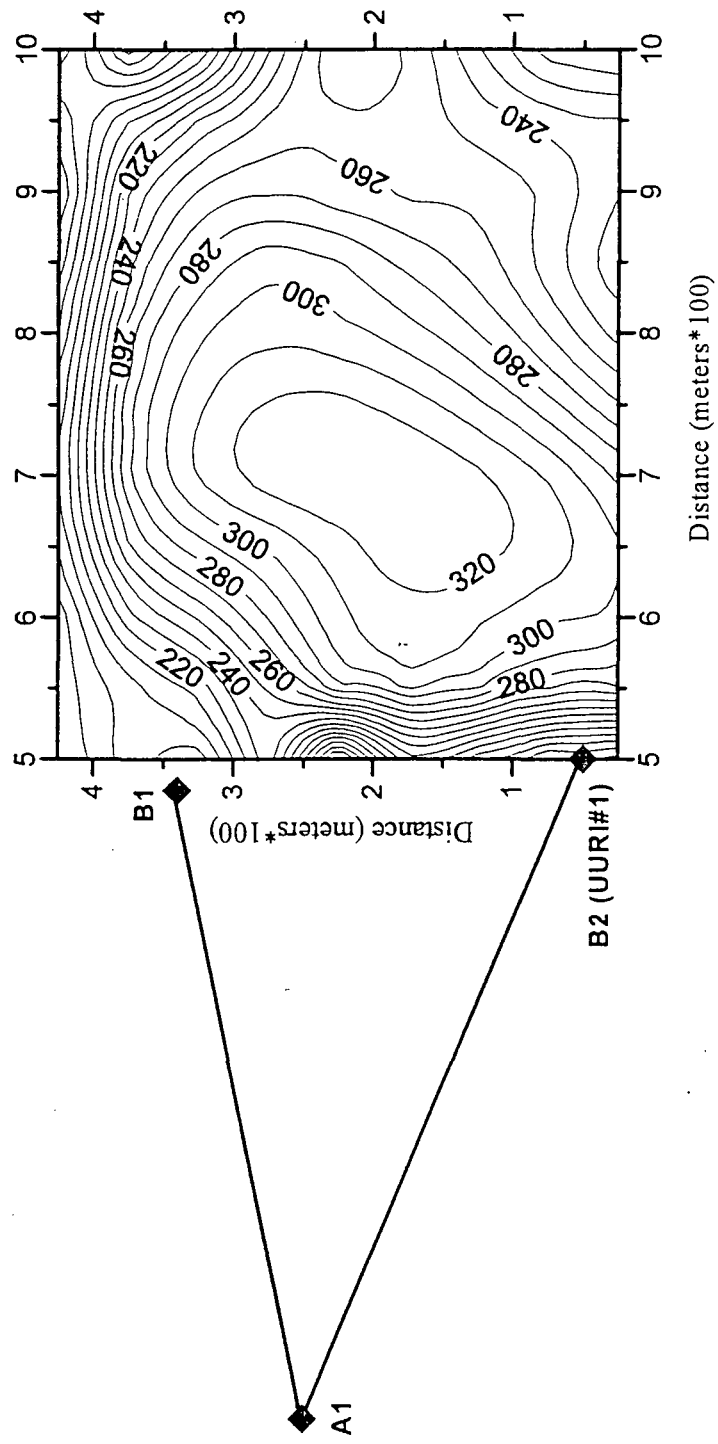


Figure 29: Contour map of the P_2 tensor invariant for UURI#1 using bipole 1 and bipole 2, as a response of 12.5 thick, 10 Ohm-m, 75 m deep layer overlaid by 12.5 m thick, 5000 Ohm-m, 50 m deep layer in 100 Ohm-m resistive host, with 80 m deep canyon on the southeast side of the study area and conductive structure close to UURI#1 location.



Our original motivation in modeling our data with a very coarsely layered earth came from our model studies, which emphasized the great screening capacity of both highly resistive and highly conductive layers. As we stated earlier, given these results we largely wished to map undulations of the upper-most conductive or resistive layers. Our data modeling reveals how such a policy can give a model which represents a lumped approximation to the finely layered environment revealed in the well-logs.

In retrospect, a more useful approach in such an environment might be to derive a starting model from a very crude interpolation between wells and an extrapolation out to the survey area. Given the paucity of well control, such an "extrapolation" would be really a guess with a misleading title, but it might be suitable in the "almost-layered" environment at Ferron.

Of course, the basic problem is exacerbated by the absence of very shallow resistivity information, which can bias the measurements if either transmitter or receiver electrodes are placed in small anomalous conductivity patches. For this reason, such experiments as ours should be conducted in conjunction with rapid surficial conductivity mapping, such as VLF.

Another recurrent problem in our study is that the interpretation software is hardly adequate to the task of modeling the very detailed geology encountered in an environment such as Ferron. The 2-D software which we have used imposes a strike direction on the geology which is not necessary valid, while 3-D interpretation software is limited to fairly simple models. Since an inversion algorithm does not exist at present for our experimental arrangement, trial and error modeling for more than a modest number of parameters is very slow and difficult. The difficulty of forward model entry and data presentation can make the data interpretation using present tools cumbersome.

Although I have not examined the effects of layer anisotropy, I expect that it too may strongly influence the Ferron data.

However, all of these problems can be overcome, using either present theory, available instrumentation, and enhanced computer capabilities. What has been demonstrated is that the tensor bipole-dipole method can be adapted to a borehole-to-surface survey. Although our data interpretation is not optimal, in arriving at it we have managed to define the procedures and requirements for the field array in an entirely novel application. We remain optimistic that resolution can be increased given the means to utilize all available information.

8. CONCLUSIONS

The field project at the Ferron Sandstone, and the interpretation of the subsequent data, partially justifies the optimism felt by many concerning the application of electrical borehole-to-surface techniques in delineating geothermal and hydrocarbon reservoirs of complex geoelectric character.

Lack of resolution and model uniqueness will always be an issue in reservoir studies, where small features are of great importance. However, in the present study inadequate interpretation algorithms proved the obstacle which prevented greater resolution of model features. Nevertheless, interpretation techniques were sufficiently well developed to illustrate the influence of many geoelectric features on the data and suggest the potential of the method.

Our model studies show that it is possible to detect conductive layers and layer perturbations of a size expected in the survey area underneath the receiver grid as long as such conductive features are not deeper than 100 m. The apparent resistivity tensor calculations are most effective for delineation of a 3-D structure. This procedure is also well suited to the case when the edge of a 2-D structure is in the measured area. By using the P_2 tensor invariant plot, it is very easy to see this interface. Also, a shallow conductive layer does a fine job of screening deeper geoelectric units. Thus, in mapping conductive features, we essentially map the depth of the upper most feature.

Our field studies required the customized design of field equipment. A special downhole current electrode was developed in order to realize the borehole-to-surface

DC resistivity experiment. The downhole electrode system worked well and is recommended for future use.

Our interpretation of the field data is provocative, insofar as it raises as many questions as it answers. However, it does demonstrate the tremendous non-uniqueness present in the interpretation of such data and the necessity in the future of severely constraining the interpretation through additional sources of information. In the future, such data should probably be used to answer a very well constrained reservoir problem, unlike our somewhat open-ended interpretational quest.

APPENDIX A

**THEORETICAL RESPONSE OF 1-D AND 2-D CONDUCTIVE
STRUCTURES IN A RESISTIVE BACKGROUND**

This appendix contains models created to help us understand our field data, for the case when the host material is resistive. Each of these models try to address some specific feature, which can have an influence on the apparent resistivity in the study area.

We have used a field electrode configuration for borehole UURI#1 through the entire appendix. The description of the field setup is given in Chapter 4. Bipole 1 is represented by the A_1B_1 current electrode pair, bipole 2 is represented by the A_1B_2 current electrode pair, and bipole 3 is represented by the A_1B_3 current electrode pair. The coordinates for these current electrodes are:

$A_1 = [32.5, 250.0, 0.0]$ m, $B_1 = [478.5, 344.1, 0.0]$ m;

$A_1 = [32.5, 250.0, 0.0]$ m, $B_2 = [500.0, 50.0, 0.0]$ m; and

$A_1 = [32.5, 250.0, 0.0]$ m, $B_3 = [500.0, 50.0, 100.0]$ m.

The receiver grid was from 550 m to 1050 m in the x-direction and from 0 m to 500 m in the y-direction. The receiver dipole length was 50 m.

Figure 30 - 35:

This figure contains a sequence of the total field apparent resistivity contour maps for each current bipole for a model consisting of a 25 m thick layer of 10 Ω -m in a 300 Ω -m background. The depth of this layer varies from 25 m to 150 m.

These models illustrate well the character of the bipole layered earth response. In each figure, the major effect is a series of circular contours centered at the near electrode. As the conductive layer deepens, the surface resistive layer becomes more pronounced and more contour relief is apparent, due to the used contour interval. The buried electrode gives an enhanced conductive response as long as it is deeper than the conductor. As soon as the conductive layer becomes deeper than the buried electrode, the buried electrode response is very similar to that of the surface electrodes and is

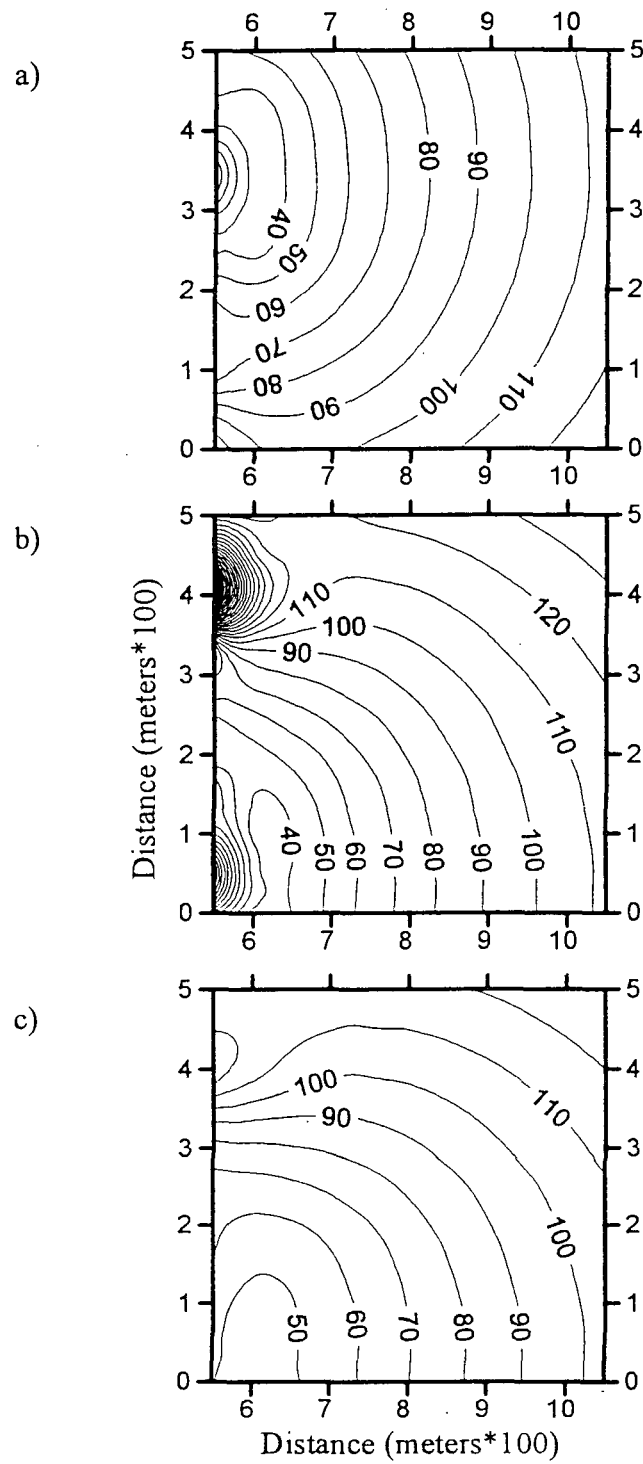


Figure 30: Total field apparent resistivity contour maps for a 25 m thick, 25 m deep layer, of 10 Ohm-m resistivity, with a background resistivity of 300 Ohm-m.

a) bipole 1, b) bipole 2, c) bipole 3

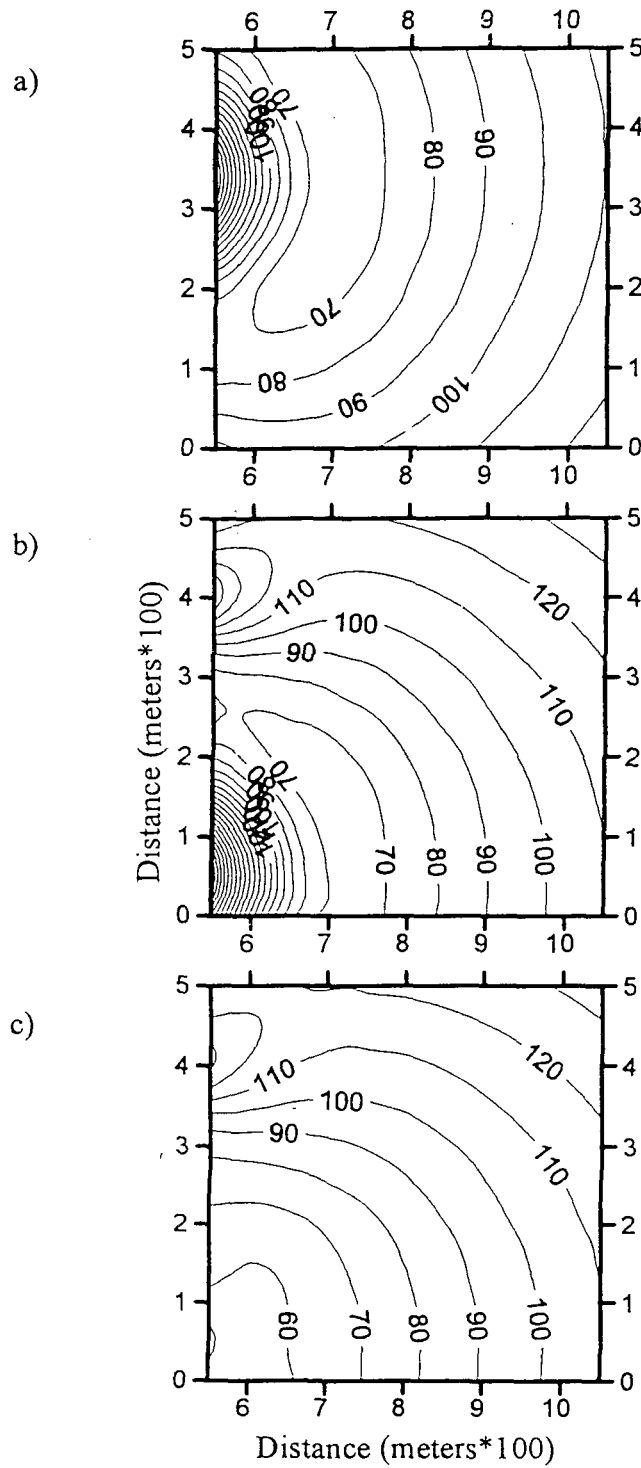


Figure 31: Total field apparent resistivity contour maps for a 25 m thick, 50 m deep layer, of 10 Ohm-m resistivity, with a background resistivity of 300 Ohm-m.

a) bipole 1, b) bipole 2, c) bipole 3

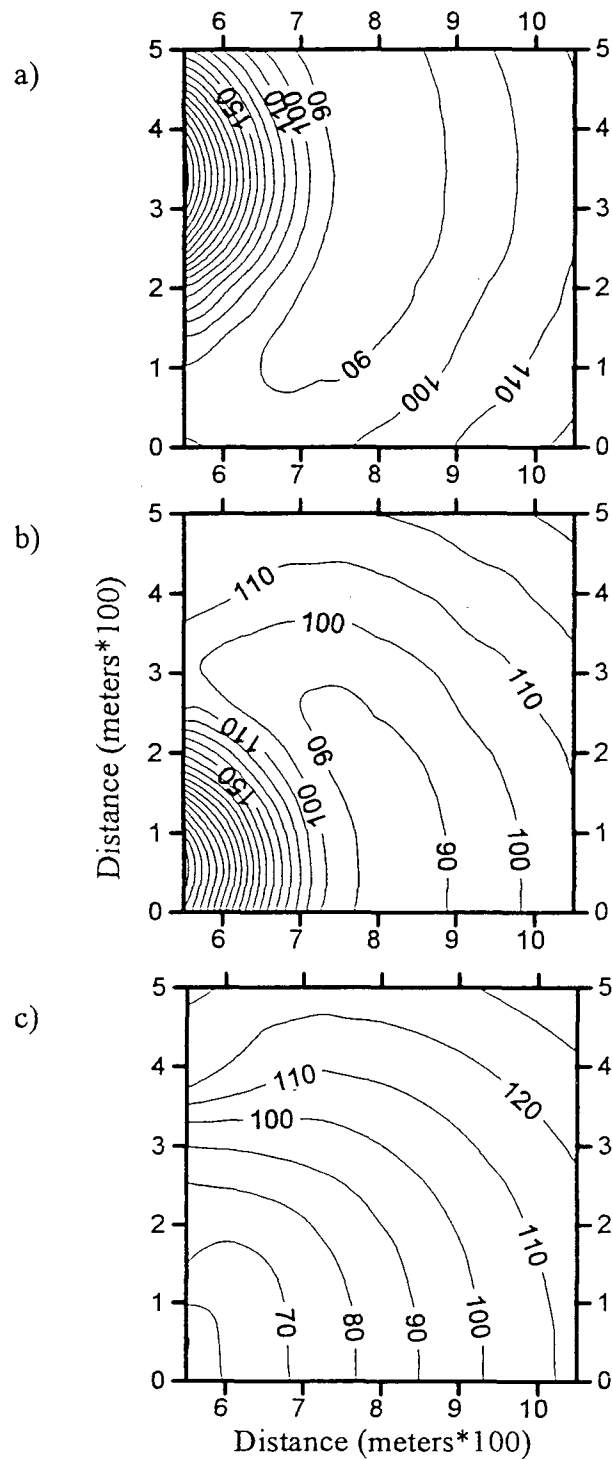


Figure 32: Total field apparent resistivity contour maps for a 25 m thick, 75 m deep layer, of 10 Ohm-m resistivity, with a background resistivity of 300 Ohm-m.

a) bipole 1, b) bipole 2, c) bipole 3

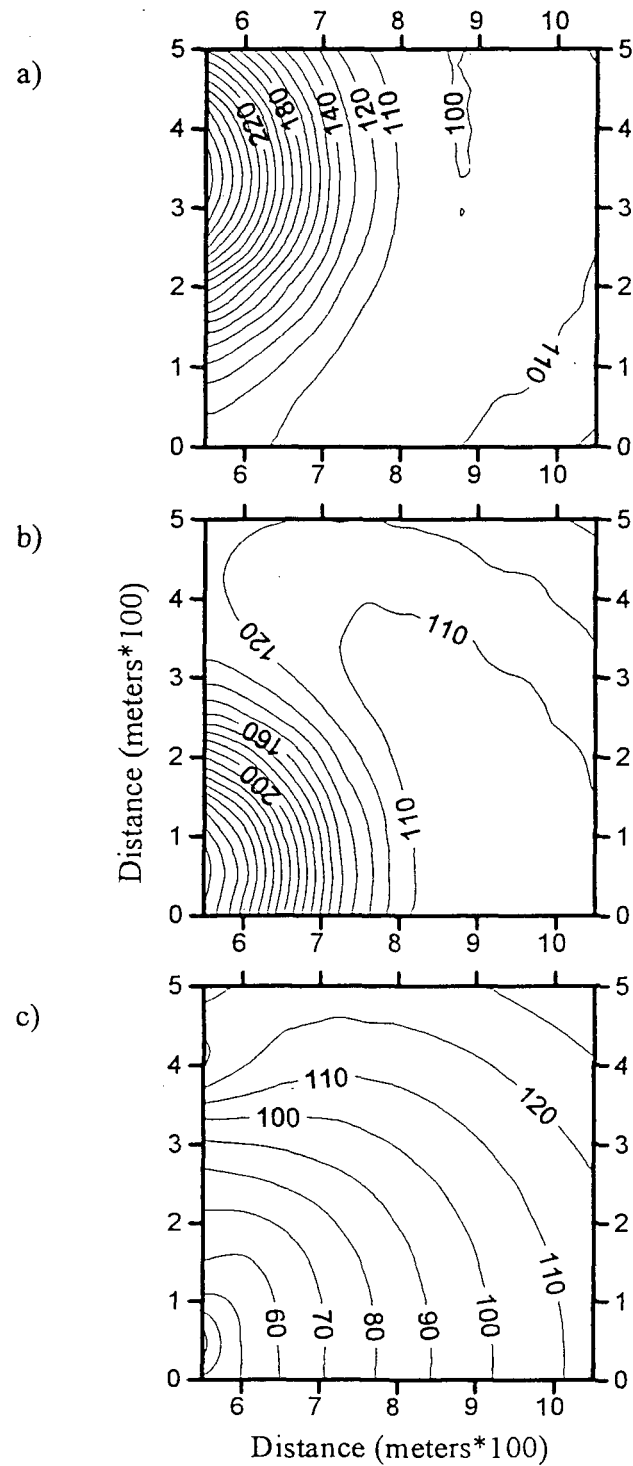


Figure 33: Total field apparent resistivity contour maps for a 25 m thick, 100 m deep layer, of 10 Ohm-m resistivity, with a background resistivity of 300 Ohm-m.

a) bipole 1, b) bipole 2, c) bipole 3

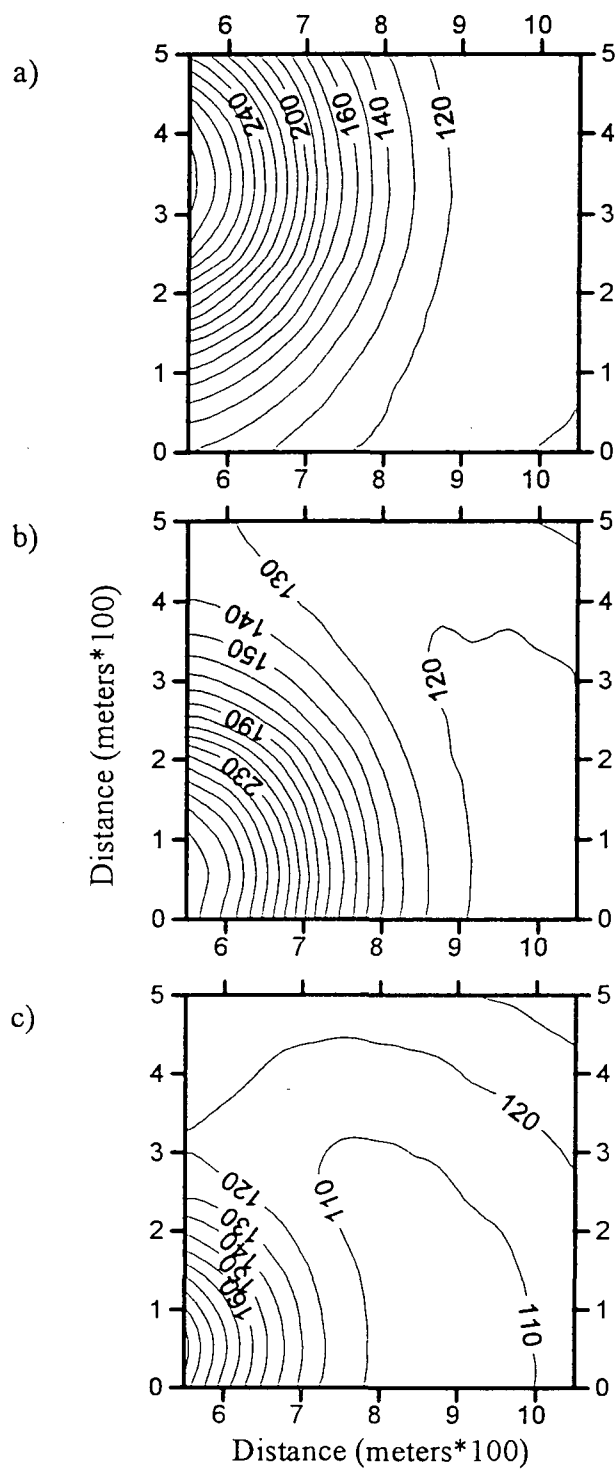


Figure 34: Total field apparent resistivity contour maps for a 25 m thick, 125 m deep layer, of 10 Ohm-m resistivity, with a background resistivity of 300 Ohm-m.
 a) bipole 1, b) bipole 2, c) bipole 3

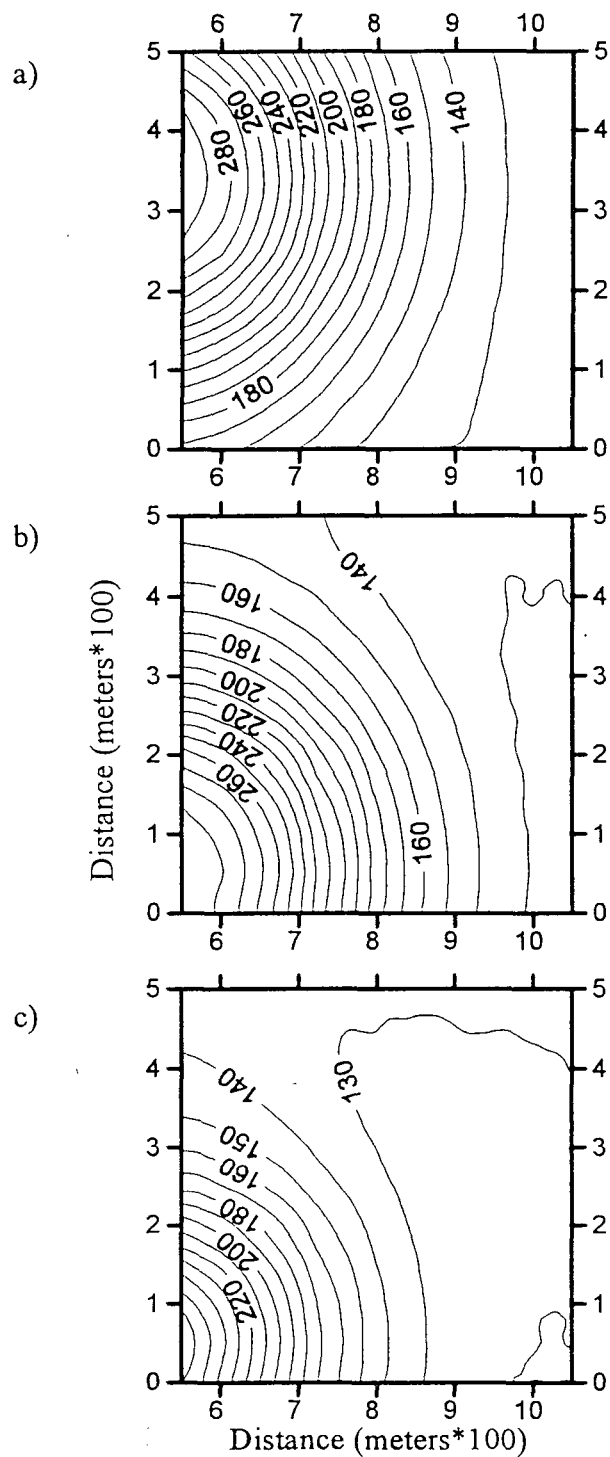


Figure 35: Total field apparent resistivity contour maps for a 25 m thick, 150 m deep layer, of 10 Ohm-m resistivity, with a background resistivity of 300 Ohm-m.
 a) bipole 1, b) bipole 2, c) bipole 3

probably not very useful in delineating such a layer. The high contour concentrations close to [550.0, 350.0] m and [550.0, 50.0] m on Figure 30b are caused by nearness of the current electrode and is rapidly attenuated as the conductive layer deepens. The source effect is present in the contour maps for both bipole 1 and bipole 2, while it is minimized in the contour map for bipole 3. Thus the borehole electrode configuration can help eliminate the source effect in our measurements.

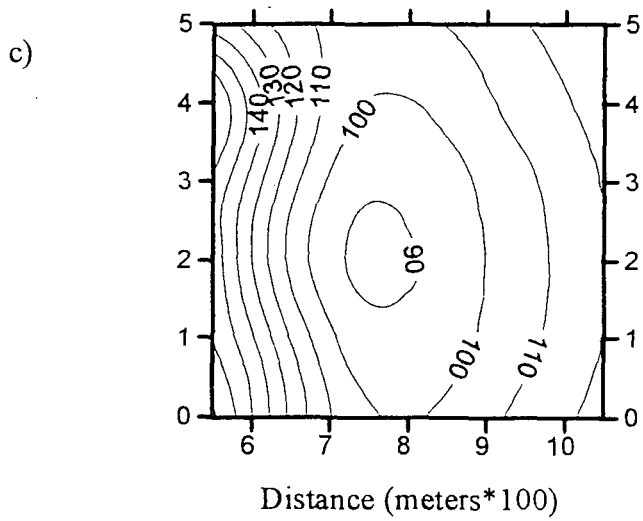
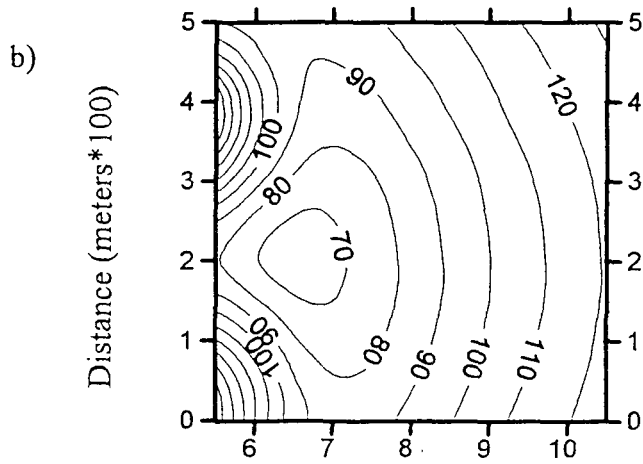
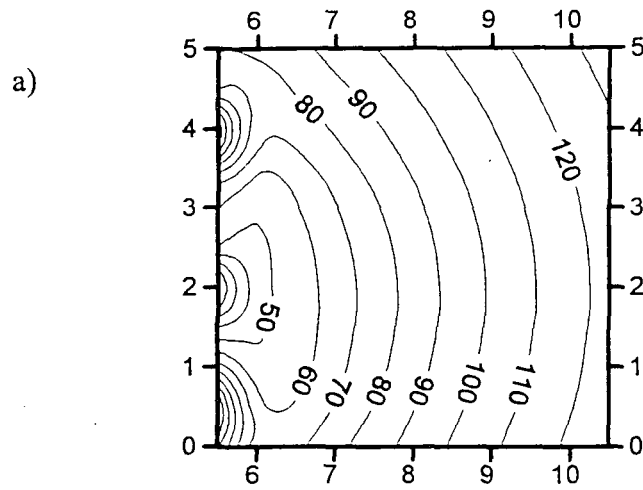
Figure 36:

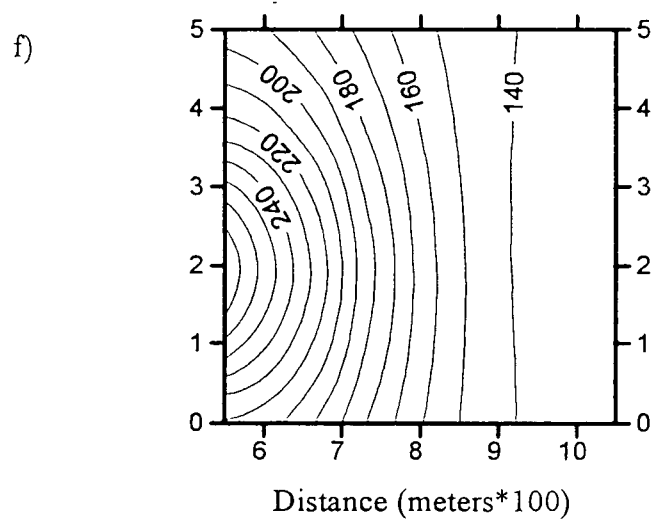
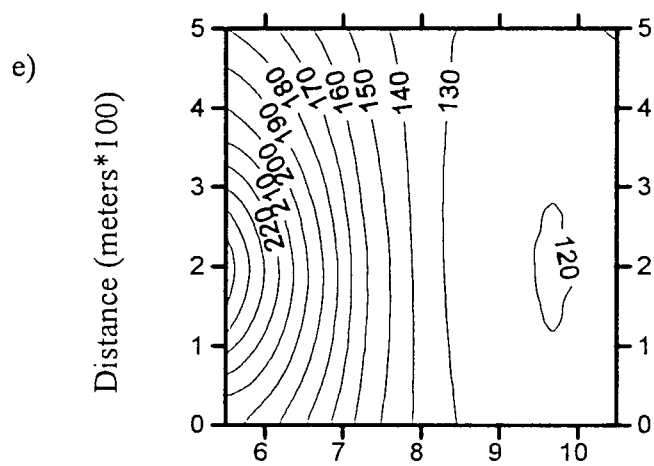
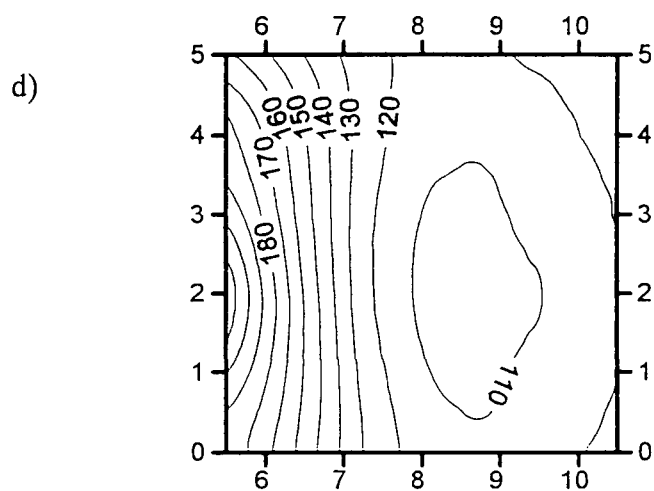
The P_2 -invariant contour maps for the model used in Figures 30 - 35, created by using a combination of bipole 1 and bipole 2 responses, are presented in this figure. The source effect noticed in Figure 30 - 35 is minimized in these contour maps. The minimum resistivity area changes with the layer depth. The minimum resistivity area localizes the maximum response of the conductive layer in the particular depth in the measured area. The maximum response of the shallow structure is close to the source, while the maximum response of the deeper structure is farther away from the source. In our particular case, the maximum response of the layer 25 m deep is between 600 and 700 m in the x-direction. For the layer at 50 m it is around $x = 700$ m, for the layer at 75 m it is between 750 and 850 m, for the layer at 100 m it is around $x = 900$ m, and for the layer at 125 m it is around $x = 1000$ m. We do not get much response from the deeper structures in the particular measured area using the surface electrode configuration.

Figure 37:

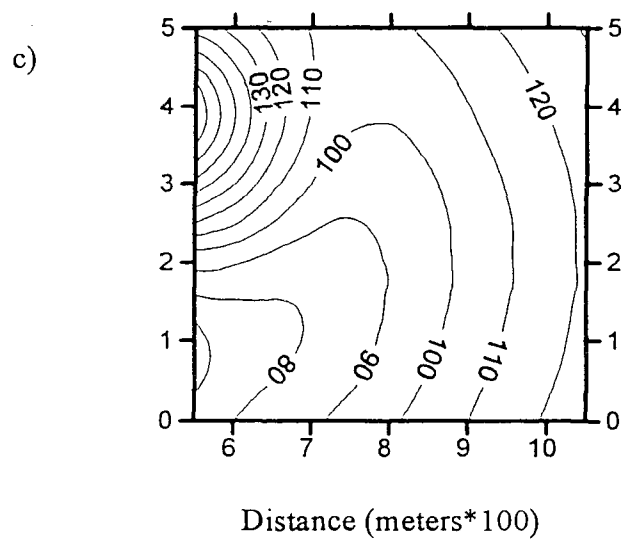
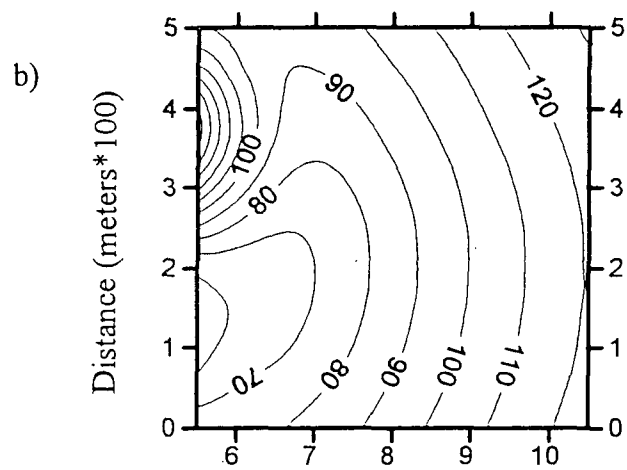
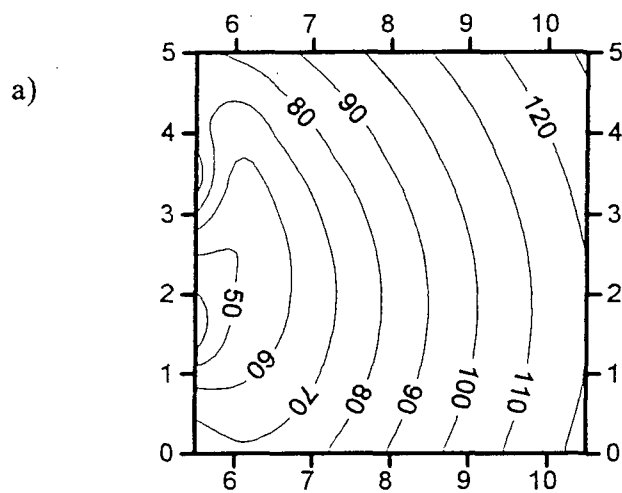
This figure is a sequence of P_2 -invariant contour maps for the same model as in Figure 36, created by using the combination of bipole 1 and bipole 3 responses. In this

- Figure 36: The P2-invariant contour maps for a 25 m thick layer, of 10 Ohm-m resistivity, with a background resistivity of 300 Ohm-m, using bipole 1 and bipole 2.
- a) 25 m deep layer
 - b) 50 m deep layer
 - c) 75 m deep layer
 - d) 100 m deep layer
 - e) 125 m deep layer
 - f) 150 m deep layer





- Figure 37: The P2-invariant contour maps for a 25 m thick layer, of 10 Ohm-m resistivity, with a background resistivity of 300 Ohm-m, using bipole 1 and bipole 3.
- a) 25 m deep layer
 - b) 50 m deep layer
 - c) 75 m deep layer
 - d) 100 m deep layer
 - e) 125 m deep layer
 - f) 150 m deep layer



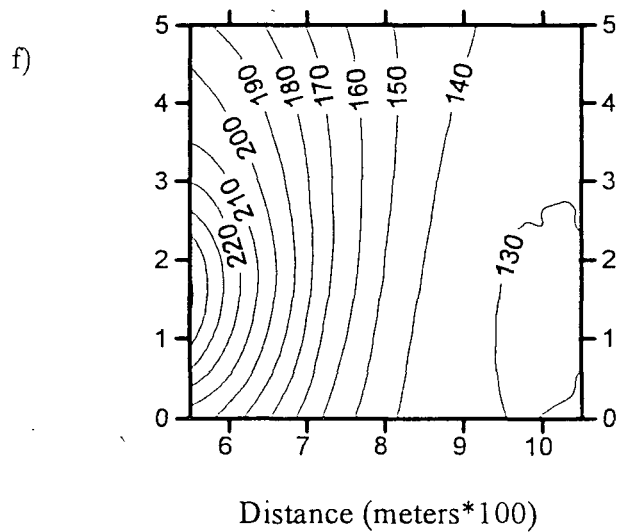
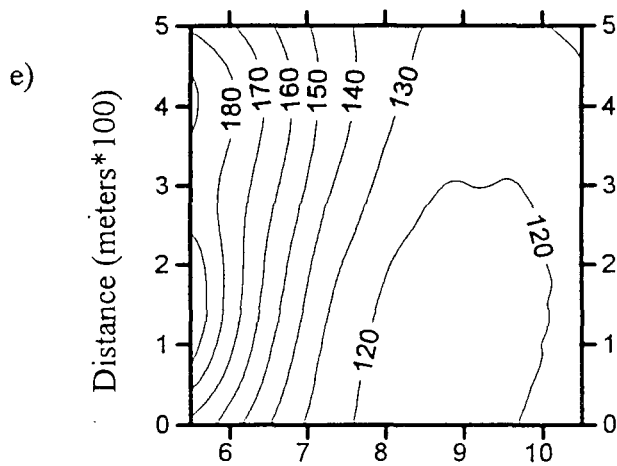
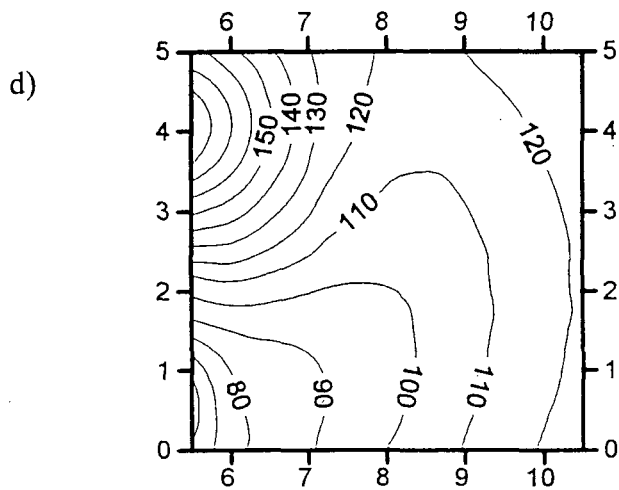


figure similar features can be seen to those in Figure 36. By using the borehole electrode configuration, a conductive layer is between transmitter and receiver electrodes, and thus we can see the influence of this layer in the whole measured area. When the layer is below the borehole current electrode, the borehole configuration behaves as does the surface configuration.

Figure 38 - 43:

The total field apparent resistivity contour maps for each bipole source as a response of a 2-D structure are presented here. The anomalous body is 200 m wide in the x-direction and 25 m thick, and is buried at different depths. The resistivity of the structure is 10 Ω -m, while the background resistivity is 300 Ω -m. A large gradient in apparent resistivity occurs close to the boundary of the body. This is a feature which we would look for in the field data if we try to localize a contact between environments with different resistivities. There is not much difference between the contour maps of bipole 1, bipole 2 or bipole 3, indicating the predominant effect of the infinite strike length. The gradient in apparent resistivity decreases with increasing depth of the anomalous body, showing that it is more difficult to delineate deeper structure using these contour maps.

Figure 44:

The P_2 -invariant contour maps for the model used in Figures 38 - 43, created by using bipole 1 and bipole 2 responses are presented in this figure. The calculation of the P_2 tensor invariant, whose contours tend to parallel the body, makes it marginally easier to localize the anomalous body in this picture. Modeling results show that this particular electrode configuration is capable of delineating a structure 25 to 75 m deep.

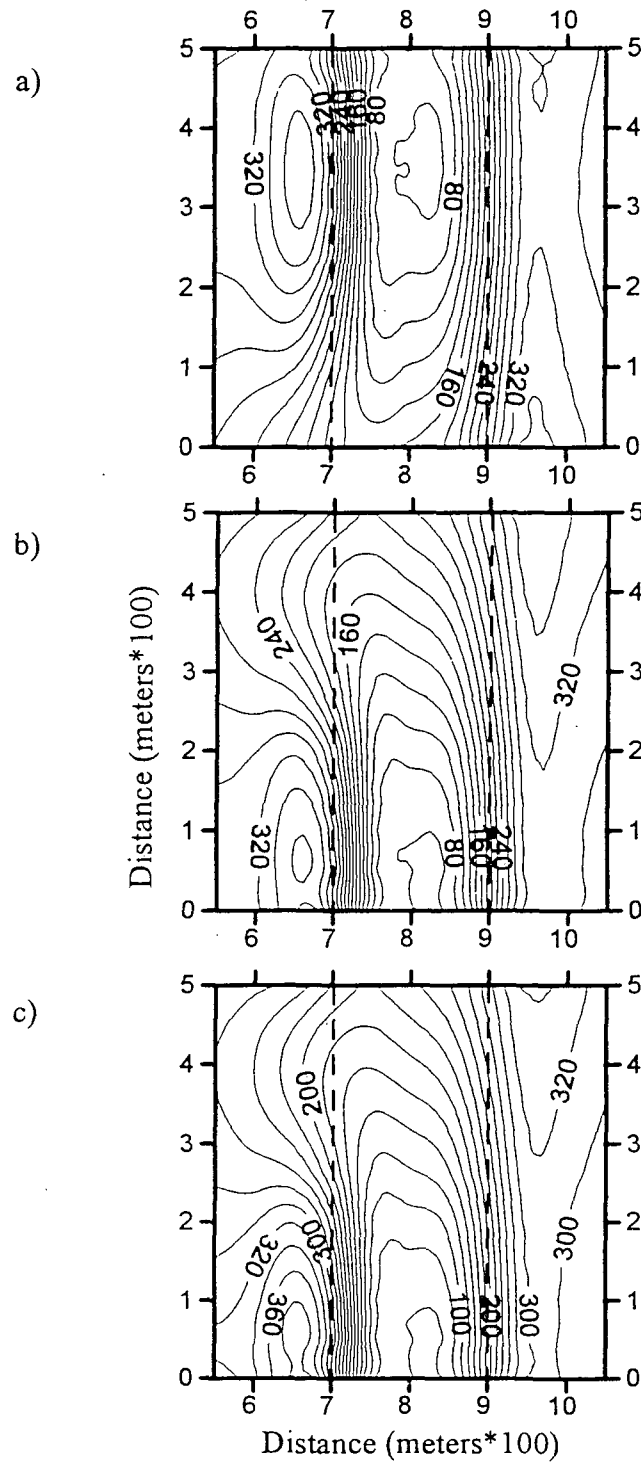


Figure 38: Total field apparent resistivity contour maps for a 25 m thick, 200 m wide, 25 m deep body, of 10 Ohm-m resistivity, with a background resistivity of 300 Ohm-m.

a) bipole 1, b) bipole 2, c) bipole 3

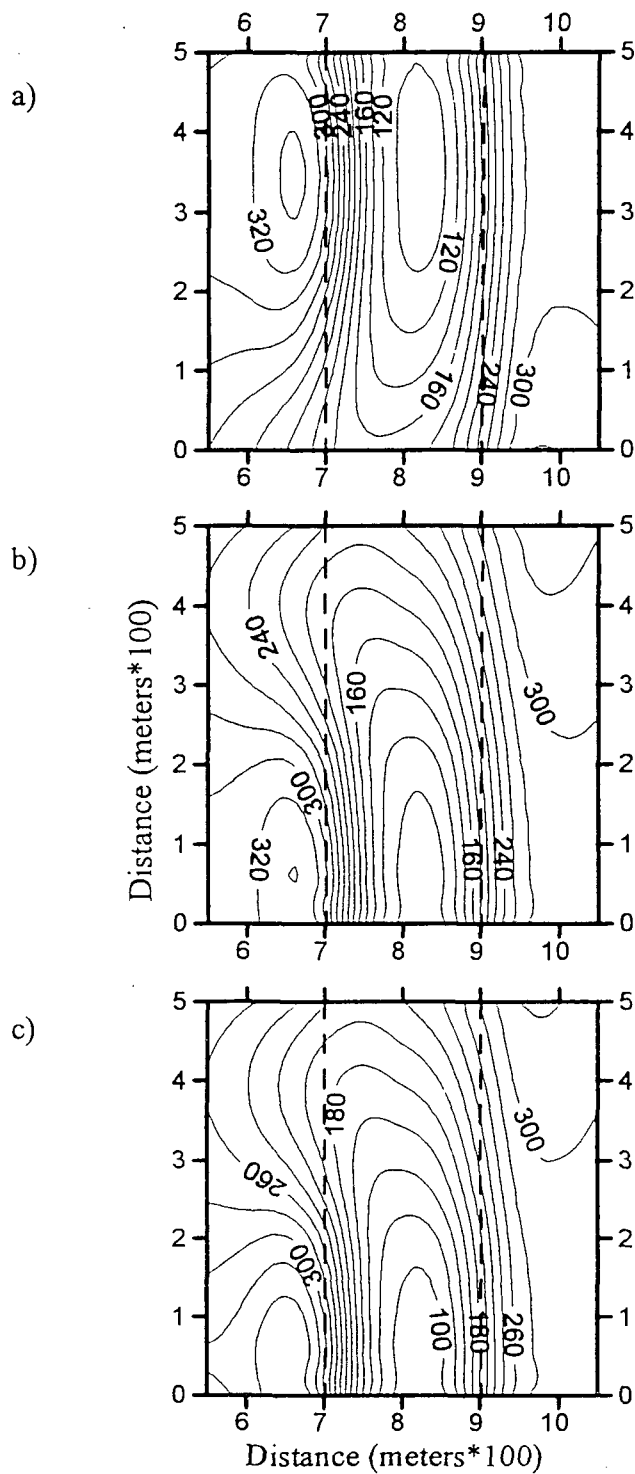


Figure 39: Total field apparent resistivity contour maps for a 25 m thick, 200 m wide, 50 m deep body, of 10 Ohm-m resistivity, with a background resistivity of 300 Ohm-m.
 a) bipole 1, b) bipole 2, c) bipole 3

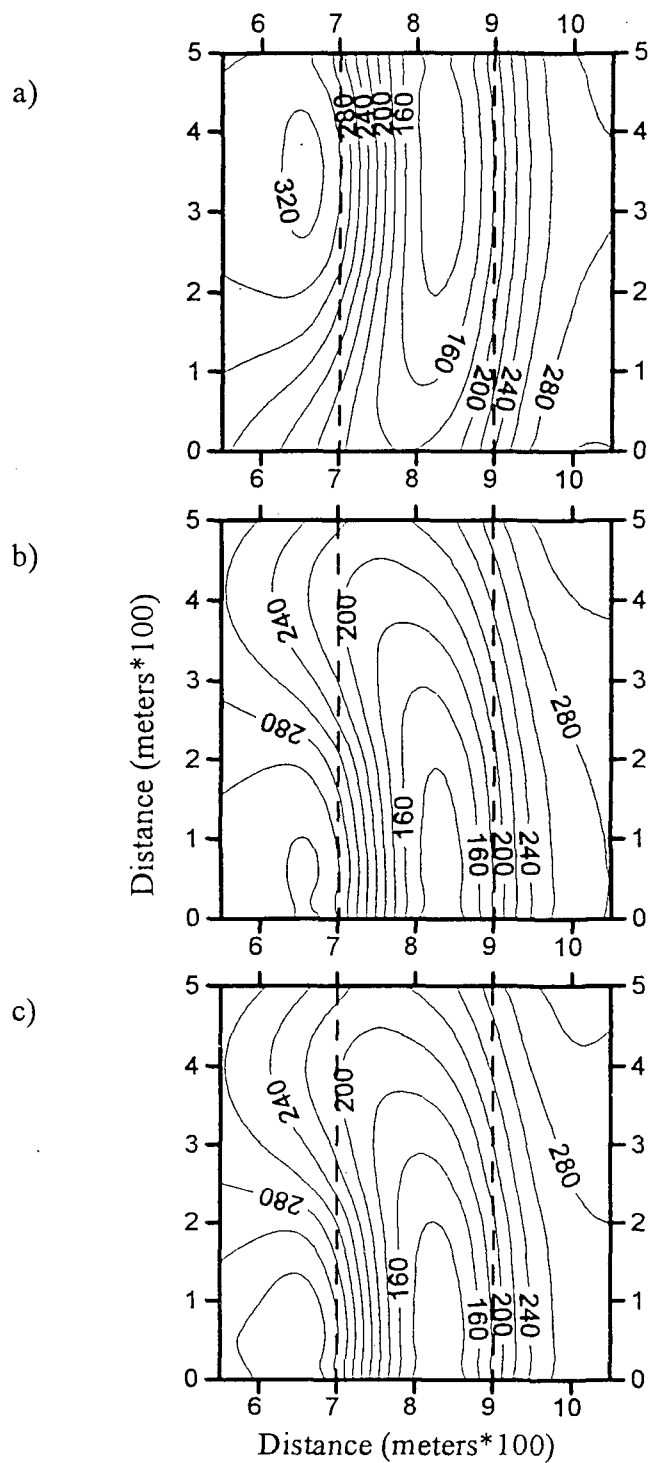


Figure 40: Total field apparent resistivity contour maps for a 25 m thick, 200 m wide, 75 m deep body, of 10 Ohm-m resistivity, with a background resistivity of 300 Ohm-m.
 a) bipole 1, b) bipole 2, c) bipole 3

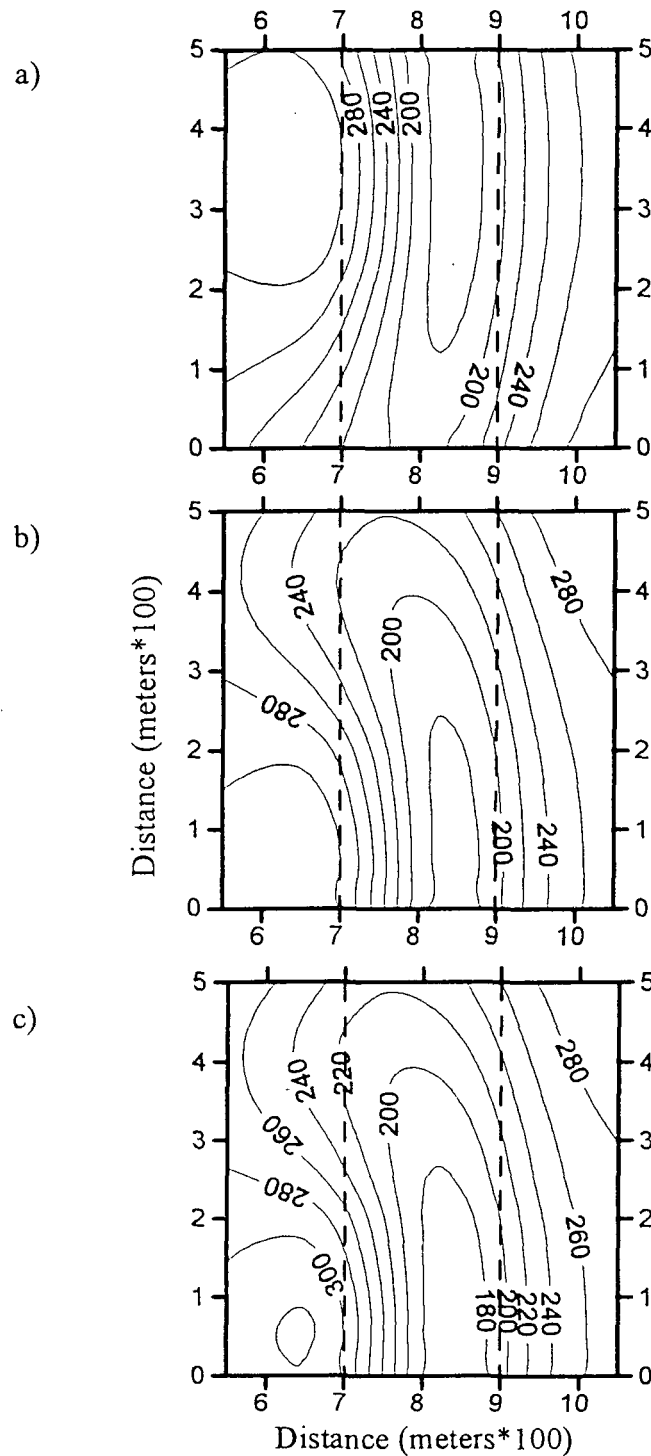


Figure 41: Total field apparent resistivity contour maps for a 25 m thick, 200 m wide, 100 m deep body, of 10 Ohm-m resistivity, with a background resistivity of 300 Ohm-m.
 a) bipole 1, b) bipole 2, c) bipole 3

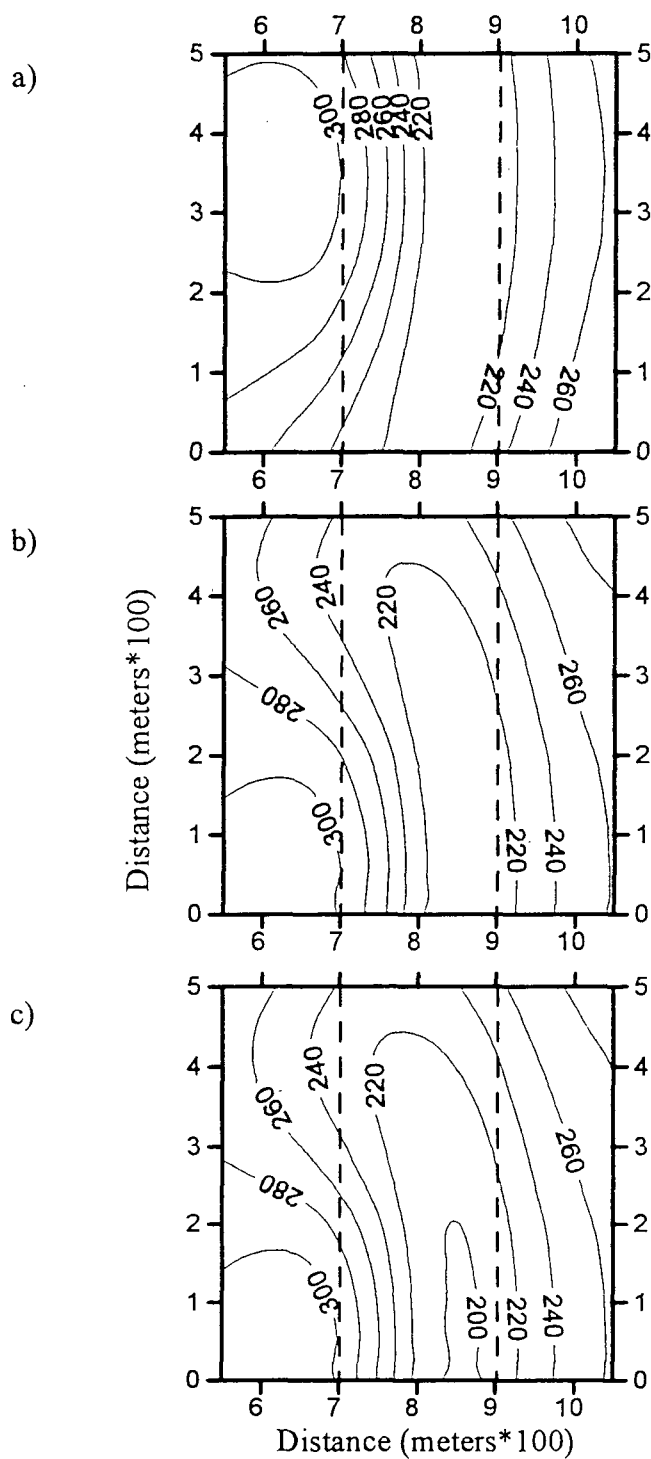


Figure 42: Total field apparent resistivity contour maps for a 25 m thick, 200 m wide, 125 m deep body, of 10 Ohm-m resistivity, with a background resistivity of 300 Ohm-m.
 a) bipole 1, b) bipole 2, c) bipole 3

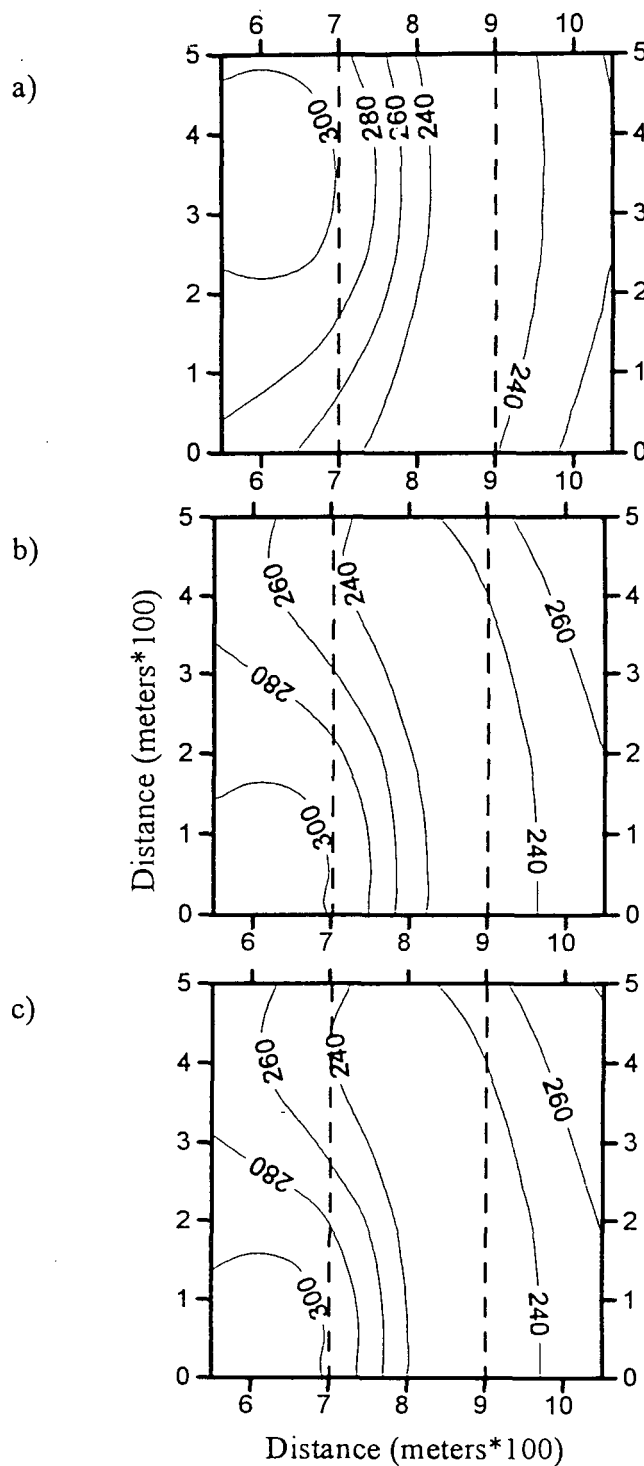
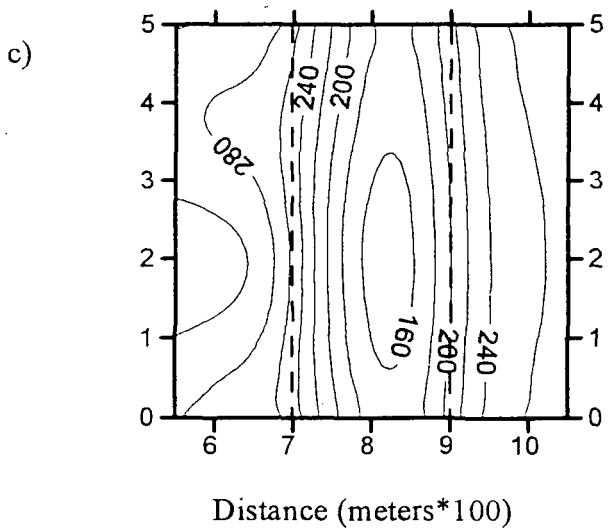
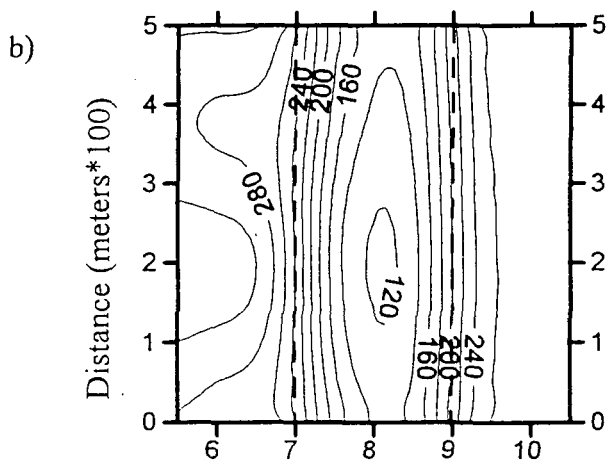
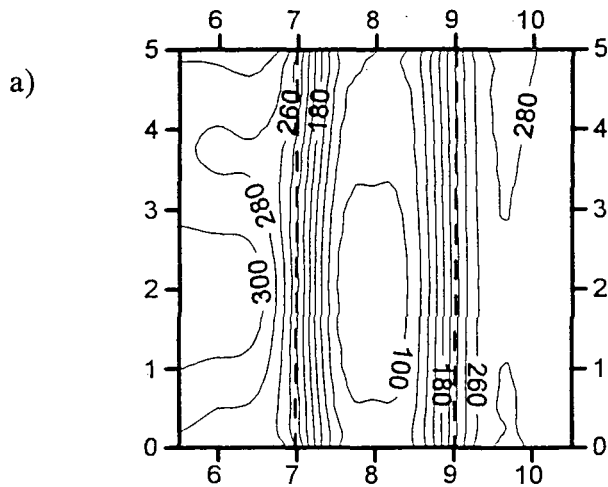
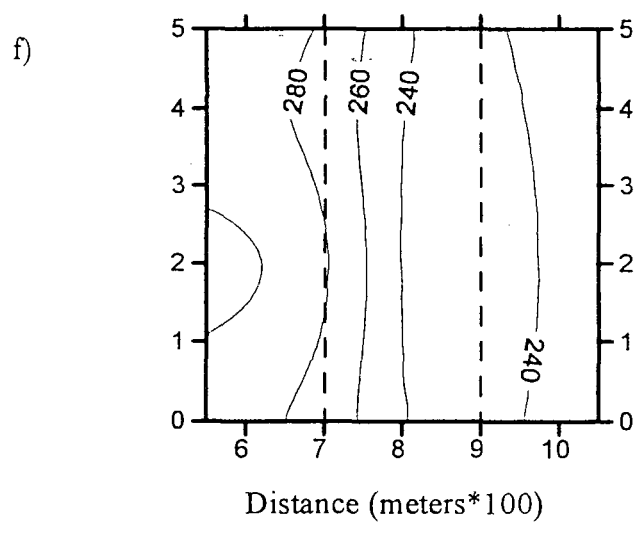
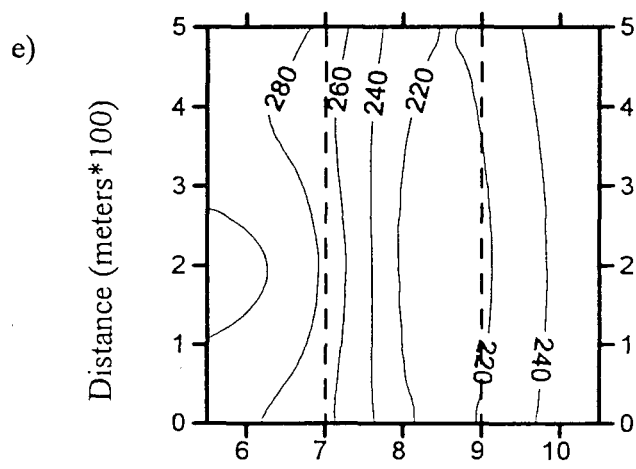
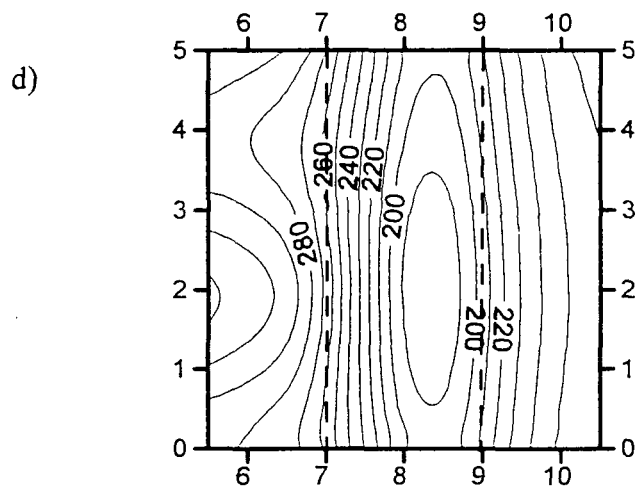


Figure 43: Total field apparent resistivity contour maps for a 25 m thick, 200 m wide, 150 m deep body, of 10 Ohm-m resistivity, with a background resistivity of 300 Ohm-m.
 a) bipole 1, b) bipole 2, c) bipole 3

- Figure 44: The P2-invariant contour maps for a 25 m thick, 200 m wide body, of 10 Ohm-m resistivity, with a background resistivity of 300 Ohm-m, using bipole 1 and bipole 2.
- a) 25 m deep body
 - b) 50 m deep body
 - c) 75 m deep body
 - d) 100 m deep body
 - e) 125 m deep body
 - f) 150 m deep body





It is difficult to localize visually a body deeper than 100 m. If a minimum value of P_2 is used as a criterion for a deep body, it is still possible to localize the body edge which is furthest from the current bipoles, although with less accuracy. This result agrees with the conclusions of Bibby and Hohmann (1993).

Figure 45:

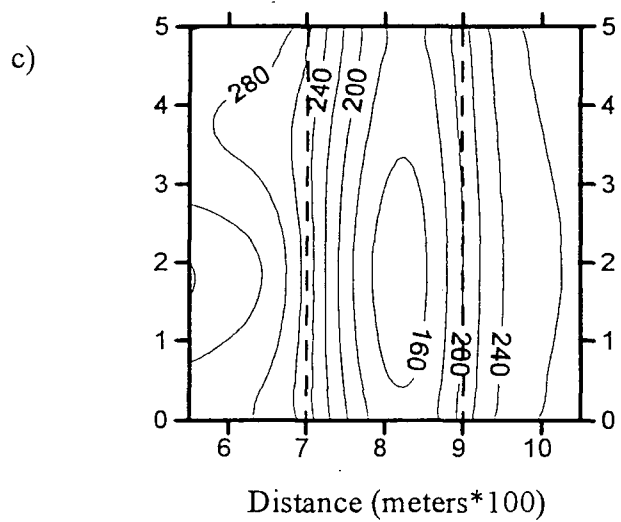
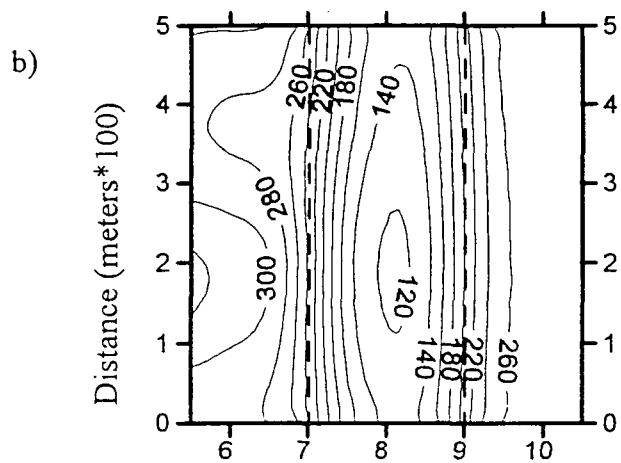
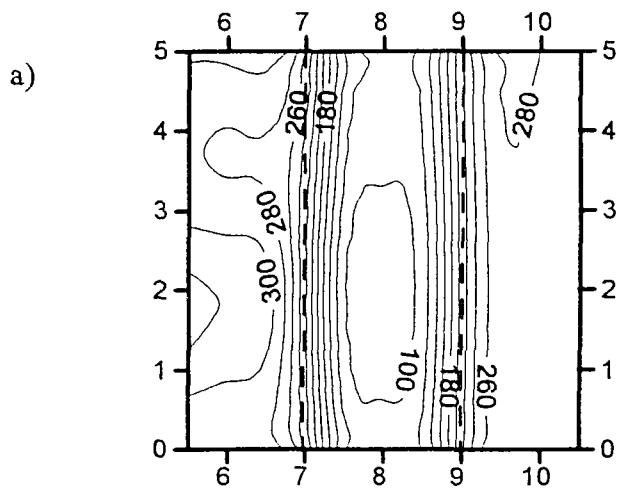
This figure contains a sequence of the P_2 -invariant contour maps for the models used in Figures 38 - 43 created by using bipole 1 and bipole 3 responses. These contour maps are almost identical to the contour maps in Figure 44. In this case using a borehole current electrode does not improve the body resolution.

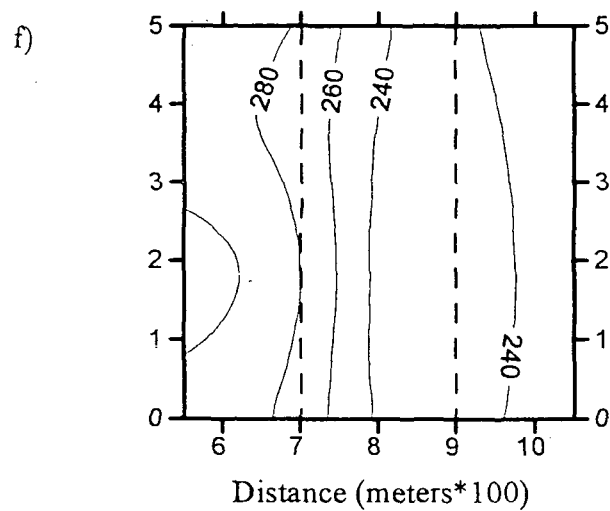
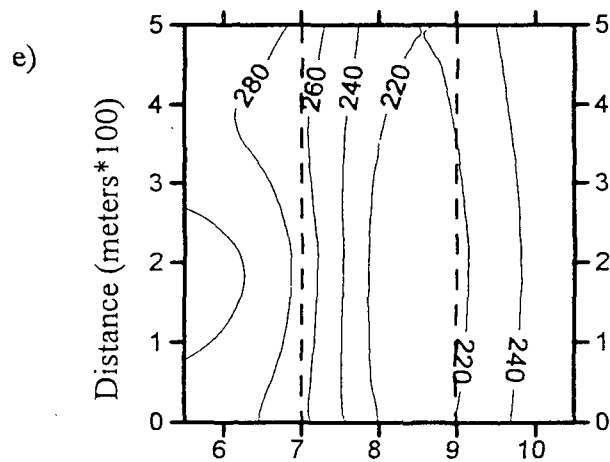
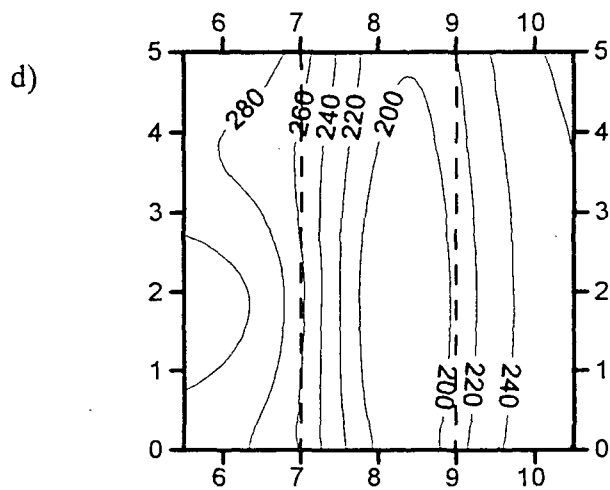
Figure 46 - 50:

Figures 46 - 50 illustrate the influence of the background host resistivity on the total field apparent resistivity contour maps for bipole 1 and bipole 2, and the P_2 -invariant contour map using bipole 1 and bipole 2. The model contains a 25 m thick layer of 10 Ω -m at the depth of 50 m. We vary the background resistivity from 100 Ω -m to 1000 Ω -m. For a background resistivity of 100 Ω -m, the apparent resistivity varies from 50 to 70 Ω -m in the measured area, which means that the 10 Ω -m layer causes a 30-50 % decrease in the background resistivity. The resistivity response for the resistivity contrast 10:200 is 30-50 % of the background resistivity value, for the contrast 10:300 it is 25-40 % of the background resistivity value, for the contrast 10:500 it is 16-30 %, and finally for the contrast 10:1000 it is 8-15 % of the background resistivity value.

Figure 45: The P2-invariant contour maps for a 25 m thick, 200 m wide body, of 10 Ohm-m resistivity, with a background resistivity of 300 Ohm-m, using bipole 1 and bipole 3.

- a) 25 m deep body
- b) 50 m deep body
- c) 75 m deep body
- d) 100 m deep body
- e) 125 m deep body
- f) 150 m deep body





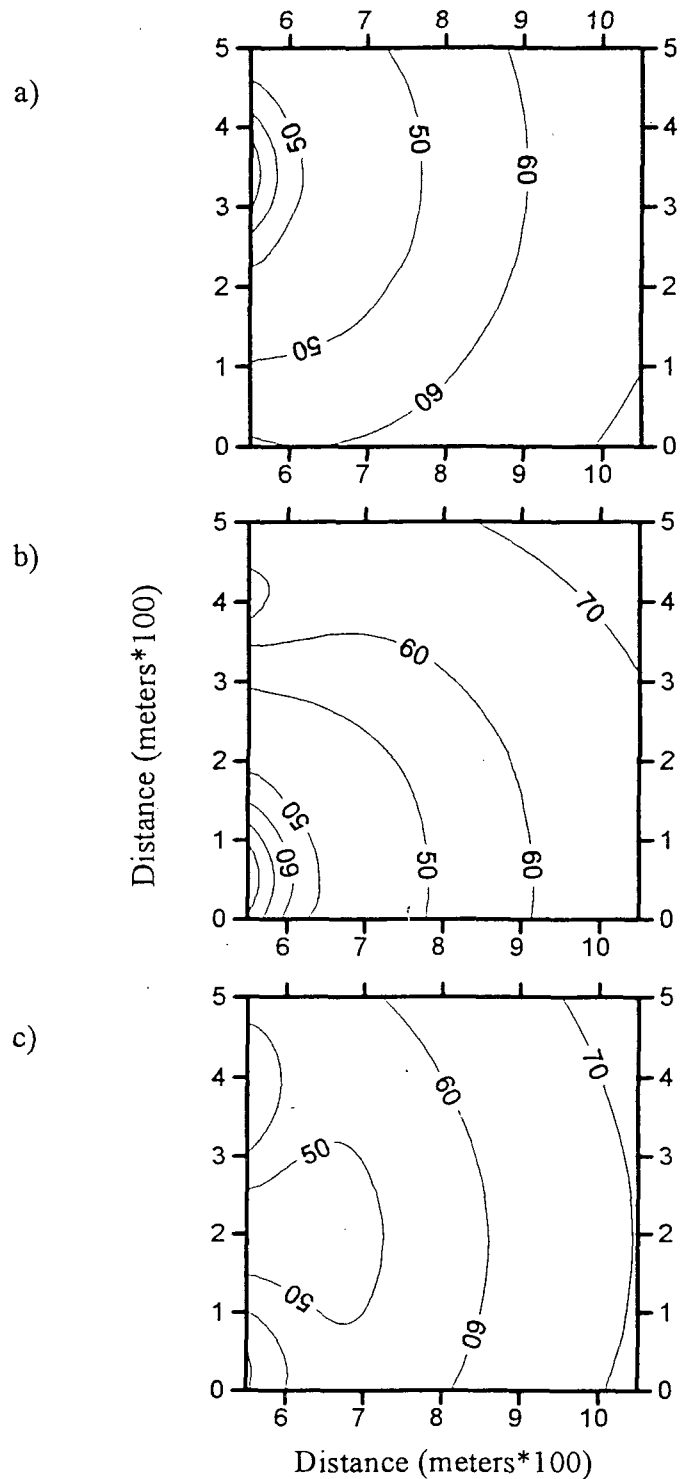


Figure 46: 25 m thick, 50 m deep layer, of 10 Ohm-m resistivity, with a background resistivity of 100 Ohm-m.

- a) total field apparent resistivity contour map for bipole 1
- b) total field apparent resistivity contour map for bipole 2
- c) P2-invariant contour map using bipole 1 and bipole 2

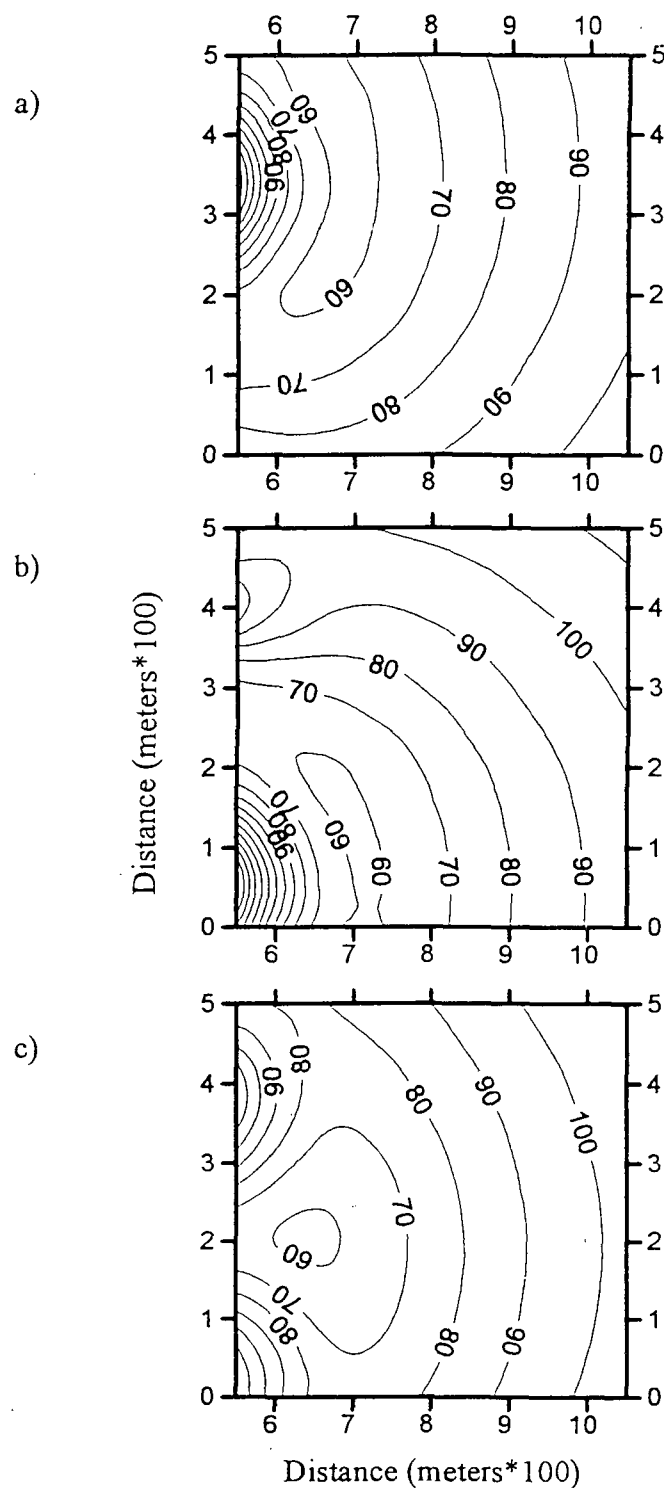


Figure 47: 25 m thick, 50 m deep layer, of 10 Ohm-m resistivity, with a background resistivity of 200 Ohm-m.

- a) total field apparent resistivity contour map for bipole 1
- b) total field apparent resistivity contour map for bipole 2
- c) P2-invariant contour map using bipole1 and bipole 2

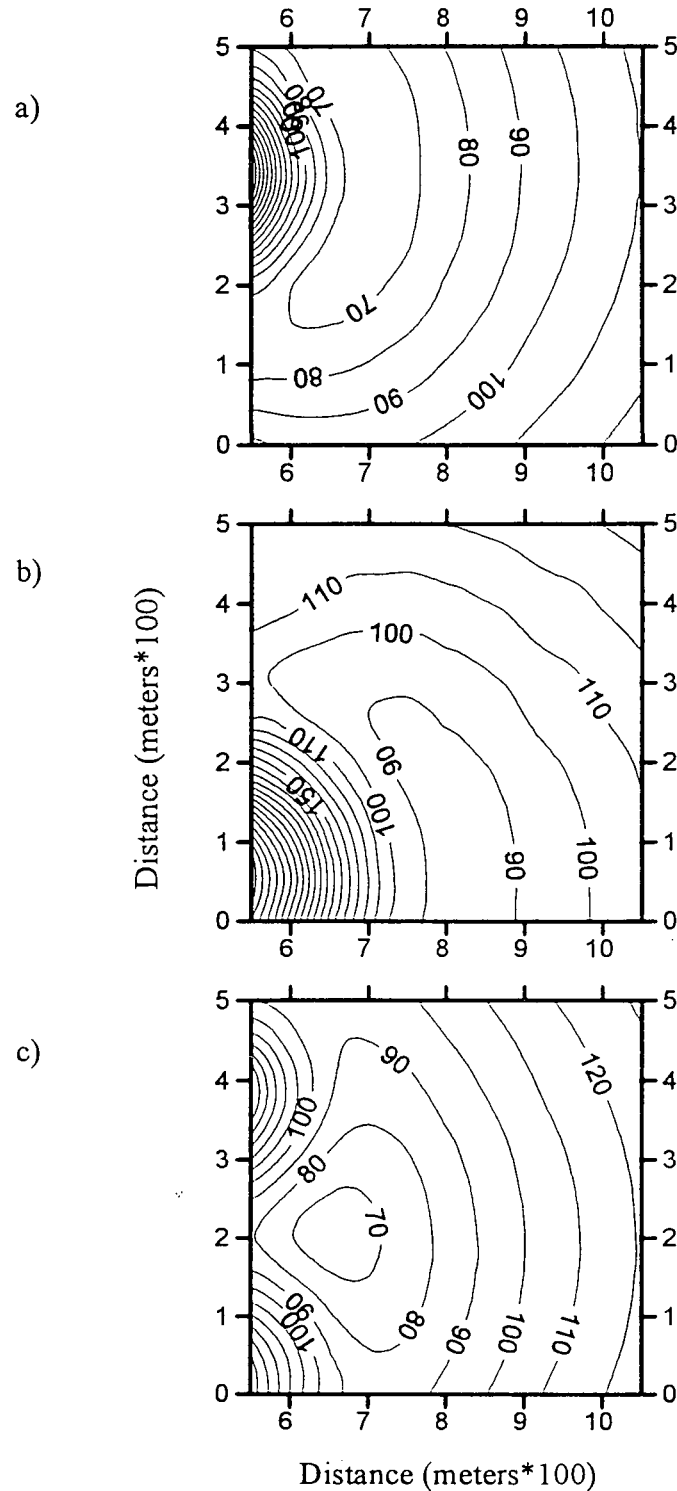


Figure 48: 25 m thick, 50 m deep layer, of 10 Ohm-m resistivity, with a background resistivity of 300 Ohm-m.
 a) total field apparent resistivity contour map for bipole 1
 b) total field apparent resistivity contour map for bipole 2
 c) P2-invariant contour map using bipole1 and bipole 2

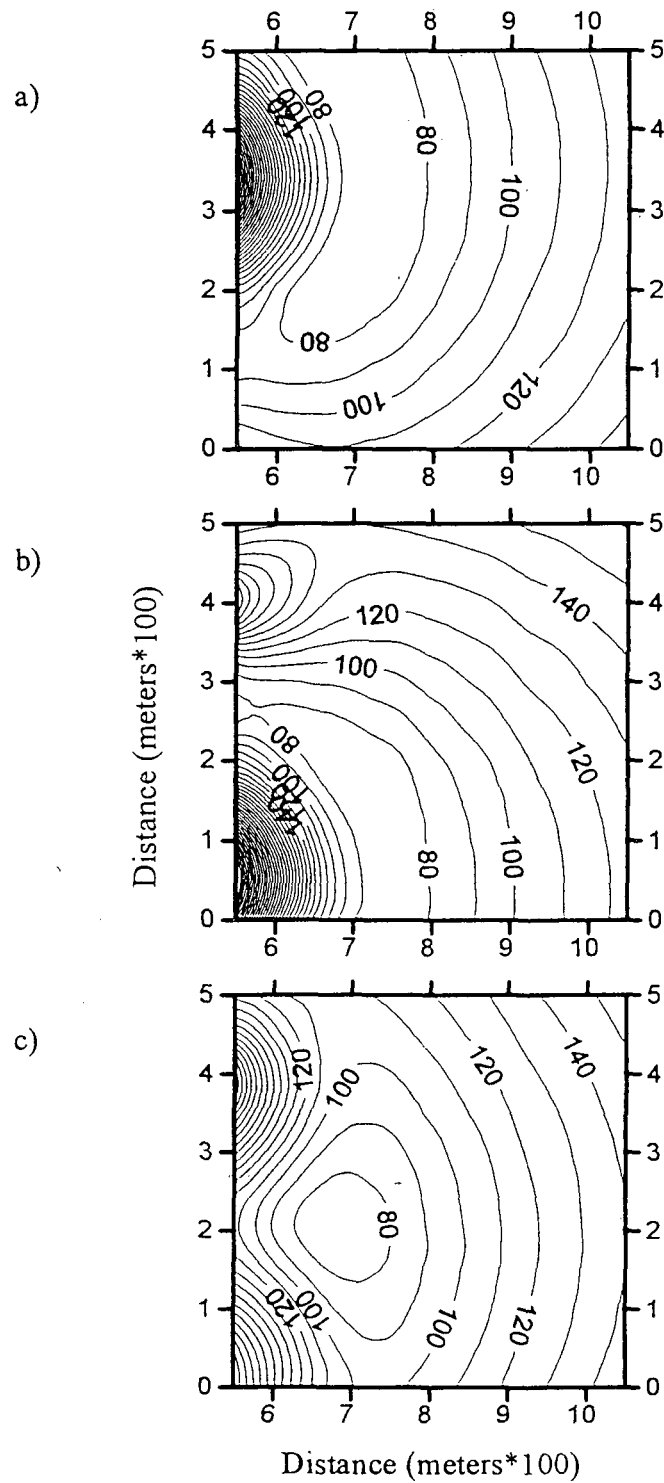


Figure 49: 25 m thick, 50 m deep layer, of 10 Ohm-m resistivity, with a background resistivity of 500 Ohm-m.

a) total field apparent resistivity contour map for bipole 1

b) total field apparent resistivity contour map for bipole 2

c) P2-invariant contour map using bipole 1 and bipole 2

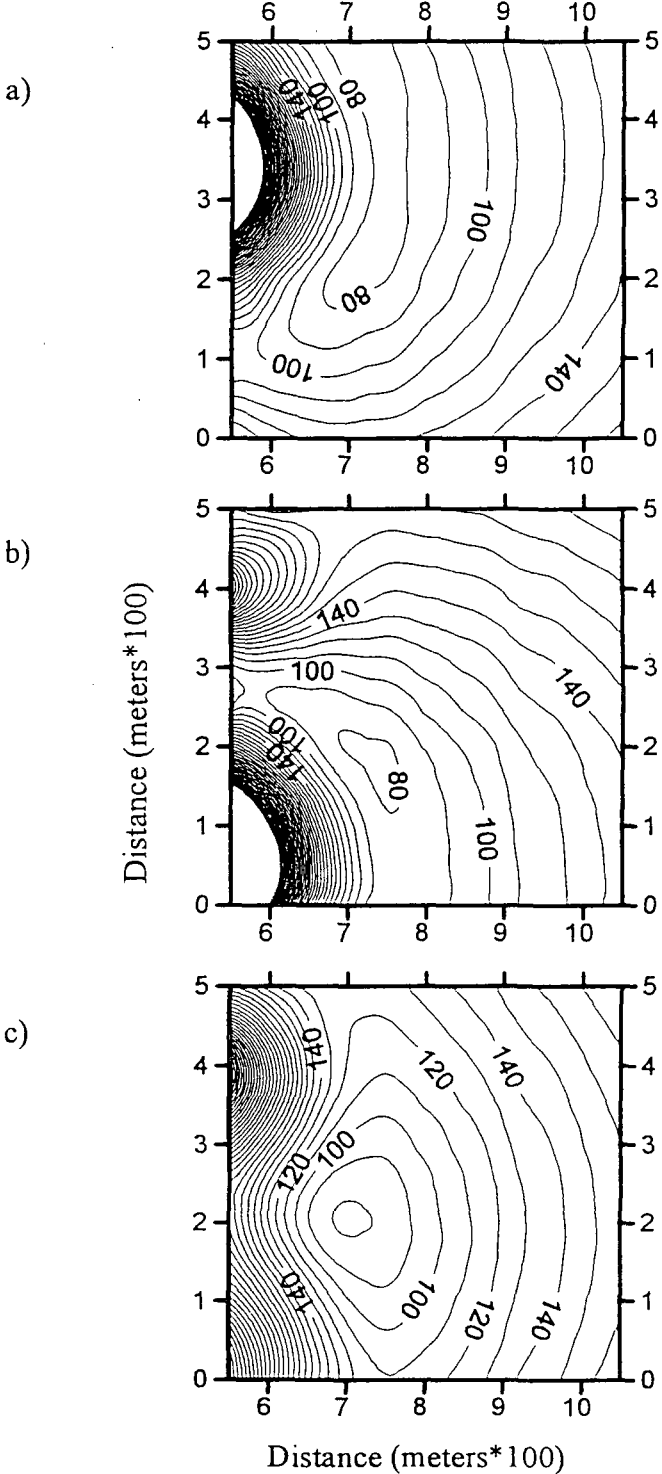


Figure 50: 25 m thick, 50 m deep layer, of 10 Ohm-m resistivity, with a background resistivity of 1000 Ohm-m.

- a) total field apparent resistivity contour map for bipole 1
- b) total field apparent resistivity contour map for bipole 2
- c) P2-invariant contour map using bipole1 and bipole 2

Figure 51 - 56:

Figures 51 - 56 illustrate the influence of different body resistivities on the total field apparent resistivity contour maps for bipole 1 and bipole 2, and the P_2 -invariant contour map using bipole 1 and bipole 2. The model contains a 25 m thick layer at the depth of 50 m in a 300 Ω -m host. The resistivity of the layer varies from 1 Ω -m to 100 Ω -m. The response of a 1 Ω -m layer in a 300 Ω -m background is about 5 % of the background resistivity value. The presence of a 10 Ω -m layer in the same environment causes a 60-75 % decrease in the background resistivity. The response of a 20 Ω -m layer in a 300 Ω -m background is 40-60 % of the background resistivity, for a 30 Ω -m layer it is 50-70 % of the background resistivity, for a 50 Ω -m layer it is 60-80 %, and for a 100 Ω -m layer it is 80-90 %. Note that the P_2 invariants remove the circularity of the contours about the individual electrodes, as in previous figures for layered earths.

Figure 57 - 61:

This figure shows the effect of saturation for a 1 Ω -m layer in a resistive host as the host resistivity is increased from 100 Ω -m to 1000 Ω -m. Thus, for models with a high resistivity contrast (more than 1:100) the total field apparent resistivity response is not very sensitive to the choice of background resistivity.

Figure 62 - 67:

The resolution of our system for a case when a conductive body is overlain by a near-surface conductive layer is shown in this figure. Figure 62 contains the total field apparent resistivity contour maps for bipole 1 and bipole 2, and the P_2 invariant contour map using a combination of bipole 1 and bipole 2 as a multiple source, for a 10 Ω -m, 10 m thick layer at the depth of 10 m. Figure 63 shows the same responses when

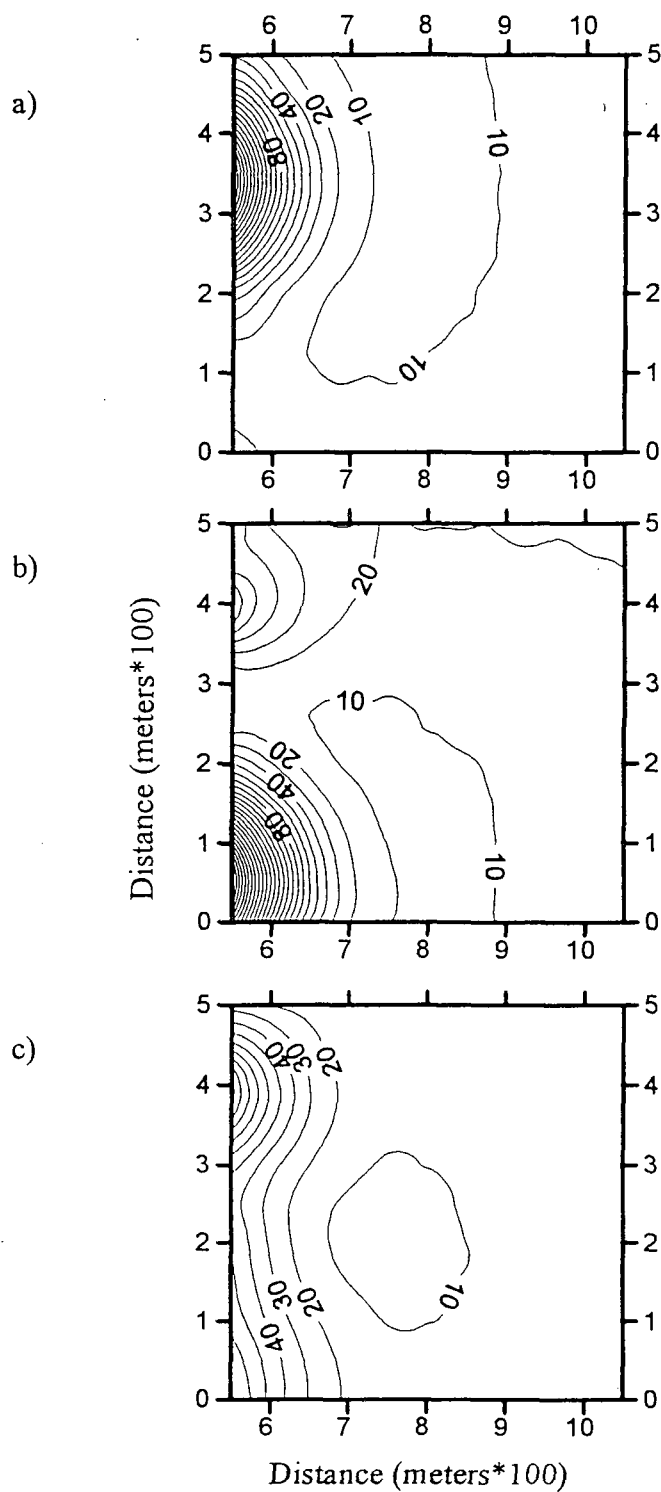


Figure 51: 25 m thick, 50 m deep layer, of 1 Ohm-m resistivity, with a background resistivity of 300 Ohm-m.
 a) total field apparent resistivity contour map for bipole 1
 b) total field apparent resistivity contour map for bipole 2
 c) P2-invariant contour map using bipole 1 and bipole 2

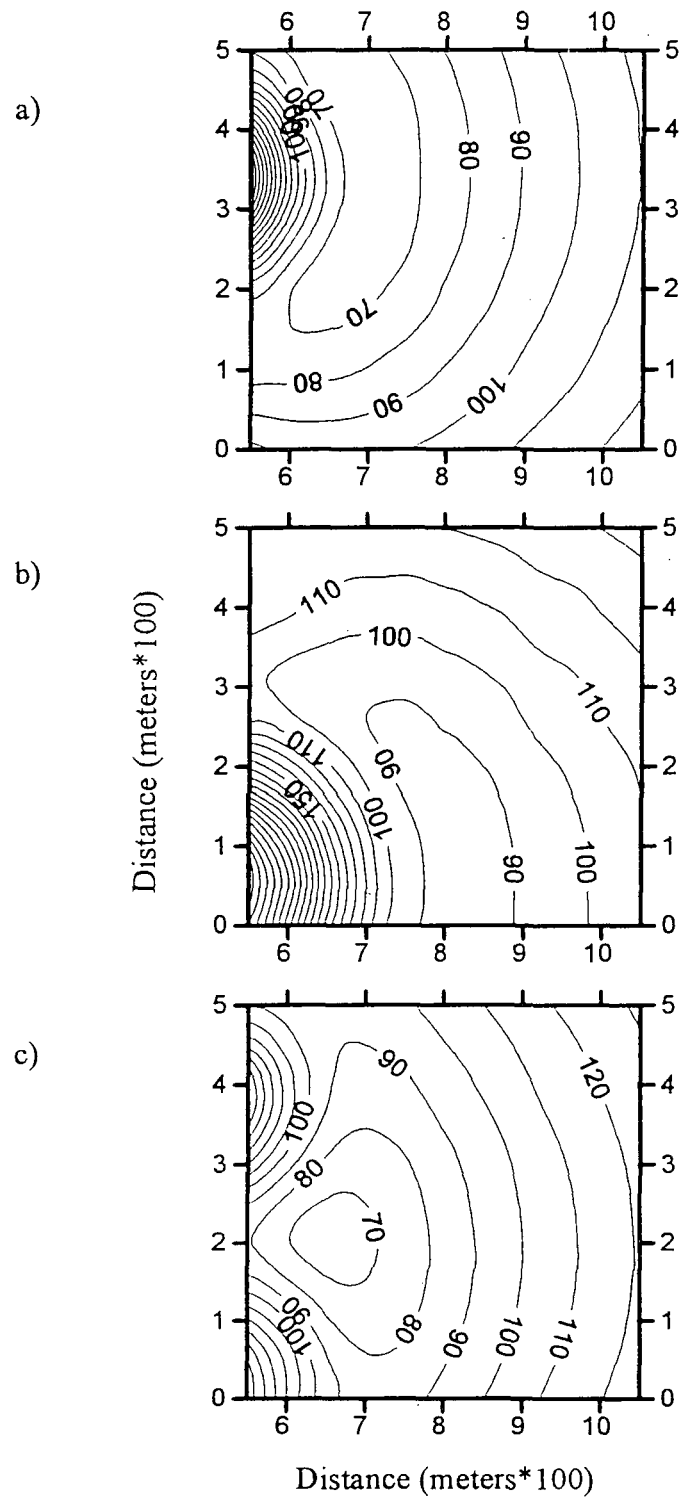


Figure 52: 25 m thick, 50 m deep layer, of 10 Ohm-m resistivity, with a background resistivity of 300 Ohm-m.

- a) total field apparent resistivity contour map for bipole 1
- b) total field apparent resistivity contour map for bipole 2
- c) P2-invariant contour map using bipole 1 and bipole 2

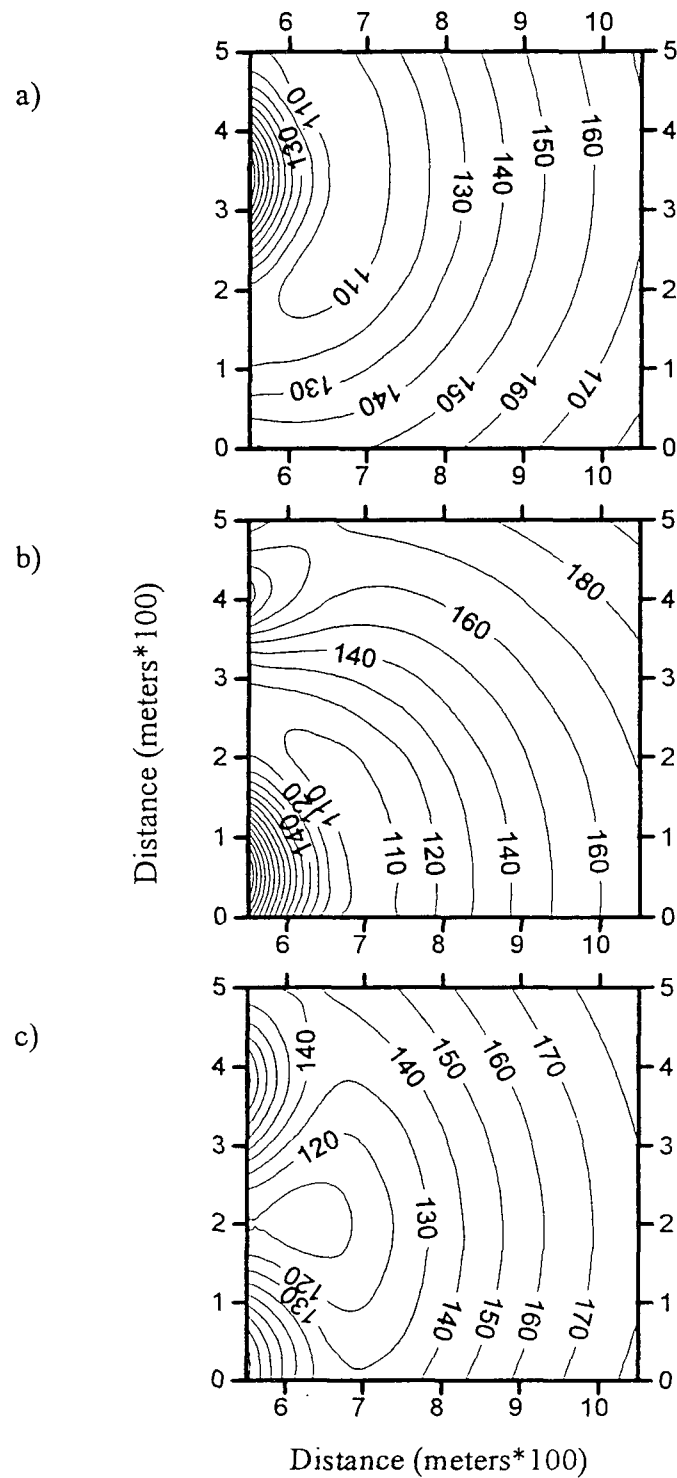


Figure 53: 25 m thick, 50 m deep layer, of 20 Ohm-m resistivity, with a background resistivity of 300 Ohm-m.

- a) total field apparent resistivity contour map for bipole 1
- b) total field apparent resistivity contour map for bipole 2
- c) P2-invariant contour map using bipole 1 and bipole 2

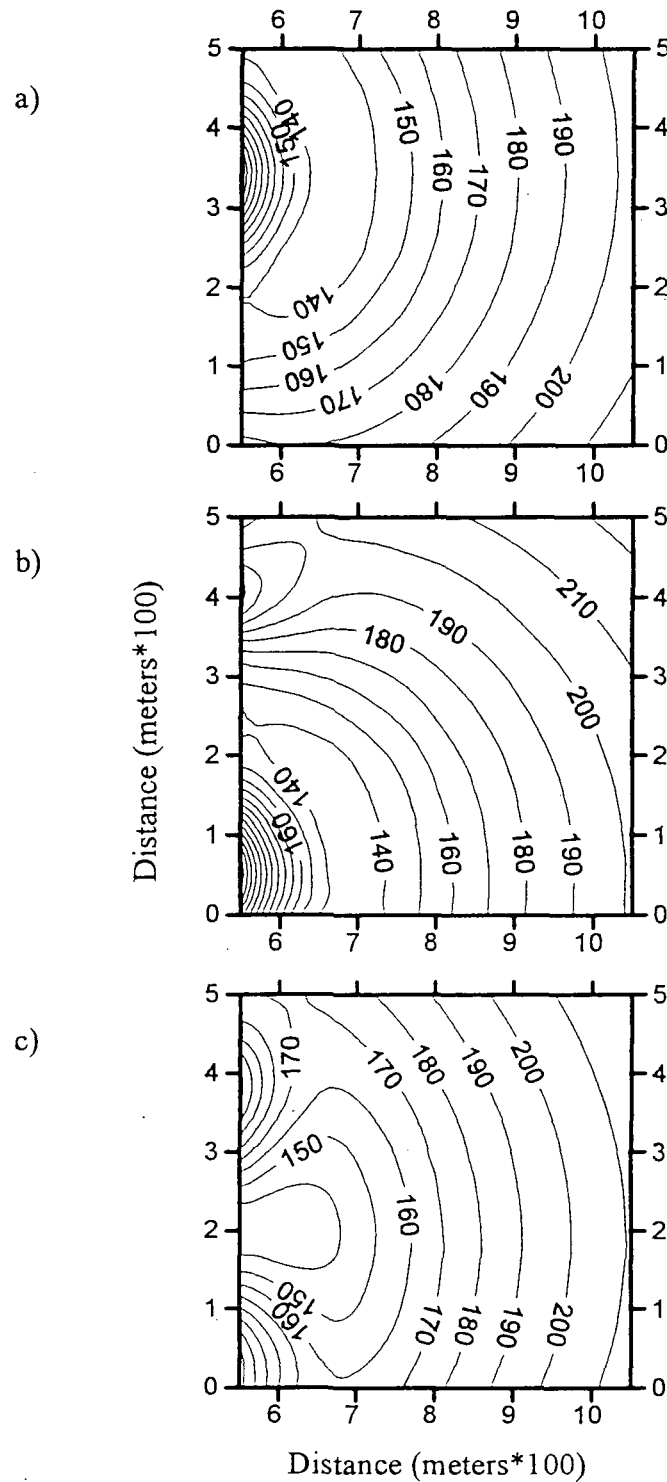


Figure 54: 25 m thick, 50 m deep layer, of 30 Ohm-m resistivity, with a background resistivity of 300 Ohm-m.

- a) total field apparent resistivity contour map for bipole 1
- b) total field apparent resistivity contour map for bipole 2
- c) P2-invariant contour map using bipole 1 and bipole 2

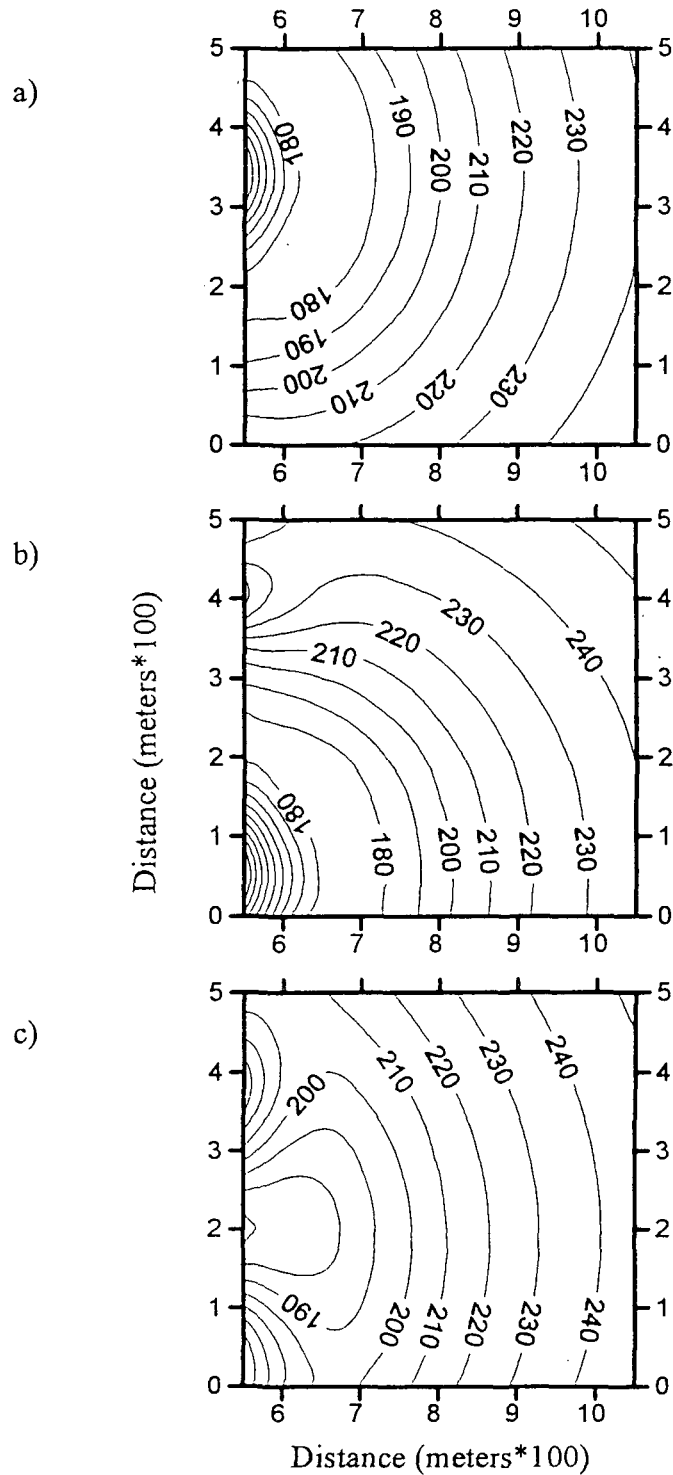


Figure 55: 25 m thick, 50 m deep layer, of 50 Ohm-m resistivity, with a background resistivity of 300 Ohm-m.

- a) total field apparent resistivity contour map for bipole 1
- b) total field apparent resistivity contour map for bipole 2
- c) P2-invariant contour map using bipole 1 and bipole 2

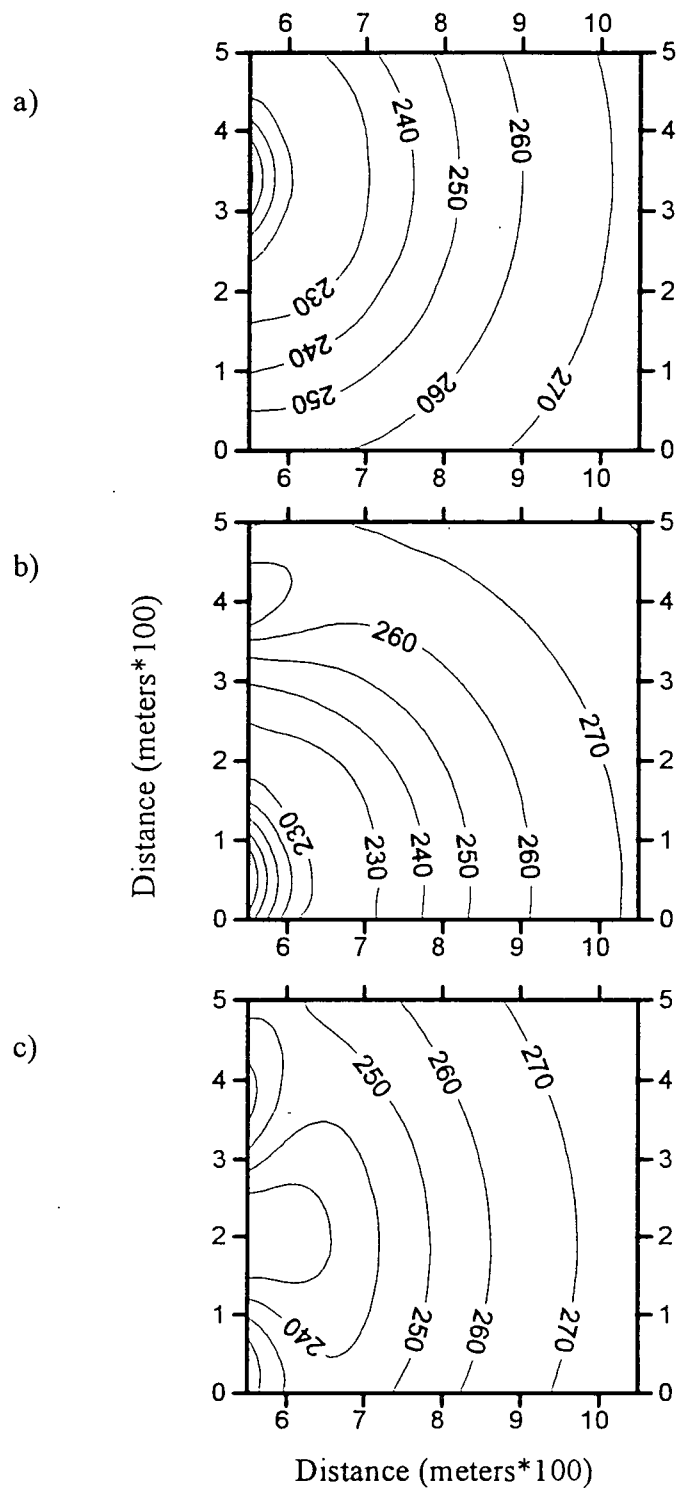


Figure 56: 25 m thick, 50 m deep layer, of 100 Ohm-m resistivity, with a background resistivity of 300 Ohm-m.

- a) total field apparent resistivity contour map for bipole 1
- b) total field apparent resistivity contour map for bipole 2
- c) P2-invariant contour map using bipole 1 and bipole 2

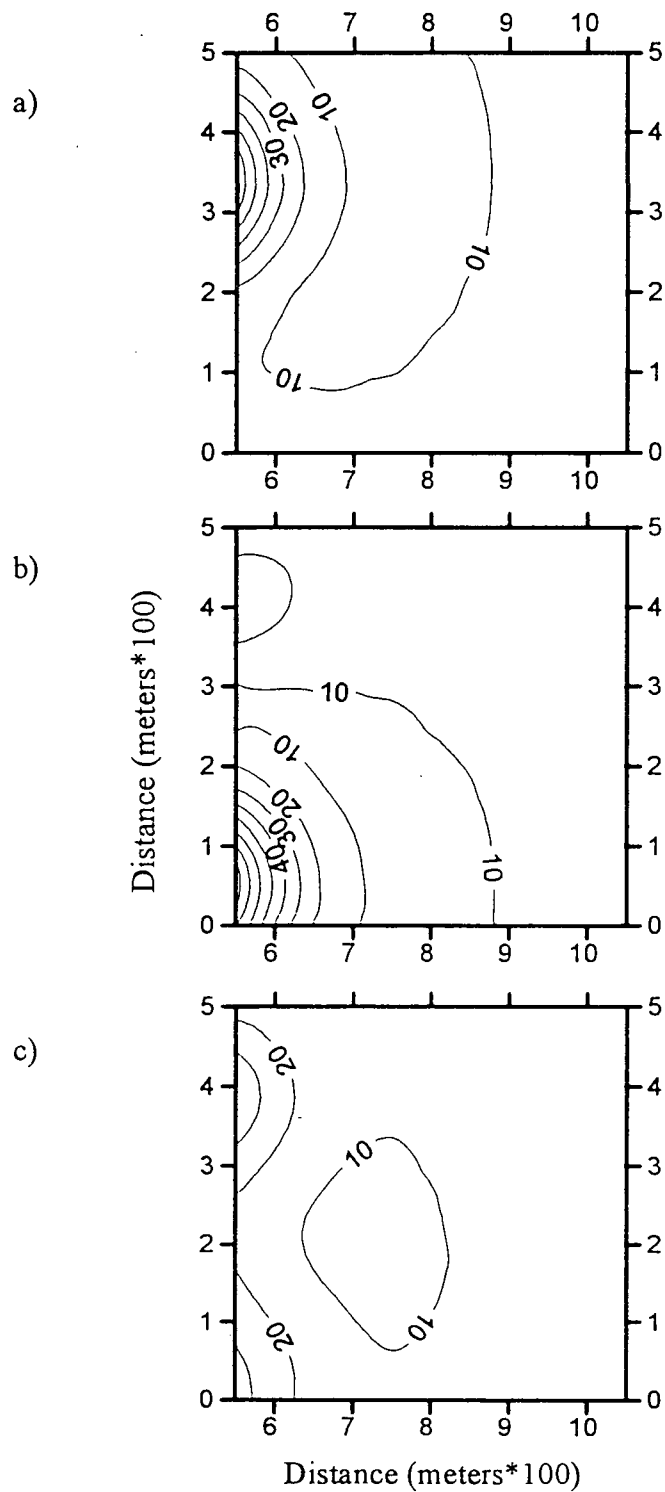


Figure 57: 25 m thick, 50 m deep layer, of 1 Ohm-m resistivity, with a background resistivity of 100 Ohm-m.

- a) total field apparent resistivity contour map for bipole 1
- b) total field apparent resistivity contour map for bipole 2
- c) P2-invariant contour map using bipole 1 and bipole 2

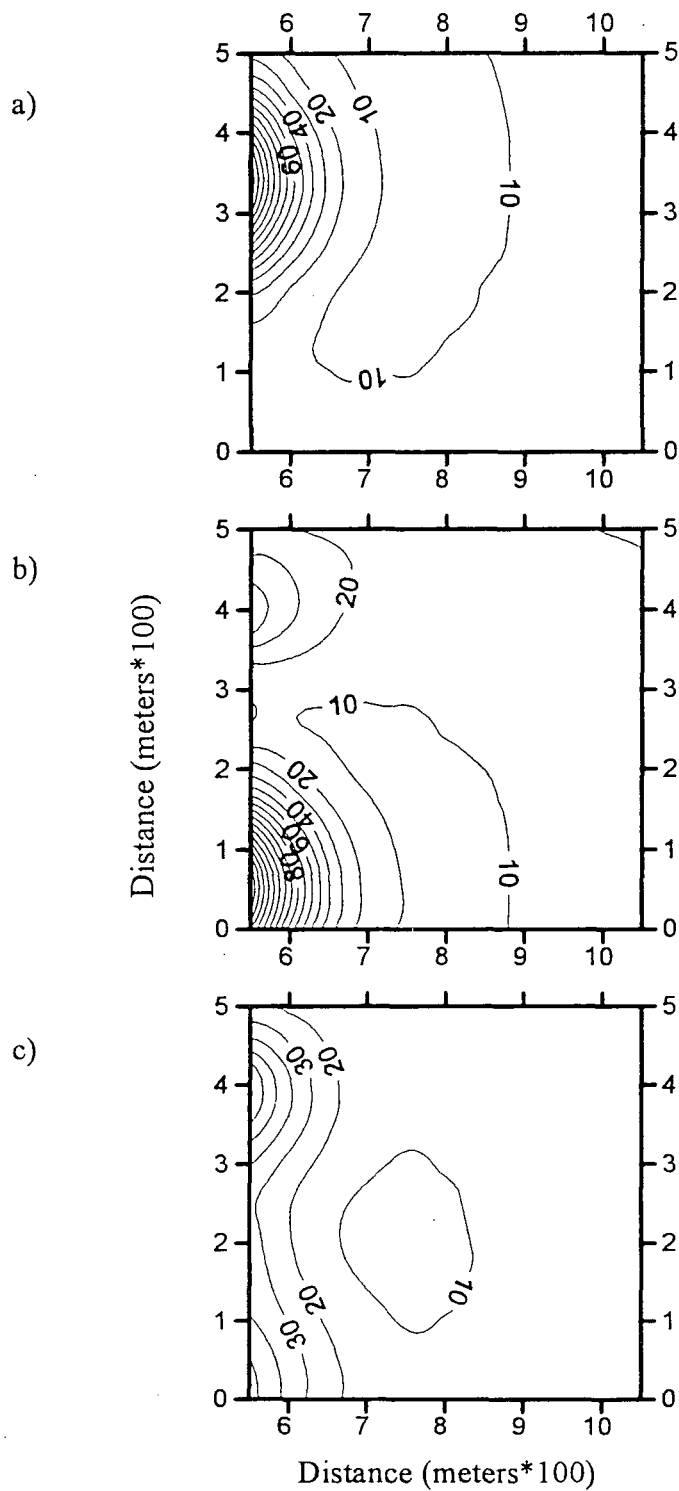


Figure 58: 25 m thick, 50 m deep layer, of 1 Ohm-m resistivity, with a background resistivity of 200 Ohm-m.

- a) total field apparent resistivity contour map for bipole 1
- b) total field apparent resistivity contour map for bipole 2
- c) P2-invariant contour map using bipole 1 and bipole 2

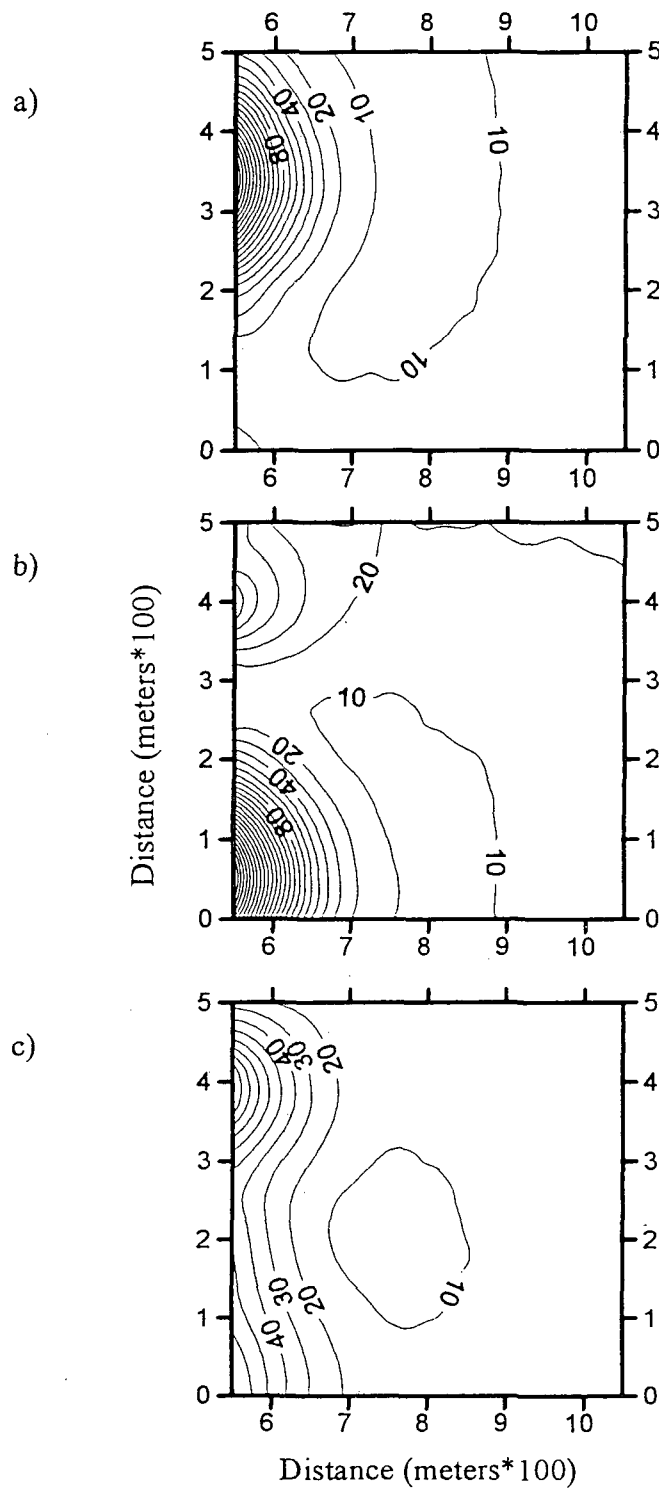


Figure 59: 25 m thick, 50 m deep layer, of 1 Ohm-m resistivity, with a background resistivity of 300 Ohm-m.

- a) total field apparent resistivity contour map for bipole 1
- b) total field apparent resistivity contour map for bipole 2
- c) P2-invariant contour map using bipole 1 and bipole 2

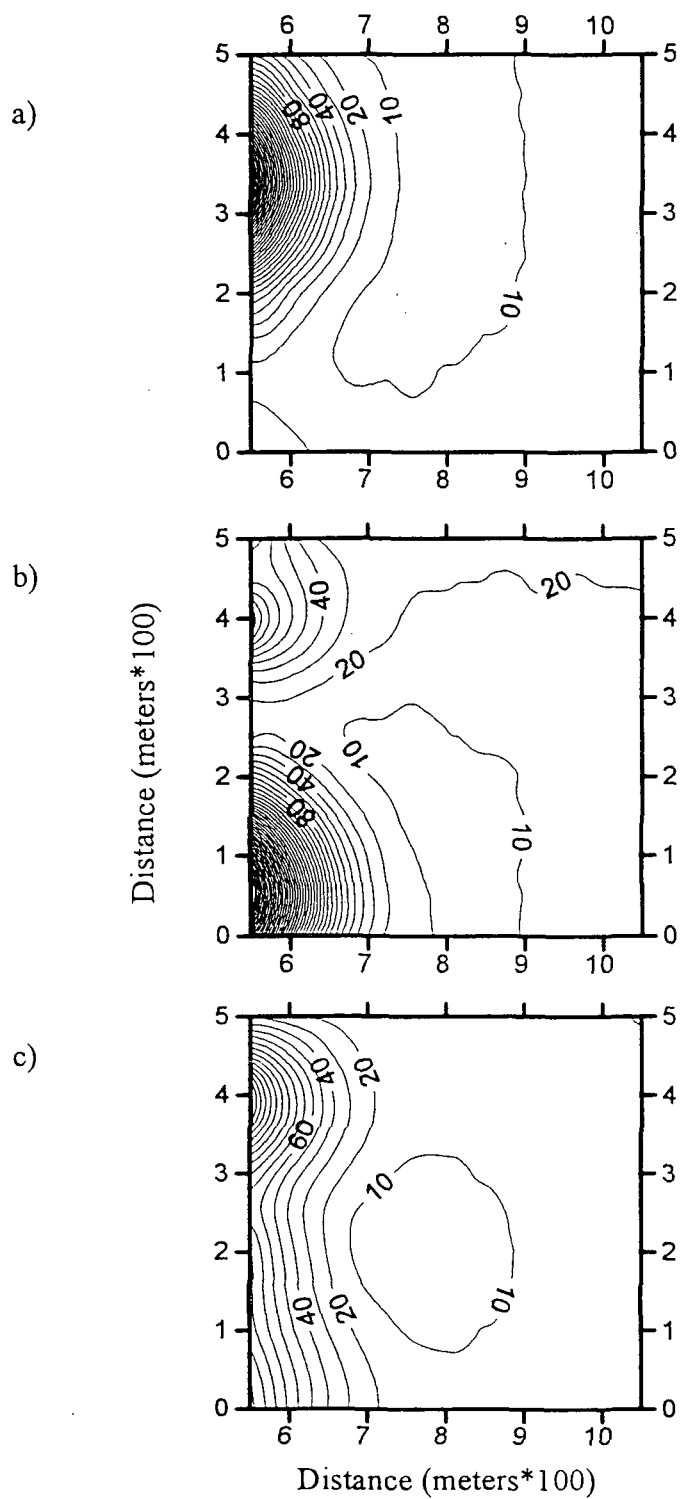


Figure 60: 25 m thick, 50 m deep layer, of 1 Ohm-m resistivity, with a background resistivity of 500 Ohm-m.

- a) total field apparent resistivity contour map for bipole 1
- b) total field apparent resistivity contour map for bipole 2
- c) P2-invariant contour map using bipole 1 and bipole 2

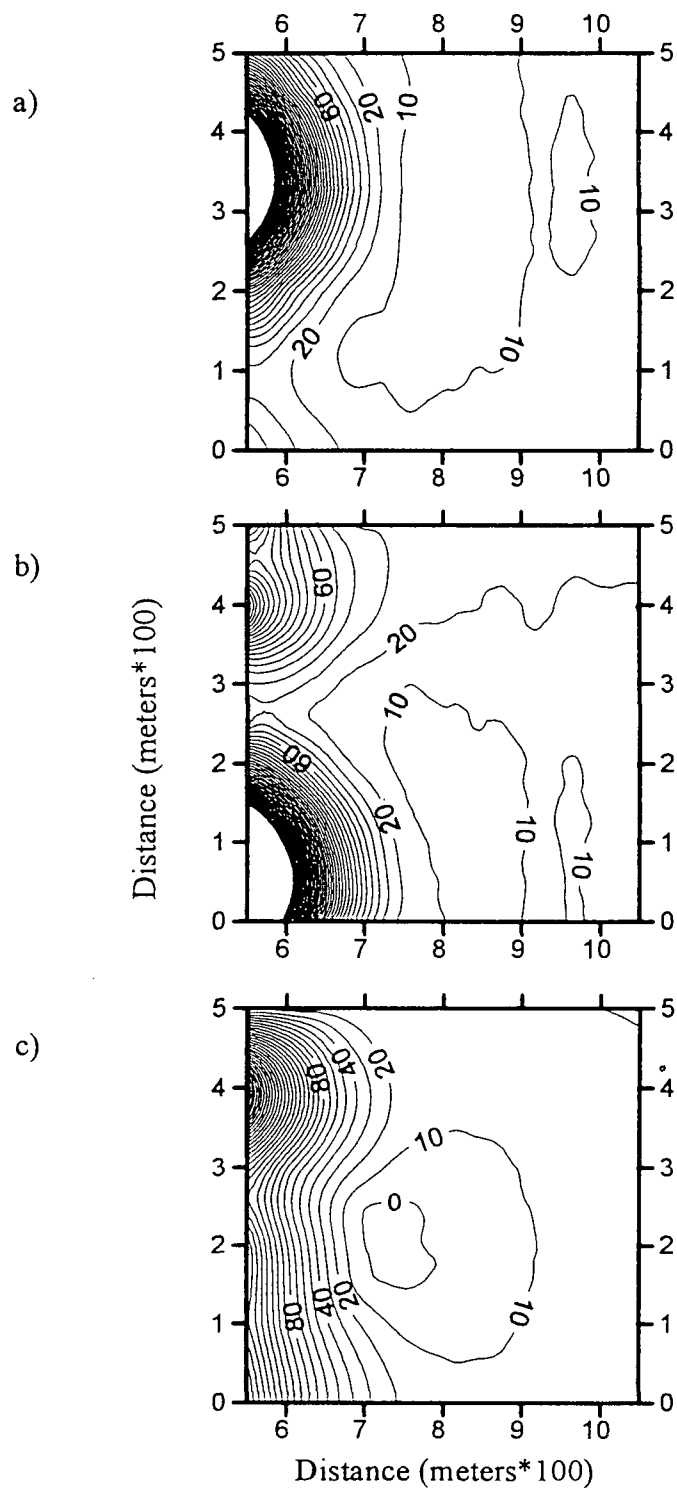


Figure 61: 25 m thick, 50 m deep layer, of 1 Ohm-m resistivity, with a background resistivity of 1000 Ohm-m.

- a) total field apparent resistivity contour map for bipole 1
- b) total field apparent resistivity contour map for bipole 2
- c) P2-invariant contour map using bipole 1 and bipole 2

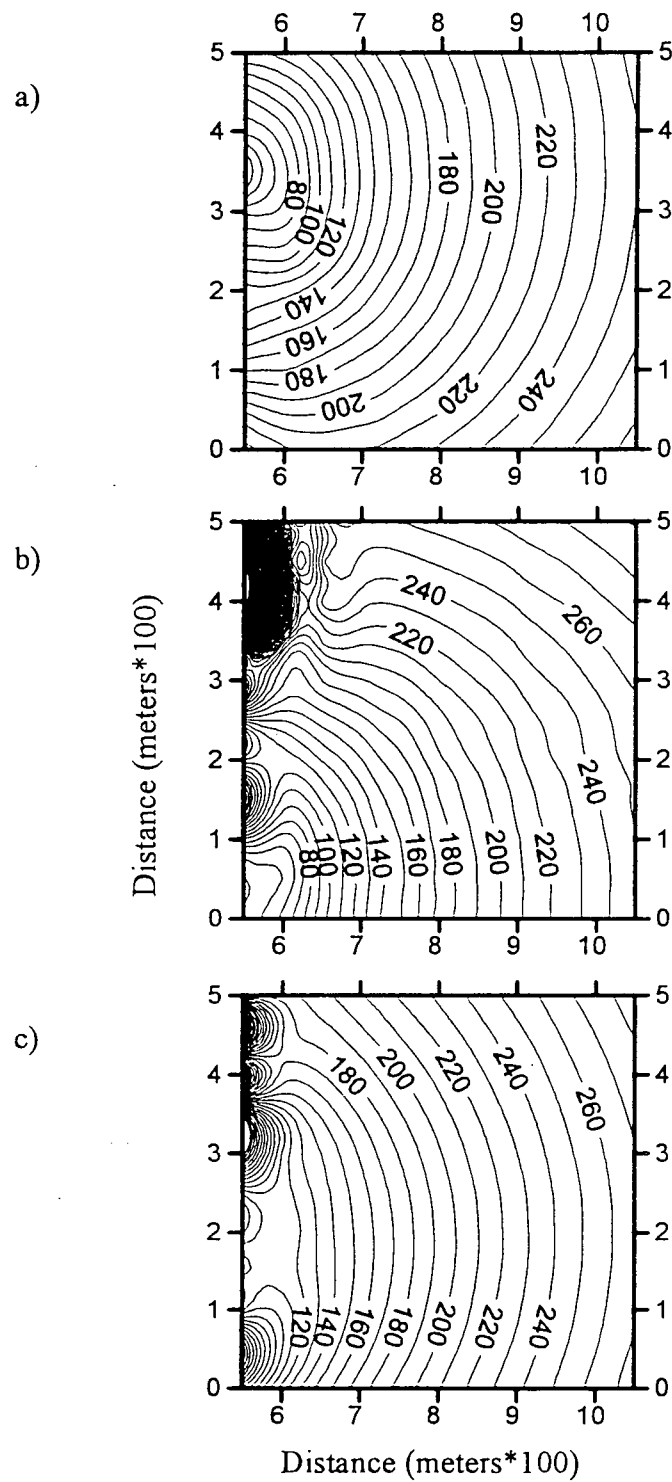


Figure 62: 10 m thick, 10 m deep layer, of 10 Ohm-m resistivity with a background resistivity of 500 Ohm-m.

- a) total field apparent resistivity contour map for bipole 1
- b) total field apparent resistivity contour map for bipole 2
- c) P2-invariant contour map using bipole 1 and bipole 2

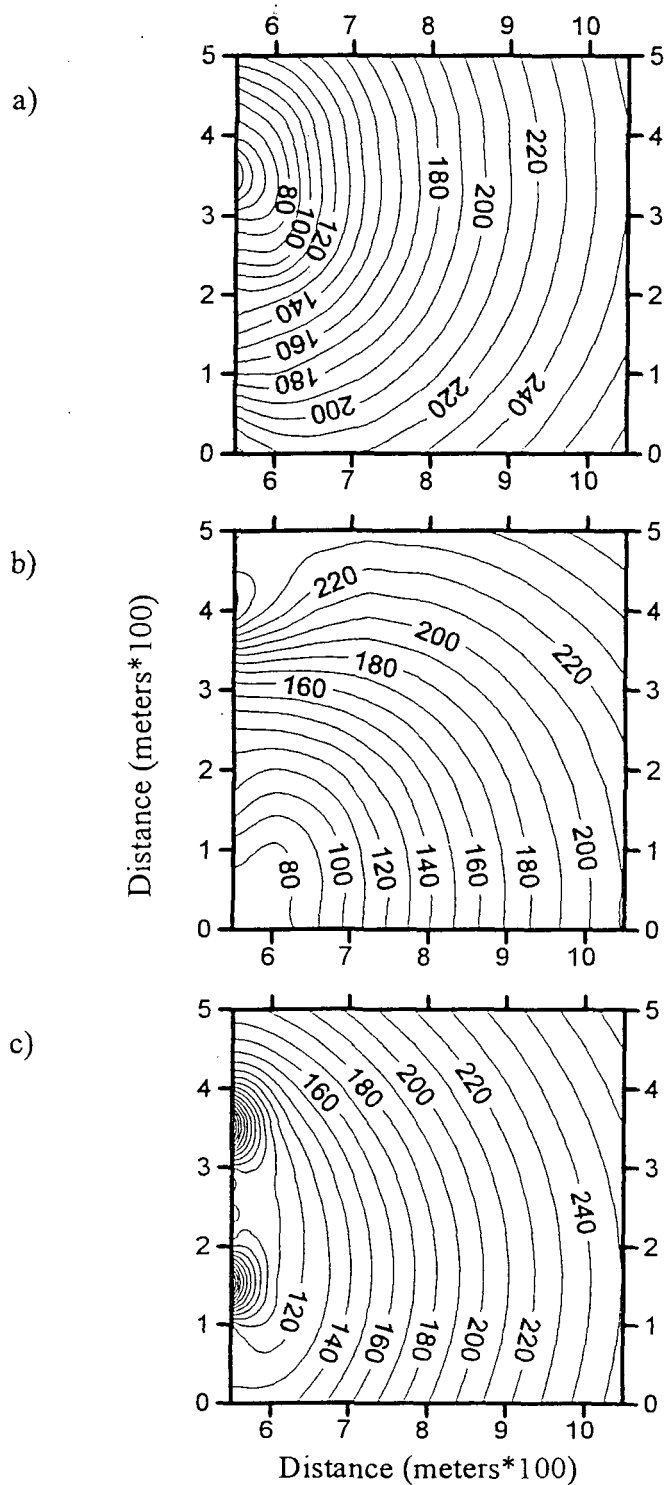


Figure 63: 10 m thick, 10 m deep layer, of 10 Ohm-m resistivity, with a background resistivity of 500 Ohm-m.

- a) total field apparent resistivity contour map for bipole 1
- b) total field apparent resistivity contour map for bipole 3
- c) P2-invariant contour map using bipole 1 and bipole 3

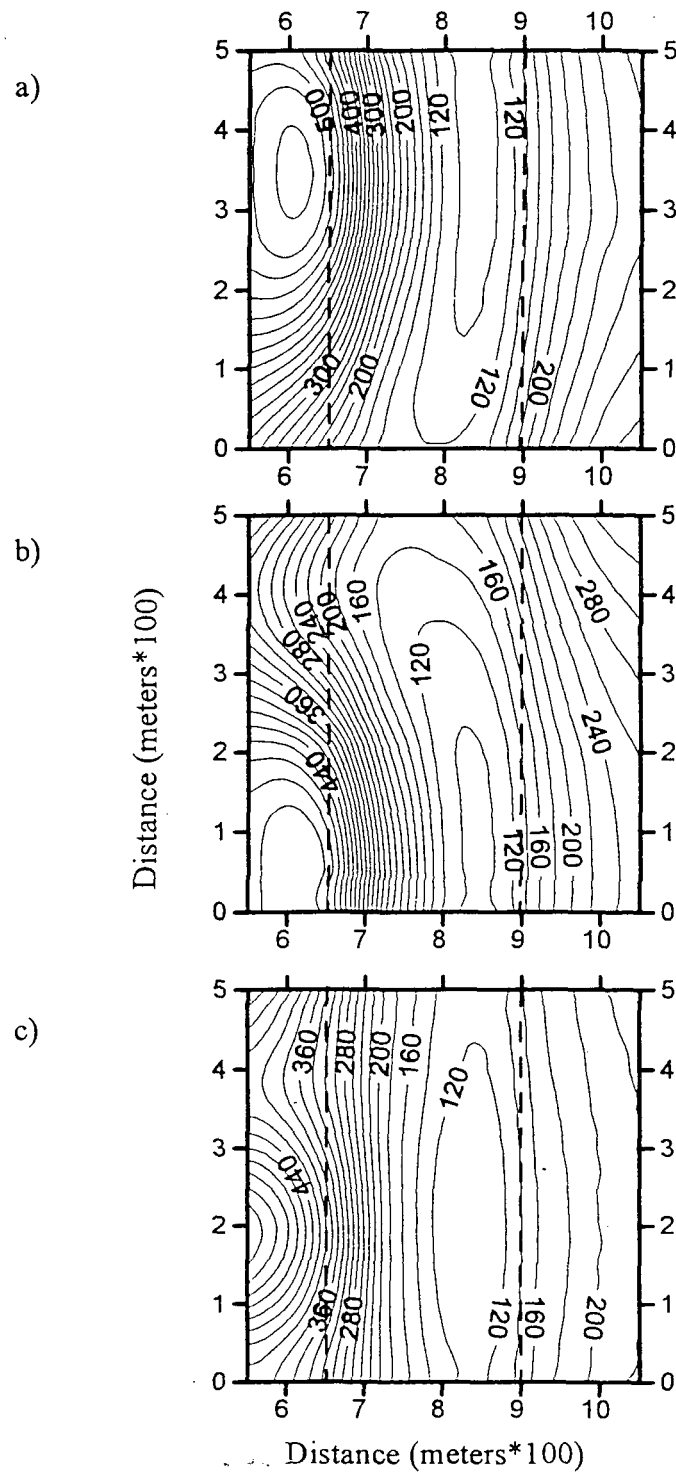


Figure 64: 100 m thick, 250 m wide, 75 m deep body, of 10 Ohm-m resistivity, with a background resistivity of 500 Ohm-m.
 a) total field apparent resistivity contour map for bipole 1
 b) total field apparent resistivity contour map for bipole 2
 c) P2-invariant contour map using bipole 1 and bipole 2

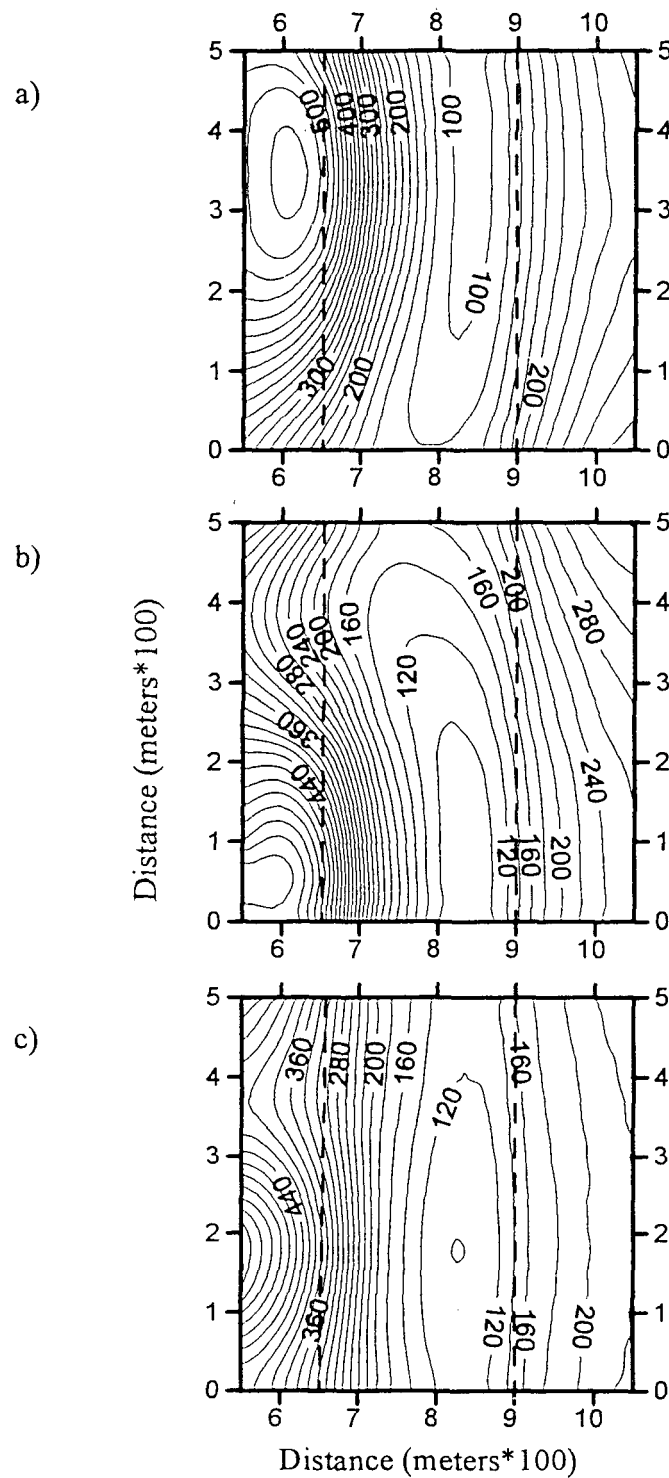


Figure 65: 100 m thick, 250 m wide, 75 m deep body, of 10 Ohm-m resistivity, with a background resistivity of 500 Ohm-m.
 a) total field apparent resistivity contour map for bipole 1
 b) total field apparent resistivity contour map for bipole 3
 c) P2-invariant contour map using bipole 1 and bipole 3

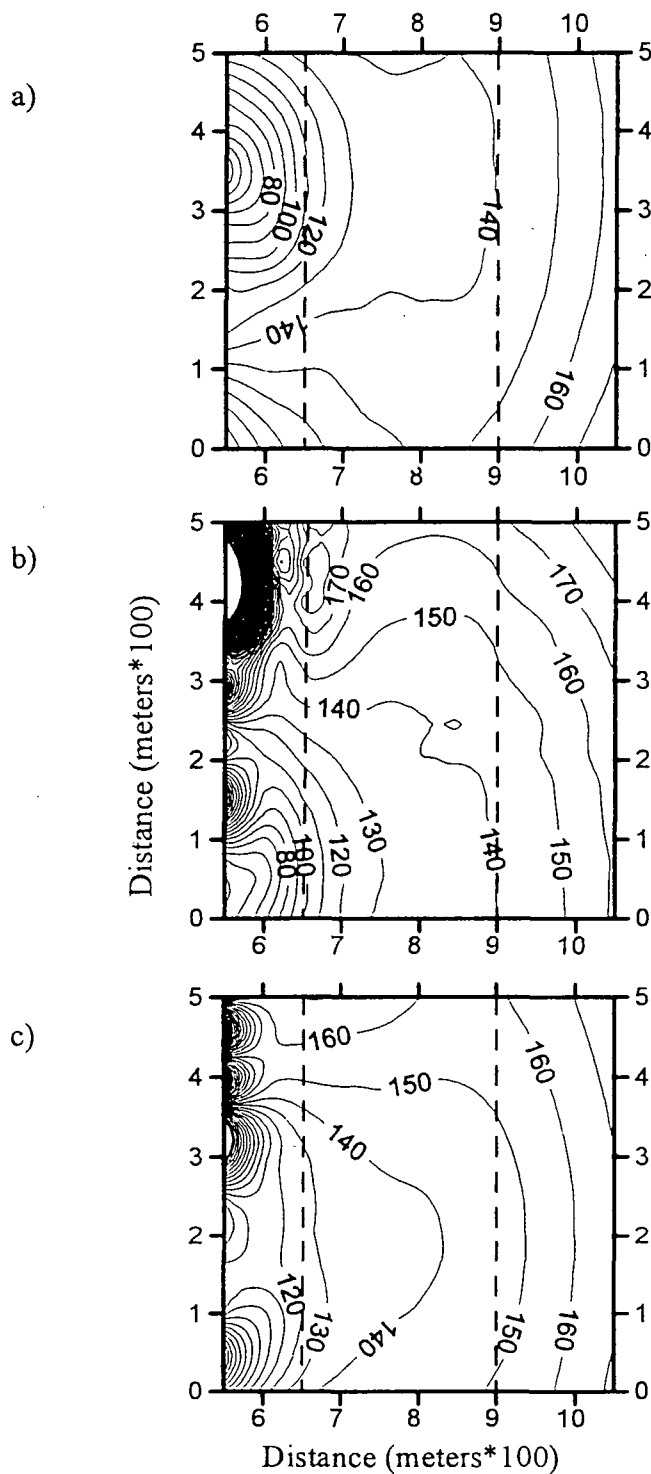


Figure 66: 100 m thick, 250 m wide, 75 m deep body, of 10 Ohm-m resistivity, with a 10 m thick, 10 m deep layer, of 10 Ohm-m resistivity, in a 500 Ohm-m background.

- a) total field apparent resistivity; contour map for bipole 1
 b) total field apparent resistivity contour map for bipole 2
 c) P2-invariant contour map using bipole 1 and bipole 2

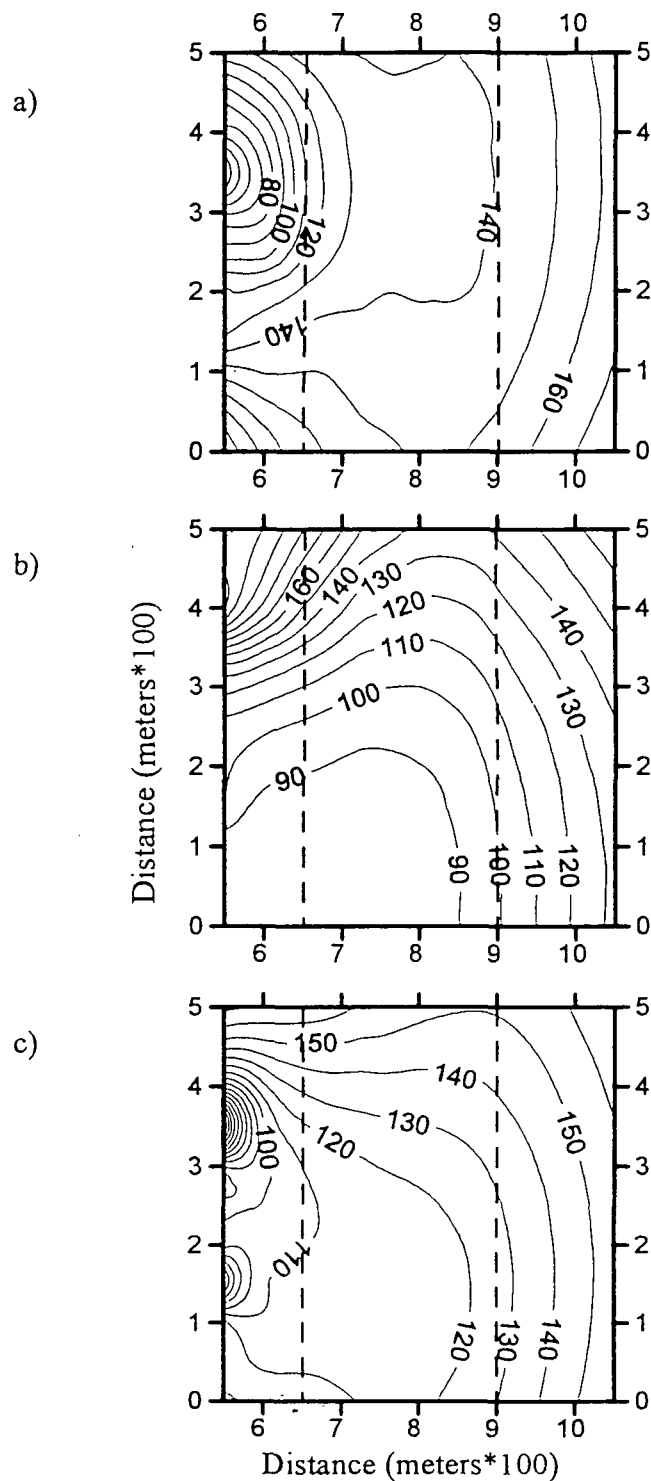


Figure 67: 100 m thick, 250 m wide, 75 m deep body, of 10 Ohm-m resistivity, with a 10 m thick, 10 m deep layer, of 10 Ohm-m resistivity, in a 500 Ohm-m background.

- a) total field apparent resistivity contour map for bipole 1
- b) total field apparent resistivity contour map for bipole 3
- c) P2-invariant contour map using bipole 1 and bipole 3

a borehole current electrode is used. There is only a slight difference between these two figures. Figures 64 and 65 are total field apparent resistivity plots for a 2-D conductive 10 Ω -m body which is 250 m wide and 100 m thick, buried at a depth of 75 m. Again, the corresponding difference between the surface and borehole configuration is small. Figures 66 and 67 are plots of the total field apparent resistivity response of the model when both a shallow conductive layer and a deep conductive body are present. Although a marked decrease in the resistivity response is seen, it is difficult to visually locate the position of the deep conductive body.

APPENDIX B

**THEORETICAL RESPONSE OF 1-D AND 2-D RESISTIVE
STRUCTURES IN A LOW RESISTIVITY BACKGROUND**

Appendix B contains a series of models of a highly resistive body in a relatively conductive background. The aim of this appendix is to show the resistivity response of a series of models, which might elucidate the interpretation of our field data.

We have used the field electrode configuration for borehole UURI#1 through the entire appendix. The description of the field setup is given in Chapter 4. Bipole 1 is represented by the A_1B_1 current electrode pair, bipole 2 is represented by the A_1B_2 current electrode pair, and bipole 3 is represented by the A_1B_3 current electrode pair. The coordinates for these current electrodes are:

$$A_1 = [32.5, 250.0, 0.0] \text{ m}, B_1 = [478.5, 344.1, 0.0] \text{ m};$$

$$A_1 = [32.5, 250.0, 0.0] \text{ m}, B_2 = [500.0, 50.0, 0.0] \text{ m}; \text{ and}$$

$$A_1 = [32.5, 250.0, 0.0] \text{ m}, B_3 = [500.0, 50.0, 100.0] \text{ m}.$$

The receiver grid was from 550 m to 1050 m in the x-direction and from 0 m to 500 m in the y-direction. Each receiver dipole length was 50 m.

Figure 68 - 73:

This figure contains a sequence of the total field apparent resistivity contour maps for each current bipole for a model which consists of a 25 m thick layer of 1000 Ω -m in a 100 Ω -m background. The depth of the layer varies from 25 m to 150 m. The large gradients near [550.0, 350.0] m in Figure 68b and near [550.0, 50.0] m in Figure 68c are caused by the close presence of current electrodes to the anomalous resistivity unit. As in other layered earth situations, the contours are approximately circular about the near electrode.

There is a very important feature here, which we have to keep in mind during the interpretation process. The highly resistive layer causes an increase of resistivity in the resistivity response if surface current bipoles are used. However, if we use a borehole current electrode the response of the resistive layer is less than the

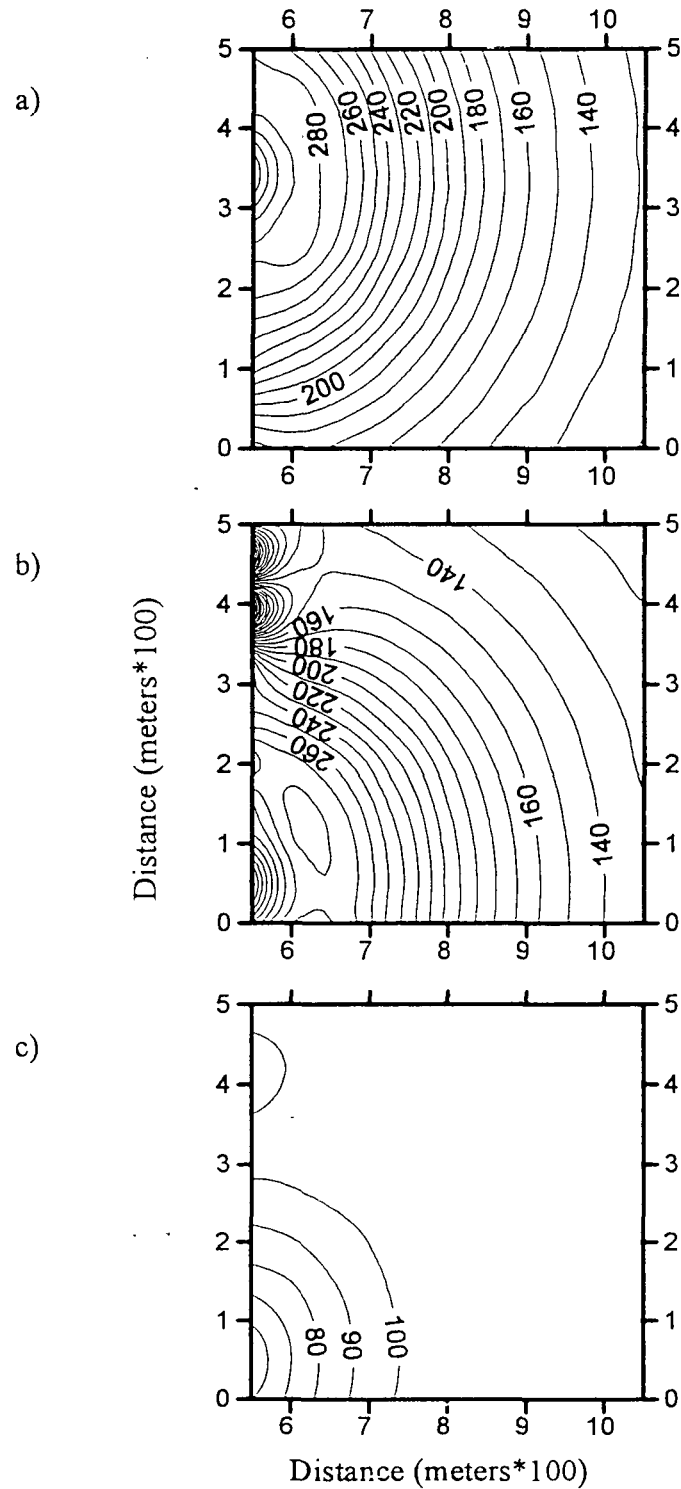


Figure 68: Total field apparent resistivity contour maps for a 30 m thick, 20 m deep layer, of 1000 Ohm-m resistivity, with a background resistivity of 100 Ohm-m.
 a) bipole 1, b) bipole 2, c) bipole 3

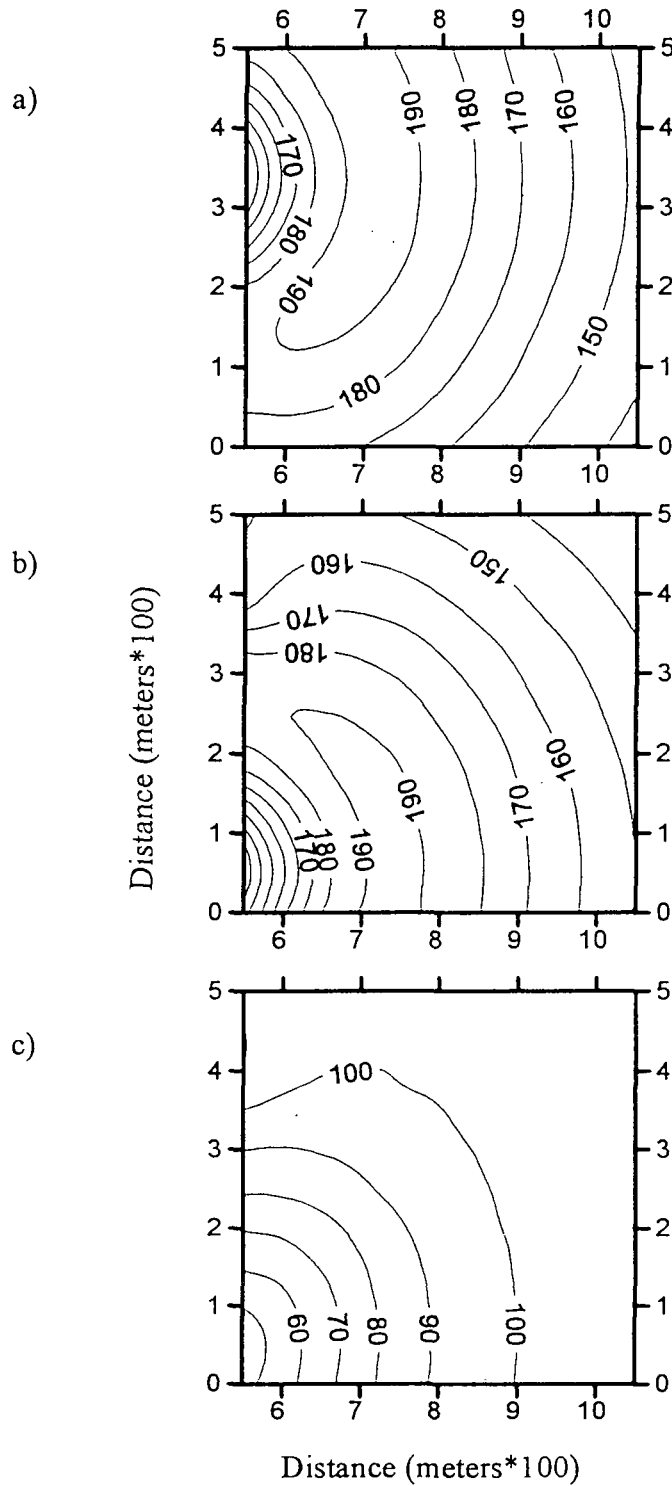


Figure 69: Total field apparent resistivity contour maps for a 25 m thick, 50 m deep layer, of 1000 Ohm-m resistivity, with a background resistivity of 100 Ohm-m.
 a) bipole 1, b) bipole 2, c) bipole 3

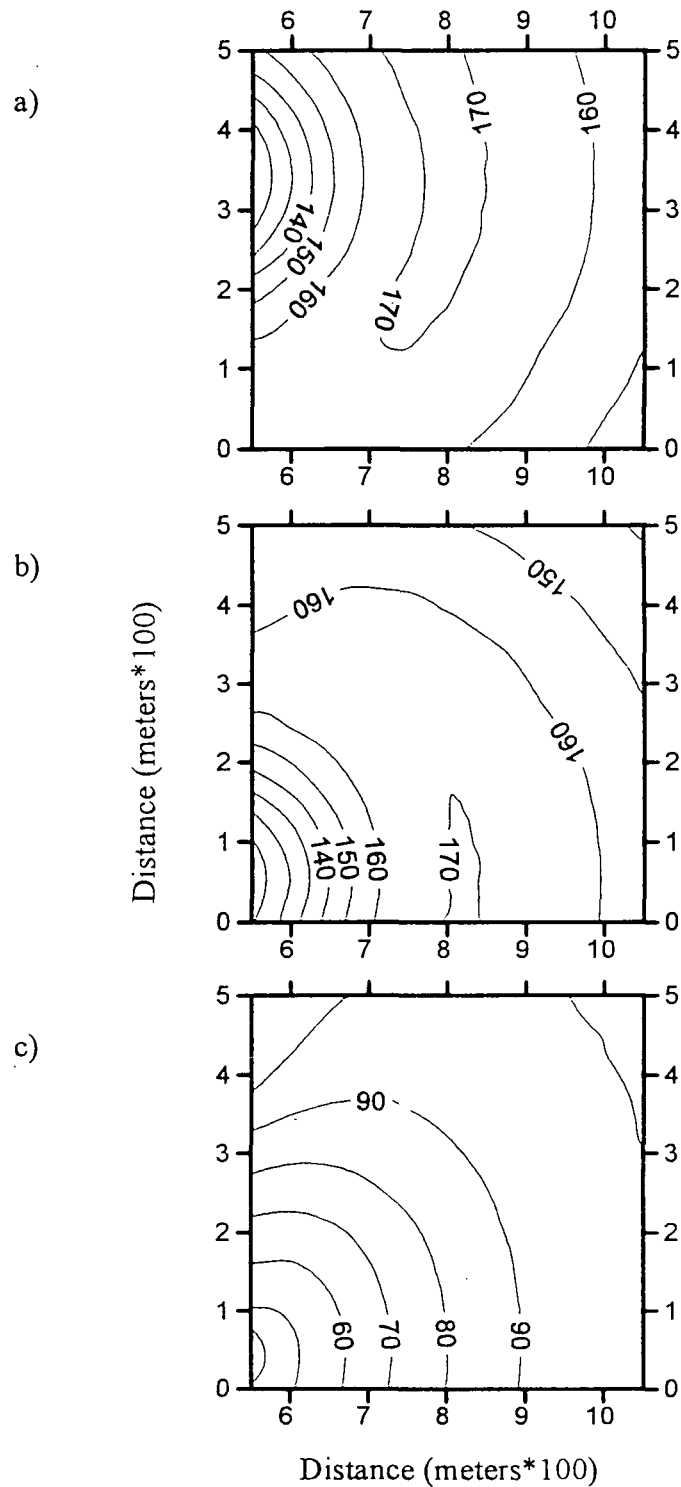


Figure 70: Total field apparent resistivity contour maps for a 25 m thick, 75 m deep layer, of 1000 Ohm-m resistivity, with a background resistivity of 100 Ohm-m.
 a) bipole 1, b) bipole 2, c) bipole 3

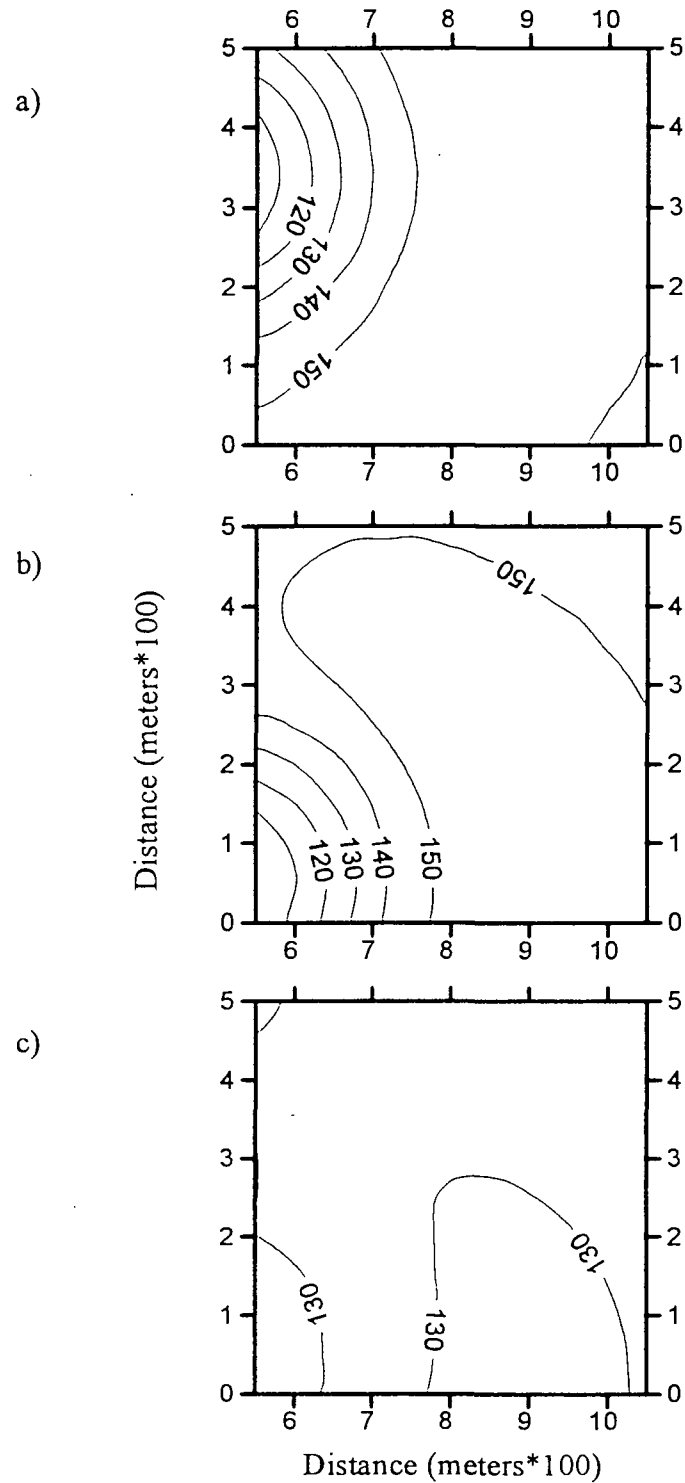


Figure 71: Total field apparent resistivity contour maps for a 25 m thick, 100 m deep layer, of 1000 Ohm-m resistivity, with a background resistivity of 100 Ohm-m.
 a) bipole 1, b) bipole 2, c) bipole 3

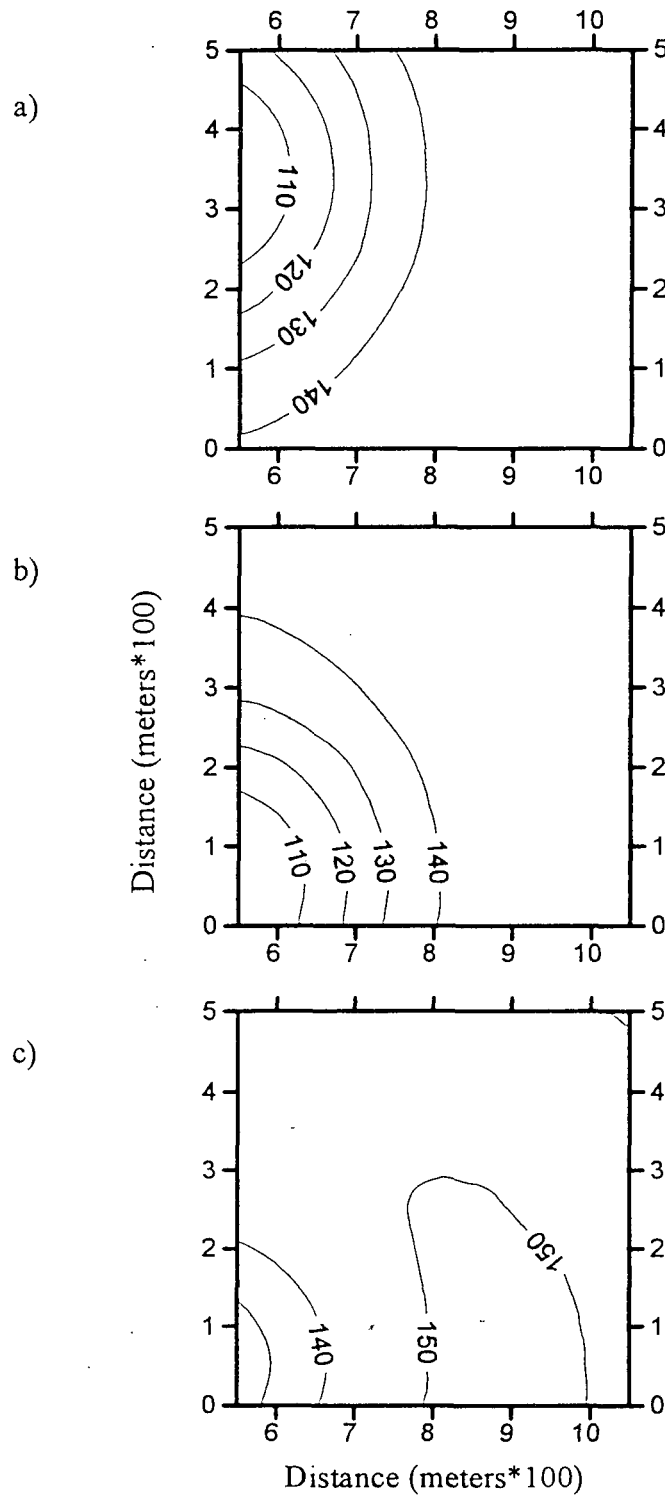


Figure 72: Total field apparent resistivity contour maps for a 25 m thick, 125 m deep layer, of 1000 Ohm-m resistivity, with a background resistivity of 100 Ohm-m.
 a) bipole 1, b) bipole 2, c) bipole 3

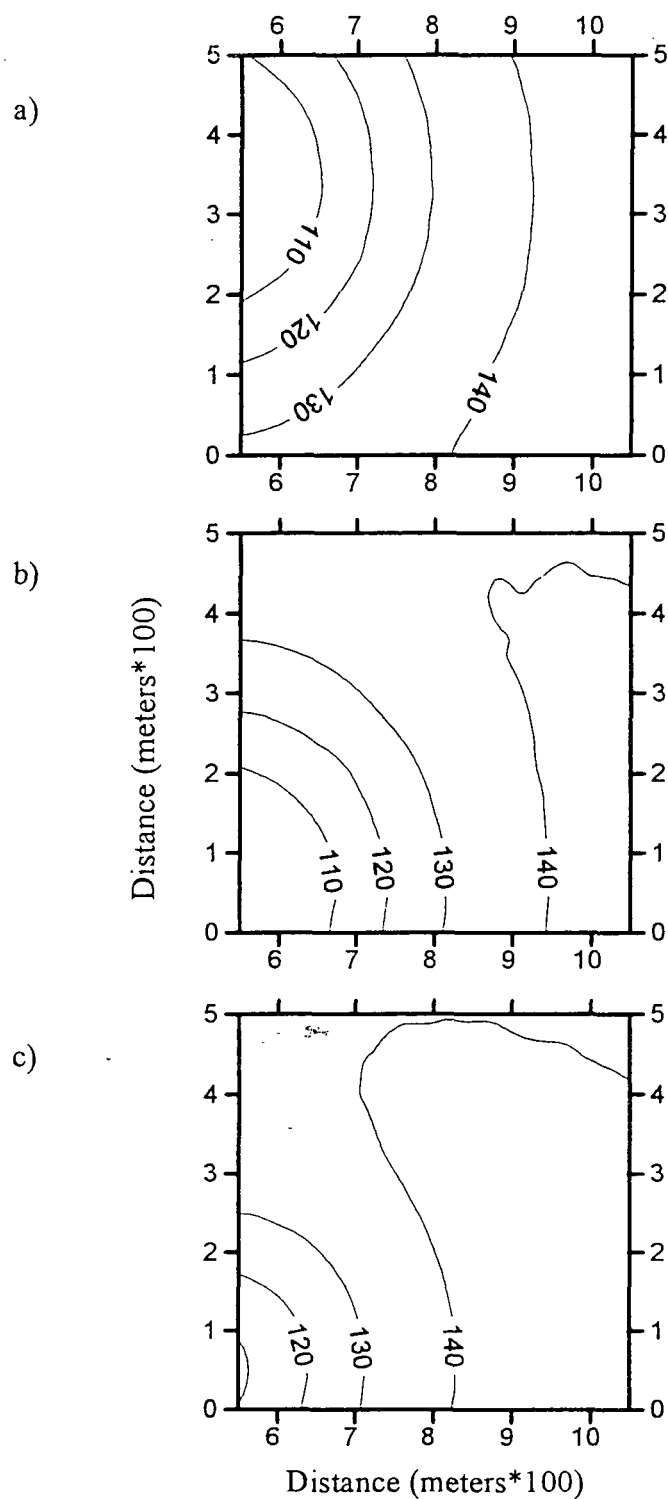


Figure 73: Total field apparent resistivity contour maps for a 25 m thick, 150 m deep layer, of 1000 Ohm-m resistivity, with a background resistivity of 100 Ohm-m.
 a) bipole 1, b) bipole 2, c) bipole 3

background resistivity if the borehole electrode is below the layer. Therefore, if we would have only the total field apparent resistivity contour map for the borehole electrode case we could easily interpret it as a response of a conductive layer. Once the layer is below a current borehole electrode position, the resistivity paradox disappears.

Figure 74:

The P_2 tensor invariant contour maps for the model used in Figures 68 - 73, created by using a combination of bipole 1 and bipole 2 responses, are presented in this figure. The P_2 -invariant is less sensitive to resistive layers than to conductive ones, such as were studied in Appendix A.

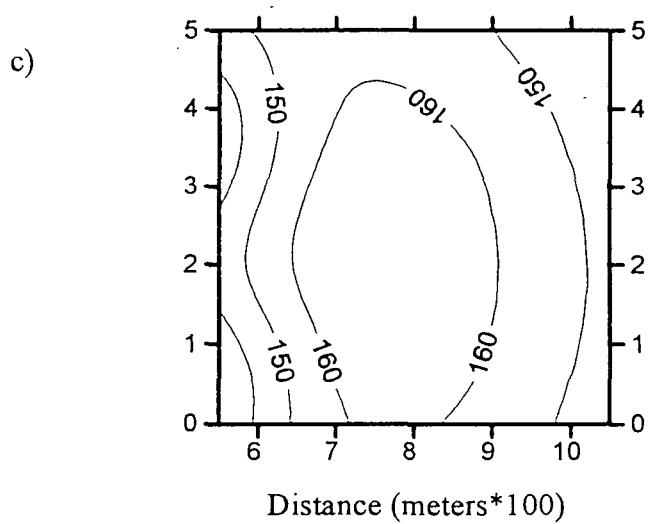
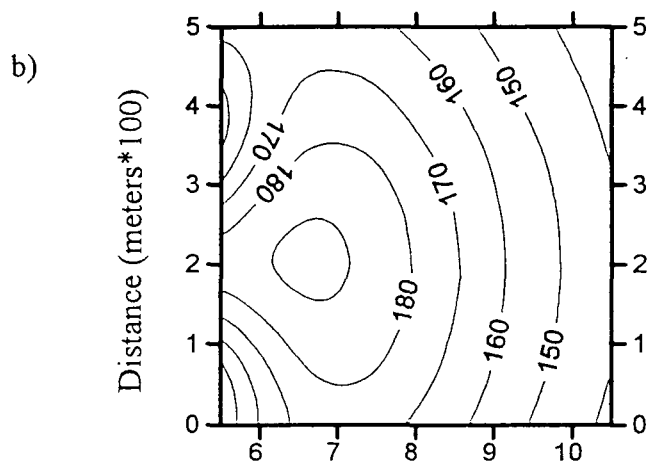
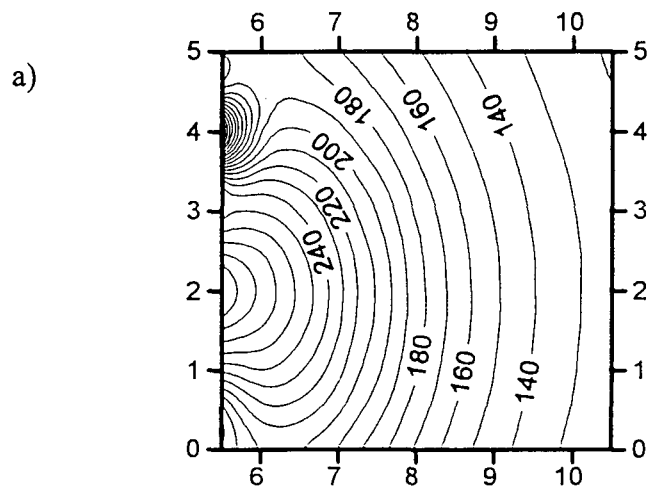
Figure 75:

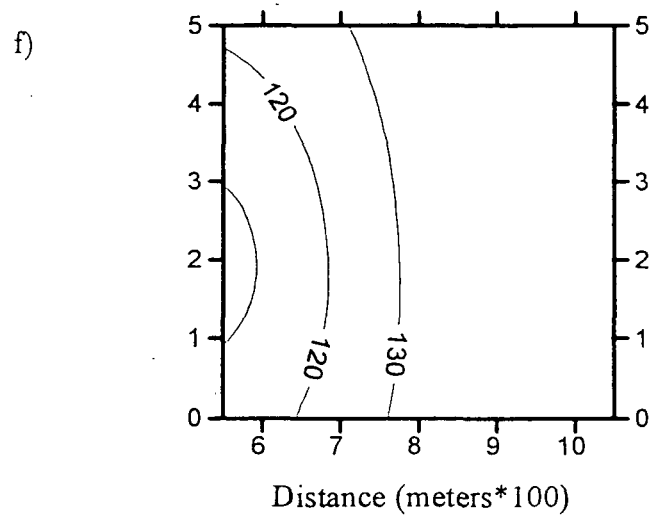
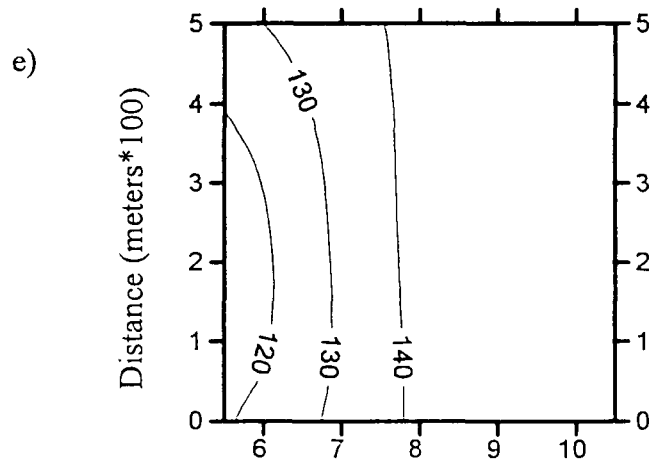
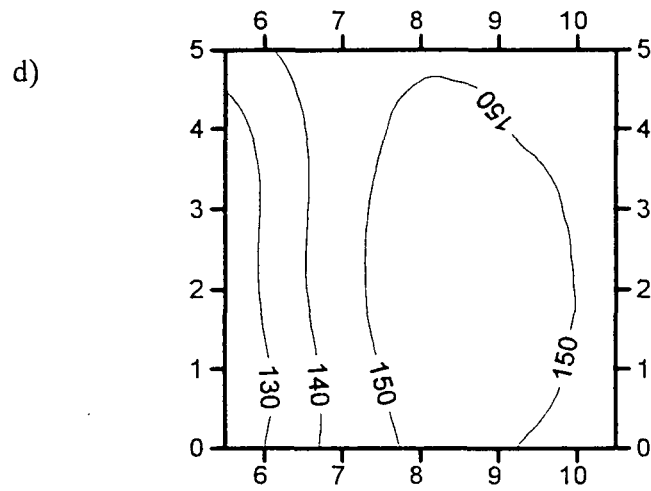
This figure is a sequence of the P_2 -invariant contour maps for the same model as in Figures 68 - 73, created by using the combination of the surface bipole 1 and the borehole bipole 3 responses. Comparison with Figure 74 shows the influence of borehole electrode, which tends to emphasize the deeper resistivities until the resistive layer is at the depth of the borehole electrode. At this point the responses become similar.

Figure 76 - 81:

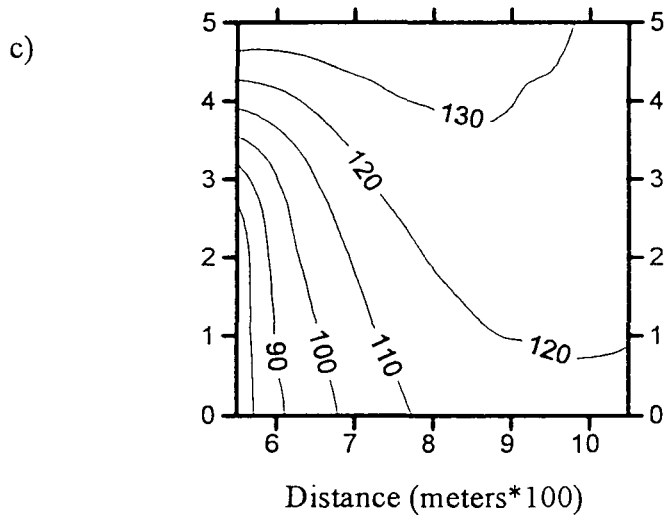
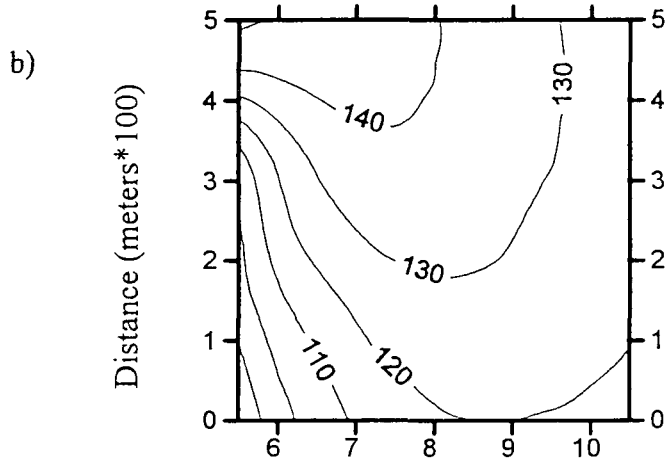
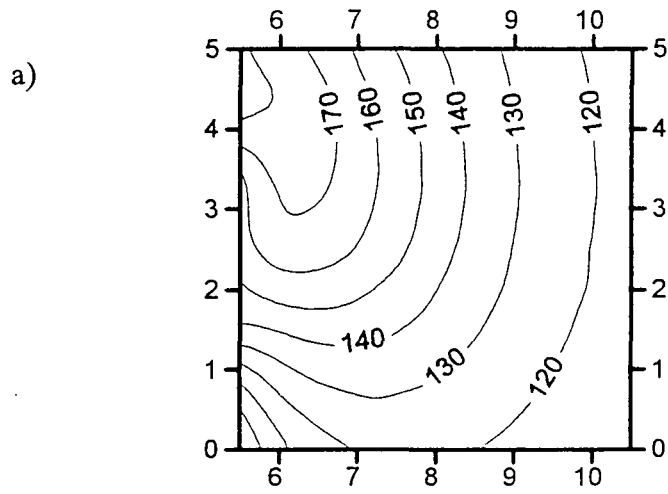
The total field apparent resistivity contour maps for the response of a 2-D structure for each bipole source are presented here. The anomalous body is 200 m wide in the x-direction and 25 m thick, and is buried at a range of depths. The resistivity of the structure is 1000 Ω -m, while the background resistivity is 100 Ω -m. We do not see large gradients in the apparent resistivity close to the boundary of the body as is the

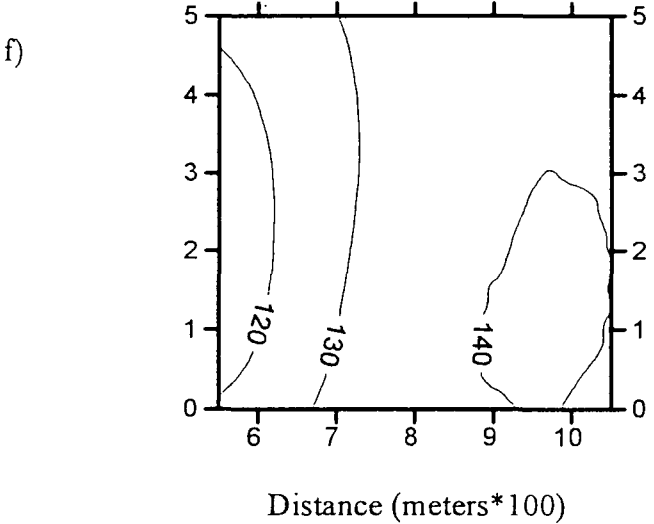
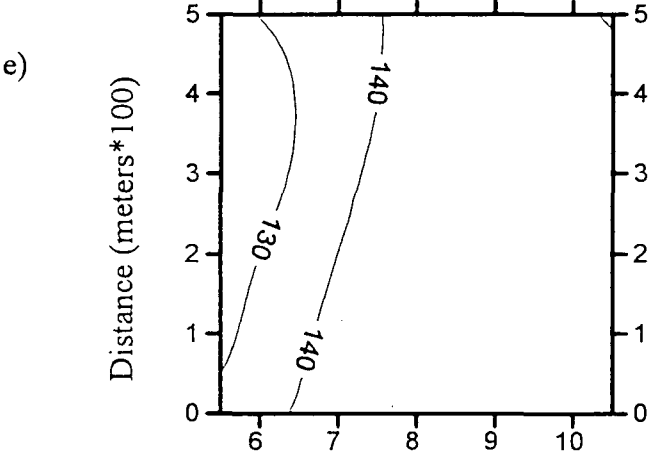
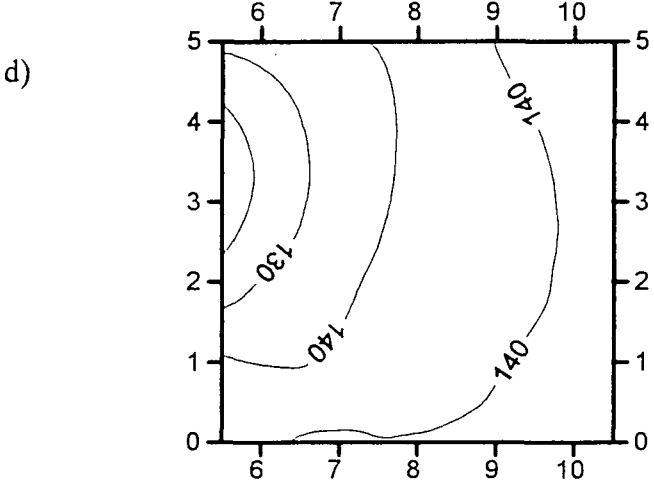
- Figure 74: The P2-invariant contour maps for a 25 m thick layer, of 1000 Ohm-m resistivity, with a background resistivity of 100 Ohm-m, using bipole 1 and bipole 2.
- a) 25 m deep layer
 - b) 50 m deep layer
 - c) 75 m deep layer
 - d) 100 m deep layer
 - e) 125 m deep layer
 - f) 150 m deep layer





- Figure 75: The P2-invariant contour maps for a 25 m thick layer, of 1000 Ohm-m resistivity, with a background resistivity of 100 Ohm-m, using bipole 1 and bipole 3.
- a) 25 m deep layer
 - b) 50 m deep layer
 - c) 75 m deep layer
 - d) 100 m deep layer
 - e) 125 m deep layer
 - f) 150 m deep layer





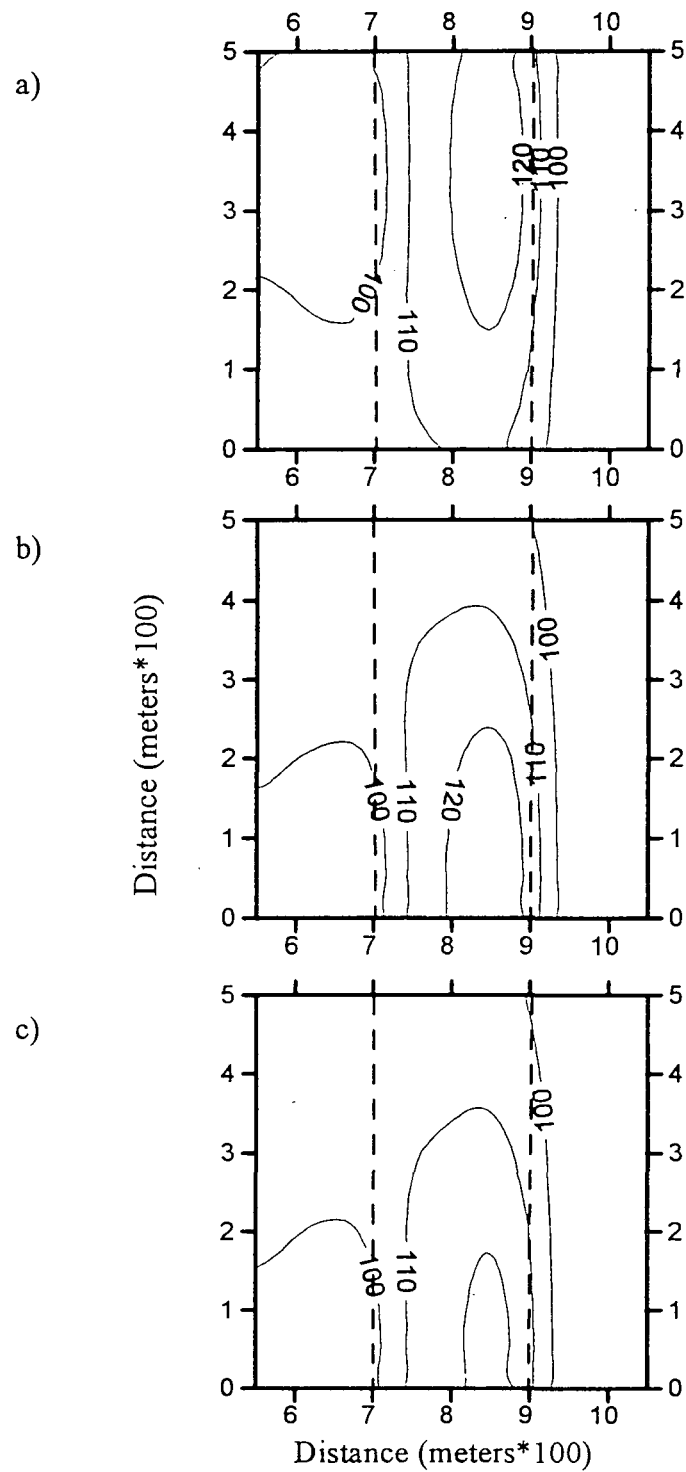


Figure 76: Total field apparent resistivity contour maps for a 25 m thick and 200 m wide body, at the depth of 25 m, of 1000 Ohm-m resistivity, with a background resistivity of 100 Ohm-m.
 a) bipole 1, b) bipole 2, c) bipole 3

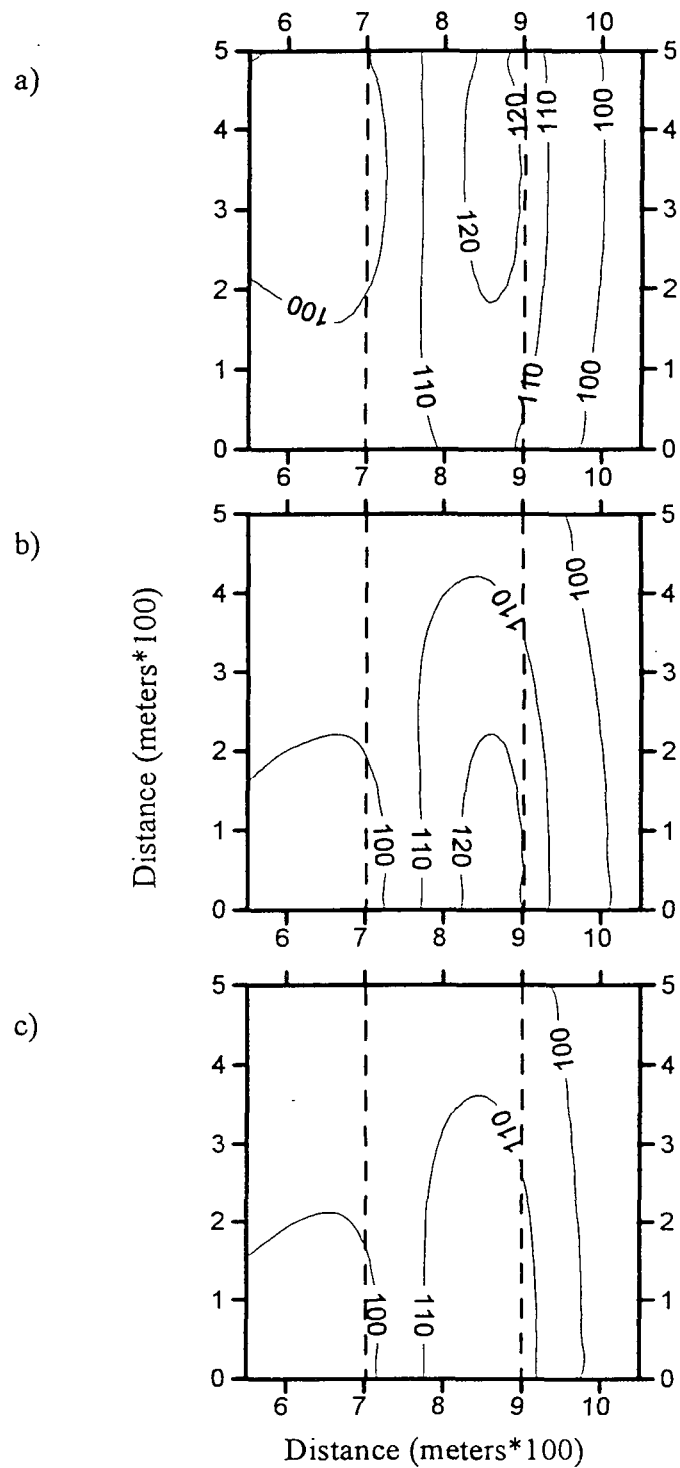


Figure 77: Total field apparent resistivity contour maps for a 25 m thick and 200 m wide body, at the depth of 50 m, of 1000 Ohm-m resistivity, with a background resistivity of 100 Ohm-m.
 a) bipole 1, b) bipole 2, c) bipole 3

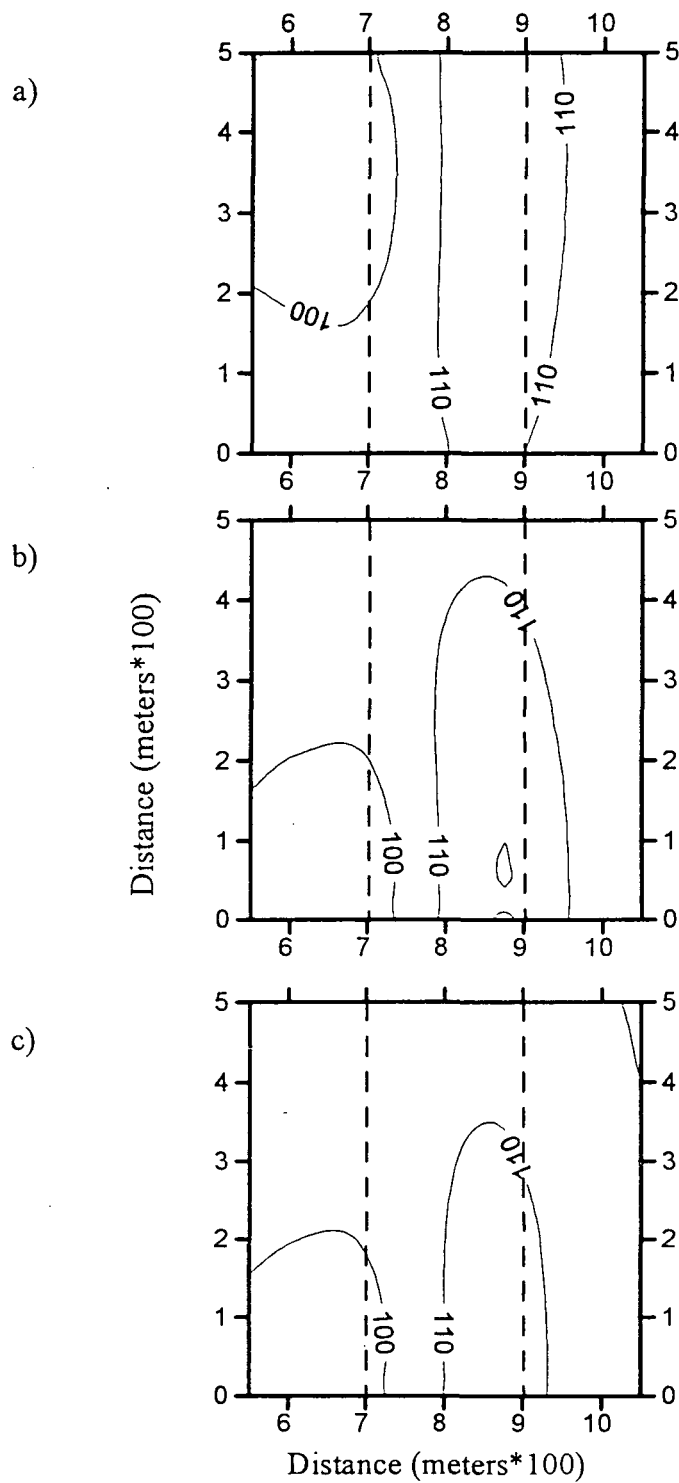


Figure 78: Total field apparent resistivity contour maps for a 25 m thick and 200 m wide body, at the depth of 75 m, of 1000 Ohm-m resistivity, with a background resistivity of 100 Ohm-m.
 a) bipole 1, b) bipole 2, c) bipole 3

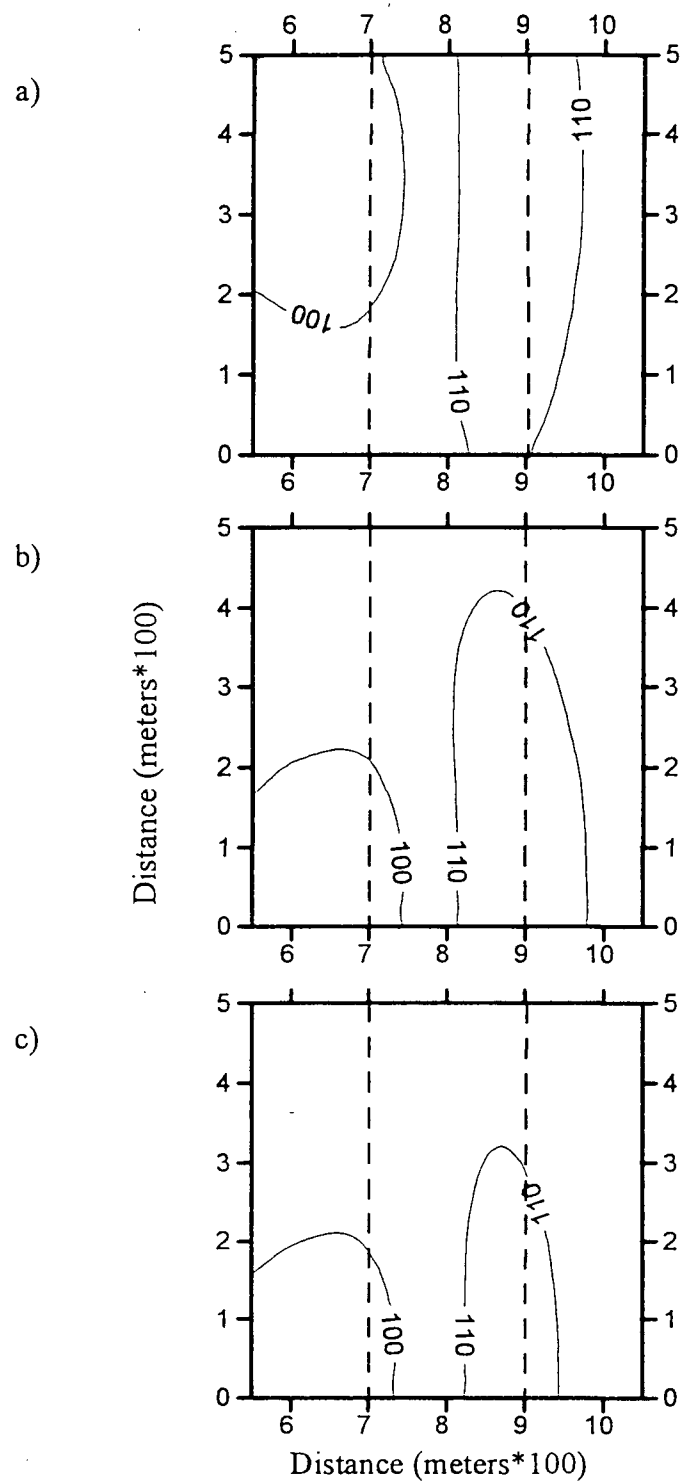


Figure 79: Total field apparent resistivity contour maps for a 25 m thick and 200 m wide body, at the depth of 100 m, of 1000 Ohm-m resistivity, with a background resistivity of 100 Ohm-m.
 a) bipole 1, b) bipole 2, c) bipole 3

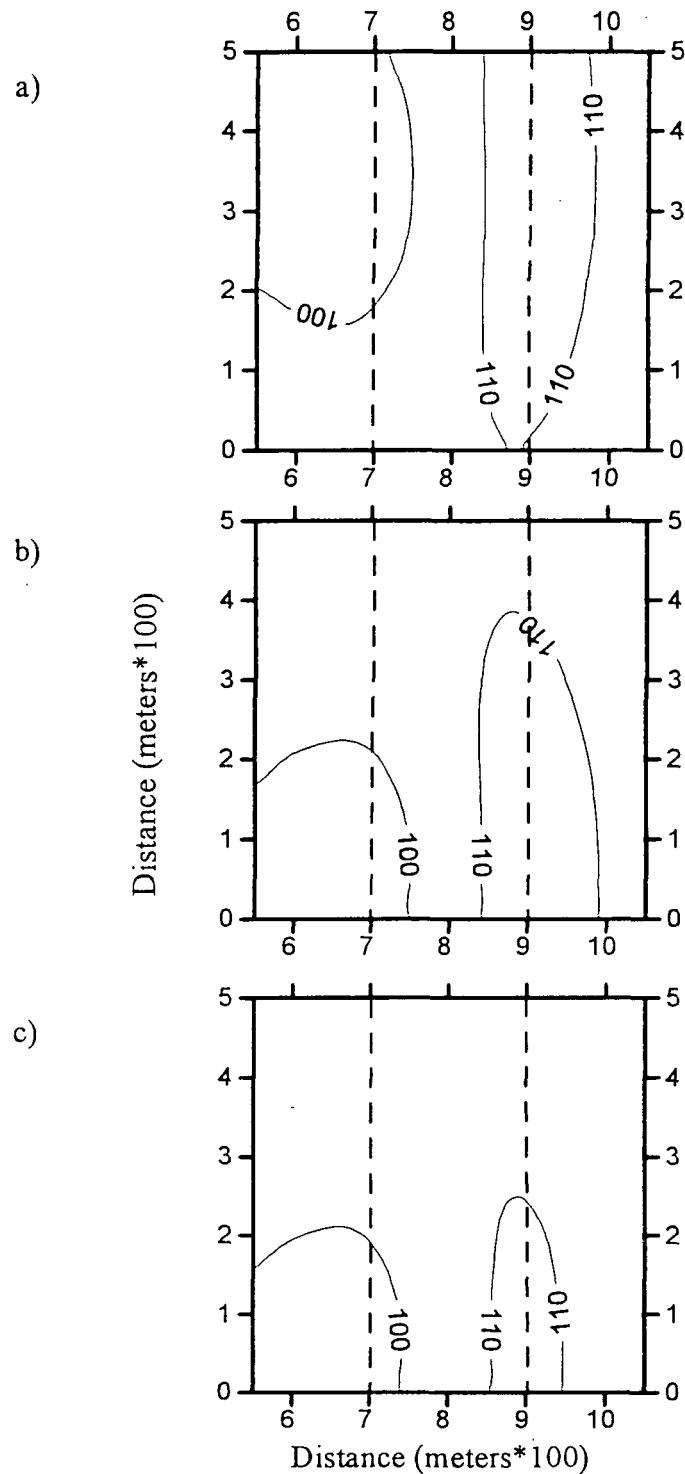


Figure 80: Total field apparent resistivity contour maps for a 25 m thick and 200 m wide body, at the depth of 125 m, of 1000 Ohm-m resistivity, with a background resistivity of 100 Ohm-m.
 a) bipole 1, b) bipole 2, c) bipole 3

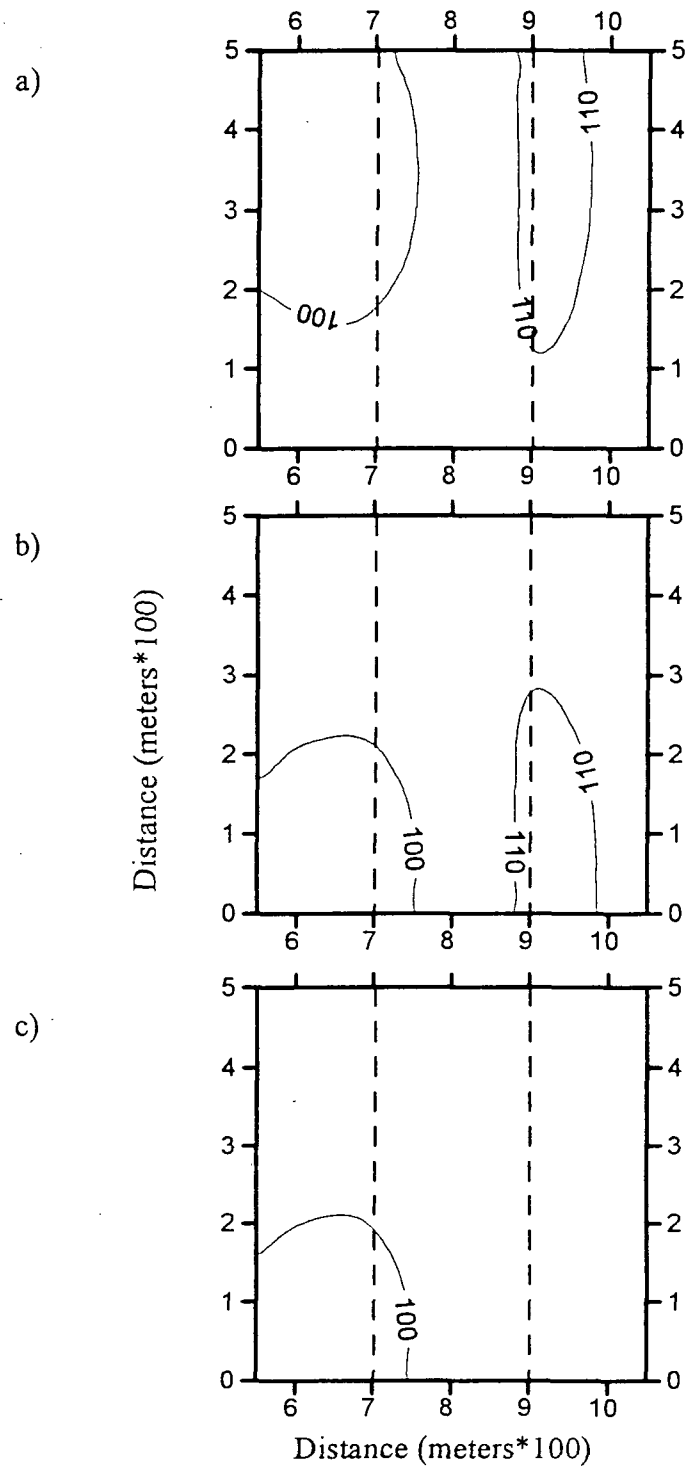


Figure 81: Total apparent resistivity contour maps for a 25 m thick and 200 m wide body, at the depth of 150 m, of 1000 Ohm-m resistivity, with a background resistivity of 100 Ohm-m.
 a) bipole 1, b) bipole 2, c) bipole 3

case for a conductive body. There is not much difference between the contour maps for bipole 1, bipole 2 or bipole 3, indicating the distance of the resistor from each bipole and the absence of a preferred current path.

Figure 82:

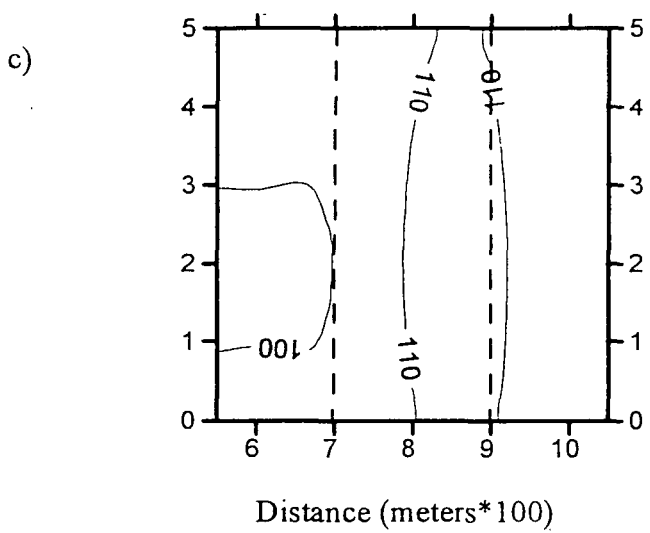
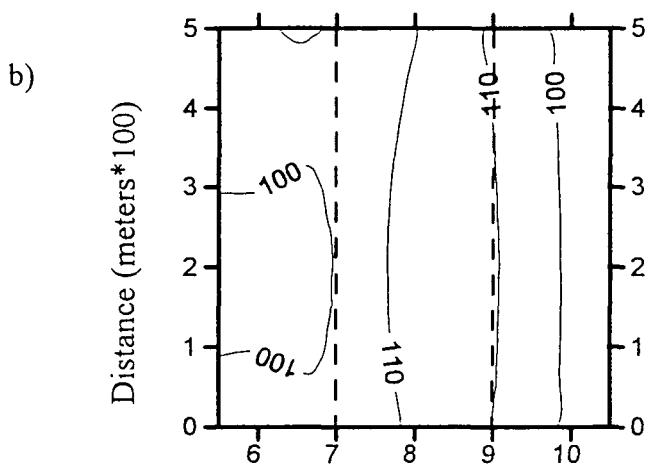
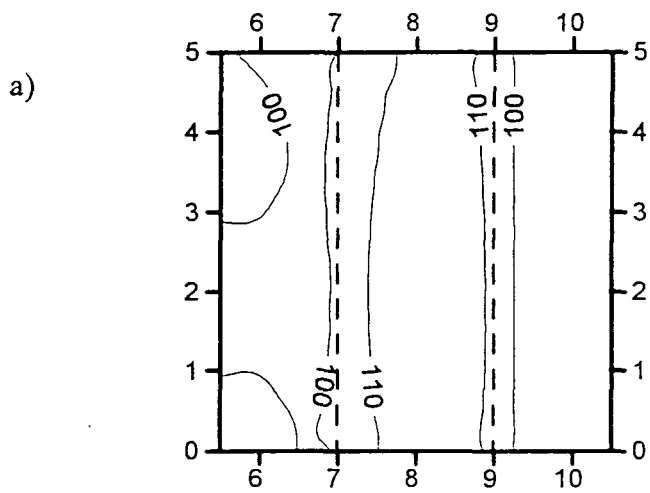
The P_2 -invariant contour maps for the model used in Figures 76 - 81, created by using bipole 1 and bipole 2 responses, are presented in this figure. The P_2 -invariant is relatively insensitive to the presence of the highly resistive body in the less resistive background.

Figure 83:

This figure contains a sequence of the P_2 -invariant contour maps for the model used in Figures 76 - 81 created by using bipole 1 and bipole 3 responses. These contour maps are almost identical to the contour maps in Figure 82, again reflecting the absence of a preferred geometry between any of the bipoles and the resistive body.

Figure 82: The P2-invariant contour maps for a 25 m thick and 200 m wide body, of 1000 Ohm-m resistivity, with a background resistivity of 100 Ohm-m, using bipole 1 and bipole 2.

- a) 25 m deep body
- b) 50 m deep body
- c) 75 m deep body
- d) 100 m deep body
- e) 125 m deep body
- f) 150 m deep body



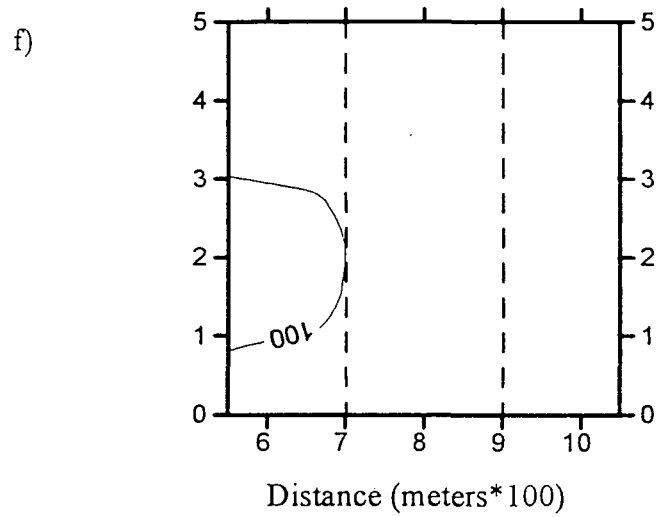
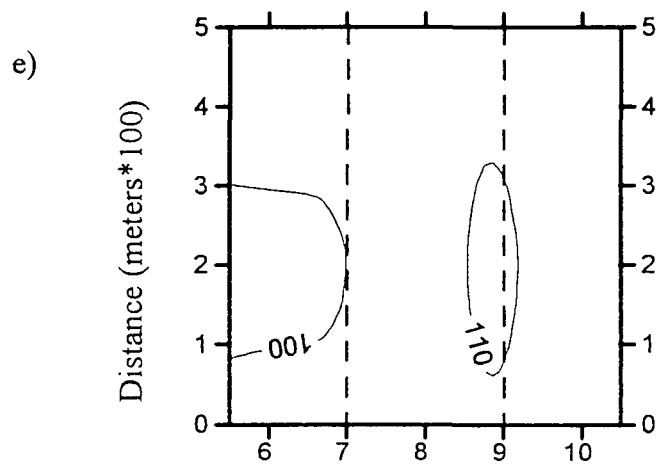
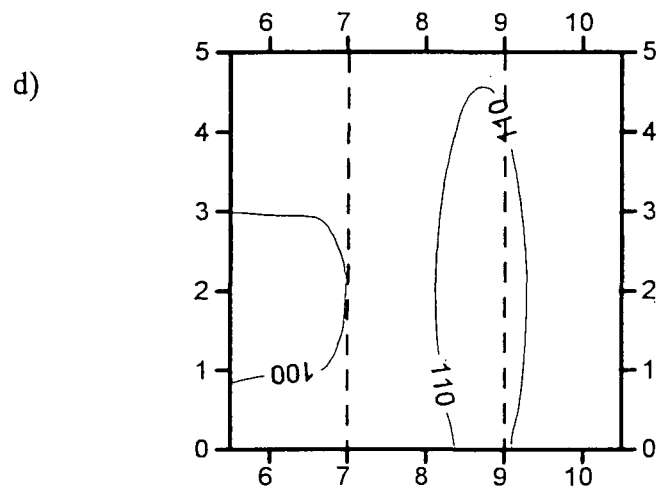
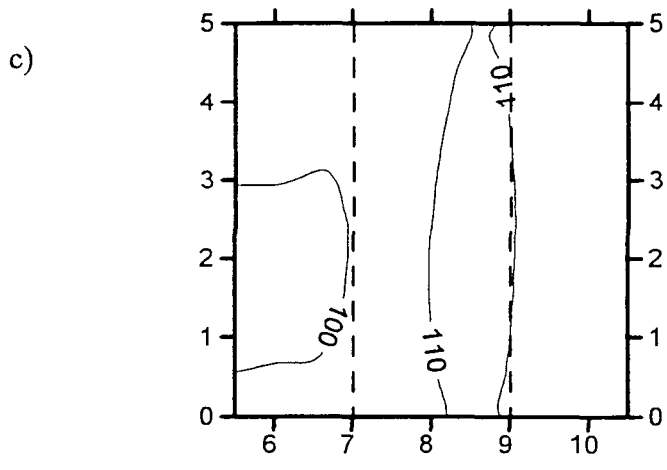
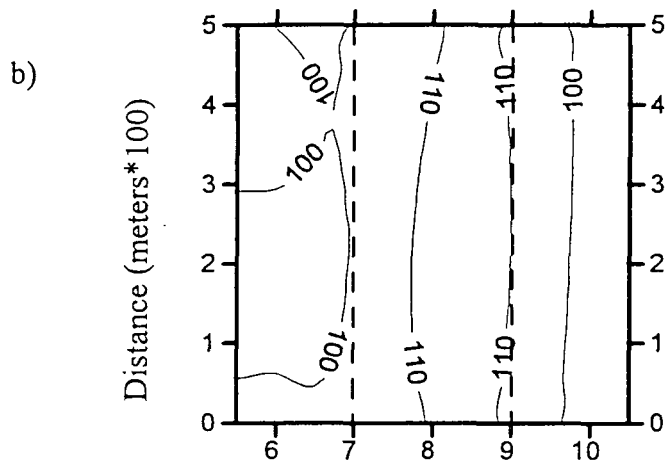
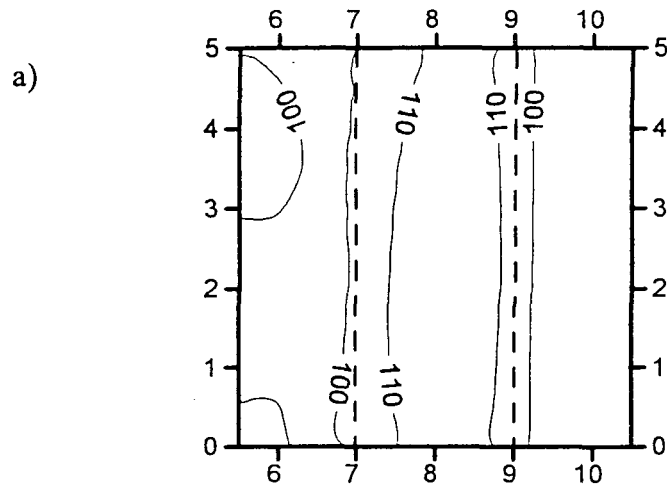
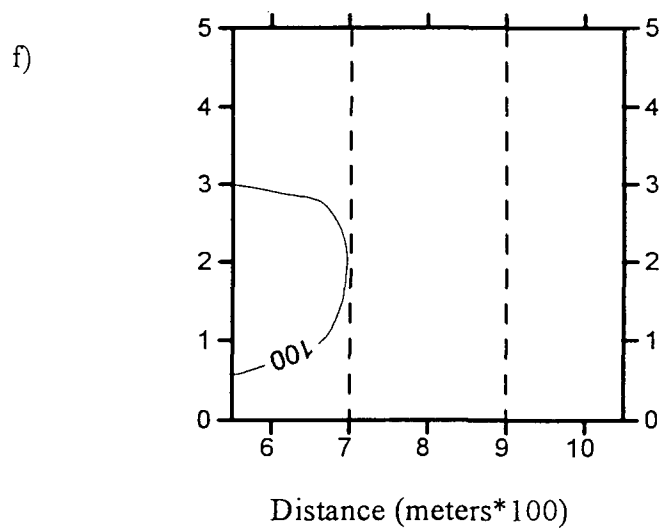
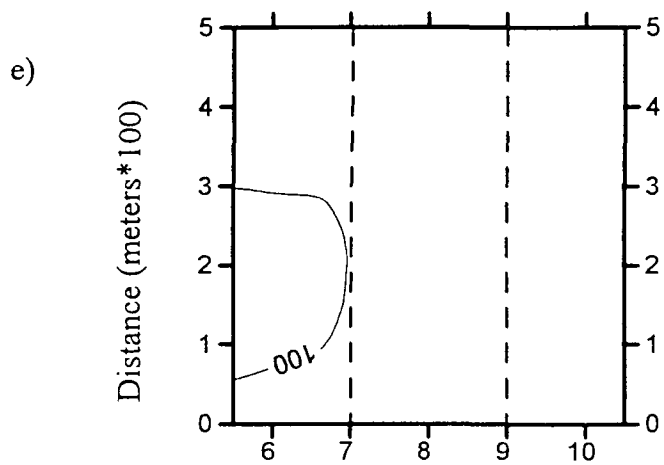
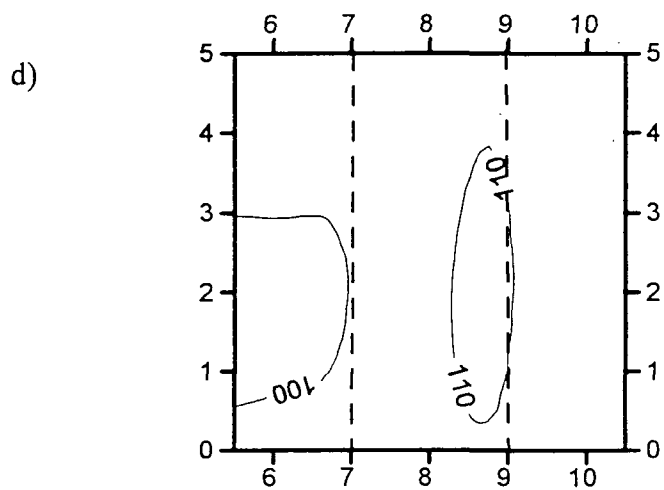


Figure 83: The P2-invariant contour maps for a 25 m thick and 200 m wide body, of 1000 Ohm-m resistivity, with a background resistivity of 100 Ohm-m, using bipole 1 and bipole 3.

- a) 25 m deep body
- b) 50 m deep body
- c) 75 m deep body
- d) 100 m deep body
- e) 125 m deep body
- f) 150 m deep body



Distance (meters*100)



APPENDIX C

**EFFECT OF INHOMOGENEITIES AT TRANSMITTER
OR RECEIVER LOCATIONS**

Appendix C contains a series of models showing the effect of inhomogeneities at transmitter or receiver locations on the observed resistivity response.

We have used the field electrode configuration for borehole UURI#1 through the entire appendix. The description of the field setup is given in Chapter 4. Bipole 1 is represented by the A_1B_1 current electrode pair, bipole 2 is represented by the A_1B_2 current electrode pair, and bipole 3 is represented by the A_1B_3 current electrode pair. The coordinates for these current electrodes are:

$A_1 = [32.5, 250.0, 0.0]$ m, $B_1 = [478.5, 344.1, 0.0]$ m;

$A_1 = [32.5, 250.0, 0.0]$ m, $B_2 = [500.0, 50.0, 0.0]$ m; and

$A_1 = [32.5, 250.0, 0.0]$ m, $B_3 = [500.0, 50.0, 100.0]$ m.

The receiver grid was from 550 m to 1050 m in the x-direction and from 0 m to 500 m in the y-direction. The receiver dipole length was 50 m.

Figure 84:

This figure shows the response of 500 Ω -m homogeneous half space if a 700 m wide and 150 m thick, 50 Ω -m block is present in the whole transmitter area. The results show that the conductive body near the transmitter electrodes has a major influence on the values of the measured apparent resistivity, which are considerably lower than the true background resistivity.

Figure 85:

A model for this figure has exactly the same geometry as a previous one, except that the resistivity values were interchanged. We are looking at the response of 50 Ω -m homogeneous half-space with a 700 m wide, 150 m thick block of 500 Ω -m resistivity at the transmitter site. The total field apparent resistivity contour maps as well as the P_2 -invariant contour map show that this structure will have an influence only on the

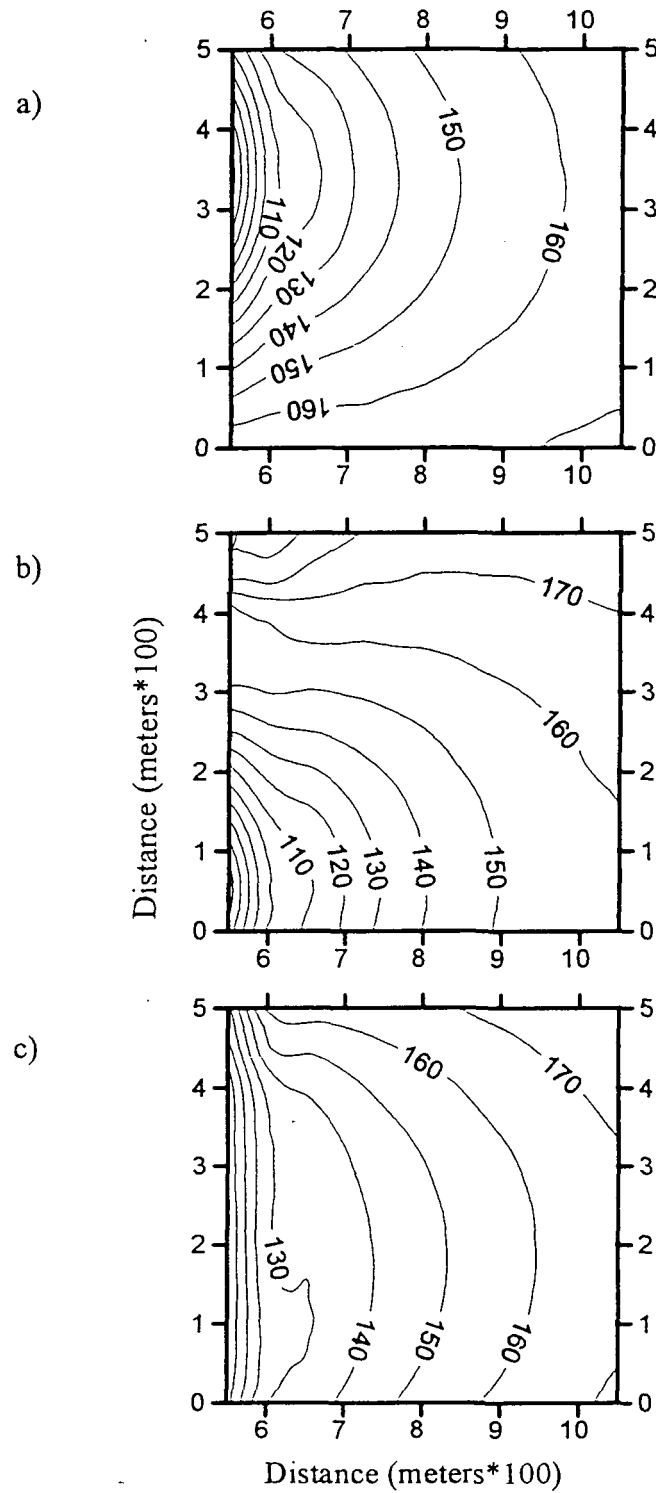


Figure 84: 50 Ohm-m block at transmitter site, with a background resistivity of 500 Ohm-m.

- a) total field apparent resistivity contour map for bipole 1
- b) total field apparent resistivity contour map for bipole 2
- c) P2-invariant contour map using bipole 1 and bipole 2

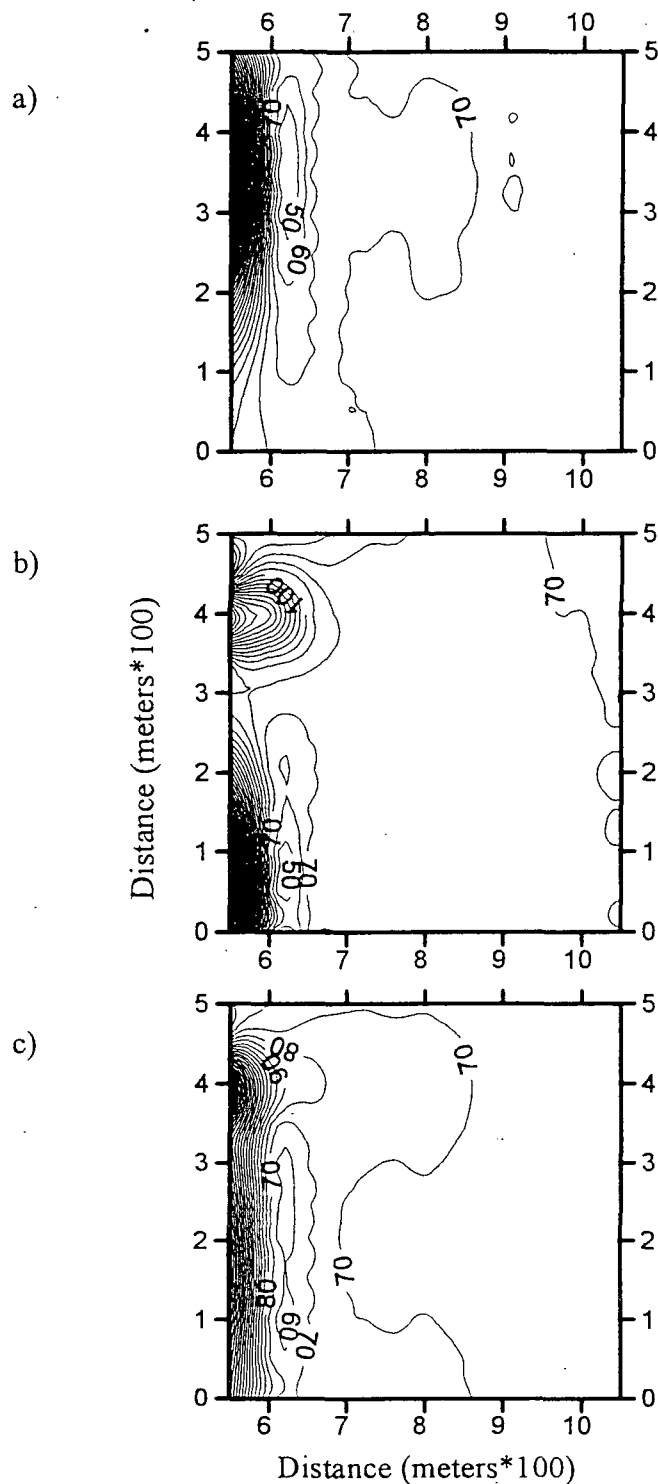


Figure 85: 500 Ohm-m block at transmitter site, with a background resistivity of 50 Ohm-m.

- a) total field apparent resistivity contour map for bipole 1
- b) total field apparent resistivity contour map for bipole 2
- c) P2-invariant contour map using bipole 1 and bipole 2

values measured with receivers on the closest line to the current electrodes. There is a very small influence of this high resistive block to the measured apparent resistivity response in the rest of the measured area. The computations presented in Figures 84 and 85 demonstrate that it is preferable to locate a transmitter on a resistive block as opposed to a conductive block, in agreement with Bibby and Hohmann (1993).

Figure 86:

The model for this figure is a 500 Ω -m half-space with a 700 m wide, 125 m thick block, of 50 Ω -m resistivity in the entire receiver area, while transmitter is located in the highly resistive area. The apparent resistivity values show that the main response is caused by this conductive inhomogeneity. Thus the area beneath the receivers is shielded by the 125 m thick 50 Ω -m cover.

Figure 87:

The response presented in this figure is a response of the 500 Ω -m half-space with a 250 m wide and 100 m thick block of infinite strike extent of 50 Ω -m running from east to west and straddling the current electrodes B_1 and B_2 , while the current electrode A_1 and all receivers are in the high resistive environment. This inhomogeneity has a strong influence on the measured apparent resistivity values and causes significant decrease of these values with respect to the true half-space resistivity.

Figure 88:

Shown is the influence of the high resistive inhomogeneity straddling the current electrodes B_1 and B_2 as in the previous figure. The model used in this case is 250 m wide, 100 m thick, and is a 500 Ω -m resistive block in a 50 Ω -m background.

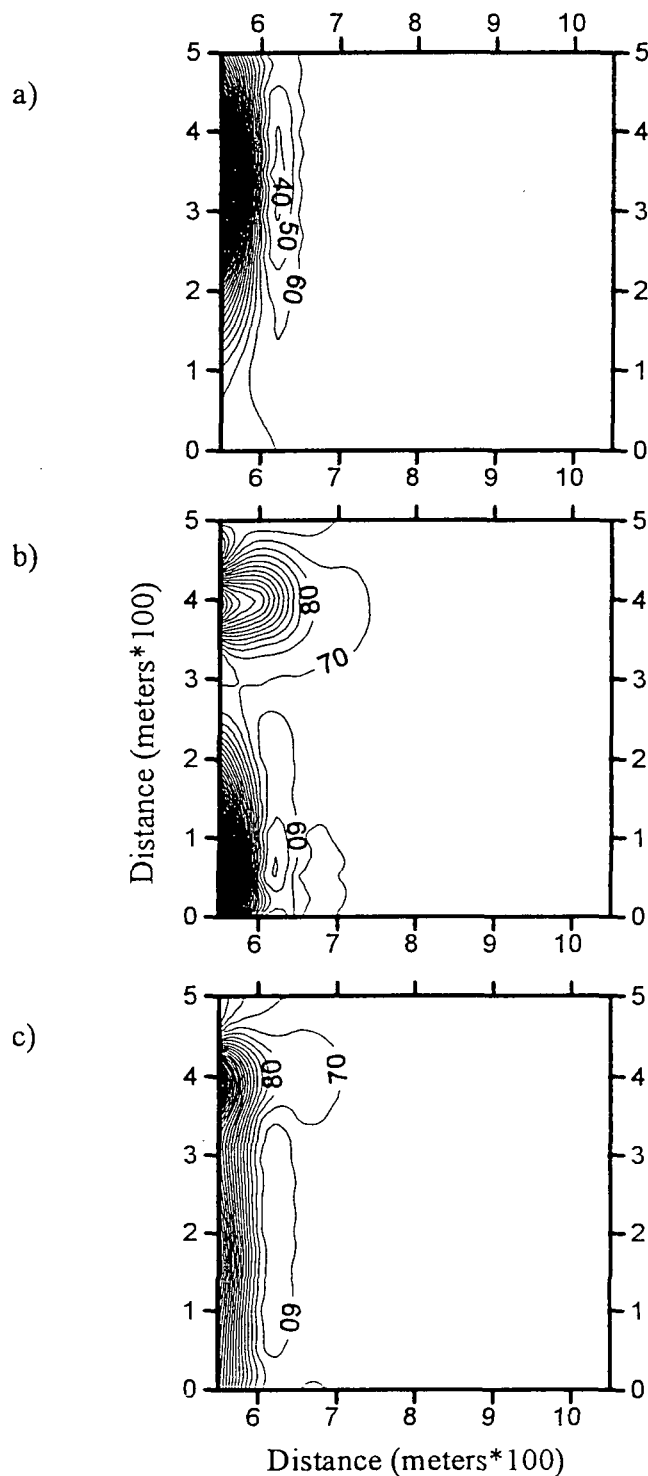


Figure 86: 50 Ohm-m block at receiver grid, with a background resistivity of 500 Ohm-m.

- a) total field apparent resistivity contour map for bipole 1
- b) total field apparent resistivity contour map for bipole 2
- c) P2-invariant contour map using bipole 1 and bipole 2

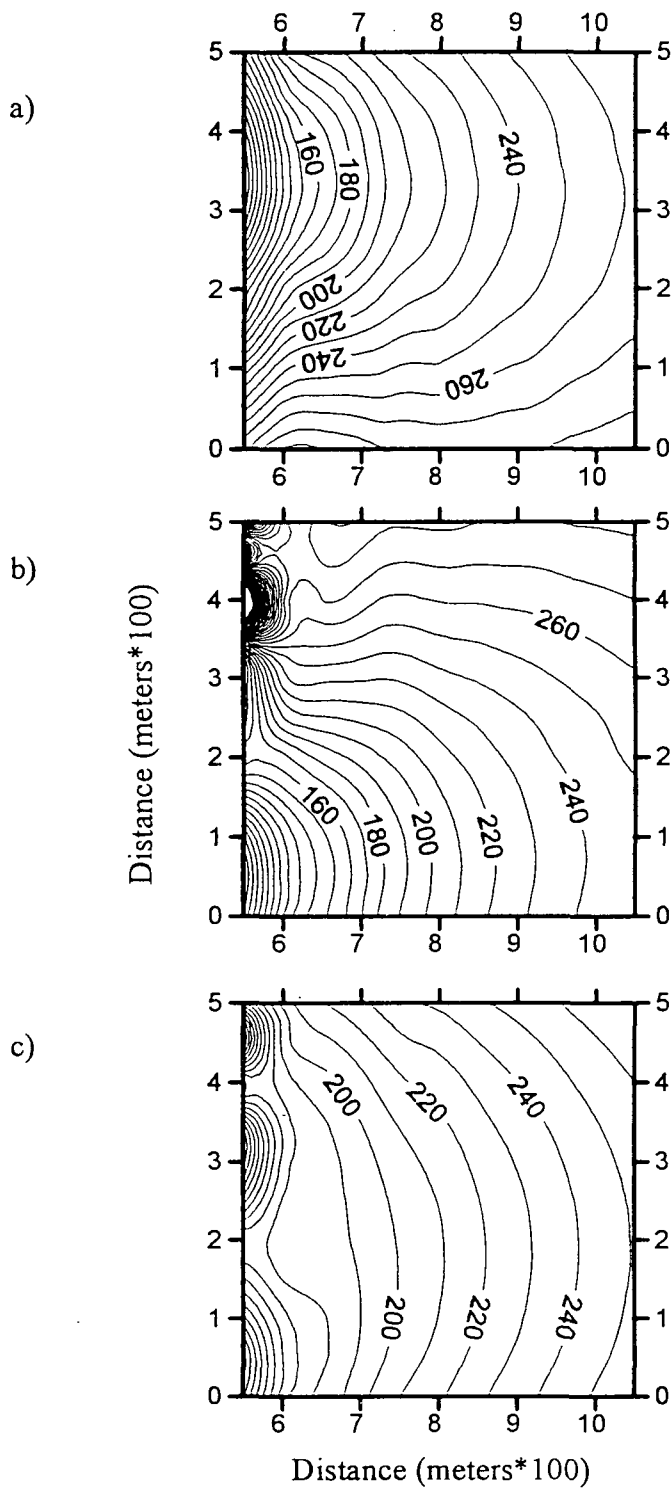


Figure 87: 50 Ohm-m block at current electrode B1 and B2 locations, with a background resistivity of 500 Ohm-m.

- a) total field apparent resistivity contour map for bipole 1
- b) total field apparent resistivity contour map for bipole 2
- c) P2-invariant contour map using bipole 1 and bipole 2

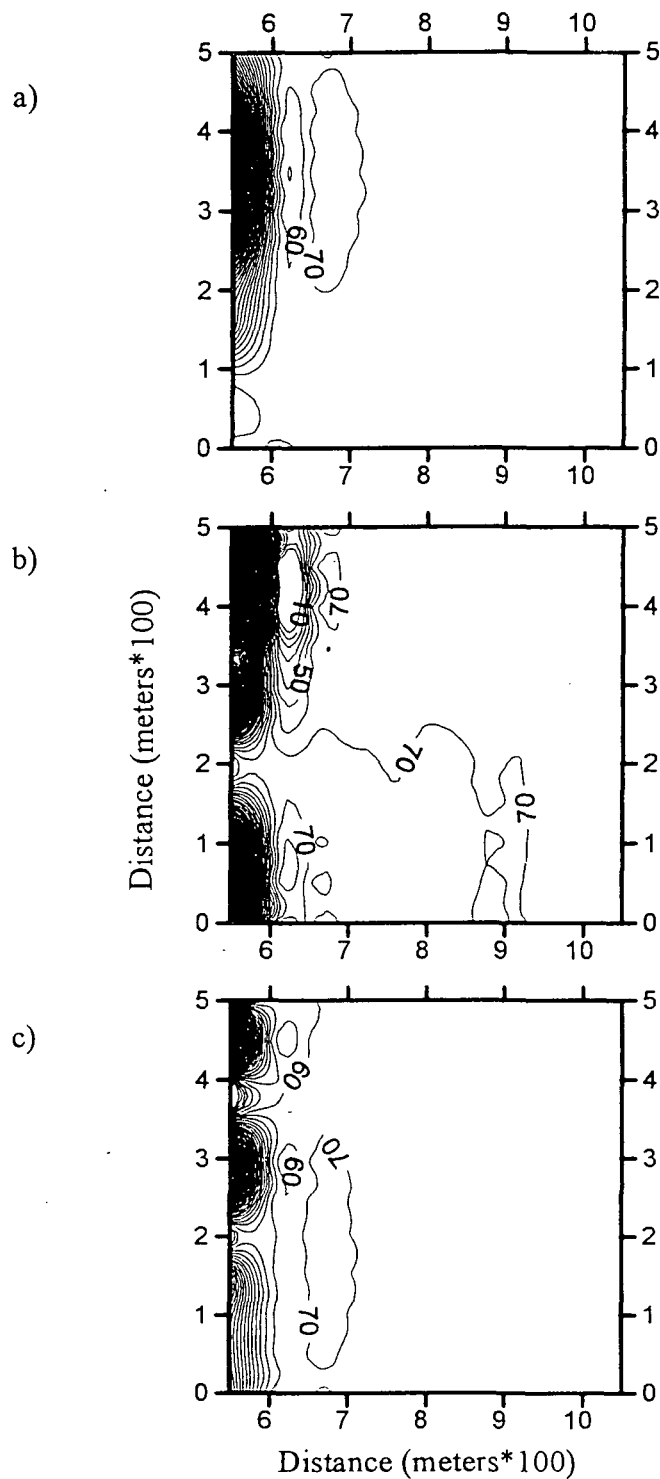


Figure 88: 500 Ohm-m block at current electrode B1 and B2 locations, with a background resistivity of 50 Ohm-m.
 a) total field apparent resistivity contour map for bipole 1
 b) total field apparent resistivity contour map for bipole 2
 c) P2-invariant contour map using bipole 1 and bipole 2

The highly resistive body close to the current electrodes does not have a significant influence on the measured response.

REFERENCES

- Alfano, L., 1962, Geoelectrical prospecting with underground electrodes: *Geophysical Prospecting*, v. 10, p. 290-303.
- Asch, T. H., and H. F. Morrison, 1989, Mapping and monitoring electrical resistivity with surface and subsurface electrode arrays: *Geophysics*, v. 54, p. 235-244.
- Bevc, D., and H. F. Morrison, 1991, Borehole-to-surface resistivity monitoring of a salt water injection experiment: *Geophysics*, v. 56, p. 769-777.
- Bibby, H. M., and G. F. Risk, 1973, Interpretation of dipole-dipole resistivity surveys using a hemispheroidal model: *Geophysics*, v. 38, p. 719-736.
- Bibby, H. M., 1977, The apparent resistivity tensor: *Geophysics*, v. 42, p. 1258-1261.
- Bibby, H. M., 1978, Direct current resistivity modeling for axially symmetric bodies using the finite element method: *Geophysics*, v. 43, p. 550-562.
- Bibby, H. M., 1986, Analysis of multiple-source bipole-quadripole resistivity surveys using the apparent resistivity tensor: *Geophysics*, v. 51, p. 972-983.
- Bibby, H. M., and G. W. Hohmann, 1993, Three-dimensional interpretation of multiple-source bipole-dipole resistivity data using the apparent resistivity tensor: *Geophysical Prospecting*, v. 41, p. 697-723.
- Daniels, J. J., 1977, Three-dimensional resistivity and induced polarization modeling using buried electrodes: *Geophysics*, v. 42, p. 1006-1019.
- Daniels, J. J., 1978, Interpretation of buried electrode resistivity data using a layered earth model: *Geophysics*, v. 43, p. 988-1001.
- Daniels, J. J., 1983, Hole-to-surface resistivity measurements: *Geophysics*, v. 48, p. 87-97.
- Doicin, D., 1976, Quadripole-quadripole arrays for direct current resistivity measurements - model studies: *Geophysics*, v. 41, p. 79-95.
- Ellis, D. V., 1987, *Well Logging for Earth Scientists*: Elsevier, New York, 532 p.

- Hearst, J. R., and P. H. Nelson, 1985, *Well Logging for Physical Properties*: McGraw-Hill, 571 p.
- Lanczos, C., 1961, *Linear Differential Operators*, Van Nostrand, 564 p.
- Landau, L. D., and E. M. Lifshitz, 1960, *Electrodynamics of Continuous Media*: Pergamon Press Inc., 417 p.
- Lutz, S. J., P. B. Anderson, and D. L. Nielson, 1993, *Stratigraphic Correlation Ferron Sandstone, Muddy Creek Area, Utah*: University of Utah Research Institute / Earth Science Laboratory, Publication # 93025-TR, Salt Lake City, Utah, 1 sheet.
- Nielson, D. L., S. J. Lutz, and P. B. Anderson, 1992, *Evaluation of reservoir heterogeneity using the statistical curvature analysis technique*. Final report: University of Utah Research Institute, Salt Lake City, 141 p.
- Ryer, T. A., 1981, *Deltaic coals of Ferron Sandstone Member of Mancos Shale - predictive model for Cretaceous coal-bearing strata of western interior*: *The American Association of Petroleum Geologists Bulletin*, v. 65, p. 2323-2340.
- Ryer, T. A., 1983, *Transgressive-regressive cycles and the occurrence of coal in some Upper Cretaceous strata of Utah*: *Geology*, v. 11, p. 207-210.
- Riemersma, P. E., 1989, *Sedimentology and depositional history of the lower Ferron Sandstone and related members of the Mancos Shale Formation, East-Central Utah*: Master's thesis, University of Utah, 142 p.
- Riemersma, P. E., and M. A. Chan, 1991, *Facies of the lower Ferron Sandstone and Blue Gate Shale Members of the Mancos Shale: lowstand and early transgressive facies architecture*: in Swift, D. J. P., G. F. Oertel, R. W. Tillman, and J. A. Thorne, eds., *Shelf Sand and Sandstone Bodies - geometry, facies and sequence stratigraphy*: Special publication of the International Association of Sedimentologists, no. 14, p. 489-510.
- Schlumberger, 1991, *Log Interpretation - Principles / Applications*: Schlumberger Educational Services, Houston, Texas, 223 p.
- Snyder, D. D., and R. M. Merkel, 1973, *Analytic models for the interpretation of electrical surveys using buried current electrodes*: *Geophysics*, v. 38, p. 513-529.

Telford, W. M., L. P. Geldart, R. E. Sheriff, and D. A. Keys, 1976, *Applied Geophysics*, Cambridge University Press, 861 p.

Zelt, F. B., 1985, *Natural Gamma-Ray Spectrometry, Lithofacies, and Depositional Environments of Selected Upper Cretaceous Marine Mudrocks, Western United States, including Tropic Shale and Tununk Member of Mancos Shale*: Ph.D. dissertation, Princeton University, Princeton, 372 p.